Geonium theory: Physics of a single electron or ion in a Penning trap

Lowell S. Brown and Gerald Gabrielse

Department of Physics, FM-15, University of Washington, Seattle, Washington 98195

A single charged particle in a Penning trap is a bound system that rivals the hydrogen atom in its simplicity and provides similar opportunities to calculate and measure physical quantities at very high precision. We review the theory of this bound system, beginning with the simple first-order orbits and progressively dealing with small corrections which must be considered owing to the experimental precision that is being achieved. Much of the discussion will also be useful for experiments with more particles in the trap, and several of the mathematical techniques have a wider applicability.

CONTENTS

. . .Even the best of them [mathematical physicists] have a tendency to treat physics as purely a matter of equations. I think this is shown by the poverty of the theoretical communications on the problems which face the experimenter today. I quite recognize that the experimenter is inclined to drop his mathematics also . . . . As a matter of fact it is extremely difficult to keep up the latter when all your energies are absorbed in experimentation.
Letter from Ernest Rutherford to Sir Arthur Schuster,
27 January, 1907

I. INTRODUCTION

The original use of magnetic and electric fields to increase the time that electrons remain within a discharge (Penning, 1936) has been greatly refined. A single particle can now be trapped indefinitely in the combination of a homogeneous magnetic field and an electrostatic quadrupole potential, which has come to be known as a Penning trap. A small cloud of stored particles is akin to a many-electron atom, but with the atomic nucleus replaced by an external trapping field that can be adjusted. Thus such a system may be called a "geonium atom,"[1] since the binding is to an external apparatus residing on the Earth. In this review we shall be concerned with the simplest such "atom," in which only a single charged particle is bound to a Penning trap. This is the analog of the hydrogen atom and, just as in the simplicity of the one-electron hydrogen atom, the properties of this single bound particle can be measured and calculated with extraordinary precision. And, just as in the hydrogen atom, such simple systems provide exceedingly precise tests and probes of the laws of nature.

To date, the most accurate measurement with a single trapped particle is of the magnetic moment of the electron, or rather its g factor (Van Dyck, Schwinberg, and Dehmelt, 1984)

$$g/2 = 1.001\,159\,652\,193(4) \, . \tag{1.1}$$

---

[1]The name is due to H. G. Dehmelt.

This is nearly 900 times more accurate than previous measurements by other techniques[2] and is surely one of the most precise measurements of the properties of an elementary particle. The great increase in accuracy comes in large part because the g value is measured essentially as the ratio of two frequencies of the same "atom." The measured value can be compared to a theoretical value that is also of exceptional precision,

$$g/2 = 1.001\,159\,652\,459(135) . \qquad (1.2)$$

This value includes the quantum-electrodynamic (QED) corrections in eighth order (see the review by Kinoshita and Sapirstein, 1984). The "theoretical" error of 135×10^{-12} is largely due to uncertainties in present measurements of the fine-structure constant α. Indeed, at the present time, one can use the measured g value and the QED calculation to obtain the most precise determination of the fine-structure constant,

$$\alpha^{-1} = 137.035\,994(10) . \qquad (1.3)$$

The effect of muonic and hadronic vacuum polarization is slightly smaller than the present experimental accuracy, and the effect of the weak interaction is much smaller yet. For comparison, the g value of the muon, measured in a storage ring (see the review by Field, Picasso, and Combley, 1979), is less precise by nearly a factor of 3000. However, the distance scale given by the Compton wavelength of this heavier lepton is also smaller by a factor of 207, so that the measured g value of the muon is already very sensitive to hadronic vacuum polarization.

A geonium atom may also be formed with a single proton. A single trapped proton has been observed, but as yet the cyclotron frequency has been measured only for a small cloud of protons (Van Dyck, Moore, Farnham, and Schwinberg, 1985). Comparing this cyclotron frequency with that of a small cloud of electrons yields the proton-electron mass ratio

$$m_p/m_e = 1836.152\,470(76) , \qquad (1.4)$$

with large increases in precision expected. Previous direct measurements of this ratio (Gärtner and Klempt, 1978; Gräff, Kalinowsky, and Traut, 1980), using small clouds of particles in a Penning trap but with a different detection technique, had an uncertainty that was larger by about an order of magnitude. Both groups are setting up to measure the ^{3}H-^{3}He mass difference in improved apparatus. This is an important quantity, whose precise measurement will be a significant contribution to the effort to measure the mass of the electron neutrino.

The g factor of the positron has also been measured with an accuracy comparable to that attained with an

electron (Van Dyck, Schwinberg, and Dehmelt, 1984). Its agreement with the electron value provides a stringent test of CPT symmetry for leptons. All quantum field theories are invariant under the CPT transformation, which simultaneously charge-conjugates, inverts in space, and reverses the direction of time. This transformation interchanges particle and antiparticle so that they must have the same magnetic moment (but with opposite sign), the same mass, and the same mean life. Experimental tests of CPT invariance are now tabulated by the Particle Data Group (1984). At present, 17 tests are listed. Of these, the most precise measurements with leptons are the comparison of the electron and positron g values in geonium and the comparison of the g values of positive and negative muons in the storage ring. The only other test of CPT of comparable precision is derived from the famous kaon mass oscillation experiment, which can be interpreted as comparison of the masses of the K^0 and $\bar{K}^0$ mesons. No precise test of CPT has yet been done with baryons. However, a precise comparison of the cyclotron frequencies of a trapped proton and antiproton is tantamount to a comparison of their masses and thus would provide a high-precision test of CPT symmetry for baryons. A program is now under way to capture antiprotons in a Penning trap, with the study of a single antiproton as its goal (Gabrielse, Kalinowsky, and Kells, 1985). This will also open up a new variety of experiments with a single particle of antimatter essentially at rest.

The accuracy of the measurements on electrons and positrons may yet be improved, and interesting physics is emerging from an attempt to do this which exploits the minute relativistic shifts on a very slow electron. Although the g factor has yet to be measured by this method, the nonlinear cyclotron resonance brought about by the relativistic mass increase has been accurately traced out (Gabrielse, Dehmelt, and Kells, 1985). The observation of this resonance, which is bistable and exhibits hysteresis, is of interest in its own right. Another interesting phenomenon observed with a single trapped electron is a change in the radiative lifetime of the cyclotron motion caused by the effective microwave cavity formed by the Penning trap electrodes (Gabrielse and Dehmelt, 1985). This was the first observation of such inhibited spontaneous emission within a cavity and demonstrates the promise of this system for radiative physics.[3]

We conclude this Introduction by giving a brief overview of the electron geonium experiments, which also introduces the topics covered in the subsequent sections. Because of the importance of the simplest system for fundamental measurements, and in order to confine our review, we restrict our discussion to the theory attached to a single trapped particle, the hydrogenlike geonium atom. Much of what we shall describe, however, is also useful for the understanding of the physics of trapped ion

---

[2]A long series of measurements by Crane, Rich, and colleagues culminated in $g/2 = 1.001\,159\,657\,700(3500)$. Final reviews of this and related work are given by Rich and Wesley (1972) and by Conti, Newman, Rich, and Sweetman (1984).

[3]A cavitylike effect was observed earlier by Drexhage (1974).

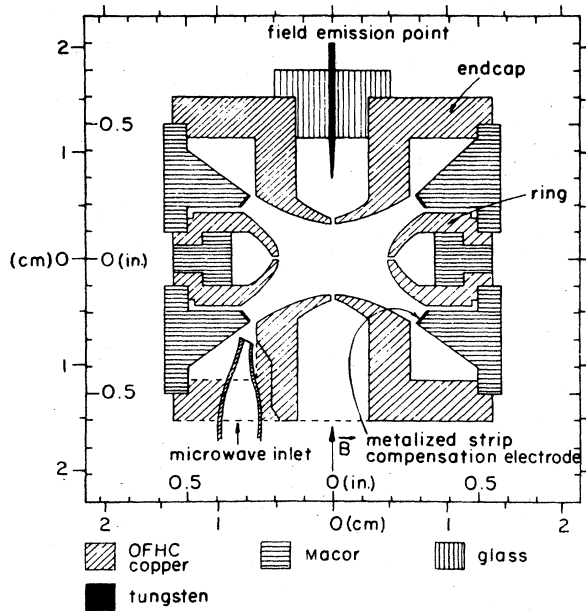FIG. 2. Electric and magnetic field configurations of the Penning trap.

FIG. 1. Scale drawing of an experimental Penning trap (Gabrielse and Dehmelt, 1985).

clouds, which are used in many recent interesting experiments (see the reviews by Wineland, Itano, and Van Dyck, 1984; Wineland, Itano, Bergquist, Bollinger, and Prestage, 1984). Moreover, although we concentrate on a particular physical system, the results we describe and the mathematical methods we employ often have a much more general applicability. A more complete collection of references is provided in the subsequent sections. We have endeavored to make our sections complete and accessible to anyone with a background in physics. We hope the reader will often be as charmed by the beautiful physics in this simple system as we have been.

A typical Penning trap configuration is shown in Fig. 1. Electrons are initially introduced into the trap by applying a high voltage to the field emission point. This produces a beam of energetic electrons that collide with the very sparse residual gas atoms to produce slow electrons, which are then captured in the trap. The electrodes of the trap are hyperbolas of revolution which produce an electric quadrupole field as indicated in Fig. 2. Superimposed along the axis of the trap is a strong uniform magnetic field. The resultant motion (Sec. II) consists of a fast circular cyclotron motion with a small radius carried along by a slow circular magnetron drift motion in a large orbit. This results in an epicyclic orbit in the xy plane. In addition, the electron oscillates harmonically along the z axis perpendicular to the xy plane, the axis of the magnetic field. The total motion is depicted in Fig. 3. In general, the particle is captured in large orbits. The radius of the cyclotron submotion shrinks rapidly under the emission of synchrotron radiation (Sec. II), while the axial oscillation is coupled, as outlined in the next paragraph, to an external detector at low temperature. Its amplitude
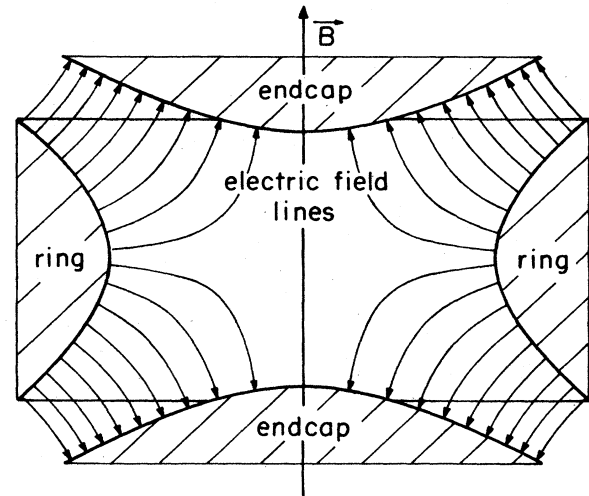
quickly decreases as it comes into thermal equilibrium with this external circuit (Sec. III). The large magnetron motion is a circle about an effective potential hill, and although this motion is unstable, it is slow and weakly coupled to its environment and is thus effectively stable. A clever refrigeration technique is used (Van Dyck, Schwinberg, and Dehmelt, 1978) to shrink the magnetron radius (Sec. IV) so that the total motion occupies only a very small spatial volume where the fields are most homogeneous. Otherwise large linewidths resulting from the nonlinearities would make precise measurements impossible.

The axial oscillation is monitored (Sec. III) by the method illustrated in Fig. 4. The moving electron induces alternating image charges in the endcap and ring electrodes, which in turn cause an oscillating current to flow
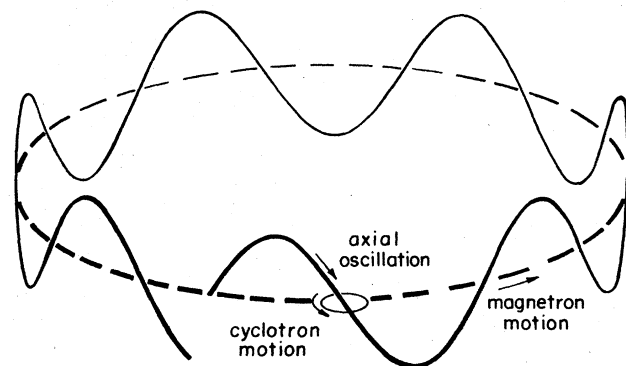

FIG. 3. Orbit of a charged particle in a Penning trap. The dashed line is the large and slow magnetron circle component of the motion. This, added to the axial oscillation, produces the guiding-center motion shown by the solid line. The total motion is given by adding the fast but small cyclotron circular motion about this moving guiding center. (Adapted from Ekstrom and Wineland, 1980.)
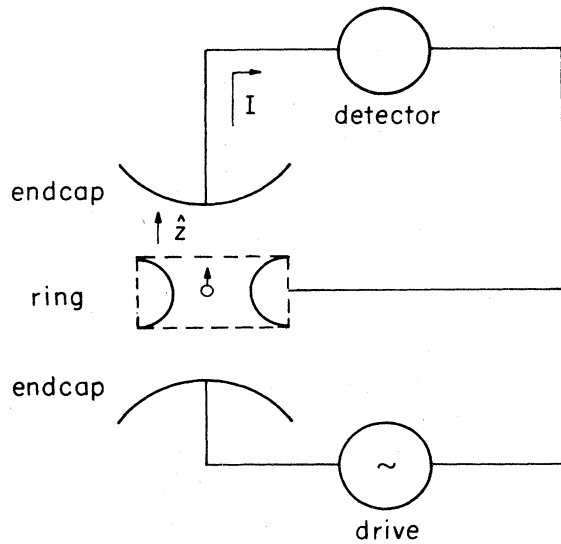
FIG. 4. Sketch indicating the detection and drive of the axial harmonic oscillation.

through the detector. Although the current induced by the undriven axial oscillation of the electron is generally too small to detect, this oscillation may be driven by applying an alternating voltage to the other endcap and ring electrode, as shown in Fig. 4, and the resulting driven oscillation is observed by phase-sensitive detection. The detected current plotted as a function of time in Fig. 5 shows a vivid step structure. This particular example is the first demonstration of a single-particle oscillator which initiated single-particle spectroscopy in a Penning trap (Wineland, Ekstrom, and Dehmelt, 1973). Several electrons were loaded and then, one after the other, they were driven from the trap with a strong driving force. The final excitation level of one step signals the presence of a single trapped electron.

The cyclotron resonance can be excited by introducing microwaves into the trap via an inlet, as shown in Fig. 1. Detection of the electron cyclotron resonance, however, is very subtle. One method currently employed (Dehmelt
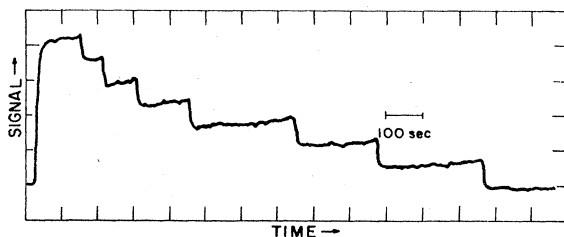

FIG. 5. Steps in the detected axial signal that appear when the axial drive is increased sufficiently to drive one electron at a time out of the trap. It is evident that there were initially seven electrons in the trap. The initial and final signal level is the noise floor (Wineland, Ekstrom, and Dehmelt, 1973).

and Ekstrom, 1973) is to deliberately place a small distortion in the strong uniform magnetic field, a magnetic "bottle" which provides a small axial magnetic field component that varies as z^2. The magnetic moment associated with the cyclotron circle couples to this bottle field and thus changes the "spring" constant of the axial motion, which in turn alters the frequency of the axial oscillation. These changes in the axial frequency measure the size of the cyclotron excitation, and thus the cyclotron resonance frequency can be determined.

The g factor of the electron equals 2 to within about one part in 10^3. Rather than measuring the g factor, which is twice the ratio of the spin frequency (ω_s) to the cyclotron frequency (ω_c), the experiments measure directly the much smaller anomaly $a = (g - 2)/2$. A similar approach was taken in the earlier muon and electron $g - 2$ measurements to gain a considerable increase in accuracy. The electron is driven with an inhomogeneous magnetic field in the xy plane whose amplitude alternates at the anomaly frequency $\omega_a = \omega_s - \omega_c$ (Sec. V). This simultaneously flips the spin and changes the cyclotron excitation. (The inhomogeneous radial variation of the field is also alternated by the motion of the electron at the cyclotron frequency ω_c. Thus the product of this additional oscillation with the basic drive oscillation produces a frequency component at $\omega_s = \omega_a + \omega_c$ which flips the spin.) After the cyclotron motion comes back into thermal equilibrium, the spin state is observed via the coupling of the spin magnetic moment to the bottle field, just as in the determination of the cyclotron resonance, and the anomaly derived from $a = \omega_a/\omega_c$. This result is slightly modified by the electrostatic trapping field (Sec. II), but this is easily accounted for in a measurable way.

The rates at which the cyclotron and spin resonances can be excited and the corresponding line shapes are discussed in Sec. V. Although at present the magnetic bottle is crucial for detection, it does have the untoward side effect of producing non-negligible linewidths (Sec. VI). These widths originate from the random thermal oscillation of the axial motion (Sec. III), which are coupled into the spin and cyclotron motions by the inhomogeneous field produced by the bottle. The resulting line profile (Sec. VI) has been calculated (Brown, 1984,1985), and the lines are accordingly being split to determine accurately the cyclotron and anomaly frequencies. Nonetheless, the experiments would be improved with the removal of the magnetic bottle. One promising method employs a variable bottle (Sec. VI). Another method exploits very small relativistic shifts (Sec. VII).

Since the experiments have obtained such extraordinary precision, one must be very careful to consider possible sources of systematic error. This we do throughout our work. For example, the effects of misalignment are treated in Sec. II and relativistic corrections in Sec. VII. The surrounding Penning trap electrodes form a crude microwave cavity. As we have already mentioned, the alteration of the radiation field from its free-space form in such a cavity changes the cyclotron radiative decay time, an effect that has been observed with an electron. The

presence of the cavity can also result in shifts of the electron and positron cyclotron frequencies (Sec. VIII), which may be important already at the present level of precision (Brown, Gabrielse, Helmerson, and Tan, 1985a,1985b). The geonium atom is unlike an ordinary atom in that the binding potential is provided by an external apparatus. Thus it is very important to understand the electrostatics of the Penning trap (Sec. IX). It is now understood quantitatively (Gabrielse, 1983) how the unwanted effects of trap imperfections are corrected by the addition of compensation electrodes (Van Dyck, Wineland, Ekstrom, and Dehmelt, 1976), which are tuned so as to minimize the anharmonic perturbations to the axial oscillation (Sec. III). The experiments with a single trapped elementary particle could not have been done without such tuning. We summarize and compare the effects of the small electrostatic, relativistic, and magnetic bottle perturbations in Sec. X.

For clarity, we have just outlined the electron geonium experiments. Throughout the review, however, we also deal with single protons and heavier ions in a Penning trap. The ion experiments proceed in a similar fashion, with the major difference being that the cyclotron frequency is at a much lower and more accessible radio frequency. The ion cyclotron motion can therefore be directly coupled to a detector in a manner (Sec. III) similar to the coupling of the axial oscillation. A magnetic bottle is not needed or useful for experiments with ions.

Finally, we mention relevant reviews. Ekstrom and Wineland (1980) have provided an excellent and colorful introduction to the g-value measurements with a single trapped electron. More details are given by Dehmelt (1983), and the measurements are reported by Van Dyck, Schwinberg, and Dehmelt (1978), with recent updates by the same authors (1984,1985). Wineland, Itano, and Van Dyck (1984) also discuss these measurements and include measurements of the ratio of the proton and electron masses as well. This latter review also summarizes the experimental developments involving microwave and laser spectroscopy of trapped ions. The most recent general surveys of fundamental measurements with leptons are given by Field, Picasso, and Combley (1979) and by Conti, Newman, Rich, and Sweetman (1984). The most recent theoretical work is reviewed by Kinoshita and Sapirstein (1984).

II. NONRELATIVISTIC MOTION

A. Classical motion

A particle of charge e and mass m in a spatially uniform magnetic field $\mathbf{B}$ travels in a circular cyclotron orbit. We choose the z axis to be parallel or antiparallel to the magnetic field, with the positive z axis indicating the sense of rotation for the cyclotron orbit by the right-hand rule. The positive z axis is thus in the direction of $-e\mathbf{B}$, and the cyclotron frequency is given by

$$\omega_c = \frac{|eB|}{mc}\hat{z} = \omega_c\hat{z} . \tag{2.1}$$

For an electron in a 60-kG field the cyclotron frequency is at a very high microwave frequency,[4] $\nu_c = \omega_c/2\pi = 164$ GHz, and the wavelength is only 2 mm. A proton in the same field oscillates at the much more accessible radio frequency of 89 MHz. Trapping and orbit parameters for an electron and proton are provided in Tables I—IV in Sec. II.F below.

A charged particle in a magnetic field is bound radially to a magnetic field line, but it is not bound axially, so that the slightest disturbance will move it along the field line. In an ideal Penning trap, the particle is bound axially by superimposing the electrostatic restoring force given by a quadrupole potential, which we write in the form

$$V = V_0 \frac{z^2 - \rho^2/2}{2d^2} . \tag{2.2}$$

The axial z motion is a bound, harmonic oscillation when $eV_0 > 0$. The radial coordinate ρ must appear in the potential as it does in order for the potential to satisfy the Laplace equation.

The quadrupole potential can in principle be produced by placing (ideal) electrodes along equipotentials of V. Three electrodes are required, as shown in Fig. 6: two endcap electrodes along the two branches of the hyperbola of revolution

$$z^2 = z_0^2 + \rho^2/2 \tag{2.3}$$

and one ring electrode along the hyperbola of revolution

$$z^2 = \tfrac{1}{2}(\rho^2 - \rho_0^2) . \tag{2.4}$$

The constants z_0 and ρ_0 are the minimum axial and radial distances to the electrodes. We choose the characteristic trap dimension d to be given by

$$d^2 = \tfrac{1}{2}(z_0^2 + \rho_0^2/2) , \tag{2.5}$$

so that V_0 is the potential difference between the endcap and the ring electrodes.

The axial motion of a charged particle in an ideal Penning trap is decoupled from the magnetic field. It is a simple harmonic motion

$$\ddot{z} + \omega_z^2 z = 0 , \tag{2.6}$$

with frequency

$$\omega_z^2 = \frac{eV_0}{md^2} . \tag{2.7}$$

Typically the quadrupole potential superimposed upon the magnetic field is a relatively weak addition in the sense that

_____

[4]Throughout this paper we shall quote either a frequency ν or an equivalent angular frequency $\omega = 2\pi\nu$, depending upon which is more convenient in the immediate context.
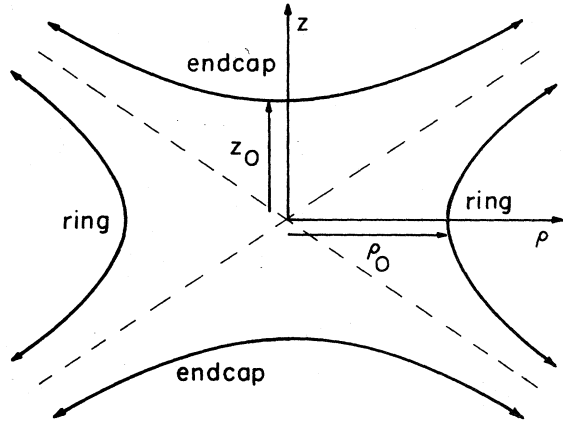
FIG. 6. Axially symmetric electrodes are used to produce a quadrupole potential of the form given by Eq. (2.2). The dashed lines represent the cones that are the asymptotes of the hyperbolas of revolution.

$$\omega_z \ll \omega_c \ . \tag{2.8}$$

For the typical electron conditions listed in Table I below, a trapping potential $V_0 = 10$ V is applied to electrodes for which $d = 0.3$ cm. This yields an axial frequency $v_z = \omega_z/2\pi = 62$ MHz, which is a convenient and easily monitored radio frequency and which is smaller than the cyclotron frequency by a large factor of 3×10^3. For the proton experiment described in Table II below, the trapping potential is increased and the trap dimension is reduced in order to compensate partially for the much larger proton mass, keeping ω_z in the convenient radiofrequency range, and to permit adequate axial damping (Sec. III). An additional result of these choices is that the proton cyclotron frequency is larger than the proton axial frequency by only a factor of 8.

With the addition of the electrostatic potential, the radial motion is described by

$$m\ddot{\boldsymbol{\rho}} = e[\mathbf{E} + (\dot{\boldsymbol{\rho}}/c) \times \mathbf{B}] \ , \tag{2.9}$$

where

$$\mathbf{E} = (V_0/2d^2)\boldsymbol{\rho} \ . \tag{2.10}$$

Writing the equation of motion in terms of the axial and cyclotron frequencies ω_z and ω_c gives

$$\ddot{\boldsymbol{\rho}} - \omega_c \times \dot{\boldsymbol{\rho}} - \tfrac{1}{2}\omega_z^2 \boldsymbol{\rho} = 0 \ . \tag{2.11}$$

For $\omega_z \to 0$, this reduces to the equation for uniform circular motion at the cyclotron frequency ω_c. The additional term $-\tfrac{1}{2}\omega_z^2 \boldsymbol{\rho}$ comes from the repulsive radial term in the electrostatic potential [Eq. (2.2)]. Before solving this radial equation of motion, let us consider two consequences of the repulsive radial potential. First, the frequency of the cyclotron rotation is reduced from ω_c to ω_c' because the repulsive radial potential reduces the centrifugal force. Second, the fast cyclotron orbit is superimposed upon a much slower, circular magnetron orbit, with

angular frequency ω_m as represented in Fig. 7(a). The resulting compound motion in the xy plane has the epicycle form shown in Fig. 7(b). The complete motion of a particle in a Penning trap is the superposition of such epicycles with the harmonic axial oscillation, as suggested in Fig. 3. None of these figures is to scale.

To see how the magnetron motion comes about, we observe that the perpendicular fields $\mathbf{E}$ and $\mathbf{B}$ comprise a velocity filter for a charged particle. That is, a charged particle with a drift velocity $\mathbf{u} = c\mathbf{E} \times \mathbf{B}/B^2$ will move through these fields unimpeded, since $\mathbf{u}/c \times \mathbf{B}$ will cancel $\mathbf{E}$ in Eq. (2.9). This is strictly true only for constant fields, which give a constant drift velocity $\mathbf{u}$. It is approximately true for the slow magnetron motion, where
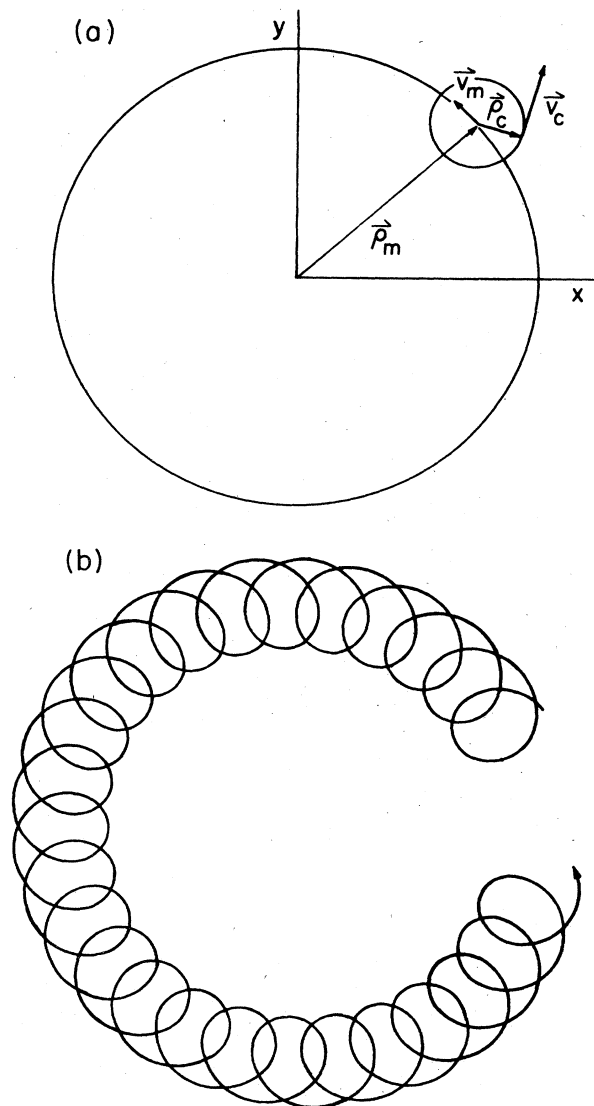

FIG. 7. Projection of the motion of a particle in a Penning trap upon the xy plane. The motion is the superposition of (a) circular magnetron and cyclotron motions producing (b) epicycles. The orbits are not to scale.

the time derivatives of $\mathbf{u}$ can be neglected. As is characteristic of such crossed-field velocity filters, this velocity does not depend upon the charge or mass of the particle. Substituting for the radial electric field $\mathbf{E}$ from Eq. (2.10) shows that the drift or magnetron motion is a circular motion with the same direction of rotation as the cyclotron orbit (see Fig. 7) but with the much smaller magnetron frequency $\omega_m \approx \omega_z^2/2\omega_c$, which is independent of e and m. We thus have the hierarchy

$$\omega_m \ll \omega_z \ll \omega_c . \tag{2.12}$$

This hierarchy is very pronounced for an electron in a large magnetic field, as is evidenced by the electron frequencies 12 kHz, 62 MHz, and 164 GHz from Table I. For more massive particles in magnetic fields of similar size, the hierarchy is much less pronounced, as illustrated by the proton frequencies 663 kHz, 10 MHz, and 76 MHz from Table II.

The magnetron motion differs from the other motions in other respects as well. The energy in the cyclotron motion is almost exclusively kinetic energy. The energy in the harmoic axial oscillation alternates between kinetic and potential energy. Reducing the energy in either of these motions reduces their amplitude; they are stable. In contrast, the energy in the magnetron motion is almost exclusively potential energy. For the typical electron trap parameters of Table I, an increase in the magnetron radius from $\rho=0$ to $\rho=\rho_0 \simeq 0.5$ cm (the radius of the ring electrode) involves an increase in kinetic energy of only 3×10^{-7} eV (corresponding to a maximum velocity of only 3×10^4 cm/sec), but the potential energy decreases by 5 eV. The magnetron motion is thus an orbit about the top of a radial potential hill. Exciting the magnetron motion causes the particle to roll down the radial hill. The magnetron motion is unbound, since any dissipative process that removes energy from the magnetron motion increases the magnetron radius until the particle strikes the ring electrode and is lost from the trap. Fortunately, the damping time for the magnetron motion is typically on the order of years (Sec. II.E), so that the magnetron motion is more than adequately metastable.

Now that the major features of the radial motion have been described, let us turn to the analytic solution of the equation of motion (2.11). The cyclotron and magnetron components of the motion are separated by introducing two vectors $\mathbf{V}^{(+)}$ and $\mathbf{V}^{(-)}$, defined by

$$\mathbf{V}^{(\pm)} = \dot{\rho} - \omega_\mp \hat{z} \times \rho , \tag{2.13}$$

where

$$\omega_\pm = \tfrac{1}{2}[\omega_c \pm (\omega_c^2 - 2\omega_z^2)^{1/2}] . \tag{2.14}$$

Equations of motion for $V^{(\pm)}$ are obtained by taking the time derivative of Eq. (2.13) and substituting the radial equation of motion (2.11) for ρ in this expression to yield

$$\dot{\mathbf{V}}^{(\pm)} = \omega_\pm \hat{z} \times \mathbf{V}^{(\pm)} . \tag{2.15}$$

We see that $\mathbf{V}^{(+)}$ rotates about a circle with the corrected cyclotron frequency ω_c'. Since $\omega_+ + \omega_- = \omega_c$, we may write this frequency as[5]

$$\omega_+ \equiv \omega_c' = \omega_c - \omega_m . \tag{2.16}$$

The vector $\mathbf{V}^{(-)}$ rotates about another circle at the magnetron frequency ω_m. Since $\omega_+\omega_- = \omega_z^2/2$,

$$\omega_- \equiv \omega_m = \omega_z^2/2\omega_c' . \tag{2.17}$$

In view of the typical hierarchy of Eq. (2.12), the magnetron frequency is generally very small and the modified cyclotron frequency in Eq. (2.16) is only slightly smaller than ω_c.

The difference $\mathbf{V}^{(+)} - \mathbf{V}^{(-)}$ is proportional to $\hat{z} \times \rho$, and taking the cross product of this difference with $\hat{z}$ we find that the solution to the radial equation of motion may be expressed as

$$\rho = -\frac{\hat{z} \times (\mathbf{V}^{(+)} - \mathbf{V}^{(-)})}{\omega_+ - \omega_-} . \tag{2.18}$$

A uniform circular motion with angular frequency $\omega\hat{z}$ and velocity $\mathbf{v}$ is described by $\omega\rho = -\hat{z} \times \mathbf{v}$. Thus the radial motion is the epicyclic superposition of two uniform circular motions, as shown in Fig. 7. Differentiating Eq. (2.18) yields the velocity

$$\dot{\rho} = \frac{\omega_+\mathbf{V}^{(+)} - \omega_-\mathbf{V}^{(-)}}{\omega_+ - \omega_-} . \tag{2.19}$$

Since $\omega_- \ll \omega_+$, the vector $\mathbf{V}^{(+)}$ is essentially equal to the velocity of the trapped particle in its cyclotron orbit. The vector $\mathbf{V}^{(-)}$, however, is much larger than the magnetron velocity by the ratio ω_+/ω_-.

The Hamiltonian for the radial motion H_ρ is the sum of the kinetic energy and the repulsive electrostatic potential energy,

$$H_\rho = \tfrac{1}{2}m(\dot{\rho}^2 - \tfrac{1}{2}\omega_z^2\rho^2) . \tag{2.20}$$

Using Eqs. (2.18), (2.19), and (2.14), we may write the radial Hamiltonian as

$$H_\rho = \frac{1}{2}m\frac{\omega_+\mathbf{V}^{(+)2} - \omega_-\mathbf{V}^{(-)2}}{\omega_+ - \omega_-} , \tag{2.21}$$

which exhibits the separation of the system into the two decoupled subsystems described by $\mathbf{V}^{(+)}$ and $\mathbf{V}^{(-)}$. Note that $\mathbf{V}^{(-)}$ gives a negative contribution to the energy, as it must, since the magnetron motion is unstable.

It is sometimes convenient to use the gauge in which the vector potential for the uniform magnetic field $\mathbf{B}$ is given by

$$\mathbf{A} = \tfrac{1}{2}\mathbf{B} \times \rho . \tag{2.22}$$

---

[5]The notation ω_+ and ω_- yields more compact formulas, while the notation ω_c' and ω_m has often been used in the literature. We employ both notations, with ω_c', ω_m used in comparisons with experiment and ω_+, ω_- in the more mathematical developments.

It is easy to check that in this gauge the canonical linear momentum

$$\mathbf{p} = m\dot{\boldsymbol{\rho}} + (e/c)\mathbf{A} \tag{2.23}$$

becomes

$$\mathbf{p} = \tfrac{1}{2}m(\mathbf{V}^{(+)} + \mathbf{V}^{(-)}) . \tag{2.24}$$

Moreover, there is rotational invariance about the z axis in this gauge, so that the z component of the canonical angular momentum

$$L_z = \hat{z} \cdot \boldsymbol{\rho} \times \mathbf{p} \tag{2.25}$$

is conserved,

$$\frac{d}{dt} L_z = 0 . \tag{2.26}$$

This angular momentum may be expressed as

$$L_z = \frac{m}{2(\omega_+ - \omega_-)} (\mathbf{V}^{(+)2} - \mathbf{V}^{(-)2}) . \tag{2.27}$$

B. Quantum motion

The classical equations of motion that we have just described are all linear. Hence they are all essentially harmonic oscillator equations that are easily quantized. A straightforward solution of the appropriate Schrödinger equation has been presented by Sokolov and Pavlenko (1965).[6] The treatment provided here relies instead upon raising and lowering operators and greatly facilitates the computation of matrix elements. The axial motion is governed by the harmonic oscillator Hamiltonian

$$H_z = \frac{p_z^2}{2m} + \frac{m\omega_z^2 z^2}{2} , \tag{2.28}$$

and the canonical commutation relation

$$[z, p_z] = i\hbar . \tag{2.29}$$

We shall review this familiar quantum system in some detail, since it is also the prototype for the radial motions. Creation and annihilation operators are defined, respectively, by

$$a_z^\dagger = \left[\frac{m\omega_z}{2\hbar}\right]^{1/2} z - i \left[\frac{1}{2m\hbar\omega_z}\right]^{1/2} p_z \tag{2.30a}$$

and

$$a_z = \left[\frac{m\omega_z}{2\hbar}\right]^{1/2} z + i \left[\frac{1}{2m\hbar\omega_z}\right]^{1/2} p_z . \tag{2.30b}$$

These operators obey the commutation relation

$$[a_z, a_z^\dagger] = 1 . \tag{2.31}$$

Equations (2.30) are easily inverted to give

$$z = \left[\frac{\hbar}{2m\omega_z}\right]^{1/2} (a_z + a_z^\dagger) \tag{2.32a}$$

and

$$p_z = \frac{1}{i} \left[\frac{m\hbar\omega_z}{2}\right]^{1/2} (a_z - a_z^\dagger) . \tag{2.32b}$$

Substituting Eqs. (2.32) into the Hamiltonian of Eq. (2.28) and using the commutation relation (2.31), we obtain the familiar result that

$$H_z = \hbar\omega_z(a_z^\dagger a_z + \tfrac{1}{2}) . \tag{2.33}$$

Orthonormal energy eigenstates $|k\rangle$, $k = 0, 1, 2, \ldots$, are built from the ground state $|0\rangle$, which is destroyed by the annihilation operator,

$$a_z |0\rangle = 0 , \tag{2.34}$$

and which is a state of unit norm,

$$\langle 0 | 0 \rangle = 1 . \tag{2.35}$$

The general state $|k\rangle$ may be constructed from the ground state

$$|k\rangle = \frac{(a_z^\dagger)^k}{\sqrt{k!}} |0\rangle \tag{2.36a}$$

with Hermitian conjugation giving

$$\langle k | = \langle 0 | \frac{(a_z)^k}{\sqrt{k!}} . \tag{2.36b}$$

Using the commutation relation (2.31) to pass a_z through the k factors of $a_z^\dagger$, it is easy to prove that

$$a_z |k\rangle = \sqrt{k} |k-1\rangle , \tag{2.37}$$

while it follows directly from the definition (2.36a) that

$$a_z^\dagger |k\rangle = \sqrt{k+1} |k+1\rangle . \tag{2.38}$$

Hence

$$H_z |k\rangle = |k\rangle E_k , \tag{2.39}$$

with

$$E_k = \hbar\omega_z(k + \tfrac{1}{2}) , \tag{2.40}$$

and we see that $|k\rangle$ are indeed energy eigenstates. Moreover, using the explicit construction (2.36b) and the lowering operator property of a exhibited in Eq. (2.37), it is easy to confirm that these states are orthonormal:

$$\langle k' | k \rangle = \delta_{k'k} . \tag{2.41}$$

In electron and proton experiments carried out so far, a classical description of the axial motion is entirely adequate. The axial motion in these experiments is coupled to an external circuit at a temperature slightly greater than the helium bath temperature of $T \approx 4.2$ K (see Sec.

---

[6]Other quantum-mechanical treatments include those of Gräff and Klempt (1967), Gräff, Klempt, and Werth (1969), and Itano and Wineland (1982).

III). As shown in Table III, this corresponds to an energy $k_B T \approx 3 \times 10^{-4}$ eV, which is much greater than both the energy $\hbar \omega_z \approx 3 \times 10^{-7}$ eV for the electron conditions listed in Table I and the smaller value that applies to the proton experiment of Table II. Thus the average axial quantum number k from $\hbar \omega_z k = k_B T$ is equal to 1×10^3 for the electron example, and it is even larger for the proton example. In both cases, $k \gg 1$, so that a classical description suffices. We note that the axial motion is typically driven to an excitation energy somewhat larger than the thermal excitation level. For an electron that is axially excited to 9×10^{-3} eV, the velocity and displacement are given by $v_z/c \approx 10^{-4}$ and $z \approx 10^{-2}$ cm. A proton excited to the same energy has a smaller velocity by a factor of approximately 40, and the rms displacement is smaller by approximately a factor of 10 for the conditions specified in Table II. If the axial motion is not coupled to a tuned circuit and is not driven, the situation is quite different. As we shall see in Sec. II.E, the axial motion is coupled to the radiation field only very weakly, with a time constant on the order of days. Under these conditions the axial motion could presumably be cooled enough so that a quantum-mechanical treatment would be required.

The radial cyclotron motion of an electron trapped in a large magnetic field, on the other hand, is often near its quantum-mechanical ground state, so that this motion must be treated quantum mechanically. The kinetic and canonical radial momenta, $m\dot{\rho}$ and $\mathbf{p}$, are related by

$$m\dot{\rho} = \mathbf{p} - \frac{e}{c}\mathbf{A} \ , \tag{2.42}$$

where $\mathbf{A}$ is a vector potential for the uniform field $\mathbf{B}$. The canonical commutation relations

$$[\rho_k, p_l] = i\hbar \delta_{kl} \ , \tag{2.43}$$

with k and l, representing the x or y components, give

$$[\rho_k, \dot{\rho}_l] = \frac{i\hbar}{m}\delta_{kl} \ , \tag{2.44}$$

and

$$[\dot{\rho}_x, \dot{\rho}_y] = \frac{ie\hbar}{m^2 c}\left[\frac{\partial A_y}{\partial x} - \frac{\partial A_x}{\partial y}\right] = \frac{-i\hbar|eB|}{m^2 c} = -i\frac{\hbar \omega_c}{m} \ . \tag{2.45}$$

These commutators in turn can be used to establish that

$$[V_k^{(+)}, V_l^{(-)}] = 0 \ , \tag{2.46}$$

so that $\mathbf{V}^{(+)}$ and $\mathbf{V}^{(-)}$ are kinematically uncoupled. Similarly, one finds that

$$\frac{\mp m}{\omega_+ - \omega_-}[V_x^{(\pm)}, V_y^{(\pm)}] = i\hbar \ , \tag{2.47}$$

so that with proper normalization $V_x^{(\pm)}$ and $V_y^{(\pm)}$ behave as a canonically conjugate pair (q,p).

Accordingly, we can treat the radial motion analogously to that given above for the axial motion by constructing annihilation and creation operators from these conjugate pairs,

$$a_\pm = \left[\frac{m}{2\hbar(\omega_+ - \omega_-)}\right]^{1/2}(V_x^{(\pm)} \mp i V_y^{(\pm)}) \tag{2.48a}$$

and

$$a_\pm^\dagger = \left[\frac{m}{2\hbar(\omega_+ - \omega_-)}\right]^{1/2}(V_x^{(\pm)} \pm i V_y^{(\pm)}) \ , \tag{2.48b}$$

which are normalized so that

$$[a_\pm, a_\pm^\dagger] = 1 \ , \tag{2.49}$$

with all other commutators vanishing. In terms of these operators, the radial Hamiltonian (2.21) is given by

$$H_\rho = \hbar \omega_+ (a_+^\dagger a_+ + \tfrac{1}{2}) - \hbar \omega_- (a_-^\dagger a_- + \tfrac{1}{2}) \ . \tag{2.50}$$

Thus the energy eigenstates of the radial Hamiltonian are direct products of two harmonic oscillator states $|n,l\rangle = |n\rangle \otimes |l\rangle$, with the radial energy eigenvalues given by

$$E_{nl} = E_n + E_l \ , \tag{2.51}$$

where

$$E_n = \hbar \omega_+ (n + \tfrac{1}{2}) = \hbar \omega_c'(n + \tfrac{1}{2}) \tag{2.52}$$

and

$$E_l = -\hbar \omega_-(l + \tfrac{1}{2}) = -\hbar \omega_m(l + \tfrac{1}{2}) \ . \tag{2.53}$$

The radial creation and annihilation operators operate upon the radial energy eigenstates $|n,l\rangle$ in the same way that the axial creation and annihilation operators operate upon the axial eigenstates. The cyclotron eigenstates are lowered and raised by a_+ and $a_+^\dagger$,

$$a_+|n,l\rangle = \sqrt{n}\,|n-1,l\rangle \ , \tag{2.54}$$

$$a_+^\dagger|n,l\rangle = \sqrt{n+1}\,|n+1,l\rangle \ , \tag{2.55}$$

while the magnetron states are lowered and raised by a_- and $a_-^\dagger$,

$$a_-|n,l\rangle = \sqrt{l}\,|n,l-1\rangle \ , \tag{2.56}$$

$$a_-^\dagger|n,l\rangle = \sqrt{l+1}\,|n,l+1\rangle \ . \tag{2.57}$$

These operators are very convenient for evaluating matrix elements.

A quantum-mechanical description is generally required for the undriven cyclotron motion of an electron trapped in a large magnetic field, as in the typical conditions listed in Table I. Under these conditions, the cyclotron motion is coupled to the radiation field with a time constant of less than a second (see Sec. II. E). The cyclotron motion thus rapidly comes into thermal equilibrium with the blackbody radiation of the trap, which is at liquid-helium temperature (4.2 K) in present experiments. As summarized in Table III, $k_B T \approx 3 \times 10^{-4}$ eV is comparable to $\hbar \omega_c \approx 7 \times 10^{-4}$ eV. A Boltzmann distribution of excitation energies applies, and the cyclotron ground state $n = 1$ is occupied about 90% of the time. In the ground state we have the rms values $v_c/c \approx 4 \times 10^{-5}$ and $\rho_c \approx 1 \times 10^{-6}$ cm. By contrast, the cyclotron motion of a

proton in a similar magnetic field can usually be described classically. The proton cyclotron frequency is reduced by the ratio of the electron and proton masses. Instead of an average cyclotron excitation number of order unity, we have $n \gg 1$. As we shall discuss in Sec. II.E, however, the coupling to the radiation field is also greatly reduced, so that the proton cyclotron motion will come into thermal equilibrium only when it is coupled to an external circuit (Sec. III). Decoupling from the tuned circuit might allow cooling to a point where a quantum description is required.

Finally, the magnetron motions can usually be described classically for both an electron and a proton. The radiative decay time of the magnetron motion is so long (Sec. II.E) that this motion is always uncoupled from the blackbody radiation of the trap and is never in thermal equilibrium. The cooling of the magnetron motion is discussed in Sec. IV, where it is shown that with the maximum axial sideband cooling possible, the motion has an average energy of

$$\langle E_l \rangle = -(\omega_m/\omega_z)k_B T ,\qquad (2.58)$$

where T is the temperature of the axial oscillation. In this case, the average quantum numbers of the magnetron and axial motions are equal, $l = k$. Recalling that $k \approx 1 \times 10^3$ for present electron experiments, we see that the magnetron motion can similarly be treated classically. With $l \approx 1 \times 10^3$, the magnetron energy for an electron trapped under the conditions summarized in Table I is about -7×10^{-8} eV. As discussed earlier, the magnetron energy is almost entirely due to the radial potential hill, so that $E_l \approx -m\omega_z^2\rho_m^2/4$. Hence the rms value of the magnetron radius is given by $\rho_m \approx 6 \times 10^{-5}$ cm, and since $v_m = \rho_m\omega_m$, we have $v_m/c \approx 1 \times 10^{-10}$. Orbit sizes, velocities, and energies are summarized at the end of this section for an electron (in Table III) and a proton (in Table IV).

C. Spin motion

A trapped particle with spin $\frac{1}{2}\hbar\sigma$ interacts with the magnetic field via its magnetic moment

$$\mu = g\frac{e\hbar}{2mc}\frac{1}{2}\sigma .\qquad (2.59)$$

The constant $e\hbar/2mc$ is the Bohr magneton. The magnetic moment of a charged particle in a cyclotron orbit is well known to be given by this expression with $g = 1$ and with the kinetic orbital angular momentum vector $\mathbf{r} \times m\mathbf{v}$ replacing the spin operator $\frac{1}{2}\hbar\sigma$. The dimensionless g value is a measure of the size of the spin magnetic moment compared to the orbital case. As discussed in the Introduction, the primary motivation for the single-particle trapping experiments we are describing has been the precise measurement of the g value of the electron and positron. Since $g \approx 2$ for these leptons, g is often written in terms of the anomaly a defined by

$$a = \frac{g-2}{2} \approx \frac{\alpha}{2\pi} \approx 10^{-3} ,\qquad (2.60)$$

which is due entirely to radiative corrections. Protons, however, owing to their more complicated hadronic structure, have $g \approx 5.59$, which is much larger than 2, so that the anomaly is a less useful parameter.

The spin Hamiltonian $-\boldsymbol{\mu} \cdot \mathbf{B}$ may be written as

$$H_s = \frac{g}{2}\hbar\omega_c\frac{1}{2}\sigma_z .\qquad (2.61)$$

If we designate the eigenvalues of σ_z by s, the energy eigenvalues are given by

$$E_s = \frac{g}{2}\hbar\omega_c\frac{s}{2} .\qquad (2.62)$$

For particles of spin $\frac{1}{2}$ there are two energy levels, corresponding to $s = \pm 1$. The separation of these two energy levels can be written as $\hbar\omega_s$, with the spin precession frequency ω_s given by

$$\omega_s = \frac{g}{2}\omega_c .\qquad (2.63)$$

Since g is only very slightly larger than 2 for the electron and positron, the spin precession frequency is only slightly larger than the cyclotron frequency. Geonium energy levels are plotted in Fig. 8. The levels, which would be degenerate if $\omega_s = \omega_c$, are split by the anomaly frequency

$$\omega_a = \omega_s - \omega_c .\qquad (2.64)$$

Notice that an anomaly transition at this frequency corresponds to the spin's flipping from up to down, along with a simultaneous, upward cyclotron transition or vice versa. The splitting is greatly exaggerated in the figure to make it visible.
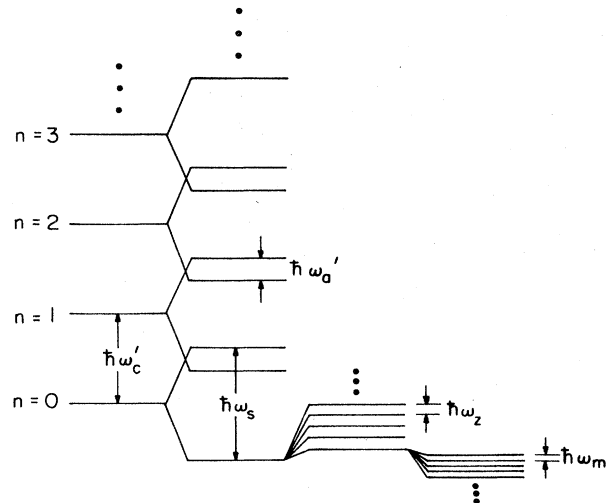

FIG. 8. Splitting of geonium energy levels for an electron (not to scale). The ladder on the far left represents the basic cyclotron energy levels. Progressing to the right, these levels are split first by the spin ($=\frac{1}{2}$), then by the axial binding, and finally by the magnetron motion. The magnetron levels are inverted, since the motion is unbound.

It is often convenient for experimental purposes to invert Eq. (2.63) in order to define operationally the g value of a spin-$\frac{1}{2}$ particle as the dimensionless ratio of two measurable frequencies,

$$\frac{g}{2} = \frac{\omega_s}{\omega_c} . \tag{2.65}$$

In a similar manner, the anomaly can be operationally defined by

$$a = \frac{\omega_s - \omega_c}{\omega_c} = \frac{\omega_a}{\omega_c} . \tag{2.66}$$

Since $\omega_s - \omega_c \approx 10^{-3}\omega_c$, large errors are incurred if ω_s and ω_c are measured separately and then subtracted to form ω_a. The geonium experiments therefore follow an earlier tradition (Wilkinson and Crane, 1963) and measure ω_a directly.

While both ω_a and ω_c are measurable frequencies for an electron or positron if only a magnetic field is present, the electrostatic field, which is added to confine the particle, modifies the measured frequencies slightly to the values ω_a' and ω_c', respectively, with

$$\omega_a' = \omega_s - \omega_c' . \tag{2.67}$$

Since $\omega_c' = \omega_c - \omega_m$ according to Eq. (2.16), the anomaly can be written as

$$a = \frac{\omega_a' - \omega_m}{\omega_c' + \omega_m} . \tag{2.68}$$

Alternatively, we can use the fact that $\omega_m = \omega_z^2/2\omega_c'$ according to Eq. (2.17) and write the anomaly as

$$a = \frac{\omega_a' - \omega_z^2/2\omega_c'}{\omega_c' + \omega_z^2/2\omega_c'} . \tag{2.69}$$

Both of these expressions apply for a perfect quadrupole potential and a homogeneous magnetic field that is perfectly aligned with the quadrupole axis. In the following section we present an invariance relationship to be used in place of Eqs. (2.68) to completely circumvent the effect of many trap misalignments and imperfections. We shall show that the use of the measured eigenfrequencies of a trapped particle in the alternative expression for the anomaly in Eq. (2.69) largely circumvents these effects for the electron and positron.

D. An invariance theorem

Real Penning traps have a variety of small imperfections. We consider here the unavoidable imperfections in a trap which alter the quadratic terms in the electrostatic potential (Brown and Gabrielse, 1982). These arise from misalignments of the trap electrodes both internally and with respect to the magnetic field direction, and from departures from ideal geometry in the trap electrodes. We shall provide an invariance theorem that makes it possible to determine precisely the cyclotron frequency ω_c and hence the anomaly from the measured eigenfrequencies of a laboratory trap, even though the trap suffers from these imperfections. The effects of other small imperfections are considered in other sections. Imperfections and

misalignments in the electrodes of a real trap cause departures from the ideal electrostatic quadrupole potential which are of higher order in the position coordinates than are the quadratic terms we consider here. However, as discussed in Sec. IX, compensation electrodes may be introduced which greatly reduce these effects. The effects of magnetic field inhomogeneities are considered in Sec. VI.

The general, quadratic electrostatic potential may be expressed as

$$V = \frac{1}{2} \sum_{k,l=1}^{3} A_{kl} x_k x_l , \tag{2.70}$$

where $x_1 = x$, $x_2 = y$, $x_3 = z$, and A_{kl} is a symmetric matrix. Laplace's equation requires that A_{kl} be traceless. A rotation of the coordinate axes produces the transformation $A \rightarrow RAR^{-1}$, where R is an orthogonal matrix. We use such a rotation to work in the "principal-axis coordinate system," where RAR^{-1} is diagonal but still, of course, traceless. In this coordinate system the potential energy U has the form

$$U = \frac{1}{2} m\omega_z^2 [z^2 - \frac{1}{2}(x^2 + y^2) - \frac{1}{2}\varepsilon(x^2 - y^2)] . \tag{2.71}$$

We see that the harmonic imperfections are represented in a completely general way by the single asymmetry parameter ε. Projections of equipotentials upon the xy plane are elliptical. For small ε this asymmetry parameter is the fractional difference in length of the principal axes of these ellipses.

When the magnetic field $\mathbf{B}$ is aligned perfectly along the positive or negative z axis, the motion along this axis is uncoupled from the motion in the xy plane. The overall multiplicative constant in Eq. (2.71) has been chosen such that ω_z is the axial harmonic oscillation frequency in this ideal limit. We shall treat the general case with a misaligned magnetic field given by

$$B_z = B \cos\theta ,$$

$$B_x = B \sin\theta \cos\varphi , \tag{2.72}$$

$$B_y = B \sin\theta \sin\varphi ,$$

in the principal-axes coordinate system. To be consistent with our convention for choosing the z-axis direction, we choose the sign of B here to make eB positive, so that the cyclotron frequency ω_c, in the absence of the Penning electrodes, is given by

$$\omega_c = eB/mc \tag{2.73}$$

and is explicitly positive.

Three coupled, linear second-order differential equations of motion are easily deduced by computing the Lorentz force and using Newton's second law. Since the equations of motion are linear, they also apply to the transition matrix elements of the Heisenberg quantum-mechanical operators. Thus the relations amongst the frequencies that we shall obtain are also valid in the quantum-mechanical case. Assuming a time dependence of the form $\exp(-i\omega t)$ yields a set of three homogeneous algebraic equations, with the determinant

$$F(\omega^2) = \begin{vmatrix} \omega^2 + \frac{1}{2}\omega_z^2(1+\varepsilon) & -i\omega\omega_c\cos\theta & +i\omega\omega_c\sin\theta\sin\varphi \\ i\omega\omega_c\cos\theta & \omega^2 + \frac{1}{2}\omega_z^2(1-\varepsilon) & -i\omega\omega_c\sin\theta\cos\varphi \\ -i\omega\omega_c\sin\theta\sin\varphi & i\omega\omega_c\sin\theta\cos\varphi & \omega^2 - \omega_z^2 \end{vmatrix} . \tag{2.74}$$

This set of equations has a solution only if the frequency is an eigenfrequency $\bar{\omega}$ determined by the characteristic equation

$$F(\bar{\omega}^2) = 0 . \tag{2.75}$$

Therefore the determinant (2.74) is a cubic polynomial of the form

$$F(\omega^2) = (\omega^2 - \bar{\omega}_c^2)(\omega^2 - \bar{\omega}_z^2)(\omega^2 - \bar{\omega}_m^2) , \tag{2.76}$$

where $\bar{\omega}_c$, $\bar{\omega}_z$, and $\bar{\omega}_m$ are, respectively, the observable cyclotron, axial, and magnetron frequencies of the misaligned trap. The determinant (2.74) is easily calculated. Expanding the result in the powers ω^0, ω^2, ω^4 and comparing the coefficients with the corresponding expansion of Eq. (2.76), we find that

$$\bar{\omega}_c^2\bar{\omega}_z^2\bar{\omega}_m^2 = \frac{1}{4}\omega_z^6(1-\varepsilon^2) , \tag{2.77}$$

$$\bar{\omega}_c^2\bar{\omega}_z^2 + \bar{\omega}_c^2\bar{\omega}_m^2 + \bar{\omega}_z^2\bar{\omega}_m^2 = \omega_c^2\omega_z^2(1 - \frac{3}{2}\sin^2\theta$$
$$- \frac{1}{2}\varepsilon\sin^2\theta\cos2\varphi)$$
$$- \frac{3}{4}\omega_z^4(1+\frac{1}{3}\varepsilon^2) , \tag{2.78}$$

and

$$\bar{\omega}_c^2 + \bar{\omega}_z^2 + \bar{\omega}_m^2 = \omega_c^2 . \tag{2.79}$$

Equation (2.79) is the invariance theorem mentioned above. It gives an exact prescription for obtaining the cyclotron frequency ω_c in the absence of the Penning electrodes, in terms of the measurable eigenfrequencies of an imperfect trap. This prescription is completely independent of the misalignment angles (θ, φ) and the distortion parameter ε. To take complete advantage of the invariance relationship for measurements of the anomaly, we write the anomaly as

$$a = \frac{\bar{\omega}_a - \omega_c + \bar{\omega}_c}{\omega_c} . \tag{2.80}$$

The observed anomaly frequency $\bar{\omega}_a$ is equal to $\omega_s - \bar{\omega}_c$. The cyclotron frequency ω_c in general must be deduced from the invariance relationship.

In the present and proposed single-particle spectroscopy experiments, the cyclotron frequency ω_c is determined by the measurement of $\bar{\omega}_c$ to great precision, with $\bar{\omega}_z$ and $\bar{\omega}_m$ measured with lesser accuracy. In some cases $\bar{\omega}_m$ need not be measured. This is possible because, as we have discussed before [Eq. (2.12)], the Penning electrodes typically contribute only a weak perturbation to the cyclotron motion of the charged particle in a strong magnetic field, giving

$$\bar{\omega}_c^2 \gg \bar{\omega}_z^2 \gg \bar{\omega}_m^2 . \tag{2.81}$$

In this case, a simple expansion of Eq. (2.79) suffices. The axial motion is uncoupled for a perfect trap. In this limit $\bar{\omega}_z = \omega_z$, and Eq. (2.77) gives $\bar{\omega}_m = \tilde{\omega}_m$, where we define $\tilde{\omega}_m$ by

$$\tilde{\omega}_m = \frac{\bar{\omega}_z^2}{2\bar{\omega}_c} \tag{2.82}$$

[cf. Eq. (2.17)]. It is convenient to add $\tilde{\omega}_m^2$ to both sides of Eq. (2.79) to obtain

$$\left[\bar{\omega}_c + \frac{\bar{\omega}_z^2}{2\bar{\omega}_c}\right]^2 = \omega_c^2 + \tilde{\omega}_m^2 - \bar{\omega}_m^2 . \tag{2.83}$$

We can now expand in the small quantity $\tilde{\omega}_m^2 - \bar{\omega}_m^2$ to secure

$$\frac{\omega_c}{\bar{\omega}_c} \simeq 1 + \frac{1}{2}\left[\frac{\bar{\omega}_z}{\bar{\omega}_c}\right]^2 + \frac{1}{8}\left[\frac{\bar{\omega}_z}{\bar{\omega}_c}\right]^4\left[\left[\frac{\bar{\omega}_m}{\tilde{\omega}_m}\right]^2 - 1\right] . \tag{2.84}$$

With the neglect of the third term on the right-hand side of Eq. (2.84), we obtain the relation for the corrected cyclotron frequency $\bar{\omega}_c = \omega_c' = \omega_+$ for an ideal trap given in Eq. (2.14). We find that the correction for trap imperfections involves the very small quantity $(\bar{\omega}_z/\bar{\omega}_c)^4$. It suffices to work to leading order in the small ratio $(\bar{\omega}_z/\bar{\omega}_c)^2$ to compute this second correction in Eq. (2.84). In this order $\bar{\omega}_c^2 \simeq \omega_c^2$, and Eq. (2.78) reduces to the statement

$$\bar{\omega}_z^2 \simeq \omega_z^2[1 - \frac{3}{2}\sin^2\theta(1 + \frac{1}{3}\varepsilon\cos2\varphi)] . \tag{2.85}$$

Equation (2.77) now informs us that

$$\bar{\omega}_m \simeq \tilde{\omega}_m(1-\varepsilon^2)^{1/2}[1 - \frac{3}{2}\sin^2\theta(1 + \frac{1}{3}\varepsilon\cos2\varphi)]^{-3/2} , \tag{2.86}$$

and thus for small imperfections with $\theta \ll 1$ and $|\varepsilon| \ll 1$,

$$\frac{\omega_c}{\bar{\omega}_c} = 1 + \frac{1}{2}\left[\frac{\bar{\omega}_z}{\bar{\omega}_c}\right]^2 + \frac{9}{16}\left[\frac{\bar{\omega}_z}{\bar{\omega}_c}\right]^4(\theta^2 - \frac{2}{9}\varepsilon^2) . \tag{2.87}$$

Either Eq. (2.85) or (2.86) can be used to study the imperfections described by θ, φ, and ε and thereby to align Penning traps. The magnetron frequency $\bar{\omega}_m$ has been observed in a variety of traps (Van Dyck, Schwinberg, and Dehmelt, 1978; Van Dyck and Gabrielse, 1982) to be larger than $\tilde{\omega}_m$. This is in accord with Eq. (2.86) and with the expectation that the angular misalignment of the magnetic field, θ, is larger than the asymmetry in the Penning electrodes, $|\varepsilon|$.

The imperfection corrections will probably be completely negligible for trapped electron experiments, with the consequence that the magnetron frequency $\bar{\omega}_m$ need not be measured. Using the typical electron conditions from Table I, we have $(\bar{\omega}_z/\bar{\omega}_c)^4 \approx 10^{-14}$. Even for an an-

gular misalignment as large as $\theta = 1°$ or for an electrode asymmetry as large as $|\varepsilon| = 1\%$, the net correction in Eq. (2.87) is only on the order of 10^{-18}. The electron and positron anomalies can therefore be deduced from the simpler formula for the anomaly

$$a = \frac{\overline{\omega}_a - \overline{\omega}_z^2/2\overline{\omega}_c}{\overline{\omega}_c + \overline{\omega}_z^2/2\overline{\omega}_c} , \tag{2.88}$$

which is an approximation that should suffice for foreseeable improvements in measurement accuracy. This formula is identical in form with Eq. (2.69) except that the measured frequencies are used.

The imperfection corrections become much more significant for more massive particles, which have much lower cyclotron frequencies. For example, the frequency ratio $(\overline{\omega}_z/\overline{\omega}_c)^4$ is 3×10^{-4} for the proton parameters in Table II. In this case, for $\theta = 1°$ or $|\varepsilon| = 1\%$, the second correction in Eq. (2.87) is about 5×10^{-8}, an important correction compared to the goal of an accuracy of 10^{-9}. The prescription for the cyclotron frequency in terms of the measurable eigenfrequencies given in Eq. (2.79) is proving to be useful for such experiments (e.g., Wineland, Bollinger, and Itano, 1983; Van Dyck, Moore, Farnham, and Schwinberg, 1985).

E. Radiation damping

An accelerated charge radiates electromagnetic waves, and there is a corresponding reaction that damps the motion of the charge. As is well known, the transition probability for such electric dipole radiation is proportional to a high power of the transition frequency; appreciable radiative decay occurs only for high transition frequencies. For protons or heavier ions in a Penning trap, the frequencies of the motion are generally in the radiofrequency range, and the radiative decay is negligibly small. This is also the case for the axial and magnetron motions of a trapped electron. The spin motion decays via magnetic dipole radiation at a rate that is exceedingly small. However, for the cyclotron motion of an electron in a strong magnetic field, radiative decay is the dominant decay mechanism, and we shall investigate it in more detail.

The energy in a classical cyclotron orbit is decreased by the power radiated, according to the familiar Larmor formula (see, for example, Jackson, 1975, Sec. 14.2)

$$-\frac{dE}{dt} = \frac{2e^2}{3c^3}\ddot{\rho}^2 . \tag{2.89}$$

Since

$$\ddot{\rho} = \omega_c \times \dot{\rho} \tag{2.90}$$

and

$$E = \tfrac{1}{2}m\dot{\rho}^2 , \tag{2.91}$$

we have

$$\frac{dE}{dt} = -\gamma_c E , \tag{2.92}$$

in which

$$\gamma_c = \frac{4e^2\omega_c^2}{3mc^3} \tag{2.93}$$

is the cyclotron damping constant. Thus the cyclotron energy decays as

$$E(t) = E_0 e^{-\gamma_c t} . \tag{2.94}$$

It is convenient to introduce the classical radius r_0 of the charged particle defined by

$$r_0 = \frac{e^2}{mc^2} \tag{2.95}$$

and write

$$\gamma_c = \left[\frac{4r_0\omega_c}{3c}\right]\omega_c . \tag{2.96}$$

For the electron $r_0 \simeq 2.8 \times 10^{-13}$ cm, and with $\omega_c/2\pi \simeq 160$ GHz we have $\gamma_c^{-1} \simeq 8 \times 10^{-2}$ sec. Thus radiation damping is fairly fast for the cyclotron motion of an electron, and it is by far the most important damping mechanism for this motion. The cyclotron frequency ω_c is proportional to the inverse mass of the charged particle, as is the classical radius r_0. Therefore the cyclotron damping constant scales as $\gamma_c \sim 1/(\text{mass})^3$, and we see that for a proton in the same magnetic field we would have $\gamma_c^{-1} \simeq 5 \times 10^8$ sec. Radiation damping of the cyclotron motion of protons is completely insignificant. As we shall discuss in Sec. III, the cyclotron motion of a heavy particle is usually damped to a much greater degree by its interaction with an external circuit.

Essentially the same result follows from the quantum-mechanical treatment of the cyclotron motion modified by a Penning trap. The quantum-mechanical decay rate $\Gamma_{N'N}$ for the $N \to N'$ transition of a nonrelativistic atomic system is given by

$$\Gamma_{N'N} = \int \frac{d^3k}{(2\pi)^3} \frac{1}{2k^0} 2\pi\delta(k^0 - E_{N'N})$$

$$\times \sum_\varepsilon |\langle N'|e_r\varepsilon\cdot\mathbf{v}|N\rangle|^2 , \tag{2.97}$$

where $E_{N'N} = E_{N'} - E_N$ is the energy release of the decay. Here, to conform to modern field theory notation, we have temporarily reverted to natural units and used the charge $e_r^2/4\pi = e^2$. Carrying out the integration, using the polarization sum $\sum_\varepsilon |\varepsilon\cdot\mathbf{v}|^2 = \tfrac{2}{3}v^2$, and passing to conventional units, we obtain

$$\Gamma_{N'N} = \frac{4}{3}\frac{e^2}{\hbar c}\frac{E_{N'N}}{\hbar}|\langle N'|\mathbf{v}/c|N\rangle|^2 . \tag{2.98}$$

We may use Eq. (2.19) to express $\mathbf{v} = \dot{\rho}$ in terms of the $\mathbf{V}^{(\pm)}$ operators and then use Eqs. (2.48) to express this in terms of the creation and annihilation operators $a_+^\dagger$ and $a_\pm$. In this way we find the quantum formula for the cyclotron decay rate:

$$\Gamma_c = \frac{4}{3}\frac{e^2}{\hbar c}\omega_+ + \left[\frac{\omega_+/c}{\omega_+ - \omega_-}\right]^2 \frac{\hbar(\omega_+ - \omega_-)}{m}$$

$$\times |\langle n-1 | a_+ | n \rangle|^2 = \gamma_c' n , \qquad (2.99)$$

where

$$\gamma_c' = \frac{4e^2\omega_+^2}{3mc^3}\frac{\omega_+}{\omega_+ - \omega_-} . \qquad (2.100)$$

The quantum-mechanical result applies to the exact, non-relativistic motion in a Penning trap, including the effect of the electrostatic quadrupole potential. The damping constant γ_c' is simply the classical damping constant for the modified cyclotron motion. It differs only very slightly from the damping constant for the simple cyclotron motion [γ_c of Eq. (2.93)] in that ω_c is replaced by $\omega_+ = \omega_c'$ and there is an additional factor $\omega_+/(\omega_+ - \omega_-)$, which is typically very close to unity in view of the hierarchy given in Eq. (2.12). The modified result could be deduced from a classical procedure similar to that employed above to compute γ_c.

To demonstrate that the γ_c' defined by Eq. (2.99) is indeed related to the classical decay rate, consider a quantum ensemble with a density matrix that is diagonal in the number representation. Then, with P_n denoting the probability for finding the nth state, Eq. (2.99) implies that

$$\frac{d}{dt}P_n = \gamma_c'[(n+1)P_{n+1} - nP_n] . \qquad (2.101)$$

Hence the average quantum number

$$\langle n \rangle = \sum_n nP_n \qquad (2.102)$$

obeys

$$\frac{d\langle n \rangle}{dt} = -\gamma_c'\langle n \rangle \qquad (2.103)$$

and thus exponentially decays

$$\langle n(t) \rangle = \langle n(0) \rangle e^{-\gamma_c' t} , \qquad (2.104)$$

which is the simple quantum analog of the classical result (2.94).

The magnetron motion is formally identical to the cyclotron motion. All that we need do is to replace ω_+ by ω_- to obtain the "damping" constant for the magnetron motion from that for the cyclotron motion:

$$\gamma_m = \frac{4e^2\omega_-^2}{3mc^3}\frac{\omega_-}{\omega_+ - \omega_-} . \qquad (2.105)$$

The magnetron motion is unstable. Its energy is decreased by increasing its quantum number l. Hence for this motion

$$\frac{d\langle l \rangle}{dt} = +\gamma_m\langle l \rangle \qquad (2.106)$$

and

$$\langle l(t) \rangle = \langle l(0) \rangle e^{+\gamma_m t} . \qquad (2.107)$$

But

$$\gamma_m = \left[\frac{\omega_-}{\omega_+}\right]^3 \gamma_c' , \qquad (2.108)$$

and since typically $(\omega_-/\omega_+)^3 \approx 3 \times 10^{-16}$, $\gamma_m^{-1} \simeq 3 \times 10^{14}$ sec for a trapped electron, corresponding to a "decay" time of 10^8 yr. The time constant for a proton is, of course, much longer. The magnetron motion is effectively stable against radiation damping. Imperfections in the trap are far more important in triggering the instability of the magnetron motion.

A particle with its spin in the upper level will decay into its lower level by emitting a photon. Since this is a magnetic rather than an electric dipole transition, the rate is much slower than that for the cyclotron decay. The spin interaction is $-\boldsymbol{\mu}\cdot\mathbf{B}$ rather than $-e(\mathbf{v}/c)\cdot\mathbf{A}$. Remembering the definition (2.59) of $\boldsymbol{\mu}$, we see that the decay rate is calculated by replacing $\boldsymbol{\varepsilon}\cdot\mathbf{v}$ in Eq. (2.97) with $(g\hbar/4m)\boldsymbol{\varepsilon}\cdot\mathbf{k}\times\boldsymbol{\sigma}$. Since $\boldsymbol{\varepsilon}$ is orthogonal to $\mathbf{k}$, the polarization sum is now given by $\sum_\varepsilon |\boldsymbol{\varepsilon}\cdot\mathbf{k}\times\boldsymbol{\sigma}|^2 = (\mathbf{k}\times\boldsymbol{\sigma})^2$. Following the calculation of the cyclotron decay rate, one finds that the spin-flip decay rate is given by

$$\Gamma_s = \frac{1}{6}\left[\frac{e^2}{\hbar c}\right]\left[\frac{g\hbar\omega_s}{mc^2}\right]^2 \omega_s \approx \frac{\hbar\omega_s}{mc^2}\gamma_c . \qquad (2.109)$$

Since $(\hbar\omega_s/mc^2) \approx 10^{-12}$ while $\gamma_c^{-1} \simeq 0.1$ sec, we see that $\Gamma_s \approx 10^{-11}$ sec^{-1}, corresponding to a decay time of 10^4 yr. The spin is effectively stable against radiative decay.

The radiation process also damps the axial motion, with the energy loss given by replacing $\ddot{\mathbf{p}}$ with $\ddot{z}$ in Eq. (2.89). Using $\ddot{z} = -\omega_z^2 z$ and averaging over a cycle so that we may use the virial theorem to write

$$\bar{E} = m\omega_z^2\overline{z^2} , \qquad (2.110)$$

we see that

$$\frac{d\bar{E}}{dt} = -\gamma_{z,\text{rad}}\bar{E} \qquad (2.111)$$

with the damping constant being given by

$$\gamma_{z,\text{rad}} = \left[\frac{2r_0\omega_z}{3c}\right]\omega_z . \qquad (2.112)$$

This is exactly analogous to the cyclotron decay constant except for a factor of 2, which appears because the cyclotron motion is equivalent to the superposition of two harmonic oscillators. For an electron with $\omega_z/2\pi \approx 60$ MHz, we have $\gamma_{z,\text{rad}}^{-1} \simeq 1 \times 10^6$ sec. The corresponding damping constant for a proton is yet much smaller. As we shall discuss in Sec. III, the axial motion is generally damped to a much greater degree by its interaction with an external circuit.

The results that we have described apply when the charged particle radiates into free space. If, on the other hand, the charged particle is confined inside a conducting

TABLE I. Trapping parameters for an electron. The numerical values are those used in the trap shown in Fig. 1 (Gabrielse and Dehmelt, 1981a). They differ from those first used to trap a single electron (Wineland, Ekstrom, and Dehmelt, 1973) principally in that the magnetic field is about 7 times larger. The parameters are essentially the same as those used more recently to measure electron and positron g values (Schwinberg, Van Dyck, and Dehmelt, 1981b), except that they use a slightly lower 50.50-kG magnetic field. The measured axial frequency is only approximately related to the potential and size of the trap by Eq. (2.7) because of electrostatic effects discussed in Sec. IX.

External parameters		
Trap potential	$V_0 = 10.22$ V	
Trap sizes	$d = z_0 = \rho_0/\sqrt{2} = 0.335$ cm	
Field strength	$B = 58.72$ kG	
Measured eigenfrequencies and energy-level spacings		
Cyclotron	$\nu_c' = 164.4$ GHz	$\hbar\omega_c' = 6.799 \times 10^{-4}$ eV
Axial	$\nu_z = 64.42$ MHz	$\hbar\omega_z = 2.581 \times 10^{-7}$ eV
Magnetron	$\nu_m = 11.85$ kHz	$\hbar\omega_m = 4.901 \times 10^{-11}$ eV
Measured damping widths		
Cyclotron	$\gamma_c/2\pi \approx 0.5$ Hz (radiative damping modified by trap cavity)	
Axial	$\gamma_z/2\pi \approx 6$ Hz (coupling to external circuit)	
Magnetron	$\gamma_m \approx$ unmeasurably small	

cavity, it can radiate only at frequencies within the linewidth of a cavity mode. A charged particle in harmonic motion can radiate only at the frequency of its oscillation. If this natural frequency lies outside the linewidth of any cavity mode, the radiation process is greatly inhibited and the corresponding damping constant reduced accordingly. The electrodes of the Penning trap form a lossy microwave cavity with a typical dimension of about 1 cm. The cyclotron radiation has a wavelength of about 0.2 cm. It could happen that the modes within the Penning trap are sufficiently sharp and widely spaced

to inhibit the damping of the cyclotron motion. Recent measurements in the trap represented in Fig. 1 (Gabrielse and Dehmelt, 1985) gave $\gamma_c^{-1} \simeq 0.3$ sec rather than the value $\gamma_c^{-1} \simeq 8 \times 10^{-2}$ sec that we have calculated. Subsequently, $\gamma_c^{-1} \approx 1$ sec was measured for a trap whose microwave properties differ principally in that its electrodes have fewer slits (Van Dyck, Schwinberg, and Dehmelt, 1984). These experimental results indicate that the trap electrodes act as a microwave cavity in the manner we have described. These cavity effects are discussed in detail in Sec. VIII.

TABLE II. Trapping parameters for a proton. The numerical values are for one version of the electron-proton mass ratio experiment (Van Dyck and Schwinberg, 1981). The measured axial frequency is only approximately related to the trap potential and trap size of Eq. (2.7) because of electrostatic effects discussed in Sec. IX.

External parameters		
Trap potential	$V_0 = 53.10$ V	
Trap sizes	$d = z_0 = \rho_0/\sqrt{2} = 0.112$ cm	
Field strength	$B = 50.50$ kG	
Measured eigenfrequencies and energy-level spacings		
Cyclotron	$\nu_c' = 76.34$ MHz	$\hbar\omega_c' = 3.157 \times 10^{-7}$ eV
Axial	$\nu_z = 10.06$ MHz	$\hbar\omega_z = 4.160 \times 10^{-8}$ eV
Magnetron	$\nu_m = 662.8$ kHz	$\hbar\omega_m = 2.741 \times 10^{-9}$ eV
Estimated damping widths (Secs. III.A and III.E)		
Cyclotron	$\gamma_c/2\pi \approx 10^{-3}$ Hz (coupling to external circuit)	
Axial	$\gamma_z/2\pi \approx 10^{-3}$ Hz (coupling to external circuit)	
Magnetron	$\gamma_m \approx$ unmeasurably small	

TABLE III. Orbit parameters for a trapped electron.

Cyclotron motion in thermal equilibrium with radiation field at 4.2 K	
Radius	$\rho_c \approx 1 \times 10^{-6}$ cm
Velocity	$v_c/c \approx 4 \times 10^{-5}$
Energy	$E_n \approx 3 \times 10^{-4}$ eV
Quantum number	$n < 1$

Axial motion in thermal equilibrium with external circuit at 4.2 K	
Amplitude	$z \approx 3 \times 10^{-3}$ cm
Velocity	$\dot{z}/c \approx 4 \times 10^{-5}$
Energy	$E_k \approx 3 \times 10^{-4}$ eV
Quantum number	$k \approx 1 \times 10^3$

Magnetron motion cooled to limit [Eq. (2.58)]	
Radius	$\rho_m \approx 6 \times 10^{-5}$ cm
Velocity	$v_m/c \approx 1 \times 10^{-10}$
Energy	$E_l \approx -7 \times 10^{-8}$ eV
Quantum number	$l \approx 1 \times 10^3$

F. Numerical summary

Tables I—IV summarize the various trap and orbit parameters that we have encountered in this section.

III. DETECTION AND DAMPING WITH AN EXTERNAL CIRCUIT

The axial resonance is of particular importance in the experiments with one electron or positron. It is at a radio frequency, which is relatively easy to use in the laborato-

TABLE IV. Orbit parameters for a trapped proton.

Cyclotron motion in thermal equilibrium with external circuit at 4.2 K	
Radius	$\rho_c \approx 5 \times 10^{-5}$ cm
Velocity	$v_c/c \approx 9 \times 10^{-7}$
Energy	$E_n \approx 3 \times 10^{-4}$ eV
Quantum number	$n \approx 1 \times 10^3$

Axial motion in thermal equilibrium with external circuit at 4.2 K	
Amplitude	$z \approx 4 \times 10^{-4}$ cm
Velocity	$\dot{z}/c \approx 9 \times 10^{-7}$
Energy	$E_k \approx 3 \times 10^{-4}$ eV
Quantum number	$k \approx 8 \times 10^3$

Magnetron motion cooled to limit [Eq. (2.58)]	
Radius	$\rho_m \approx 1 \times 10^{-4}$ cm
Velocity	$v_m/c \approx 2 \times 10^{-8}$
Energy	$E_l \approx -2 \times 10^{-5}$ eV
Quantum number	$l \approx 8 \times 10^3$

ry, while the cylotron and spin resonances are at very high microwave frequencies, which are much less accessible. As a result, all information about cyclotron and spin excitations is detected via small couplings, which produce corresponding small shifts in the axial resonance frequency. Fractional shifts $\Delta\omega_z/\omega_z \approx 2 \times 10^{-8}$ are routinely measured. We thus treat the axial motion in particular detail, beginning with its damping and detection in Sec. III.A. Thermal Johnson noise, which itself drives the axial motion, is discussed in Sec. III.B. The trapping potential is often frequency modulated for experimental convenience (Wineland, Ekstrom, and Dehmelt, 1973). Although this is useful, we show in Sec. III.C that it does not alter essentially the simple model of Sec. III.A. Laboratory Penning traps do not produce a pure quadrupole electrostatic potential, but they can be tuned to improve the potential (Van Dyck, Wineland, Ekstrom, and Dehmelt, 1976). The axial oscillation in a potential that deviates slightly from a pure quadrupole potential can provide an illustration of an anharmonic oscillator that is of textbook clarity. However, it is extremely important to make the axial oscillation as harmonic as possible if small shifts are to be detected. This is done by monitoring the shape of the axial resonance, which we discuss in Sec. III.D, while making small adjustments to a compensation potential (discussed later in Sec. IX). The cyclotron frequency is also an accessible radio frequency for protons and heavier ions. In Sec. III.E we describe how the ion cyclotron motion can be damped and detected in a similar way.

A. Axial motion

The axial oscillations of a particle bound to a Penning trap are usually in the radio-frequency range. The radio-frequency structure of the trap may be represented by the idealized circuit shown in Fig. 9 (Walls and Dehmelt, 1968). The oscillating charged particle induces alternating image charges in the electrodes, which in turn cause
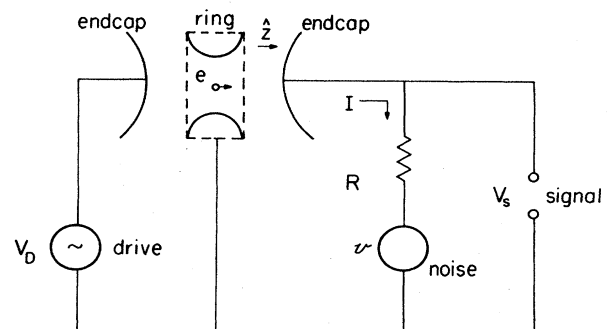
FIG. 9. Idealization of the radio-frequency circuit used to damp and detect the axial oscillation of a trapped particle. A charge e moving toward the right induces a current I through the resistor. The axial motion is driven by the oscillatory potential V_D and by the Johnson noise from the resistor v, while the signal voltage V_S is detected.

an oscillating current I to flow through a resistor R. In practice, a pure resistive impedance is realized at radio frequencies near ω_z by tuning out the trap capacitance, which is parallel to R, with an appropriate parallel inductor.[7] The voltage v represents the thermal noise in this effective resistor, which is at temperature T. The axial motion is monitored by amplifying and detecting V_S, the voltage between one endcap electrode and the ring electrode. It is the sum of the noise voltage v and the IR drop across the resistor. The detected signal is so small that it is most often necessary to drive the axial oscillation with an external drive potential V_D applied between the opposite endcap and the ring to increase the oscillation amplitude to a level where it can be detected above the noise.[8]

Energy lost in the effective resistance R damps the axial oscillation. To understand this damping, let us consider the situation where there is no external drive potential $(V_D=0)$ and where the temperature T of the resistor is so low that the noise voltage is negligible $(T=0, v=0)$. A trapped particle of charge e moving with velocity $\dot{z}$ toward the endcap connected to the resistor causes a current I to flow through R, and hence a voltage IR is induced between this endcap and the ring. Near the center of the trap, this potential produces an axial electric field $\kappa(IR)/2z_0$, where $2z_0$ is the spacing of the endcap electrodes along the z axis and κ is a dimensionless constant of order unity. This constant, which would be exactly equal to 1 if the endcaps were infinite flat plates with the ring removed, is discussed in Sec. IX.D.[9] The electric field produces an axial force on the trapped particle given by

$$f = -e\kappa IR/2z_0 ,$$ (3.1)

which opposes its motion. The energy of the charged particle decreases at the rate $\dot{z}f$, and this power is dissipated in the resistor:

$$-\dot{z}f = I^2 R .$$ (3.2)

Comparing this pair of equations yields (Shockley, 1938; Sirkis and Holonyak, 1966)

$$I = \kappa(e/2z_0)\dot{z} .$$ (3.3)

The current I is proportional to the velocity $\dot{z}$ as one would expect, and therefore the force given in Eq. (3.1) is a dissipative force,

$$f = -m\gamma_z\dot{z} ,$$ (3.4)

with the damping constant for the axial motion, γ_z, given by (Walls and Dehmelt, 1968; Wineland and Dehmelt, 1975b)

$$\gamma_z = \left[\frac{e\kappa}{2z_0}\right]^2 \frac{R}{m} .$$ (3.5)

Note that the damping constant is inversely proportional to the mass. A proton or heavier particle is much less damped than is an electron.

To obtain convenient experimental units, we express the damping constant as

$$\gamma_z = \kappa^2 \frac{r_0 c}{4z_0^2} \frac{4\pi R}{\Omega_0} ,$$ (3.6)

where

$$r_0 = \frac{e^2}{4\pi\varepsilon_0 mc^2}$$ (3.7)

is the classical radius of the charged particle, and

$$\Omega_0 = \frac{1}{\varepsilon_0 c} = \left[\frac{\mu_0}{\varepsilon_0}\right]^{1/2} \simeq 377 \ \Omega$$ (3.8)

is the usual impedance of the vacuum, in mks units. For the electron, $r_0 = 2.8 \times 10^{-13}$ cm, and using the typical values $2z_0 = 0.67$ cm (Table I), $\kappa = 0.80$ (Gabrielse, 1984; see Sec. IX.D), and[10] $R = 1.6 \times 10^5 \ \Omega$, which pertain to the trap shown in Fig. 1, we have $\gamma_z/2\pi = 10$ Hz. This should be compared to $\nu_z = 62$ MHz; the axial motion is only very slightly damped, with a quality factor $Q = \omega_z/\gamma_z \approx 10^7$. The much more massive proton in a trap three times smaller (Table II), with $R = 6.5 \times 10^4 \ \Omega$, has a much smaller damping constant $\gamma_z/2\pi = 50$ mHz. The correspondingly higher $Q \approx 10^9$ allows a more accurate measurement of the axial frequency ω_z. On the other hand, the more massive proton moves with a much slower velocity, the induced current I is much smaller, and the signal IR is quite small, making it more difficult to obtain a good signal-to-noise ratio.

Let us now include the effect of the drive and noise. Placing the damping term on the left-hand side of the equation of motion, we have

---

[7]The resistance R is generally made as large as possible to improve signal-to-noise [see the discussion below Eq. (3.13)]. In fact, the effective R often results from the very small radio-frequency loss still present when the tuned circuit is submerged in liquid helium, with R being proportional to the inverse of this series resistive loss. The $Q \approx 10^3$ of the tuned circuit is much smaller than the $Q \approx 10^7$ of the axial resonance. Hence, after the resonant frequency of the LCR circuit has been adjusted to coincide with that of the axial oscillation, it acts as a pure resistor throughout the range of the axial resonance.

[8]As mentioned in the introductory paragraph, the actual drive may involve frequency modulation, so as effectively to eliminate the rf feedthrough from one endcap to the other. This modification is discussed in Sec. III.C below. It does not modify significantly the results of the simple model analyzed here.

[9]Section IX describes the electrostatics of the trap more precisely, as well as treating higher-order, nonlinear terms in the potential.

[10]The effective radio-frequency resistance R is determined indirectly from a measurement of the inductance L, which cancels the trap capacitance, together with a measurement of the Q of the tuned circuit, with $R = Q\omega_z L$.

$$m\left[\frac{d^2}{dt^2}+\gamma_z\frac{d}{dt}+\omega_z^2\right]z(t)=F(t) \ , \tag{3.9}$$

where ω_z is the axial frequency of Eq. (2.7), a parameter that specifies the strength of the restoring force of the electric quadrupole potential. Referring to the discussion of Eq. (3.1), we see that the nondissipative force is given by

$$F=(e\kappa/2z_0)(V_D-v) \ . \tag{3.10}$$

The two voltages appear with opposite signs because they are applied to opposing endcaps.

In view of Eq. (3.3), the detected voltage V_S, the voltage between the ring and one endcap is given by

$$V_S=v+\frac{e\kappa}{2z_0}R\dot{z} \ . \tag{3.11}$$

Fourier-transforming $(z\sim e^{-i\omega t})$ the equation of motion (3.9) gives

$$z(\omega)=\left[\frac{e\kappa}{2z_0 m}\right]\frac{V_D(\omega)-v(\omega)}{\omega_z^2-\omega^2-i\omega\gamma_z} \tag{3.12}$$

and, remembering the definition (3.5) of γ_z,

$$V_S(\omega)=\frac{(\omega_z^2-\omega^2)v(\omega)-i\omega\gamma_z V_D(\omega)}{\omega_z^2-\omega^2-i\omega\gamma_z} \ . \tag{3.13}$$

A good axial resonance curve is shown in Fig. 10. We shall discuss the observed signal in more detail in Sec. III.B, but it is worth making several comments now. First, we see that as the drive $V_D(\omega)$ sweeps over frequency we have a Lorentzian response with a full width γ_z at half maximum. This leads to the measured value $\gamma_z/2\pi=6$ Hz for the trap shown in Fig. 1, to be compared with the theoretical value $\gamma_z/2\pi=10$ Hz discussed above. The discrepancy between these two numbers is
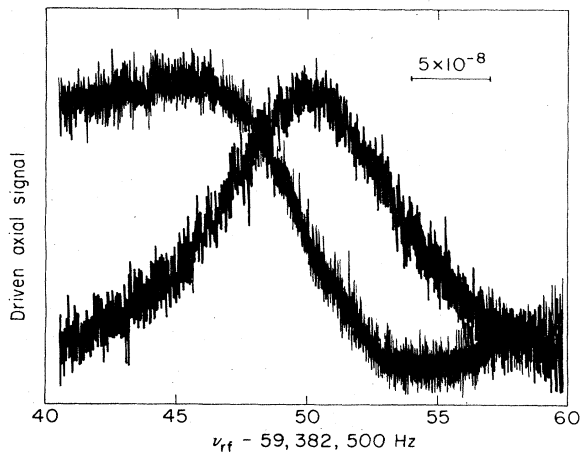

FIG. 10. Two observations of the axial resonance of a single electron. The absorption and dispersion profiles correspond to $\varphi=0$ and to $\varphi=-\pi/2$ in Eq. (3.36). Notice that the noise decreases by approximately a factor of 2 on resonance (Van Dyck, Schwinberg, and Dehmelt, 1978).

typical of several traps (Gabrielse, 1984), and it is as yet not understood. Second, we note that the resistor noise $v(\omega)$ corresponds to the familiar Johnson noise, which we shall discuss in detail in Sec. III.B. As is well known, $v(\omega)$ is proportional to $R^{1/2}$, while γ_z is proportional to R. Equation (3.13) therefore shows that the signal-to-noise ratio is improved by increasing the resistance R. Finally Eq. (3.13) shows that the noise is "shorted out" on resonance[11] $\omega=\omega_z$, with $V_S(\omega_z)=V_D(\omega_z)$. It is evident from Fig. 10 that very little "shorting out" is observed. This is, presumably, the result of nonlinearities and other imperfections in the trapping system. For example, electrostatic anharmonicities make the instantaneous value of ω_z depend upon the amplitude of the axial oscillation, and thus upon the noise that is, in part, driving the oscillation. Hence ω_z jiggles, keeping $\omega=\omega_z$ from being precisely defined.

B. Axial noise

We turn now to an analysis of the Brownian motion undergone by the axial oscillation in response to the noise voltage $v(t)$. We shall need the results of this analysis in order to discuss more fully the noise in the axial resonance as well as for our later discussion of the cooling limit of the magnetron motion and of the line shape of the cyclotron and anomaly resonances. Many of the results that we shall describe contain elements that are well known in the theory of the Johnson noise of a resistor.

First, we obtain the general solution of the equation of motion (3.9) by introducing the corresponding retarded Green's function $G_z(t-t')$, which obeys

$$\left[\frac{d^2}{dt^2}+\gamma_z\frac{d}{dt}+\omega_z^2\right]G_z(t-t')=\delta(t-t') \ . \tag{3.14}$$

Fourier-transforming Eq. (3.14) with

$$G_z(t-t')=\int\frac{d\omega}{2\pi}\widetilde{G}_z(\omega)e^{-i\omega(t-t')} \tag{3.15}$$

gives

$$\widetilde{G}_z(\omega)=(\omega_z^2-i\omega\gamma_z-\omega^2)^{-1} \ . \tag{3.16}$$

The integral in the Fourier transform (3.15) is easily performed by standard contour methods. Neglecting the very small quantity $(\gamma_z/\omega_z)^2$, one finds that

$$G_z(t-t')=\frac{\theta(t-t')}{\omega_z}e^{-\gamma_z(t-t')/2}\sin\omega_z(t-t') \ , \tag{3.17}$$

in which $\theta(t-t')$ is the usual unit step function. [One

---

[11]This effect was derived by Wineland and Dehmelt (1975b), who observed that a trapped particle obeys, with a suitable definition of parameters, the differential equation of a series LCR circuit. The trapped particle can thus be replaced by a series LCR circuit connected between the endcap electrodes. On resonance, the L and C cancel, shorting the endcaps.

can, of course, verify directly that Eq. (3.17) does indeed obey Eq. (3.14).] The axial motion is driven by the sum of the noise $v(t)$ and the coherent drive $V_D(t)$, and since the equation of motion is linear we may write correspondingly

$$z(t) = z_N(t) + z_D(t) \ . \tag{3.18}$$

Neglecting transient effects which decay in a time $1/\gamma_z$, we have

$$z_N(t) = -(e\kappa/2z_0 m) \int_{-\infty}^{\infty} dt_1 G_z(t-t_1)v(t_1) \tag{3.19}$$

and a similar formula for $z_D(t)$ with $-V_D$ replacing v.

The noise voltage $v(t)$ is a random, fluctuating variable with a vanishing average value, $\langle v(t) \rangle = 0$. This noise voltage arises from atomic processes in the external circuit which are much faster than the time scale ω_z^{-1} of the axial oscillation. Hence, on the time scale of the axial oscillation, the noise voltages are effectively uncorrelated at different times, with

$$\langle v(t_1)v(t_2) \rangle = 0, \quad t_1 \neq t_2 \ . \tag{3.20}$$

Within the time resolution of the oscillation, the average correlation of two noise voltages is a sharp δ function in time, $\delta(t_1 - t_2)$. Thus the voltage $v(t)$ is effectively white noise, which is uniformly distributed in frequency since the Fourier transform of the δ function is a constant. The only parameters available to characterize the effective resistor that represents the external detection circuit are its resistance R and temperature T. The combination $k_B TR$ has the dimensions of voltage squared multiplied by time. Therefore the coefficient of the δ function is $k_B TR$ multiplied by some purely numerical factor, since the δ function has the dimensions of inverse time. We anticipate this number in writing

$$\langle v(t_1)v(t_2) \rangle = 2k_B TR \delta(t_1 - t_2) \ . \tag{3.21}$$

The average correlation of the oscillator coordinates in the absence of a coherent drive ($V_D = 0$),

$$C(t-t') = \langle z(t)z(t') \rangle \ , \tag{3.22}$$

is important for our later work. Using Eqs. (3.19) and (3.21) we have

$$C(t-t') = 2k_B TR \left[\frac{e\kappa}{2z_0 m} \right]^2$$

$$\times \int_{-\infty}^{\infty} dt_1 G_z(t-t_1)G_z(t'-t_1) \ . \tag{3.23}$$

Writing the correlation function as a Fourier transform

$$C(t-t') = \int \frac{d\omega}{2\pi} \widetilde{C}(\omega)e^{i\omega(t-t')} \tag{3.24}$$

and recalling the definition (3.5) of γ_z, one obtains

$$\widetilde{C}(\omega) = (2k_B T\gamma_z/m) \, | \, \widetilde{G}_z(\omega) \, |^2 \ . \tag{3.25}$$

The correlation function $C(t-t')$ may now be evaluated by inserting Eq. (3.25) in Eq. (3.24), using Eq. (3.16), and calculating the integral by contour integration. Again

neglecting the small ratio $(\gamma_z/\omega_z)^2$, we find that

$$C(t-t') = (k_B T/m\omega_z^2)e^{-\gamma_z|t-t'|/2}\cos\omega_z(t-t') \ . \tag{3.26}$$

We may now justify the numerical factor of 2 on the right-hand side of Eq. (3.21). The equal time limit of Eq. (3.26) gives

$$\langle z^2 \rangle = C(0) = \frac{k_B T}{m\omega_z^2} \ , \tag{3.27}$$

and we see that the factor of 2 is necessary to obtain the thermodynamic equipartition of energy.

With these results in hand, we can discuss in more detail the signal produced by the axial oscillation. The motion driven with a single frequency

$$V_D(t) = V_d \cos\omega t \tag{3.28}$$

gives the response

$$z_D(t) = V_d \frac{e\kappa}{2z_0 m} \text{Re}[\widetilde{G}_z(\omega)e^{-i\omega t}] \ , \tag{3.29}$$

where Re denotes the real part. The noise component (3.19) adds to this to produce the full motion (3.18). Recalling that the signal voltage is given by Eq. (3.11), we see that we may also write V_S as the sum of terms corresponding to the external drive and the noise,

$$V_S = V_{S,D} + V_{S,N} \ , \tag{3.30}$$

in which, according to Eqs. (3.5) and (3.9)—(3.11),

$$V_{S,D} = \left[\frac{e\kappa}{2z_0} \right] R\dot{z}_D = \left[\frac{2z_0 m}{e\kappa} \right] \gamma_z \dot{z}_D \tag{3.31}$$

and

$$V_{S,N} = - \left[\frac{2z_0 m}{\kappa e} \right] \left[\frac{d^2}{dt^2} + \omega_z^2 \right] z_N \ . \tag{3.32}$$

The signal is often measured using phase-sensitive detection so as to substantially reduce the effect of the noise. The voltage $V_S(t)$ is multiplied by (mixed with) a voltage that oscillates at the drive frequency ω but that is shifted by a phase φ. The product is sent through a filter with a narrow bandwidth $\Delta\omega$. This process produces a signal

$$S = \int dt \, F(t)V_S(t) \ , \tag{3.33}$$

in which

$$F(t) = F(\omega, \Delta\omega, \varphi; t)$$

$$= 2 \int_{-\Delta\omega/2}^{\Delta\omega/2} \frac{d\omega'}{2\pi} \cos[(\omega + \omega')t - \varphi] \ . \tag{3.34}$$

To verify this, we note that if $V_S(t)$ in Eq. (3.33) is replaced by $\cos(\omega_1 t - \psi)$, one obtains $S = \cos(\varphi - \psi)$ if $\omega - \Delta\omega/2 < \omega_1 < \omega + \Delta\omega/2$ but zero otherwise. As in Eq. (3.30) we write

$$S = S_D + S_N \ . \tag{3.35}$$

Using Eqs. (3.29), (3.31), and (3.33), we find that near resonance the drive produces a signal given by

$$S_D = V_d \frac{(\gamma_z^2/4)\cos\varphi + (\gamma_z/2)(\omega - \omega_z)\sin\varphi}{(\omega - \omega_z)^2 + \gamma_z^2/4} . \qquad (3.36)$$

Choosing $\varphi = 0$ or $\varphi = -\pi/2$ gives the familiar absorptive or dispersive Lorentzian line profiles. Both choices are used experimentally, as shown in Fig. 10.

To include the effect of the noise, we imagine performing the experiment a large number of times, so as to produce an ensemble average, the average we have previously used in deriving the correlation function $C(t - t')$. Since $\langle v \rangle = 0$, the average value of the signal is due entirely to the coherent drive,

$$\langle S \rangle = S_D . \qquad (3.37)$$

The magnitude of the noise fluctuations is assessed by

$$\Delta S^2 = \langle (S - \langle S \rangle)^2 \rangle = \langle S_N^2 \rangle . \qquad (3.38)$$

Thus ΔS is the rms noise fluctuation in S. Employing Eqs. (3.32), (3.33), and (3.22), we have

$$\Delta S^2 = \left[\frac{2z_0 m}{e\kappa} \right]^2 (\omega_z^2 - \omega^2)^2$$

$$\times \int dt\, dt'\, F(t) F(t') C(t - t')$$

$$= \left[\frac{2z_0 m}{e\kappa} \right]^2 (\omega_z^2 - \omega^2)^2 \int \frac{d\bar{\omega}}{2\pi} |\tilde{F}(\bar{\omega})|^2 \tilde{C}(\bar{\omega}) . \qquad (3.39)$$

In the first line we have integrated by parts so as to replace double time derivatives by the factor $-\omega^2$, which appears when these derivatives act on the filter function F in the narrow bandpass limit that we assume. In the second line we have replaced the time convolution by the equivalent Fourier transform. In the narrow bandpass limit, it is not difficult to see that we have, effectively,

$$|\tilde{F}(\bar{\omega})|^2 = \Delta\omega[\delta(\bar{\omega} - \omega) + \delta(\bar{\omega} + \omega)] . \qquad (3.40)$$

Since $\tilde{C}(\omega)$ is an even function of ω, we now find that

$$\Delta S^2 = \frac{\Delta\omega}{\pi} \left[\frac{2z_0 m}{e\kappa} \right]^2 (\omega^2 - \omega_z^2)^2 \tilde{C}(\omega) . \qquad (3.41)$$

Recalling the definitions of γ_z [Eq. (3.5)] and the relationship of $\tilde{C}(\omega)$ to $\tilde{G}_z(\omega)$ [Eq. (3.25)], we may write Eq. (3.41) in the form

$$\Delta S^2 = (2\Delta\omega k_B TR/\pi)(\omega_z^2 - \omega^2)^2 |\tilde{G}_z(\omega)|^2$$

$$= 4k_B T \left[\frac{\Delta\omega}{2\pi} \right] \frac{(\omega_z^2 - \omega^2)^2}{(\omega_z^2 - \omega^2)^2 + (\omega\gamma_z)^2} . \qquad (3.42)$$

This explicitly displays the "noise shorting" on resonance for the idealized model that we have discussed previously. Far away from resonance we have $\Delta S^2 = 4k_B TR\,\Delta\nu$,

which is the familiar result for the squared Johnson noise voltage for a resistance R at temperature T in a bandwidth $\Delta\nu$.

The size of the Johnson noise voltage sets a rough lower bound on the magnitude of the coherent excitation of the axial motion necessary in order to observe an axial resonance. Without a coherent drive, the electron absorbs power from the noise and comes into thermal equilibrium with an axial energy of $k_B T$. The coherent drive increases the energy in the axial oscillation by an amount we shall call the coherent energy in the axial oscillation, E. To estimate how large E must be to be detected, we examine the minimal condition that the coherent signal be larger than the rms signal fluctuation, $S_D \gtrsim \Delta S$. We use the off-resonance Johnson noise, $\Delta S^2 = 4k_B TR\,\Delta\nu$, since little shorting of the noise is yet observed in present experiments. For the signal S_D, we use the peak of the absorption signal ($\varphi = 0$, $\omega = \omega_z$), $S_D = V_d$, as given by Eq. (3.36). Recalling Eqs. (3.29), (3.16), and (3.5), it is easy to see that on resonance $E = (V_d^2/2\gamma_z R)$. Thus we obtain the rough estimate

$$E \gtrsim k_B T(2\Delta\nu/\gamma_z) \qquad (3.43)$$

for the excitation level necessary to observe the axial resonance. Note that the phase-sensitive detection with a narrow-band filter makes it possible to observe coherent energy excitations that are less than the thermal excitation, $E < k_B T$, when the filter bandwidth is less than $\frac{1}{2}\gamma_z$, as is most often the case in the geonium experiments. For typical electron values of $\gamma_z/2\pi = 6$ Hz and $\Delta\nu = 1$ Hz, Eq. (3.43) yields $E \gtrsim 5 \times 10^{-2} k_B T$. Even when additional amplifier and detector noise (which are beyond the scope of this paper) are included, one can estimate that coherent excitations with an energy $E \approx k_B T$ are still observable. To provide an estimate of the size of the detected signal potentials, we take $T \approx 10$ K, $R \approx 10^5$ Ω, and $\Delta\nu \approx 1$ Hz. Using $\Delta S^2 = 4kTR\,\Delta\nu$, we have $\Delta S \approx 10^{-8}$ V, or a detected power of $\Delta S^2/R \approx 10^{-21}$ W.

Correlation functions for arbitrary products of $z(t)$ at different times are needed for the calculation of line shapes, which we shall discuss later in Sec. VI.C. These are the correlation functions for $z(t)$ in the absence of a coherent drive. They are given by a Gaussian factorization. Thus, for the four-time correlation function, we have

$$\langle z(t_1)z(t_2)z(t_3)z(t_4) \rangle = C(t_1 - t_2)C(t_3 - t_4)$$

$$+ C(t_1 - t_3)C(t_2 - t_4)$$

$$+ C(t_1 - t_4)C(t_2 - t_3) , \qquad (3.44)$$

with a similar factorization in terms of all possible pairings holding for the higher correlations. This factorization follows from that of the noise voltage driving terms where, for example,

$$\langle v(t_1)v(t_2)v(t_3)v(t_4) \rangle = \langle v(t_1)v(t_2) \rangle \langle v(t_3)v(t_4) \rangle + \langle v(t_1)v(t_3) \rangle \langle v(t_2)v(t_4) \rangle + \langle v(t_1)v(t_4) \rangle \langle v(t_2)v(t_3) \rangle . \qquad (3.45)$$

The factorization follows in turn from simple dimensional analysis and the fact that the voltage $v(t)$ is effectively white noise. For example, there is no intrinsic four-time correlation for $v(t)$ because the noise is white, and such an intrinsic correlation would involve

$$\delta(t_1-t_2)\delta(t_2-t_3)\delta(t_3-t_4) \ ,$$

but this product of three δ functions cannot be adjusted to have the correct dimensions by multiplying it by any powers of $k_B T$ and R. The Gaussian factorization is most simply expressed in terms of the generating functional

$$Z[f]=\left\langle \exp\left[i \int dt\, f(t)z(t) \right]\right\rangle \ . \tag{3.46}$$

The coefficient of the expansion of $Z[f]$ in terms of n factors of $f(t)$ is simply related to the n-time correlation function. In terms of the generating functional, the Gaussian factorization is expressed as

$$Z[f]=\exp\left[-\tfrac{1}{2} \int dt\, dt' f(t)C(t-t')f(t') \right] \ . \tag{3.47}$$

Clearly the term involving two powers of $f(t)$ agrees with Eq. (3.23), while that involving four powers of $f(t)$ reproduces Eq. (3.44), and so forth.

We have yet to explain why the overall constant in the factorization illustrated by Eq. (3.44) is unity. (The appearance of the sum of terms is necessary to represent the symmetry of the n-time correlation.) To prove this, we compute the probability $P(z)$ to observe the oscillator to have the coordinate z,

$$P(z)=\langle \delta[z-z(t)]\rangle \ . \tag{3.48}$$

Using the Fourier representation of the δ function along with Eqs. (3.46) and (3.47), we get

$$
\begin{aligned}
P(z)&= \int_{-\infty}^{\infty} \frac{dk}{2\pi}e^{-ikz}\exp[-\tfrac{1}{2}C(0)k^2]\\
&= \frac{1}{\sqrt{2\pi C(0)}}e^{-C(0)^{-1}z^2/2}\\
&= \left[\frac{m\omega_z^2}{2\pi k_B T} \right]^{1/2} \exp(-\tfrac{1}{2}m\omega_z^2 z^2/k_B T) \ .
\end{aligned}
\tag{3.49}
$$

This is precisely the required Boltzmann distribution, and to obtain it the generating functional must have the form given in Eq. (3.47).

C. Frequency-modulated trapping potential

The trapping potential V_0 is often weakly modulated with a frequency ω_1 which is much lower than the axial resonance frequency ω_z. Typically ω_1/ω_z is about 10^{-2}. With this addition, the axial motion can be driven at the sideband frequencies $\omega_z\pm\omega_1$. The advantage of this method is that, coupled with appropriate tuned circuits and radio-frequency filters, it virtually eliminates the direct feedthrough from the drive endcap to the detector endcap (Wineland, Ekstrom, and Dehmelt, 1973).

The effect of the modulated trapping potential is to re-

place ω_z^2 by the frequency-modulated form

$$\overline{\omega}_z^2(t)=\omega_z^2(1+\varepsilon\cos\omega_1 t) \ , \tag{3.50}$$

where $\varepsilon\ll1$ is the relative amplitude of the modulation. The only modification of our previous work brought about by this new drive is the replacement of the Green's function $G_z(t-t')$ with the function $\overline{G}_z(t,t')$ defined by

$$\left[\frac{d^2}{dt^2}+\gamma_z\frac{d}{dt}+\overline{\omega}_z^2(t) \right]\overline{G}_z(t,t')=\delta(t-t') \tag{3.51}$$

and the same retarded boundary conditions. Since the modulation is weak ($\varepsilon\ll1$) and slow ($\omega_1\ll\omega_z$), a simple generalization of the construction of $G_z(t-t')$ given by Eq. (3.17) suffices:

$$
\overline{G}_z(t,t')\simeq\frac{\theta(t-t')}{[\overline{\omega}_z(t)\overline{\omega}_z(t')]^{1/2}}e^{-\gamma_z(t-t')/2}
$$

$$
\times\sin\left[\int_{t'}^{t}d\overline{t}\,\overline{\omega}_z(\overline{t}) \right] \ . \tag{3.52}
$$

Substituting this into the Green's-function equation (3.51), one finds that the equation is obeyed except for terms of order $\ddot{\overline{\omega}}_z(t)/\overline{\omega}_z^3(t)$ and $[\dot{\overline{\omega}}_z(t)/\overline{\omega}_z^2(t)]^2$. For our case, these are terms of relative order $\varepsilon^2\omega_1^2/\omega_z^2$, which are negligibly small. An additional term of order $\varepsilon\omega_1^2/\omega_z^2$ is removed by an insignificant renormalization of the coupling strength ε.

Expanding the square root defining $\overline{\omega}_z(t)$ in powers of ε, we see that the phase of the Green's function defined by Eq. (3.52) is given by

$$
\int_{t'}^{t}d\overline{t}\,\overline{\omega}_z(\overline{t})\simeq\omega_z\left[1-\frac{\lambda^2}{16}\right](t-t')
$$

$$
+\beta(\sin\omega_1 t-\sin\omega_1 t') \ , \tag{3.53}
$$

where

$$\beta=\frac{\varepsilon\omega_z}{2\omega_1} \ . \tag{3.54}$$

The parameter β is commonly referred to as the modulation index in the literature on frequency modulation. It is the ratio of the frequency excursion amplitude $\varepsilon\omega_z/2$ to the modulation frequency ω_1. In the geonium experiments ε is kept small enough so that $\beta\ll1$ even though $\omega_z\gg\omega_1$. We see from Eq. (3.53) that in the presence of the frequency modulation the fundamental axial resonance frequency is shifted to

$$\omega_z'=\omega_z\left[1-\frac{\varepsilon^2}{16}\right] \ . \tag{3.55}$$

In the experiments, this shift is used to calibrate the strength of the modulation. After the calibration, the modulation is reduced until the shift can no longer be observed. In the electron geonium experiments, for example, where $\nu_1=1$ MHz, the modulation drive strength is often reduced until the axial resonance frequency is shift-

ed by less than 1 Hz out of 60 MHz. This corresponds to $\varepsilon < 5 \times 10^{-4}$ and $\beta < 1.5 \times 10^{-2}$.

Again examining the phase integral in Eq. (3.53), we see that the frequency modulation also produces small sidebands, overtones, and undertones at the modified frequency ω_z' plus or minus an integer times the modulation frequency ω_1. The corresponding Fourier components are identified by the use of the generating function for the Bessel functions

$$\exp(i\beta\sin\theta) = \sum_{n=-\infty}^{\infty} e^{in\theta} J_n(\beta) . \tag{3.56}$$

We obtain

$$\sin\left[\int_{t'}^{t} d\bar{t}\,\bar{\omega}_z(\bar{t})\right] \simeq \sum_{n,n'} J_n(\beta) J_{n'}(\beta) \sin[(\omega_z' + n\omega_1)t$$

$$- (\omega_z' + n'\omega_1)t'] . \tag{3.57}$$

Thus a drive at frequency $\omega_z' + n'\omega_1$ produces a response at frequency $\omega_z' + n\omega_1$, where n' and n are arbitrary positive or negative integers. We are particularly interested in the situation of a small modulation index β. In this case only the fundamental with $n=0$ and the sidebands at $n = \pm 1$ are of any importance, since $J_n(\beta) \sim \beta^{|n|}$, and we may use

$$J_0(\beta) \simeq 1 \tag{3.58a}$$

and

$$J_1(\beta) = -J_{-1}(\beta) \simeq \tfrac{1}{2}\beta . \tag{3.58b}$$

With this review of some general aspects of frequency modulation in hand, we return to the geonium experiments in which there is a potential applied to an endcap,

$$V_D^{(\pm)}(t) = V_d \cos(\omega \pm \omega_1)t . \tag{3.59}$$

Here ω is near ω_z, and thus the $+$ and $-$ denote upper and lower sidebands adjacent to ω_z. This drive produces the response [cf. Eq. (3.19)]

$$z_D^{(\pm)}(t) = \left[\frac{e\kappa}{2z_0 m}\right] V_d \int dt' \bar{G}_z(t,t') \cos(\omega \pm \omega_1)t . \tag{3.60}$$

Since the modulation amplitude is very small ($\varepsilon \ll 1$), we approximate $\bar{\omega}_z(t) \simeq \omega_z \simeq \bar{\omega}_z(t')$ in the square root factors in the Green's function defined by Eq. (3.52) and use Eq. (3.57) for the sine appearing in this Green's function. We retain only the component at frequency $\omega_z + \omega_1$ (or $\omega_z - \omega_1$) in the t' dependence of the Green's function, since the other components are nonresonant and give very small contributions. On the other hand, we need keep only the components at frequency ω_z in the t dependence of the Green's function. The amplitudes for other frequencies are smaller by at least a factor of β, and these frequencies also do not pass through the rf filter. Using Eqs. (3.58) for small β, we find that

$$z_D^{(\pm)}(t) = \pm \tfrac{1}{2}\beta \left[\frac{e\kappa}{2z_0 m}\right] \frac{V_d}{2\omega_z} \mathrm{Re}\left[\frac{e^{-i\omega t}}{\omega_z - \omega - i\gamma_z/2}\right] . \tag{3.61}$$

Except for the factor $\pm\beta/2$, this result is identical to the resonant terms in Eq. (3.29), which gives the response for the unmodulated case. Therefore the effect on the detected signal of the modulation of the axial frequency is simply to make the replacement

$$S_D \rightarrow \pm\tfrac{1}{2}\beta S_D . \tag{3.62}$$

For the same applied endcap drive amplitude V_d, there is no effect on the signal other than reducing it by an overall factor of the modulation index $\beta/2$ and changing its phase by 180° for a drive on the lower $(-)$ sideband.

Following the derivation of the noise fluctuations given in Eq. (3.39) for the unmodulated case, the effect of the modulation may be accounted for by writing

$$\Delta S^2 = \left[\frac{2z_0 m}{e\kappa}\right]^2 \int dt\, dt'\,[\bar{\omega}_z^2(t) - \omega^2][\bar{\omega}_z^2(t') - \omega^2]$$

$$\times F(t)F(t')\bar{C}(t,t') , \tag{3.63}$$

in which now

$$\bar{C}(t,t') = \frac{k_B T}{m\omega_z} \frac{1}{[\bar{\omega}_z(t)\bar{\omega}_z(t')]^{1/2}} e^{-\gamma_z|t-t'|/2}$$

$$\times \cos\left[\int_{t'}^{t} d\bar{t}\,\bar{\omega}_z(\bar{t})\right] . \tag{3.64}$$

The various overtones and undertones give negligible, nonresonant corrections. However, since we do have a sharp resonant denominator, small secular frequency shifts could be important. Thus we need only retain the time averages

$$\left\langle \frac{\bar{\omega}_z^2(t) - \omega^2}{[\bar{\omega}_z(t)]^{1/2}} \right\rangle \simeq \frac{\omega_z'^2 - \omega^2}{(\omega_z')^{1/2}} \tag{3.65}$$

and

$$\left\langle \int_{t'}^{t} d\bar{t}\,\bar{\omega}_z(\bar{t}) \right\rangle \simeq (t - t')\omega_z' . \tag{3.66}$$

Therefore the only effect of any appreciable size caused by the modulation is to replace the resonant frequency ω_z in the result (3.42) for the unmodulated case by the perturbed resonant frequency ω_z' given in Eq. (3.55). In particular, we see that the noise is still "shorted out" at the slightly shifted resonance frequency.

D. Anharmonic axial resonance

The axial motion of a trapped particle in a laboratory Penning trap can provide a vivid illustration of an anharmonic oscillator. The anharmonicity arises because actual Penning traps do not produce a pure quadrupole potential, since their electrodes are not infinitely extended, per-

fect hyperbolas of revolution. Even when the anharmonicity in the potential is very small, its effect on the axial oscillation can be large because the quality factor Q of the oscillation is so large—small nonlinear forces on a very weakly damped oscillator produce large perturbations. The amount of anharmonicity can be altered by changing the voltage on compensation electrodes (see Sec. IX). Adjustments are made to minimize the anharmonicity by monitoring the shape of the axial resonance, which we consider here. This anharmonicity compensation process is crucial in precision experiments. It makes possible the observation of the small shifts in this axial frequency (of order 10^{-8}) which arise from cyclotron transitions, spin flips, and magnetron excitations, so that these are detectable.

Traps for precision work are constructed to maintain carefully the basic symmetries of the quadrupole potential: invariance under rotations about the z axis and invariance under the reflection $z \rightarrow -z$. Thus a small octupole potential

$$\Delta V = \frac{1}{2} V_0 C_4 \left[\frac{r}{d} \right]^4 P_4(\cos\theta)$$

$$= \frac{1}{2} V_0 C_4 \left[\frac{1}{d^4} \right] (z^4 - 3z^2\rho^2 + 3\rho^4/8) \qquad (3.67)$$

gives the leading anharmonic correction. Higher-order terms are less significant for a particle that occupies only a small volume at the center of the trap. The $z^2\rho^2$ term in the octupole potential (3.67) couples the axial and radial motions. Replacing ρ^2 by its average value produces a slight shift in the axial frequency, which remains fixed as long as the magnetron radius is not disturbed. Otherwise, the effect of this coupling is insignificant, since the frequencies of the radial and axial motions differ greatly and the coupling parameter is very small. Thus we need concentrate only on the z^4 term in the octupole potential, which modifies the previous axial equation of motion (3.9) to read

$$m \left[\frac{d^2}{dt^2} + \gamma_z \frac{d}{dt} + \omega_z^2 \left[1 + \lambda \frac{8z^2}{3d^2} \right] \right] z = F . \qquad (3.68)$$

Recalling that $\omega_z^2 = eV_0/md^2$ [Eq. (2.7)], we see that $\lambda = (3/4)C_4$. As will be discussed in Sec. IX, $|\lambda|$ ranges from about 10^{-3} for a good but uncompensated trap to 10^{-5} for a compensated trap.

With a sufficiently strong drive such that the noise is relatively small, we may approximate the total force by that of the coherent drive

$$F(t) = \frac{e\kappa}{2z_0} V_d \cos\omega t . \qquad (3.69)$$

This drive produces a response at the drive frequency ω plus overtones at odd-integer multiples of ω. The overtones involve powers of the very small coupling λ and may be neglected. Hence the driven oscillation is still basically harmonic, with the response

$$z(t) = a \cos(\omega t - \psi) . \qquad (3.70)$$

Neglecting the overtones gives

$$z(t)^3 \simeq \frac{3}{4} a^2 z(t) , \qquad (3.71)$$

and reduces the nonlinear equation of motion (3.68) to a linear equation with an amplitude-dependent resonant frequency

$$\omega_z(a) = \left[1 + \lambda \frac{a^2}{d^2} \right] \omega_z . \qquad (3.72)$$

This effectively linear equation has the familiar solution

$$a e^{i\psi} = \frac{e\kappa V_d}{2z_0 m} [\omega_z^2(a) - i\omega\gamma_z - \omega^2]^{-1} . \qquad (3.73)$$

The absolute square of Eq. (3.73) yields, in the narrow resonance approximation,

$$a^2 = \frac{a_{max}^2 \gamma_z^2/4}{[\omega - \omega_z(a)]^2 + \gamma_z^2/4} , \qquad (3.74)$$

where

$$a_{max} = \frac{e\kappa V_d}{2z_0 m \gamma_z \omega_z} . \qquad (3.75)$$

This nonlinear resonance is nicely discussed by Landau and Lifshitz (1976, Sec. 29), and we follow their approach. Since $\omega_z(a)$ depends linearly on a^2 [Eq. (3.72)], the resonant form (3.74) gives a cubic equation for the squared amplitude a^2. In general, the maximum amplitude $a = a_{max}$ is obtained at a shifted resonant frequency $\omega = \omega_z(a_{max})$. With a small drive the maximum amplitude a_{max} is small, the nonlinear correction is negligible, and the resonance curve has a Lorentzian shape, as shown in Fig. 11. In this case, two of the roots of the cubic are always complex and a^2 is a single-valued function of the drive frequency ω. With a large drive, however, the cubic
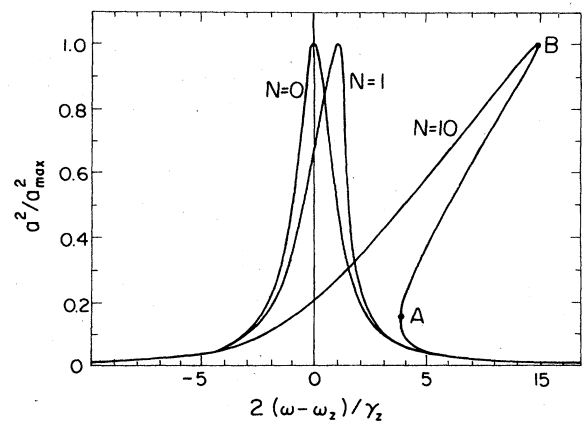

FIG. 11. Squared amplitude of an anharmonic oscillation vs the frequency of the driving force for three values of the anharmonicity parameter N defined by Eq. (3.79b). For $N = 0$ the response curve is the familiar Lorentzian. For the critical value $N = 1$, the response is skewed to the right but remains single valued. With $N > 1$ the response has a triple-valued region, as illustrated by the curve for $N = 10$.

has three real roots for a certain range of the drive frequency ω, and a^2 is a triple-valued function of ω in this range. Figure 11 also shows a plot of a^2 vs ω for this case of large drive.[12]

The triple-valued region is the range in ω between the points labeled by A and B in Fig. 11, the two points where the slope of the graph is infinite, $da^2/d\omega = \infty$. In general, differentiating Eq. (3.74) with respect to ω, using Eq. (3.72), and rearranging the terms, one finds that

$$\frac{da^2}{d\omega} = -2a^2[(\omega - \omega_z) - \lambda\omega_z a^2/d^2]$$

$$\times [(\omega - \omega_z)^2 - 4(\omega - \omega_z)\lambda\omega_z a^2/d^2$$

$$+ 3(\lambda\omega_z a^2/d^2)^2 + \gamma_z^2/4]^{-1} \, . \tag{3.76}$$

At the points A and B, the second quantity in square brackets in Eq. (3.76) vanishes, giving a quadratic equation for $(\omega - \omega_z)$ which has two solutions. These roots together with Eq. (3.74) determine the positions of points A and B. The oscillation corresponding to the portion of the resonance curve between points A and B is unstable—a small disturbance gives rise to a correction which grows exponentially in time.[13] Thus the nonlinear resonance exhibits hysteresis: If the resonance is excited by starting at a low drive frequency and then slowly increasing the frequency, the amplitude of the response increases until point B is reached, at which point the amplitude discontinuously drops to the lower branch of the resonance curve and stays on this branch as the frequency is further increased. On the other hand, starting with a high drive frequency and then lowering the frequency gives a response which follows the resonance curve until point A is reached, at which point the amplitude discontinuously jumps to the upper branch and continues along this branch as the frequency is further decreased. This phenomenon is illustrated by the theoretical curves in Fig. 12 and by the experimental results in Fig. 13.

The threshold for this nonlinear behavior is defined by the condition that the two points A and B coincide, the condition that the second quantity in square brackets in Eq. (3.76) has a double root in $(\omega - \omega_z)$:

$$|\lambda|\omega_z a^2/d^2 = \gamma_z/2 \, . \tag{3.77}$$

The double root appears at

$$\omega - \omega_z = 2\lambda\omega_z a^2/d = \pm\gamma_z \, . \tag{3.78}$$

---

[12]Note that it is simpler to plot ω as a function of a^2 first, for this entails only the solution of a quadratic rather than a cubic equation.

[13]This can be shown by examining the first-order perturbation of the equation of motion (3.68) about the steady-state solution (3.70). The resulting linear equation contains a parameter that varies as $\cos 2\omega t$, producing parametric amplification if the steady-state solution belongs to the resonance curve between A and B.
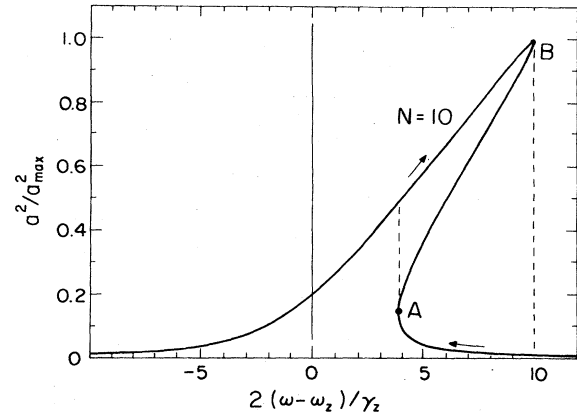
FIG. 12. The resonance profiles that would be observed experimentally by sweeping the frequency of the driving force up or down through the anharmonic axial resonance given for $N = 10$ in Fig. 11.

Inserting these constraints into the nonlinear resonance formula (3.74) gives $a^2 = \frac{1}{2}a_{max}^2$, and Eq. (3.77) now yields the condition for the threshold

$$|N| > 1 \, , \tag{3.79a}$$

where

$$N = \lambda \left[\frac{\omega_z}{\gamma_z}\right]\left[\frac{a_{max}}{d}\right]^2 \, . \tag{3.79b}$$

axial drive frequency
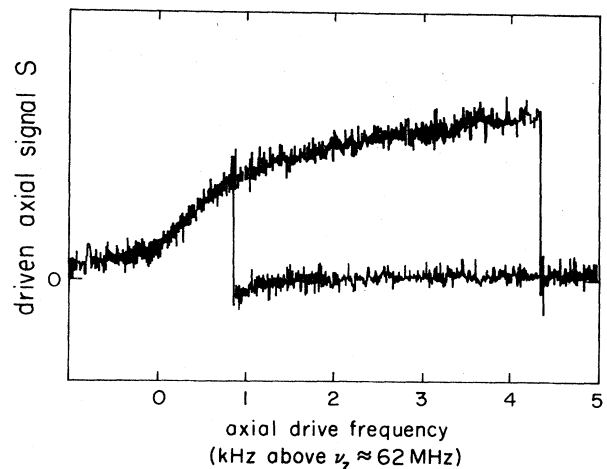(kHz above $\nu_z \approx 62$ MHz)

FIG. 13. Anharmonic axial resonance of a single trapped electron in the trap of Fig. 1 observed under detection conditions which correspond to $\varphi = 0$ in Eq. (3.36). The axial oscillation was made deliberately anharmonic by adjusting the potential applied to the compensation electrodes, and the frequency of the driving force was swept in opposite directions (indicated by the arrows) through resonance. When the trap was tuned to be as harmonic as possible, the axial linewidth was only 6 Hz out of 62 MHz, so that this figure shows the resonant frequency being shifted by approximately 700 linewidths. The shape of these resonances is somewhat different from that of those of Fig. 12 because the detection electronics was saturating due to the large oscillation being observed (Gabrielse and Dehmelt, 1982).

As we noted at the beginning of this section, even for a small anharmonicity $|\lambda|$ and a small maximum driven amplitude a_{max}^2, a nonlinear resonance can appear, since the damping constant γ_z is so small. To put this in clear experimental parameters, we rewrite Eq. (3.79a) in terms of the energy in the axial oscillation at maximum amplitude, $E_{max} = \frac{1}{2} m \omega_z^2 a_{max}^2$, and the quality factor $Q = \omega_z / \gamma_z$. Remembering that $\omega_z^2 = eV_0 / md^2$, where V_0 is the voltage applied between ring and endcaps, we get

$$E_{max} \geq \frac{eV_0}{2|\lambda|Q} \cdot$$ (3.80)

We recall from Tables I and III that, even for a thermally excited axial oscillation, $E/eV_0 \approx 10^{-4}$, while $Q \approx 10^7$. Hence, even at this minimal level of axial oscillation, the motion will be in the nonlinear regime unless $|\lambda| < 10^{-3}$.

In general, the dimensionless parameter N completely describes the shape of the nonlinear resonance. To see this all we need do is to use Eqs. (3.79b) and (3.72) to write the resonance form (3.74) in terms of scaled variables:

$$\frac{a^2}{a_{max}^2} = \left[1 + 4 \left[\frac{\omega - \omega_z}{\gamma_z} - N \frac{a^2}{a_{max}^2} \right]^2 \right]^{-1} \cdot$$ (3.81)

With $N = 0$ we get the familiar Lorentzian profile. As N increases we obtain a family of resonance curves, as shown in Fig. 11. With $|N|$ large, the curve is, for the most part, a narrow sheaf of thickness $\delta\omega \approx \gamma_z$ about the line $(\omega - \omega_z)/\gamma_z = Na^2/a_{max}^2$, as shown in Fig. 14.

E. Ion cyclotron motion

The cyclotron oscillation of a trapped proton or a heavier ion is typically at a radio frequency. Unlike the cyclotron motion of an electron in a strong magnetic field, this motion can be interrogated in a way very similar to that we have discussed for the axial oscillation.
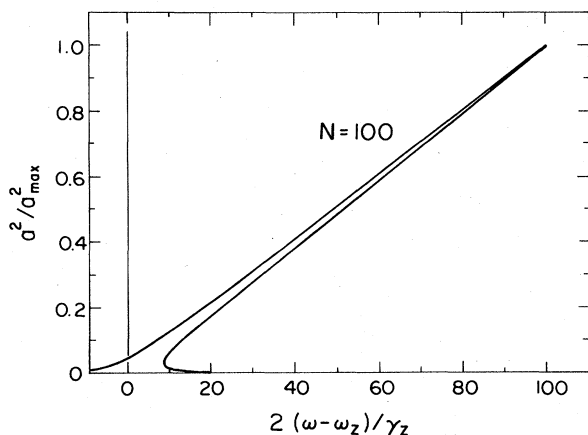
Moreover, the radiative damping that was significant for the case of the electron is negligible for a cyclotron motion at a radio frequency. Thus an external circuit must be used to damp the cyclotron motion. To allow the cyclotron motion to induce a current through an effective resistor that represents the external detection circuit, it is necessary to split the ring into at least two parts, which are then connected with the resistor. To emphasize the analogy with the axial detection and damping circuit in Fig. 9, we show a possible idealized circuit in Fig. 15. The ring electrode is divided into 4 quadrants, as was done by Van Dyck, Schwinberg, and Bailey (1980), but with somewhat different electrical connections. The left quadrant is driven, and the resistor is connected to the right quadrant, in direct analogy to the endcaps in Fig. 9. The upper and lower quadrants make up the current return paths for both the drive current and the induced current I, in direct analogy to the ring electrode in Fig. 9.

The radial cyclotron and magnetron motion $\rho(t)$ follow from an argument that parallels the discussion of the axial motion given in Sec. III.A. The electric field induced by the signal and drive voltages produces a force on the ion:

$$\mathbf{F} = \frac{e\kappa'}{2\rho_0}(V_D - V_S)\hat{x} \cdot$$ (3.82)

Here κ' is a dimensionless constant of order unity, which depends on the specific geometry of the trap. This constant would be exactly equal to one if the opposing ring sections were flat plates with no screening from the other electrodes. The signal voltage is given by

$$V_S = IR + v \,,$$ (3.83)

where, as before, v is the Johnson noise voltage in the effective resistor R. As described in Sec. III.A, the conservation of energy requires that the radial motion induce a current I given by

FIG. 14. Squared amplitude of an anharmonic oscillation vs the frequency of the driving force for a large value of the anharmonicity parameter, $N = 100$.
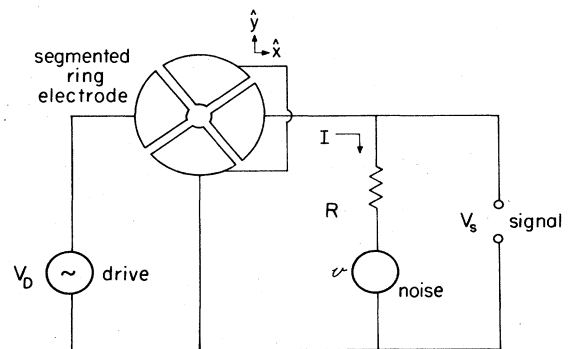

FIG. 15. Idealized radio-frequency circuit, which could be used to damp and detect the cyclotron oscillation of a trapped particle when this frequency is a radio frequency. The x component of the cyclotron motion induces a current I through the resistor. The cyclotron motion is driven by the oscillatory potential V_D and by the Johnson noise from the resistor v, while the signal voltage V_S is detected. This circuit is directly analogous to the circuit in Fig. 9 for the axial motion.

$$I = \frac{e\kappa'}{2\rho_0}\dot{\rho}_x \ . \tag{3.84}$$

Looking back over the derivation of the equation of motion (2.15), and recalling the formula (2.19) for $\dot{\rho}_x$, it is easy to see that with the addition of the force $\mathbf{F}$ we now have

$$\dot{\mathbf{V}}^{(\pm)} = \omega_\pm \hat{z} \times \mathbf{V}^{(\pm)} - (\gamma_+ V_x^{(+)} - \gamma_- V_x^{(-)})\hat{x}$$

$$+ \frac{e\kappa'}{2\rho_0 m}(V_D - v)\hat{x} \ , \tag{3.85}$$

where

$$\gamma_\pm = \left[\frac{e\kappa'}{2\rho_0}\right]^2 \frac{R}{m}\frac{\omega_\pm}{\omega_+ - \omega_-} \ . \tag{3.86}$$

The cyclotron and magnetron motions are coupled together by the first term in parentheses in Eq. (3.85). Since the two motions have very different resonant frequencies, this coupling is proportional to a very small parameter $\gamma_\pm/(\omega_+ - \omega_-)$, and it may be neglected. Omitting this nonresonant contribution of $\mathbf{V}^{(-)}$ to the cyclotron equation of motion for $\mathbf{V}^{(+)}$, taking the time derivative of the x component of this equation, and substituting the equation of motion for $\dot{V}_y^{(+)}$ yields the second-order equation of motion

$$\left[\frac{d^2}{dt^2} + \gamma_+ \frac{d}{dt} + \omega_+^2\right]V_x^{(+)} = \frac{e\kappa'}{2\rho_0 m}(\dot{V}_D - \dot{v}) \ . \tag{3.87}$$

This result is a precise analog of the axial equation of motion, Eqs. (3.9) and (3.10). In particular, γ_+ is the damping constant for the energy in the cyclotron motion. Taking $\kappa' = 1$ and using $R = 1.6 \times 10^5 \ \Omega$ and the proton parameters listed in Table II, we obtain $\gamma_+/2\pi = \gamma_c/2\pi \approx 10$ mHz, which was listed in Table IV. As was the case with the axial resonance, the noise is "shorted out" on resonance.

A similar second-order equation of motion describes the magnetron motion $\mathbf{V}^{(-)}$ but with the damping constant γ_+ replaced by $-\gamma_-$. This equation produces an exponential increase in the magnetron radius, since removing energy from this motion causes the ion to run down the radial potential hill. The rate of exponential increase γ_- is, however, smaller than γ_+ by a factor ω_-/ω_+. This factor is the ratio of the magnetron to cyclotron velocities for equal radii and thus is the ratio of the currents that these two motions induce. In addition, since the detector consists of a tuned circuit, the effective resistance R is generally very different at the cyclotron and magnetron frequencies. If the circuit tuned to detect and damp the cyclotron motion has a quality factor Q, then the effective resistance for a magnetron motion far below this resonance is the much smaller series resistance of the circuit, $r = R/Q^2$, and the rate of exponential increase of the magnetron motion can be very small, $\gamma_- = \gamma_+ \omega_-/\omega_+ Q^2$. Using the typical values for the pro-

ton $\omega_-/\omega_+ \approx 10^{-2}$ and $Q \approx 10^3$, we have a very long time constant $1/\gamma_- \approx 10^{10}$ sec, which is, nevertheless, much shorter than the time constant for radiative "decay" derived in Sec. II.E. This illustrates how the trap imperfections can be more important in heating the magnetron motion than is the radiative "decay."

The illustrative circuit in Fig. 15 suffers from the same experimental difficulty as does its axial analog in Fig. 9: the drive signal V_D is capacitively coupled to the detection electronics. This direct feedthrough can be reduced in the axial case by modulating the trapping potential (as discussed in Sec. III.C). The axial drive is then applied at a frequency different from the oscillation frequency of the trapped particle that is detected. An analogous frequency modulation in the cyclotron case is a modulation of the magnetic field, but this is difficult to implement experimentally. A detailed discussion of alternative experimental techniques for reducing the direct feedthrough is beyond the scope of this work, but these techniques do not modify our previous discussion in any essential way. For example, a sample of the drive signal can be fed directly to the top of the resistor (as has been done in the axial case by Wineland, Ekstrom, and Dehmelt, 1973). The amplitude and phase of this sample are adjusted to cancel the direct feedthrough. A variation being used in a current proton experiment is to drive the opposite segments of the "quad ring" on the y axis and connect the effective resistor across the segments on the x axis (Van Dyck, Schwinberg, and Bailey, 1980). Proper adjustment of the phases of the driving signals causes the directly-fed-through signals to cancel exactly. A third possibility is alternately to drive and detect, as is done in pulsed NMR experiments.

IV. COOLING THE MAGNETRON MOTION

Precision experiments on geonium require that the charged particle go about very small orbits. The inhomogeneities in the electrostatic potential and in the magnetic field broaden and shift the observed lines if the orbits are large (see Secs. III.D and VI.C). The axial and cyclotron motions are rapidly cooled to the ambient temperature by resistive and radiative damping (see Secs. II.E, III.A, and III.E). On the other hand, the magnetron motion must be cooled separately. This motion is unstable, and any dissipative process that removes energy from it increases the magnetron radius until the particle strikes the ring electrode and is lost from the trap. Fortunately, the damping time is very long, so that the magnetron motion is essentially stable. This same stability, however, implies that a charged particle injected into a large magnetron orbit (as often occurs) remains in that large orbit. Thus it is crucial that an external mechanism for cooling the magnetron motion be employed. This has, in fact, been done (Van Dyck, Schwinberg, and Dehmelt, 1978) with the method of "motional sideband cooling" (Wineland and Dehmelt, 1975a). The method is described in this section. Related theoretical work is given by Vyatchanin (1977)

and by Wineland (1979). We do not discuss laser cooling of ions.[14]

Since the magnetron motion is unstable, this cooling involves adding energy to move the particle to the top of the repulsive radial potential hill. Although this is entirely a classical process, we first outline the cooling mechanism using the language of quantum mechanics and thermodynamics (Sec. IV.A), since this provides a simple, basic description. We then discuss cooling and heating rates (Sec. IV.B). The prototype used in both of these sections is the cooling and heating of the magnetron motion via a coupling to the axial motion. In Sec. IV.C we extend these results to include heating and cooling of the axial motion as well as the magnetron motion, via couplings to the cyclotron motion. Finally, in Sec. IV.D, we return to the prototype. A rigorous mathematical treatment using the Green's-function technique shows how the cooling limit is achieved and demonstrates that the axial motion is decoupled from a resonant axial drive when the cooling drive is exactly resonant. This decoupling phenomenon is useful for measuring the magnetron frequency.

A. Cooling limit

The energy levels for the combined axial and magnetron harmonic oscillations (with quantum numbers k and l, respectively) are sketched in Fig. 16. Suppose that a system initially in the (k,l) level interacts with a photon of energy $\hbar(\omega_z + \omega_m)$. The interaction proceeds in two ways. On the one hand, the magnetron motion is cooled when the photon is absorbed via the transition $(k,l) \rightarrow (k+1, l-1)$, since the magnetron quantum number is reduced. The transition rate for this cooling process involves the square of the matrix element of the operator $a_z^\dagger a_-$, and thus it contains the factor $(k+1)l$. On the other hand, the magnetron motion is heated when the photon stimulates the transition $(k,l) \rightarrow (k-1, l+1)$. The transition rate for this heating process involves the operator $a_z a_-^\dagger$, and thus it contains the factor $k(l+1)$. Except for these different factors, the two rates are otherwise identical.

The cooling rate dominates if $l > k$. This is the situation that pertains for a large magnetron radius. Cooling of the magnetron motion continues as additional photons of energy $\hbar(\omega_z + \omega_m)$ are supplied, until $l = k$, at which point the cooling and heating rates are equal. No long-term change in the level of axial excitation occurs in this process as long as the axial oscillation is in contact with a thermal reservoir, which removes the excess energy (the reservoir is the external circuit that acts as a resister at
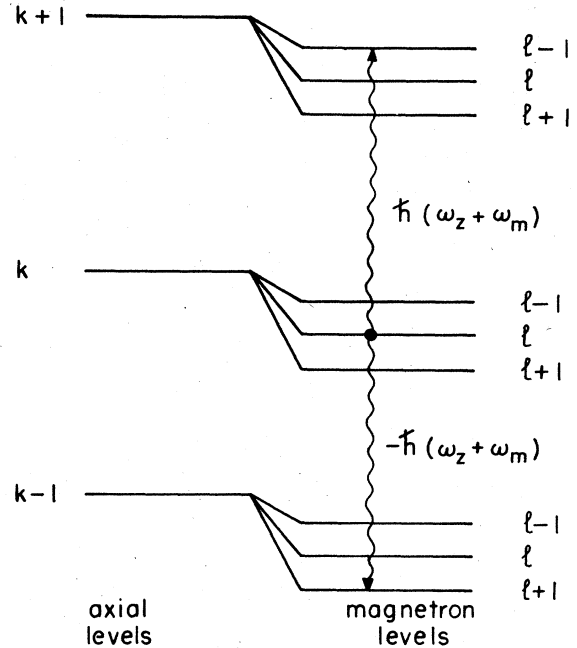
---

[14]Photon emission also causes recoil heating of trapped ions. In the case of laser cooling of ions, the cooling limit provided by such recoil heating is larger than the thermodynamic limit discussed in this section (Wineland and Itano, 1979).

FIG. 16. Energy levels for combined axial and magnetron oscillations, with quantum numbers k and l, respectively.

temperature T_z). Because a thermal distribution of energies is involved, the cooling continues until the thermal-averaged quantum numbers are equal, $\langle l \rangle = \langle k \rangle$. Since the axial and magnetron energy levels are given by $E_k = \hbar \omega_z (k + \frac{1}{2})$ and $E_l = -\hbar \omega_m (l + \frac{1}{2})$, this corresponds to a maximum magnetron energy

$$\langle E_{\mathrm{mag}} \rangle = -\frac{\omega_m}{\omega_z} \langle E_{\mathrm{axial}} \rangle = -\frac{\omega_m}{\omega_z} k_B T_z \ . \tag{4.1}$$

This is the result quoted in Eq. (2.58), and it was used to obtain the magnetron orbit parameters displayed in Tables III and IV. This limit was discussed by Vyatchanin (1977) and Wineland (1979).

The magnetron motion is always heated if the system interacts with a photon of energy $\hbar(\omega_z - \omega_m)$. In this case the "upward" transition rate for $(k,l) \rightarrow (k+1, l+1)$ involves the square of the matrix element of the operator $a_z^\dagger a_-^\dagger$ and thus contains the factor $(k+1)(l+1)$, while the "downward" rate for $(k,l) \rightarrow (k-1, l-1)$ involves $a_z a_-$ and contains the factor kl. Hence the "upward" rate always exceeds the "downward" rate, resulting in a net heating of the magnetron motion.

The cooling limit for the magnetron motion, Eq. (4.1), can also be obtained from a thermodynamical argument (Wineland and Itano, 1979). The absorption of a photon of energy $\hbar(\omega_z + \omega_m)$ may be thought of as adding heat $\Delta Q_z = \hbar \omega_z, \Delta Q_m = \hbar \omega_m$ to the axial and magnetron motions, which are at the temperatures T_z, T_m. Since $\langle E_{\mathrm{mag}} \rangle = k_B T_m < 0$, the magnetron "temperature" T_m is negative. The net entropy change in this process is given by

$$\Delta S = \frac{\Delta Q_z}{T_z} + \frac{\Delta Q_m}{T_m} .$$ (4.2)

The cooling can continue until a reversible cycle is established where $\Delta S = 0$. Thus the magnetron temperature can be cooled to the limit

$$T_m = -\frac{\Delta Q_m}{\Delta Q_z} T_z = -\frac{\omega_m}{\omega_z} T_z ,$$ (4.3)

which is equivalent to Eq. (4.1).

Planck's constant $\hbar$ does not enter into the cooling limit [Eq. (4.1)]. Moreover, the quantum numbers even in the cooled limit are very large ($k = l \simeq 10^3$). Hence the cooling process can be described by an entirely classical treatment, which has the advantage of providing complete information on this process in a relatively straightforward way. This is done in the following sections. Here we note that although the simple argument used to derive the cooling limit [Eq. (4.1)] assumed that the drive was exactly on resonance, $\omega_d = \omega_z + \omega_m$. We show in Sec. IV.D that this limit is achieved even when the drive is off resonance by many line widths γ_z, and even if the amplitude of the cooling drive is large.

A very clear demonstration of sideband cooling and heating is given in Fig. 17. The axial oscillation frequency (vertical scale) was monitored as a function of time (horizontal scale). The magnetron motion was first cooled for a long period by the application of an inhomogeneous electric field at frequency $\omega_z + \omega_m$. The frequency of this field was then changed to $\omega_z - \omega_m$, giving a heating drive. As we shall explain in the next section, the magnetron radius grows exponentially, and this growth is observed as an exponentially increasing shift in the axial frequency because the magnetic bottle used in this experiment makes $\Delta\omega_z \sim \rho_m^2$ (see Sec. VI.A). When the heating drive was turned off, the exponential growth stopped. Finally, the cooling drive was reapplied to return the magnetron motion to its original size. By fitting the exponential, the minimum value of the magnetron radius was
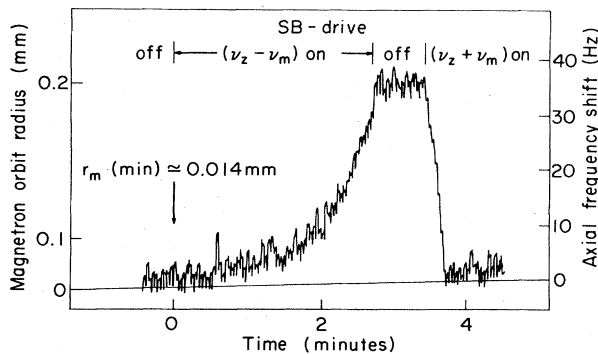

FIG. 17. Demonstration of sideband cooling and heating by Van Dyck, Schwinberg, and Dehmelt (1978). Changes in the axial oscillation frequency (vertical scale) are proportional to the square of the magnetron radius because of the presence of a magnetic bottle and are monitored as a function of time (horizontal scale).

determined to be $\rho_m = 1.4 \times 10^{-3}$ cm. This is a factor of 20 larger in radius and a factor of 400 larger in energy than the cooling limit from Eq. (4.1) that was listed in Table III. More recently, another measurement (Gabrielse and Dehmelt, 1982) was carried out in a different trap that had no magnetic bottle. The calibrated electrostatic anharmonicity (see Sec. IX.B) was used to make changes in the magnetron radius observable as shifts in the axial frequency. The same value of the minimum magnetron radius was measured.

B. Cooling and heating rates

The cooling or heating of the magnetron motion is accomplished by the introduction of an inhomogeneous, oscillatory electric field, which couples the otherwise isolated magnetron motion to the axial motion, which in turn is in contact with a thermal bath. Such a drive can be produced by applying an oscillating voltage between a segment of a compensation electrode and the ring electrode of the Penning trap (cf. Fig. 1) or between other probes introduced into the trap and the ring electrode. The applied drive at frequency ω_d produces a potential near the center of the trap given by

$$V = \kappa''(V_d/d^2)xz \cos\omega_d t .$$ (4.4)

Here V_d is the amplitude of the drive voltage, d is the characteristic trap dimension [Eq. (2.5)], and κ'' is a dimensionless constant that depends in an essential way on the electrode geometry and that is, therefore, difficult to estimate. Recalling that $\omega_z^2 = eV_0/md^2$ [Eq. (2.7)], we find that it is convenient to write this oscillating potential as

$$V = a(m\omega_z^2/e)xz \cos\omega_d t ,$$ (4.5)

in which

$$a = \kappa'' V_d/V_0$$ (4.6)

is a dimensionless parameter. Including the oscillating potential (4.5) and an extra external force, $mf_z(t)$, in the axial equation of motion gives

$$\left[\frac{d^2}{dt^2} + \gamma_z \frac{d}{dt} + \omega_z^2\right] z(t) = -a\omega_z^2 x(t)\cos\omega_d t + f_z(t) .$$ (4.7)

Looking back over the introduction of the vectors $\mathbf{V}^{(\pm)}$ [Eqs. (2.13)—(2.15)], it is easy to see that the effect of the oscillatory potential on the radial motion can be conveyed by

$$\frac{d}{dt} V_x^{(\pm)}(t) = -\omega_\pm V_y^{(\pm)}(t) - a\omega_z^2 z(t)\cos\omega_d t + f_x(t)/\omega_-$$ (4.8a)

along with

$$\frac{d}{dt} V_y^{(\pm)}(t) = \omega_\pm V_x^{(\pm)}(t) ,$$ (4.8b)

which is identical to Eq. (2.15). Here we have reverted to the notation $\omega_+ = \omega'_c, \omega_- = \omega_m$ and included an extra external force, $mf_x(t)/\omega_-$, for the x component of the motion. According to Eq. (2.18) we can write the coordinate $x(t)$, which appears in the axial equation of motion (4.7), in terms of $V^{(\pm)}$,

$$x(t) = \frac{V_y^{(+)}(t) - V_y^{(-)}(t)}{\omega_+ - \omega_-} , \qquad (4.9)$$

and thus close the system of equations. We shall assume that the drive frequency ω_d is near to one of the two frequencies $\omega_z \pm \omega_-$. Since the velocities $V^{(\pm)}$ resonate at the frequencies $\omega_\pm$, we see that only the magnetron motion $V^{(-)}$ contributes terms close to the resonant frequency ω_z. The off-resonance terms produce a negligible response. Thus we write the axial equation of motion as

$$\left[\frac{d^2}{dt^2} + \gamma_z \frac{d}{dt} + \omega_z^2 \right] z(t) = \frac{a\omega_z^2}{\omega_+ - \omega_-} V_y^{(-)}(t)\cos\omega_d t$$

$$+ f_z(t) . \qquad (4.10)$$

Taking the time derivative of Eq. (4.8b) and substituting the result in Eq. (4.8a) yields a second-order equation for the magnetron motion:

$$\left[\frac{d^2}{dt^2} + \omega_-^2 \right] V_y^{(-)}(t) = -a\omega_- \omega_z^2 z(t)\cos\omega_d t + f_x(t) . $$

$$(4.11)$$

Equations (4.10) and (4.11) are the basic equations that we shall use to describe the magnetron cooling and heating.

Before solving these coupled equations, it is worthwhile to comment on some of their general features. Note that there is no damping on the left-hand side of the magnetron equation of motion (4.11). Hence if there were a nonvanishing effective force on the magnetron motion [the right-hand side of Eq. (4.11)] oscillating at the resonant frequency ω_-, the amplitude of the magnetron motion would increase without bound. An axial oscillation $z(t)$ driven by an extra force $mf_z(t)$ at the frequencies $\omega = \omega_d \pm \omega_-$ would produce such resonance force on the magnetron motion. As we shall show in detail in Sec. IV.D, however, an extra force $mf_z(t)$ at the frequencies $\omega = \omega_d \pm \omega_-$ actually produces no response in the axial oscillation, and thus the magnetron motion is not blown away by this mechanism. This decoupling of the axial motion provides an accurate method of measuring the magnetron frequency. The axial motion is monitored, as is often the case, by measuring the feedback voltage that must be added to the trapping potential to keep the axial oscillation at a fixed frequency ω_z. When the drive frequency ω_d is swept through $\omega_d \pm \omega_- = \omega_z$, the amplitude of the axial oscillation vanishes, and the feedback system becomes unstable since it receives no signal. This behavior is illustrated in Fig. 18.

The cooling or heating occurs in the absence of extra external forces. Thus we set $f_z = 0 = f_x$ in Eqs. (4.10) and

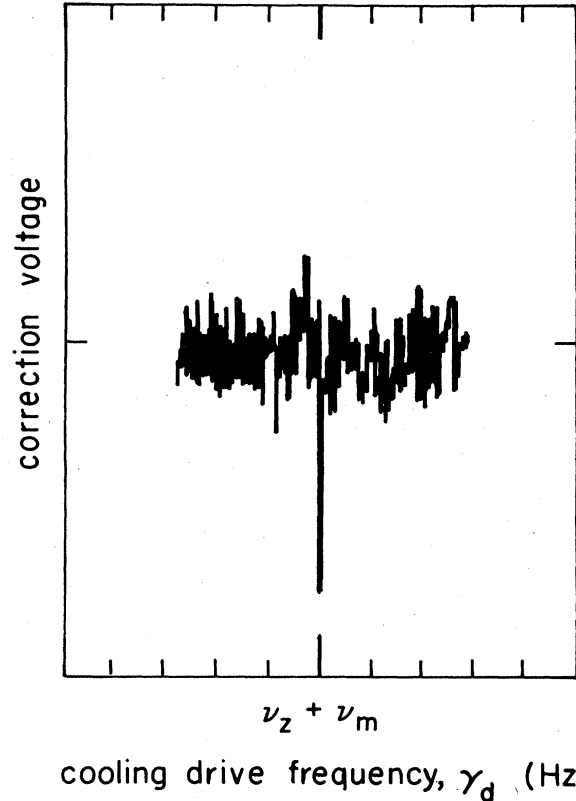

cooling drive frequency, γ_d (Hz)

FIG. 18. Narrow feature arising from the decoupling of an axial drive at ν_z when a cooling drive at $\nu_z + \nu_m$ is applied (Gabrielse and Dehmelt, 1982). Because the axial motion is decoupled from its drive, the shape of this feature depends on the electronics of the locking loop. The width of this feature is at least as narrow as the 0.1-Hz resolution in the drive frequency. Such measurements give a precise determination of the magnetron frequency.

(4.11). The differences in the signs of the oscillatory coupling terms on the right-hand sides of Eqs. (4.10) and (4.11) reflect the instability of the magnetron motion, which has a negative Hamiltonian. It is this difference in sign in the classical equations of motion that causes the heating to occur at $\omega_d \approx \omega_z - \omega_-$ and cooling to occur at $\omega_d \approx \omega_z - \omega_-$ rather than the other way around. To see how this happens, let the drive be exactly on resonance, $\omega_d = \omega_z \pm \omega_-$, and replace the exact magnetron motion by the approximate short-term behavior $V_y^{(-)}$ $\sim \exp(-i\omega_- t)$. Inserting this on the right-hand side of Eq. (4.10) gives a driving force at the axial frequency and thus a resonant axial response $z(t)$ $\sim \pm i \exp(\mp i\omega_z t)$. Inserting this in turn on the right-hand side of Eq. (4.11) produces a resonant force proportional to $\pm dV_y^{(-)}(t)/dt$, which drives the magnetron motion. With a cooling drive (lower $-$ sign) this is a viscous, damping force; a heating drive (upper $+$ sign) gives an antidamping force.

Let us now derive the rate at which the magnetron motion is heated by a drive at the frequency $\omega_d \approx \omega_z - \omega_-$ or cooled by a drive at $\omega_d \approx \omega_z + \omega_-$. The formulas are simplified by writing

$$\omega_d = \omega_z \mp \omega_- + \varepsilon ,\qquad (4.12)$$

with the upper sign in what follows always referring to heating, the lower to cooling. We look for a solution in which $V_y^{(-)}(t) \sim \exp(-i\omega t)$, where $\omega \approx \omega_-$. Neglecting the nonresonant part, the coupling of $V_y^{(-)}(t)$ in Eq. (4.10) leads to an axial oscillation

$$z(t) \sim \exp\{\mp i [\omega_z \mp (\omega_- - \omega) + \varepsilon]t\} .$$

Again neglecting the nonresonant part, the coupling of $z(t)$ in Eq. (4.11) reproduces the $\exp(-i\omega t)$ behavior. In this way the pair of coupled differential equations (4.10) and (4.11) are reduced to a pair of simultaneous, homogeneous, algebraic equations. Such equations have a solution only if their determinant vanishes. In the narrow resonance approximation, the determinant here is given by

$$D_\mp(\omega) = \begin{vmatrix} \mp(\omega-\omega_-)-\varepsilon\mp i\gamma_z/2 & -\frac{1}{4}a\omega_z/(\omega_+ - \omega_-) \\ \frac{1}{4}a\omega_z^2 & \omega_- - \omega \end{vmatrix} .$$

$$(4.13)$$

The condition $D_\mp(\omega)=0$ is a quadratic eigenvalue equation for ω.

The two roots of the eigenvalue equation give the two normal modes of the coupled system. With the coupling constant a small, one solution is $\omega \approx \omega_-$, corresponding to an excitation of the magnetron motion $V_y^{(-)}(t) \sim \exp(i\omega_- t)$, the other solution is $\omega \approx \omega_- \mp \varepsilon$ corresponding to an excitation of the axial motion $z(t) \sim \exp(\mp i\omega_z t)$. We are interested in the normal mode that corresponds to magnetron excitation in the limit $a \to 0$. (The other normal mode, corresponding to axial excitation in this same limit is discussed in Sec. IV.D.) A short calculation shows that this normal mode has the complex eigenfrequency

$$\omega = \omega_- + \Delta\omega_m^{(\mp)}(\varepsilon) - \frac{i}{2}\gamma_m^{(\mp)}(\varepsilon) ,\qquad (4.14)$$

where

$$\gamma_m^{(\mp)}(\varepsilon) = \mathrm{Im}\left\{(\varepsilon+i\gamma_z/2)\left[1-\left[1\mp\frac{\gamma_0\gamma_z}{(\varepsilon+i\gamma_z/2)^2}\right]^{1/2}\right]\right\} ,$$

$$(4.15)$$

with

$$\gamma_0 = \frac{a^2\omega_z^3}{4\gamma_z(\omega_+ - \omega_-)} ,\qquad (4.16)$$

while $\Delta\omega_m^{(\mp)}(\varepsilon)$ is a small frequency shift roughly of order $\gamma_m^{(\mp)}(\varepsilon)$, which we do not write down explicitly since it is of less experimental interest. The magnetron amplitude behaves as
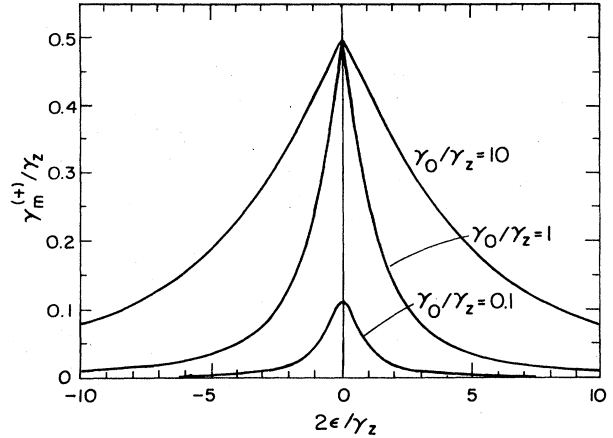

FIG. 19. Line shapes of the cooling rate $\gamma_m^{(+)}$, as given by Eq. (4.15) for several values of γ_0/γ_z. With appropriate interpretation, these line shapes apply to the analogous decay constants of Sec. III.C as well.

$$V_y^{(-)}(t) \sim \exp[-\tfrac{1}{2}\gamma_m^{(\mp)}(\varepsilon)t] ,\qquad (4.17)$$

where the upper $-$ sign denotes the heating drive and the lower $+$ sign denotes the cooling drive.

The line shapes for $\gamma_m^{(\pm)}(\varepsilon)$ from Eq. (4.15) are plotted in Figs. 19 and 20. This line shape is more general than the specific coupled equations used to derive it. It will reappear repeatedly in Sec. IV.C, with γ_c replacing γ_z, to describe cooling and heating of axial and magnetron motions via various couplings to the cyclotron motion. The rate γ_0, however, will depend upon the specific coupling. To see its significance, consider drives that are sufficiently gentle, $4\gamma_0 \ll \gamma_z$, so that energy is transferred into the axial motion at a rate much slower than the axial decay rate. Expanding the square root in Eq. (4.15) gives the Lorentzian profile
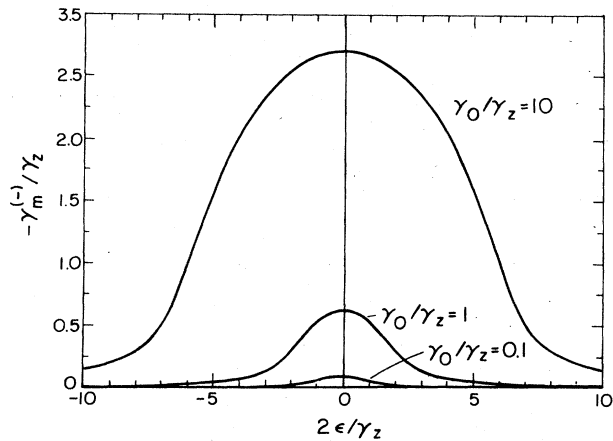

FIG. 20. Line shapes of the heating rate $-\gamma_m^{(-)}$, as given by Eq. (4.15) for several values of γ_0/γ_z. With appropriate interpretation, these line shapes apply to the analogous decay constants of Sec. III.C as well.

$$\gamma_m^{(\mp)}(\varepsilon) \simeq \mp \gamma_0 \frac{\gamma_z^2/4}{\varepsilon^2 + \gamma_z^2/4} \cdot \qquad (4.18)$$

Thus γ_0 is the rate of heating or cooling on resonance ($\varepsilon = 0$) for a weak drive. Figures 19 and 20 show that both $\gamma_m^{(+)}(\varepsilon)$ and $\gamma_m^{(-)}(\varepsilon)$ have a nearly Lorentzian line shape for $\gamma_0/\gamma_z = 0.1$. For higher drive powers the exact formula (4.15) is required. The cooling rates (Fig. 19) differ substantially from the heating rates (Fig. 20) in both magnitude and shape. The most pronounced difference is that the maximum cooling rate $\gamma_m^{(+)}(\varepsilon = 0)$ saturates at exactly $\gamma_z/2$ for $\gamma_0 \geq \gamma_z/4$, while no such saturation occurs for strong heating drives. The corresponding frequency shifts $\Delta\omega_m^{(\mp)}(\varepsilon)$ are about the same size but have a dispersive rather than an absorptive profile.

The Lorentzian shape of $\gamma_m^{(-)}(\varepsilon)$ and the broadened shapes for higher-power drives were directly observed with a single electron as illustrated in Fig. 21. The magnetron motion was first cooled as much as possible by a strong inhomogeneous drive at $\omega_z + \omega_-$. The drive was then decreased in amplitude and applied near the heating sideband, at frequency $\omega_z - \omega_- + \varepsilon$. This weak heating drive caused the magnetron radius to increase exponentially until, after a time on the order of 10^3 sec, the magnetron radius was large enough that the electron was sampling the anharmonic electrostatic potential away from the center of the trap. The axial frequency (which was being monitored throughout this process) shifted, and the time required to produce a shift $\Delta\omega_z/\omega_z \approx 10^{-7}$ was recorded. This process was repeated as a function of the
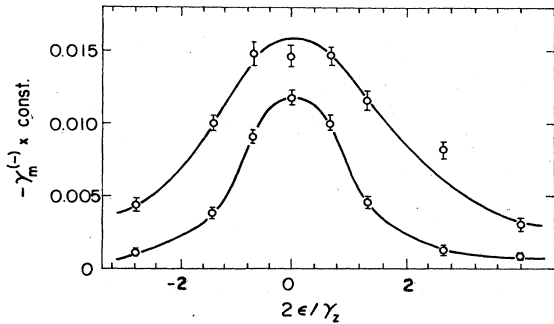

FIG. 21. Experimental observations of the heating line shapes $\gamma_m^{(-)}(\varepsilon)$ by Gabrielse and Dehmelt (1982), as described in the text. The error bars are statistical, and smooth curves are included to aid the eye. The vertical scale is the inverse of the time required to heat the magnetron motion from the smallest obtainable magnetron radius to the larger, observable radius. Such measurements are rather time consuming, taking about 3 h of averaging time for each of the points farthest from the center. The upper, broader curve corresponds to a higher power, so that power broadening is clearly demonstrated, but the power ratio is not well calibrated, owing to the very small amplitude of the drives and the presence of radio-frequency leakage paths. Moreover, it is difficult for the existing electronics to follow the fast increase in the magnetron radius near resonance, making the heights of the center points somewhat suspect.

heating drive frequency $\omega_d = \omega_z - \omega_- + \varepsilon$. For a weak drive, the observed width of the Lorentzian is the same as that observed by sweeping out the axial resonance with a drive near ω_z. As the drive was increased, the resonance width was significantly power broadened, as illustrated by the upper curve in Fig. 21. At these strong drives, $\gamma_0 \approx \gamma_z$ (or larger). Using the parameters in Tables I and II, we see that this corresponds to $\gamma_0/2\pi \simeq 6$ Hz, which implies that $a \approx 10^{-5}$. This is realized experimentally in the trap shown in Fig. 1 with a drive amplitude V_d on the order of microvolts.

C. Cooling and heating via the cyclotron motion

We have seen how the axial and magnetron motions may be coupled to cool the magnetron motion. In a similar fashion, oscillatory fields at the cyclotron sideband frequencies $\omega_+ - \omega_z$ and $\omega_+ + \omega_-$ can couple the cyclotron motion to the axial and magnetron motions to cool them. The attractive feature of using the cyclotron motion is that very low cooling limits,

$$T_z = \frac{\omega_z}{\omega_+} T_c \qquad (4.19)$$

and

$$T_m = -\frac{\omega_-}{\omega_+} T_c , \qquad (4.20)$$

apply in light of the typical hierarchy of eigenfrequency magnitudes [Eq. (2.12)]. We should note that these limits again correspond to equal quantum numbers. For the electron parameters in Tables I and III, for example, the cyclotron motion is in equilibrium with the blackbody radiation of the trap, so that $T_c = 4.2$ K and $n \leq 1$. The axial cooling limit temperature is thus $T_z = 2 \times 10^{-3}$ K, provided that the axial motion is decoupled from its external resistor (Sec. III) during the cooling process. For the magnetron motion, the cooling limit is $T_m = -3 \times 10^{-7}$ K, which is many orders of magnitude lower than what is attainable using the axial sideband. For the proton parameters in Tables II and IV, the cyclotron temperature is again $T_c = 4.2$ K when this motion is coupled to the thermal bath via an external resistor. The axial and magnetron limits from Eqs. (4.19) and (4.20) are still well below the temperature of the thermal bath, with $T_z = 0.6$ K and $T_m = -0.04$ K, but are not nearly so low as in the electron case, since the eigenfrequencies are much closer to each other.

While these cooling limits are very low, the rates for achieving these limits are also very slow in some common situations. To discuss the rates we must distinguish two cases. For protons and heavier ions, the cyclotron frequency (and hence the sidebands we are interested in here) are radio frequencies. The wavelengths $\lambda_c = c/\nu_c$ associated with these frequencies are thus much larger than the dimensions of a trap, d. Just as for the axial sidebands already considered (Sec. IV.B), electric fields with sufficient

gradients can be produced by applying oscillatory potentials to trap electrodes or electrode sections, since the center of the trap is in the "near-field" region. For an electron in a high magnetic field, as in Table I, however, the cyclotron wavelength is $\lambda_c = 0.2$ cm, which is on the order of the trap dimension $d = 0.34$ cm, so that microwave drives directed between trap electrodes or through slits in these electrodes are required. Coupling of the motions to achieve cooling thus depends upon gradients in the radiation electric fields and upon magnetic forces that turn out to be of similar effectiveness. The microwave cavity produced by the trap electrodes may also significantly modify the radiation fields when $\lambda_c \approx d$ (Sec. VIII).

For a cyclotron motion at a radio frequency, the cooling of the axial motion via a coupling to the cyclotron motion is very much like the magnetron cooling described in the previous sections. The same oscillatory drive potential [Eq. (4.4)] couples the motions except that the drive frequency is now given by

$$\omega_d = \omega_+ \pm \omega_z + \varepsilon , \tag{4.21}$$

with the upper and lower signs again referring to heating and cooling, respectively. The signs here are reversed compared to Eq. (4.12), which involves the inverted magnetron motion. The axial equation of motion,

$$\left[\frac{d^2}{dt^2} + \omega_z^2\right] z(t) = -a\omega_z^2 x(t)\cos\omega_d t , \tag{4.22}$$

differs from Eq. (4.7) for magnetron cooling only insofar as there is now no damping. The axial motion is assumed to be decoupled from the effective damping resistor when the oscillatory potential is applied, in order to allow this motion to be cooled below the temperature of the resistor. The first-order cyclotron equations (4.8), with the inclusion of cyclotron damping, yield the second-order equation

$$\left[\frac{d^2}{dt^2} + \gamma_c \frac{d}{dt} + \omega_+^2\right] V_y^{(+)}(t) = -a\omega_+ \omega_z^2 z(t)\cos\omega_d t . \tag{4.23}$$

No additional external forces are included here.

The solution of this pair of coupled, second-order equations exactly parallels the solution of the earlier coupled oscillator equations (4.7) and (4.11). The normal mode that corresponds to the axial oscillation in the limit where the coupling is removed (i.e., $a \to 0$) has a complex eigenfrequency

$$\omega = \omega_z + \Delta\omega_z^{(\pm)}(\varepsilon) - \frac{i}{2}\gamma_z^{(\pm)}(\varepsilon) \tag{4.24}$$

with

$$\gamma_z^{(\pm)}(\varepsilon) = \mathrm{Im}\left\{(\varepsilon + i\gamma_c/2)\left[1 - \left[1\mp\frac{\gamma_0\gamma_c}{(\varepsilon+i\gamma_c/2)^2}\right]^{1/2}\right]\right\} \tag{4.25}$$

and

$$\gamma_0 = \frac{a^2\omega_z^3}{4\gamma_c(\omega_+ - \omega_-)} . \tag{4.26}$$

These latter two expressions differ from their counterparts in Eqs. (4.15) and (4.16) in Sec. IV.B (for magnetron cooling and heating via a coupling to the axial motion) only insofar as γ_c replaces γ_z. For weak axial drives such that $4\gamma_0 \ll \gamma_c$, an expansion of Eq. (4.25) [just as in Eq. (4.18)] yields a Lorentzian, and γ_0 is the rate of cooling or heating exactly on resonance ($\varepsilon = 0$). Again, the cooling rate $\gamma_z^{(-)}$ saturates at $\gamma_c/2$ for increasingly strong drives, while the heating rate continues to increase.

Although the cooling limits are much lower for an electron in a high magnetic field, it may be difficult to apply a strong enough microwave drive to achieve reasonable cooling rates. Since $\lambda_c \approx d$, the analysis of this case is complicated because the propagation direction of the applied drive must be taken into account and because it has been demonstrated that the trap electrodes act as a microwave cavity, which modifies the microwave fields. To illustrate the principal features of cooling with a microwave drive, we neglect the cavity effects and consider the coupling of the cyclotron and axial motions by means of a microwave field traveling along the z axis,

$$\mathbf{E} = \hat{x}\mathscr{E} \sin\omega_d(t - z/c) , \tag{4.27a}$$

$$\mathbf{B} = \hat{y}\mathscr{E} \sin\omega_d(t - z/c) , \tag{4.27b}$$

with ω_d again given by Eq. (4.21). Plane waves propagating in other directions generally give cooling and heating effects of the same order. Referring to Tables I and III, one finds that an electron initially in thermal equilibrium at $T_z = 10$ K has an axial oscillation amplitude that is small compared to λ_c. In particular, $z\omega_d/c \approx 10^{-1}$ and the plane wave in Eq. (4.27) can be expanded in powers of this small ratio, and all but the leading terms that couple the cyclotron and axial motions can be neglected. Including the radiative damping of the cyclotron motion and proceeding in a manner that closely parallels the derivation of Eq. (4.11), one finds that the cyclotron equation of motion is given by

$$\left[\frac{d^2}{dt^2} + \gamma_c \frac{d}{dt} + \omega_+^2\right] V_y^{(+)}(t) = -\frac{e\mathscr{E}\omega_+\omega_d}{mc} z(t)\cos\omega_d t . \tag{4.28}$$

Notice from the right-hand side of this expression that if the axial oscillation $z(t)$ is directly on resonance at ω_z, an effective cyclotron drive near resonance at ω_+ is produced with effective strength reduced by the factor $z\omega_d/c \approx 10^{-1}$. The axial force is the magnetic Lorentz force, $(e/c)\dot{\rho} \times B$. Using Eq. (2.19) to write $\dot{\rho}_x$ in terms of $\omega_+ V_x^{(+)} \simeq \dot{V}_y^{(+)}$, the axial equation of motion is given by

$$\left[\frac{d^2}{dt^2} + \omega_z^2\right] z(t) = \frac{e\mathscr{E}}{mc(\omega_+ - \omega_-)} \dot{V}_y^{(+)}(t)\sin\omega_d t . \tag{4.29}$$

As in Eq. (4.22), no axial damping constant is included here corresponding to the requirement of decoupling the

axial motion from an external resistor. The coupled pair of equations, (4.28) and (4.29), are very similar to those we have been discussing, and it is easy to show that the coupling of the axial and cyclotron motions by the plane wave in Eq. (4.27) produces an axial "damping" constant $\gamma_z^{(\pm)}(\varepsilon)$ given by the earlier Eqs. (4.24) and (4.25) but with

$$\gamma_0 = \frac{e^2 \mathcal{E}^2 \omega_+ \omega_d}{4\gamma_c m^2 c^2 \omega_z (\omega_+ - \omega_-)} \tag{4.30}$$

as the basic rate constant.

Relatively higher-power microwave drives are required for heating and cooling than for direct cyclotron excitation. To illustrate this we note that a direct cyclotron drive on resonance,

$$\mathbf{E} = \hat{x} \mathcal{E} \cos\omega_+ t , \tag{4.31}$$

produces a cyclotron excitation energy

$$E_c = \frac{1}{2} \frac{m\omega_+}{\omega_+ - \omega_-} \left[\frac{e\mathcal{E}}{\gamma_c m} \right]^2 . \tag{4.32}$$

This can be used to eliminate $\mathcal{E}$ in the rate γ_0, yielding

$$\gamma_0 = \frac{1}{2} \gamma_c \frac{E_c}{mc^2} \frac{\omega_d}{\omega_z} . \tag{4.33}$$

Using the typical electron parameters, we see that achieving $\gamma_0 \approx \gamma_c$ requires a microwave drive that would produce a cyclotron excitation energy $E_c \approx 1$ keV if directly applied. The largest excitation measured so far, however, is only 10 eV (Gabrielse, Dehmelt, and Kells, 1985). However, slower rates could still be useful and higher microwave powers can certainly be generated.

The magnetron motion can also be heated or cooled with an oscillatory drive at frequency

$$\omega_d = \omega_+ \mp \omega_- + \varepsilon , \tag{4.34}$$

which couples the magnetron and cyclotron motions. As before, the upper − sign appears for heating, the lower + sign for cooling. Let us first consider the case of an ion in which the cyclotron motion is at a radio frequency, so that the wavelength λ_c associated with the cyclotron frequency is much larger than a typical trap dimension d. The inhomogeneous field can be produced by applying an oscillating voltage to trap electrodes. It might seem that one could cool and heat the magnetron motion by simply modulating the trapping potential,

$$V = V_0 \frac{z^2 - \rho^2/2}{2d^2}(1 + a \cos\omega_d t) . \tag{4.35}$$

The cyclotron and magnetron motions are coupled by the ρ^2 term. However, closer scrutiny shows that the driving field rotates in such a way as to produce only heating but no cooling of the magnetron motion. On the other hand, the ring electrode can be split and oscillatory potentials applied so as to produce the potential

$$V = a (m\omega_z^2/e)xy \cos\omega_d t . \tag{4.36}$$

The corresponding pair of coupled differential equations

of motion are akin to those already considered. Now one finds that only a cooling drive can be produced. The solution of the equation of motion yields a complex eigenfrequency (4.14), in which cooling rate $\gamma_m^{(+)}(\varepsilon)$ is given by Eq. (4.15) with the lower + sign in the square root, with γ_z replaced by γ_c, and with

$$\gamma_0 = \frac{4a^2 \omega_z^4}{\gamma_c (\omega_+ - \omega_-)^2} . \tag{4.37}$$

This is the damping rate for a weak, on-resonance drive.

To understand the case when the wavelength corresponding to the cyclotron motion λ_c is on the order of the trap dimension d, we again use plane waves similar to those given in Eq. (4.27), but with oscillation frequency ω_d given by Eq. (4.34) and with the roles of z and y interchanged. Expanding the plane waves and solving the resulting coupled equations, with the neglect of small terms of order ω_-/ω_+, yields again the complex eigenfrequency given in Eqs. (4.14) and (4.15). The basic rate, however, is now given by

$$\gamma_0 = \frac{1}{4\gamma_c} \left[\frac{e\mathcal{E}}{mc} \right]^2 . \tag{4.38}$$

Comparing this rate to that for the axial motion in Eqs. (4.30) and (4.33) shows that it is smaller by approximately the ratio ω_z/ω_+, which is less than 10^{-3} for the electron parameters in Table I. Such a rate would be very difficult to observe with the relatively weak microwave sources presently used in the precision experiments.

D. Detailed calculation

We now return to the prototype problem of cooling and heating the magnetron motion via the coupling in Eq. (4.4), which was discussed earlier in Sec. IV.B. The rigorous mathematical treatment provided here shows directly how the cooling limit is approached and demonstrates the decoupling of the axial motion from a resonant axial drive which occurs when the cooling drive is exactly resonant. We solve the driven, coupled pair of equations (4.10) and (4.11) by the Green's-function technique and use operator methods to simplify and clarify the overall procedure. To introduce the notation, consider first the uncoupled case with $a = 0$. In this case, the Green's function for the axial equation of motion (4.10) is the function $G_z(t - t')$ defined by Eq. (3.14). In the operator notation

$$G_z(t - t') = (t \mid G_z \mid t') , \tag{4.39}$$

$$\delta(t - t') = (t \mid 1 \mid t') , \tag{4.40}$$

the Green's-function equation (3.14) appears as simply

$$G_z^{-1} G_z = 1 , \tag{4.41}$$

in which

$$(t \mid G_z^{-1} \mid t') = \left[\frac{d^2}{dt^2} + \gamma_z \frac{d}{dt} + \omega_z^2 \right] \delta(t - t') . \tag{4.42}$$

The ordinary Green's-function equation (3.14) is obtained by taking the $(t \mid \mid t')$ matrix element of Eq. (4.41) and inserting the resolution of the identity

$$1 = \int d\bar{t} \mid d\bar{t})(d\bar{t} \mid \qquad (4.43)$$

between the two operators G_z^{-1} and G_z. The uncoupled magnetron Green's operator G_m is defined by

$$G_m^{-1}G_m = 1 , \qquad (4.44)$$

where

$$(t \mid G_m^{-1} \mid t') = \left[\frac{d^2}{dt^2} + \omega_-^2 \right] \delta(t - t') . \qquad (4.45)$$

The steady-state solution to the driven, coupled pair of equations (4.10) and (4.11) is obtained by a 2×2 matrix of Green's operators,

$$\begin{bmatrix} z \\ V_y^{(-)} \end{bmatrix} = \begin{bmatrix} G_{zz} & G_{zm} \\ G_{mz} & G_{mm} \end{bmatrix} \begin{bmatrix} f_z \\ f_x \end{bmatrix} . \qquad (4.46)$$

To make sure that our notation is understood, let us write out explicitly that Eq. (4.46) gives

$$z(t) = \int dt' G_{zz}(t,t')f_z(t') + \int dt' G_{zm}(t,t')f_x(t') \qquad (4.47a)$$

and

$$V_y^{(-)}(t) = \int dt' G_{mz}(t,t')f_z(t') + \int dt' G_{mm}(t,t')f_x(t') . \qquad (4.47b)$$

The matrix form (4.46) gives the solution to a coupled pair of equations if the 2×2 matrix Green's operator obeys

$$\begin{bmatrix} G_z^{-1} & -\dfrac{a\omega_z^2}{\omega_+ - \omega_-}\cos\omega_d \underline{t} \\ a\omega_-\omega_z^2\cos\omega_d\underline{t} & G_m^{-1} \end{bmatrix}$$
$$\times \begin{bmatrix} G_{zz} & G_{zm} \\ G_{mz} & G_{mm} \end{bmatrix} = \begin{bmatrix} 1 & 0 \\ 0 & 1 \end{bmatrix} . \qquad (4.48)$$

Here $\underline{t}$ denotes the operator for the time coordinate, $\underline{t} \mid t') = \mid t')t'$, $(t \mid \underline{t} = t(t \mid$. Multiplying out the matrices, it is easy to solve for the off-diagonal elements in terms of the diagonal elements,

$$G_{zm} = \frac{a\omega_z^2}{\omega_+ - \omega_-}G_z\cos\omega_d\underline{t}G_{mm} \qquad (4.49a)$$

and

$$G_{mz} = -a\omega_-\omega_z^2 G_m\cos\omega_d\underline{t}G_{zz} . \qquad (4.49b)$$

Using Eqs. (4.49) to eliminate the off-diagonal elements in Eq. (4.48), we secure a pair of uncoupled equations for the diagonal elements:

$$\left[G_z^{-1} + \frac{a^2\omega_z^4\omega_-}{\omega_+ - \omega_-}\cos\omega_d\underline{t}G_m\cos\omega_d\underline{t} \right] G_{zz} = 1 \qquad (4.50a)$$

and

$$\left[G_m^{-1} + \frac{a^2\omega_z^4\omega_-}{\omega_+ - \omega_-}\cos\omega_d\underline{t}G_z\cos\omega_d\underline{t} \right] G_{mm} = 1 . \qquad (4.50b)$$

The cooling potential appears in these equations in the form

$$(t \mid \cos\omega_d\underline{t}G \cos\omega_d\underline{t} \mid t')$$
$$= \tfrac{1}{4}(e^{i\omega_d(t-t')} + e^{-i\omega_d(t-t')}$$
$$+ e^{i\omega_d(t+t')} + e^{-i\omega_d(t+t')})G(t-t') , \qquad (4.51)$$

where G is either G_z or G_m. The effects of the terms involving $\exp[\pm i\omega_d(t+t')]$ are very small. Treating these terms as a perturbation, one finds that they give rise to sideband oscillations displaced in frequency by $\pm 2\omega_d, \pm 4\omega_d, \ldots$, with these sidebands suppressed by large, nonresonant denominators. We neglect them. The remaining terms are invariant under time translations. Hence we may Fourier transform according to the generic formula

$$G(t-t') = \int \frac{d\omega}{2\pi}\widetilde{G}(\omega)e^{-i\omega(t-t')} \qquad (4.52)$$

to secure

$$\left[\widetilde{G}_z^{-1}(\omega) + \frac{a^2\omega_z^4\omega_-}{4(\omega_+ - \omega_-)}[\widetilde{G}_m(\omega+\omega_d) + \widetilde{G}_m(\omega-\omega_d)] \right]$$
$$\times \widetilde{G}_{zz}(\omega) = 1 \qquad (4.53a)$$

and

$$\left[\widetilde{G}_m^{-1}(\omega) + \frac{a^2\omega_z^4\omega_-}{4(\omega_+ - \omega_-)}[\widetilde{G}_z(\omega+\omega_d) + \widetilde{G}_z(\omega-\omega_d)] \right]$$
$$\times \widetilde{G}_{mm}(\omega) = 1 . \qquad (4.53b)$$

The Fourier transforms of the uncoupled Green's functions that appear here are given by

$$\widetilde{G}_z^{-1}(\omega) = \omega_z^2 - i\gamma_z\omega - \omega^2 \qquad (4.54a)$$

and

$$\widetilde{G}_m^{-1}(\omega) = \omega_-^2 - \omega^2 . \qquad (4.54b)$$

The structure of the axial Green's function is rather simple. Using Eqs. (4.54) in Eq. (4.53a), we find that

$$\widetilde{G}_{zz}(\omega) = \left[\omega_z^2 - i\gamma_z\omega - \omega^2 \right.$$
$$+ \frac{a^2\omega_z^4\omega_-}{4(\omega_+ - \omega_-)}\left[\frac{1}{\omega_-^2 - (\omega+\omega_d)^2} \right.$$
$$\left. \left. + \frac{1}{\omega_-^2 - (\omega-\omega_d)^2} \right] \right]^{-1} . \qquad (4.55)$$

According to Eq. (4.47a), the Fourier transform of this function gives the axial response $z(t)$ to an axial force $f_z(t)$. A term in the large parentheses in Eq. (4.55) diverges when $\omega=\omega_d+\omega_-$ or $\omega=\omega_d-\omega_-$, and $\widetilde{G}_{zz}(\omega)$ vanishes at these frequencies. Thus an axial drive at the frequency $\omega=\omega_d-\omega_-$ or at the frequency $\omega=\omega_d+\omega_-$, applied along with the sideband drive at ω_d, produces no response in the axial motion. This is the decoupling phenomenon mentioned in Sec. IV.B, which is used to measure the magnetron frequency.

The roots of the denominator in the Green's function (4.55) determine the frequencies that give the resonance responses to axial forces applied in addition to the cooling/heating drive. Since $\gamma_z \ll \omega_z$, the narrow resonance approximation suffices. In this approximation there are two roots. Except for a displacement by the frequency ω_d, these are essentially the two roots of the determinant $D_{\mp}(\omega)$ defined in Eq. (4.13). The root attached to the ordinary axial oscillation in the limit where the cooling/heating drive vanishes $(a\rightarrow0)$ is given by

$$\omega_{r,z}^{(\mp)}=\omega_z+\varepsilon-\tfrac{1}{2}(\varepsilon+i\gamma_z/2)\left[1+\left[1\mp\frac{\gamma_0\gamma_z}{(\varepsilon+i\gamma_z/2)^2}\right]^{1/2}\right]$$

$$\simeq\omega_z-i\gamma_z/2\pm\frac{\gamma_0\gamma_z/4}{\varepsilon+i\gamma_z/2}\ . \tag{4.56}$$

Here the upper signs correspond to heating, the lower to cooling. As before, we have written the heating/cooling drive frequency as $\omega_d=\omega_z\mp\omega_-+\varepsilon$, and γ_0 is the measure of the strength of this drive given by Eq. (4.16). The approximate equality in Eq. (4.56) obtains when $\gamma_0 \ll \gamma_z$. We see that a weak drive produces small shifts in the axial resonance frequency [the real part of Eq. (4.56)] and small changes in the axial decay constant [the imaginary part of Eq. (4.56)]. The second root is at

$$\omega_{r,m}^{(\mp)}=\omega_z+\varepsilon-\tfrac{1}{2}(\varepsilon+i\gamma_z/2)\left[1-\left[1\mp\frac{\gamma_0\gamma_z}{(\varepsilon+i\gamma_z/2)^2}\right]^{1/2}\right]$$

$$\simeq\omega_z+\varepsilon\mp\frac{\gamma_0\gamma_z/4}{\varepsilon+i\gamma_z/2}\ . \tag{4.57}$$

This is an axial resonance induced by the coupling to the magnetron motion. In the narrow resonance approximation, the Green's function

$$\widetilde{G}_{zz}(\omega)=\frac{(\omega_z+\varepsilon-\omega)/2\omega_z}{(\omega-\omega_{r,z}^{(\mp)})(\omega-\omega_{r,m}^{(\mp)})} \tag{4.58}$$

relates the response of the axial oscillation to an axial drive at frequency ω when a cooling or heating drive with frequency specified by ε is simultaneously applied. With a weak heating/cooling drive, Eq. (4.58) shows that the response to an axial force at frequency ω near $\omega_{r,m}^{(\pm)}$ is always small; the amplitude is reduced relative to the normal axial response by a factor that is at most $\gamma_0/2\gamma_z$. On the other hand, so long as $|\varepsilon|\geq\gamma_z$, Eq. (4.58) shows that the response to an axial force at a frequency ω near $\omega_{r,z}^{(\pm)}$ is given by the usual form

$$\widetilde{G}_{zz}(\omega)=\frac{1}{2\omega_z}\frac{1}{\omega_{r,z}^{(\mp)}-\omega}\ . \tag{4.59}$$

Insofar as a weak and off-resonance cooling drive (or no cooling drive at all) is typically applied during precise measurements of the axial frequency, the condition $|\varepsilon|\geq\gamma_z$ is most often satisfied. With $|\varepsilon|<\gamma_z$ the response is more complex, with the decoupling phenomenon described above appearing when $\omega=\omega_z+\varepsilon$.

The Green's function for the magnetron motion, $\widetilde{G}_{mm}(\omega)$, is large only when ω is near resonance, say $\omega\approx+\omega_-$. The effect of the drive will be appreciable only if $\widetilde{G}_z(\omega+\omega_d)$ or $\widetilde{G}_z(\omega-\omega_d)$ is large. This requires that $\omega_d\approx\omega_z-\omega_-$ or $\omega_d\approx\omega_z+\omega_-$, corresponding to a heating or cooling drive as discussed in Sec. IV.B above. Thus we retain only

$$\widetilde{G}_z(\omega\pm\omega_d)\simeq\frac{1}{2\omega_z}\frac{1}{\mp(\omega-\omega_-)-\varepsilon\mp i\gamma_z/2} \tag{4.60}$$

in Eq. (4.53b) to obtain

$$\widetilde{G}_{mm}(\omega)=\frac{1}{4\omega_z\omega_-}\frac{\widetilde{G}_z(\omega\pm\omega_d)^{-1}}{D_{\mp}(\omega)}\ , \tag{4.61}$$

where $D_{\mp}(\omega)$ is the determinant defined by Eq. (4.13). Thus $\widetilde{G}_{mm}(\omega)$ has a pole when this determinant vanishes. Recalling the discussion of Sec. IV.B, we see that with a small coupling constant a, $\widetilde{G}_{mm}(\omega)$ has one pole at $\omega\approx\omega_-$, corresponding to a basic magnetron excitation, and another pole at $\omega\approx\omega_-\mp\varepsilon$, corresponding to a basic axial excitation. Examining Eq. (4.61) one finds that the residue of the pole at $\omega\approx\omega_-$ is approximately $1/2\omega_-$, while the residue of the pole at $\omega\approx\omega_-\mp\varepsilon$ is much smaller. This just reflects the trivial fact that when a is small the magnetron motion is weakly coupled to the axial motion. The imaginary part of the position of the pole near ω_- gives, of course, precisely the rate constant $\gamma_m^{(\mp)}(\varepsilon)$ defined by Eq. (4.15).

We should note that one can also arrange $\widetilde{G}_{zz}(\omega)$ given by Eq. (4.55) in a form similar to that given by Eq. (4.61) for $\widetilde{G}_{mm}(\omega)$, but with the roles of the residues of the two poles interchanged. For example, with ω near $-\omega_z$ and for a cooling drive, we have

$$\widetilde{G}_{zz}(\omega)=\frac{1}{4\omega_z\omega_-}\frac{\widetilde{G}_m(\omega+\omega_d)^{-1}}{D_+(\omega+\omega_d)}\ . \tag{4.62}$$

We shall soon make use of this result.

Since the axial and magnetron motions are coupled, driving the axial motion also produces a magnetron response, as is evident from Eq. (4.47b). The case in which the axial force $f_z(t)$ is the random, thermal drive on the axial motion is of particular interest. This yields the lowest floor of average magnetron excitation to which the system can be cooled. Thus an initially excited magnetron motion will be damped out after a time long in comparison to $\gamma_m^{(-)}(\omega_d)^{-1}$, leaving the random motion produced by this force, which comes from the external, effective resistor that plays the role of a heat bath at temperature T. Referring to our previous discussion of the

axial noise, Sec. III.B [particularly Eqs. (3.19)—(3.24)], we see that in this limit we have the ensemble average

$$\langle V_y^{(-)}(t)V_y^{(-)}(t')\rangle = \frac{2k_B T\gamma_z}{m}\int d\bar{t}\, G_{mz}(t,\bar{t})G_{mz}(t',\bar{t}) \ .$$

(4.63)

To evaluate the integral, we use Eq. (4.49b) for the off-diagonal Green's function G_{mz} and neglect small sideband terms to obtain

$$\langle V_y^{(-)}(t)V_y^{(-)}(t')\rangle = \frac{2k_B T\gamma_z}{m}(a\omega_-\omega_z^2)^2$$

$$\times \int \frac{d\omega}{2\pi}\, |\, \tilde{G}_m(\omega)\tilde{G}_{zz}(\omega-\omega_d)\, |^{\,2}$$

$$\times \cos\omega(t-t') \ . \qquad (4.64)$$

Examining the integral in Eq. (4.64), one finds that the poles near $\omega=\omega_-$ and $\omega=\omega_-+\varepsilon$ dominate in the narrow resonance approximation. Hence we can use Eq. (4.62) to obtain

$$\langle V_y^{(-)}(t)V_y^{(-)}(t')\rangle = \frac{k_B T\gamma_z a^2\omega_z^2}{8m}$$

$$\times \int \frac{d\omega}{2\pi}\frac{\cos\omega(t-t')}{|D_+(\omega)|^2} \ . \qquad (4.65)$$

Although the algebra is a little tedious, this integral is readily evaluated by the standard contour method. We shall not present the result here, since it has a cumbersome form. But the structure of this result is clear: It is the sum of two damped, oscillatory correlations, one corresponding to the basic magnetron excitation, the other to the basic axial excitation. In the limit of weak coupling and an on-resonance drive, $\varepsilon=0$, there is no contribution from the axial excitation, while as the drive goes off resonance and/or the coupling is increased, the axial excitation begins to contribute.

The equal time limit of Eq. (4.65) yields the average squared magnetron velocity and thus the thermal excitation level of the magnetron motion. It is worthwhile to compute this limit, since it provides a rigorous justification of the heuristic arguments given in Sec. IV.A. Using the standard contour method, one finds after some calculation that

$$\langle V_y^{(-)2}\rangle = k_B T\frac{\omega_+-\omega_-}{m\omega_z} \ . \qquad (4.66)$$

Since to within a very good approximation $\langle V_x^{(-)2}\rangle = \langle V_y^{(-)2}\rangle$, this result in conjunction with Eq. (2.21) shows that $\langle -E_{\text{mag}}\rangle = (\omega_-/\omega_z)k_B T$, the limit discussed in Sec. IV.A. It should be emphasized that this limit holds even if the drive is far from resonance, $|\varepsilon| \gg \gamma_z$ (so long, of course, as $|\varepsilon| \ll \omega_-$) and even if the drive is strong.

V. ELECTRON TRANSITION RATES

A. Spin resonance

To set a foundation and introduce the notation for our discussion of spin flips and cyclotron and anomaly $(g-2)$ transitions for an electron or a positron, we first review the familiar Rabi description of an idealized spin resonance. The spin $1/2\hbar\sigma$ moves under the joint action of a large, uniform field **B**, which is constant in time, and a small, perpendicular, oscillatory field **b**(t) that lies in the xy plane. Thus the spin motion is governed by the Hamiltonian

$$H = -g\frac{e\hbar}{2mc}\frac{1}{2}\sigma\cdot[\mathbf{B}+\mathbf{b}(t)] \ . \qquad (5.1)$$

With our sign convention for the direction of $\hat{z}$, the uniform field **B** alone causes the spin to precess in a positive sense about the z axis at the angular frequency

$$\omega_s = g\frac{|eB|}{2mc} \ . \qquad (5.2)$$

In general, any perpendicular oscillating field **b**(t) can be decomposed into components that co-rotate and counter-rotate with respect to this spin precession. The counter-rotating component is nonresonant, and it makes a negligible contribution.[15] Thus there is no essential loss in generality in taking the oscillatory field to be purely a co-rotating field

$$\mathbf{b}(t) = b_0(\hat{x}\cos\omega t +\hat{y}\sin\omega t) \ . \qquad (5.3)$$

The effect of this driving field is most easily seen by passing to a coordinate frame that co-rotates at the driving frequency ω. This is accomplished by first writing

$$H = H_0 + H_1 \ , \qquad (5.4)$$

where

$$H_0 = \hbar\omega\tfrac{1}{2}\sigma_z \qquad (5.5)$$

and

$$H_1 = \tfrac{1}{2}\hbar(\omega_s-\omega)\tfrac{1}{2}\sigma_z + \tfrac{1}{2}\hbar\Omega_s[\sigma_x\cos\omega t +\sigma_y\sin\omega t] \ . \qquad (5.6)$$

Here we have introduced the Rabi frequency

$$\Omega_s = g\frac{eb_0}{2mc} \ . \qquad (5.7)$$

We go into the rotating frame by working in the interaction picture, where

---

[15]The major effect of the counter-rotating part is to shift the resonant frequency by an amount on the order of Ω_s^2/ω_s^2, where Ω_s is the Rabi frequency defined in Eq. (5.7) (Bloch and Siegert, 1940). Since $\Omega_s < 10/\text{sec}$, while $\omega_s > 10^{11}/\text{sec}$, this is indeed a negligible correction.

$$H_1(t)=e^{iH_0t/\hbar}H_1e^{-iH_0t/\hbar}$$

$$=\tfrac{1}{2}\hbar[(\omega_s-\omega)\sigma_z+\Omega_s\sigma_x] . \tag{5.8}$$

We see that, in this new frame, the spin rotates with angular frequency

$$\Omega=[\Omega_s^2+(\omega_s-\omega)^2]^{1/2} \tag{5.9}$$

about the axis in the xz plane

$$\hat{n}=\frac{\Omega_s}{\Omega}\hat{x}+\frac{\omega_s-\omega}{\Omega}\hat{z} . \tag{5.10}$$

This is illustrated in Fig. 22. With the drive on resonance, $\omega=\omega_s$, the axis of rotation is the $\hat{x}$ axis, and an initial spin-up state (along the z axis) can be maximally rotated into a spin-down state. This takes place at the Rabi frequency Ω_s.

The finite spin rotation about the axis $\hat{n}$ produced in the preceding idealized description is usually not directly applicable to the geonium experiments. In these experiments, small fluctuations spread the spin precession frequency ω_s over a range $\delta\omega_s$. The frequency spread $\delta\omega_s$ is always much greater than the Rabi frequency Ω_s, $\delta\omega_s\gg\Omega_s$. Hence, after an infinitesimal spin rotation (correctly described by the previous discussion), the coherent rotation of the spin is destroyed and a linewidth is introduced. The fluctuations arise, for example, from the Brownian motion of the axial oscillation, which is coupled to the spin motion either via special relativity (Sec. VII) or by the slightly inhomogeneous field introduced by a magnetic bottle (Sec. VI). In either case, the
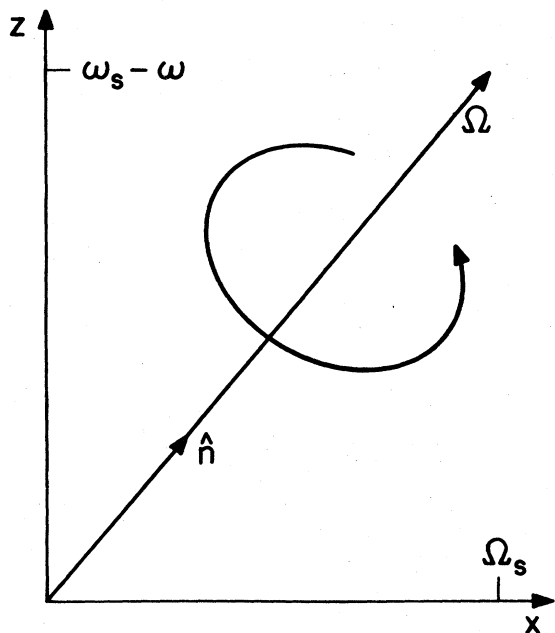
FIG. 22. The axis $\hat{n}$ defined by Eq. (5.10) is stationary in the xz plane of the coordinate system which co-rotates with the drive at the angular frequency ω. The spin rotates with angular velocity Ω about this axis.

fluctuations can be represented by effective fluctuations in the uniform field B. Fluctuations in the magnetic field also occur with components that are perpendicular to $\mathbf{B}$. However, these fluctuations, which take place with time scales slow in comparison to the spin precession time $1/\omega_s$, are averaged to zero by the fast precession, and they may be neglected.

We begin our treatment of the line shape (which is that given by Brown, 1984,1985) by considering the limit in which the Rabi rotation frequency Ω_s is very small. In this limit we compute the probability that the spin is flipped from up to down using first-order perturbation theory. To do this, we must now use the interaction picture in which the unperturbed Hamiltonian H_0 includes the fluctuation

$$H_0=\hbar\omega_1(t)\tfrac{1}{2}\sigma_z , \tag{5.11}$$

with

$$\omega_1(t)=\omega_s[1+\xi(t)] , \tag{5.12}$$

where $\xi(t)$ is a small random variable. The application of oscillatory drive in the time interval $t_2<t<t_1$ produces a first-order transition amplitude given by

$$(-t_2\mid+t_1)=\frac{-i}{\hbar}\int_{t_1}^{t_2}dt(-\mid H_1(t)\mid+) , \tag{5.13}$$

where

$$H_1(t)=-g\frac{e\hbar}{2mc}\frac{1}{2}\sigma(t)\cdot\mathbf{b}(t) , \tag{5.14}$$

with the time dependence of $\sigma(t)$ governed by H_0. Only the component

$$\sigma_-(t)=\tfrac{1}{2}[\sigma_x(t)-i\sigma_y(t)]$$

$$=\sigma_-(0)\exp\left[-i\int_0^t dt'\omega_1(t')\right] \tag{5.15}$$

contributes to the $(-\mid\ \mid+)$ matrix element, and so we have, recalling Eqs. (5.3) and (5.7),

$$(-t_2\mid+t_1)=-\tfrac{1}{2}\Omega_s\int_{t_1}^{t_2}dt\,e^{i\omega t}\exp\left[-i\int_0^t dt'\omega_1(t')\right] . \tag{5.16}$$

The transition probability for a specified history of the time dependence of $\omega_1(t)$ is given by the absolute square of the amplitude (5.16). With a fluctuating angular frequency $\omega_1(t)$, an average over such histories must be performed. Hence the transition probability is given by

$$P=\tfrac{1}{4}\Omega_s^2\int_{t_1}^{t_2}dt\int_{t_1}^{t_2}d\bar{t}\,e^{i\omega(t-\bar{t})}$$

$$\times\left\langle\exp\left[-i\int_{\bar{t}}^t dt'\omega_1(t')\right]\right\rangle . \tag{5.17}$$

The classical, statistical average denoted by the angular brackets in Eqs. (5.17) is invariant under overall time translations and so defines

$$\widetilde{\chi}_s(t-\bar{t}) = \left\langle \exp\left[-i\int_0^{t-\bar{t}} dt' \omega_1(t')\right] \right\rangle$$
$$= e^{-i\omega_s(t-\bar{t})} \left\langle \exp\left[-i\omega_s \int_0^{t-\bar{t}} dt' \xi(t')\right] \right\rangle .$$

$$(5.18)$$

This correlation function vanishes for time differences $t-\bar{t}$ that are large in comparison with $1/\delta\omega_s$, a time that is very short in comparison with the time interval t_2-t_1 during which the drive field is applied. Hence we may change integration variables to $T = \frac{1}{2}(t+\bar{t})$, $\tau = t-\bar{t}$ and integrate $+\infty < \tau < -\infty$ to secure

$$P = \frac{\pi}{2}\Omega_s^2(t_2-t_1)\chi_s(\omega) .$$

$$(5.19)$$

We see that we have a time-independent transition rate $R = P/(t_2-t_1)$. The line profile $\chi_s(\omega)$ is given by the Fourier transform of the correlation function:

$$\chi_s(\omega) = \int_{-\infty}^{\infty} \frac{d\tau}{2\pi} e^{i\omega\tau}\widetilde{\chi}_s(\tau) .$$

$$(5.20)$$

Since

$$\widetilde{\chi}_s(0) = 1 ,$$

$$(5.21)$$

we have the normalization

$$\int_{-\infty}^{\infty} d\omega \chi_s(\omega) = 1 .$$

$$(5.22)$$

Roughly speaking, the line profile is peaked at $\omega = \omega_s$, and this peak has a width $\delta\omega_s$. The normalization (5.22) informs us that the peak has a height $1/\delta\omega_s$. Thus the resonance transition rate is approximately given by

$$P/(t_2-t_1) \approx \frac{\pi}{2}(\Omega_s/\delta\omega_s)\Omega_s .$$

$$(5.23)$$

The fluctuations reduce the Rabi rotation rate Ω_s by the small factor $\Omega_s/\delta\omega_s$.

The result (5.19) that we have just derived applies only for drives that are sufficiently weak and that are applied for time intervals sufficiently short to keep the transition probability well below unity, $P \ll 1$. Although the drive is generally quite small, in the sense that $\Omega_s/\delta\omega_s \ll 1$, it is often applied for a sufficiently long time interval (t_2-t_1) to violate this restriction. To deal with this general case, all orders of the drive field perturbation must be taken into account. However, in the geonium experiments the drive rate Ω_s is small in comparison with the linewidth $\delta\omega_s$. Moreover, the spin rotation time $1/\Omega_s$ is small in comparison with the noise correlation time[16] $1/\gamma$, so that the statistical average of a product of exponentials with fluctuating phases can be replaced by a product of averages [cf. Eq. (5.56) below]. With these conditions met, spin transitions may be described by a simple evolution equation for the spin-density matrix ρ,

which includes an ensemble average over the fluctuating phases. With $\rho_{++}(t)$ and $\rho_{--}(t)$ giving the probability for finding spin-up and spin-down, respectively, we have

$$\dot{\rho}_{--}(t) = 4R[\rho_{++}(t) - \rho_{--}(t)]$$

$$(5.24a)$$

and

$$\dot{\rho}_{++}(t) = 4R[\rho_{--}(t) - \rho_{++}(t)] .$$

$$(5.24b)$$

(The rapidly fluctuating random phases keep $\rho_{-+} = 0 = \rho_{+-}$.) These coupled rate equations preserve the total probability

$$\rho_{++}(t) + \rho_{--}(t) = 1 .$$

$$(5.25)$$

Starting with (say) spin-up at $t = 0$, we have the solution

$$\rho_{--}(t) = \frac{1}{2}(1 - e^{-2Rt})$$

$$(5.26a)$$

and

$$\rho_{++}(t) = \frac{1}{2}(1 + e^{-2Rt}) .$$

$$(5.26b)$$

taking the limit of small t, we see that the rate R is given by $R = P/(t_2-t_1)$, with P defined by Eq. (5.19). Thus, in general, the probability P for the spin to flip (up to down or vice versa) is given, in view of Eq. (5.26a), by the exponential form[17]

$$P = \frac{1}{2}\{1 - \exp[-\pi\Omega_s^2(t_2-t_1)\chi_s(\omega)]\} .$$

$$(5.27)$$

Applying a drive near resonance for a long time interval will saturate the transition with $P = \frac{1}{2}$.

B. Cyclotron resonance

The line profile function $\chi(\omega)$ describes the cyclotron resonance as well as the spin resonance, as we shall now demonstrate.

Microwaves near the cyclotron frequency ω_c are introduced into the trap via a microwave inlet, as shown in Fig. 1. Thus, including the radiative damping, we have the driven cyclotron equation of motion

$$\dot{v}(t) = i\omega_2(t)v(t) - \frac{1}{2}\gamma_c v(t) + \frac{e}{m}\mathscr{E}(t) .$$

$$(5.28)$$

Here, to simplify the analysis, we have utilized the complex notation

$$v(t) = v_x(t) + iv_y(t) .$$

$$(5.29)$$

Since the cyclotron orbit is very much smaller than the wavelength of the microwave radiation, the dipole approximation suffices, and we neglect the spatial variation in writing $\mathscr{E}(t)$. Regardless of the state of polarization of the microwave field, only the co-rotating component can be in resonance, and so it also suffices to take

---

[16]When the fluctuations result from those of the axial motion, $\gamma = \gamma_z$ is the decay rate of the axial motion. See Sec. VI.

[17]A more rigorous derivation of this result is given in Brown (1985).

$$\mathscr{E}(t)=\mathscr{E}_0 e^{i\omega t} .\tag{5.30}$$

The time-dependent angular frequency $\omega_2(t)$ arises from fluctuations in the effective magnetic field, just as was the case for the spin resonance, and we have

$$\omega_2(t)=\omega_c'[1+\xi(t)] ,\tag{5.31}$$

where $\xi(t)$ is a very small, random variable. We have simplified the discussion by neglecting the quadrupole electrostatic trapping potential. Its only effect is to replace the cyclotron frequency ω_c by $\omega_c'=\omega_c-\omega_m=\omega_+$ defined in Eq. (2.14). We should note that our discussion should hold for the quantum as well as the classical case, since the quantum Heisenberg equations of motion are linear. On the other hand, our discussion does not apply to the highly nonlinear relativistic cyclotron resonance that has recently been observed by Gabrielse, Dehmelt, and Kells (1985).

In the geonium experiments, cyclotron excitations are observed by measurements of the cyclotron orbit at a time T after the microwave drive, which was on for an interval $-T_0<t<0$, has been turned off. The drive is on for a time T_0, which may be on the order of the cyclotron re-

laxation time $1/\gamma_c$. It is convenient to replace this abrupt initial switching on of the cyclotron drive by an adiabatic damping factor $\exp(t/T)$ for $t<0$, with the drive suddenly switched off for $t>0$. As we shall see, this modification of the drive is not significant. With this drive Eq. (5.28) has the solution

$$v(T)= \frac{e}{m}\mathscr{E}_0 e^{-\gamma_c T/2}$$
$$\times\int_{-\infty}^0 dt \exp\left[i\int_t^T dt_1\omega_2(t_1)\right]e^{\gamma_c t/2}e^{i\omega t}e^{t/T} .\tag{5.32}$$

Thus the adiabatic switching simply replaces γ_c in the integrand by γ_c', where

$$\gamma_c'=\gamma_c+\frac{2}{T} .\tag{5.33}$$

The experiments measure the magnetic moment of the cyclotron orbit or, equivalently, the energy

$$E_c(T)=\tfrac{1}{2}m\,|v(T)|^2 .\tag{5.34}$$

Taking the statistical average, we have

$$E_c(T)=\frac{e^2\mathscr{E}_0^2}{2m}e^{-\gamma_c T}\int_{-\infty}^0 dt\int_{-\infty}^0 dt' e^{\gamma_c'(t+t')/2}e^{i\omega(t-t')}\left\langle\exp\left[-i\int_{t'}^t dt_1\omega_2(t_1)\right]\right\rangle .\tag{5.35}$$

The quantity with the angular brackets of the statistical average is just the correlation function $\widetilde{\chi}_c(t-t')$ defined in Eq. (5.18) except, of course, that ω_s is replaced by ω_c'. The time integrations in Eq. (5.35) can be evaluated by inverting the Fourier transform (5.20),

$$\left\langle\exp\left[-i\int_{t'}^t dt_1\omega_2(t_1)\right]\right\rangle=\int_{-\infty}^\infty d\omega' e^{-i\omega'(t-t')}\chi_C(\omega') .\tag{5.36}$$

The time integrations are now elementary, and they give

$$E_c(T)= \frac{e^2\mathscr{E}_0^2}{2m\gamma_c'}e^{-\gamma_c T}$$
$$\times\int_{-\infty}^\infty d\omega'\left[\frac{\gamma_c'}{(\omega'-\omega)^2+\gamma_c'^2/4}\right]\chi_C(\omega') .\tag{5.37}$$

In general, we see that the response to a cyclotron drive is given by the convolution of the line profile function $\chi_C(\omega)$, with the Lorentzian line shape of a noise-free but damped cyclotron resonance with the modified damping constant γ_c'. In the geonium experiments, however, the decay rate γ_c' is much smaller than the linewidth parameter $\delta\omega_c$. In this case $\chi_C(\omega')$ is slowly varying in the interval γ_c', and the limit $\gamma_c'\to 0$ may be taken in the term in large parentheses in Eq. (5.37) to produce $2\pi\delta(\omega'-\omega)$. Thus we secure

$$E_c(T)=\frac{e^2\mathscr{E}_0^2}{2m\gamma_c'}e^{-\gamma_c T}2\pi\chi_C(\omega) .\tag{5.38}$$
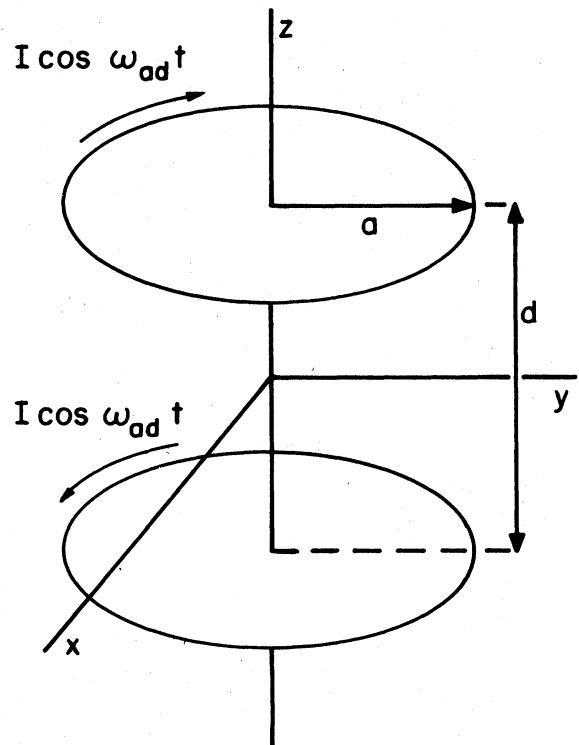

FIG. 23. Effective current loops, which produce the alternating magnetic field near the center of the trap given by Eq. (5.39), with the constant b_1 having the value $b_1=(\pi a^2 I/c)3d(a^2+d^2/4)^{-5/2}$ (in Gaussian units).

The only effect of the initial abrupt switching is to replace the large parentheses in the convolution in Eq. (5.37) by a more complicated expression, which has, however, the same properties. Thus the result (5.38) describes the experimental line shape except for an insignificant alteration of the overall factor.

C. Anomaly resonance

We have now described the line shapes for spin flips and cyclotron excitations. As in earlier $g-2$ experiments (Schupp, Pidd, and Crane, 1961), the geonium experiments do not measure the spin transition frequency and subtract from it the cyclotron frequency $\omega_a = \omega_s - \omega_c$. This would entail the subtraction of large numbers to determine a number 10^{-3} smaller, resulting in a loss of accuracy. The anomaly transition (a spin flip increasing the energy accompanied by a cyclotron transition decreasing the energy or vice versa) is observed directly in the geonium experiments. This is accomplished by splitting the upper and lower portions of the trap electrodes so as to obtain two effective current loops. The loops are driven with oppositely directed currents at the anomaly drive frequency ω_{ad}, as shown in Fig. 23. This produces a small alternating magnetic field near the center of the trap,

$$\mathbf{b}(t) = b_1 \rho(t) \cos \omega_{ad} t \, , \tag{5.39}$$

which is perpendicular to the main, constant magnetic field. Since $\rho(t)$ goes about a circle at the modified cyclotron frequency $\omega'_c = \omega_c - \omega_m$, $\mathbf{b}(t)$ has a component at the frequency $\omega'_c + \omega_{ad}$ which flips the spin when $\omega'_c + \omega_{ad} = \omega_s$, or when the drive frequency equals the modified anomaly frequency $\omega_{ad} = \omega'_a = \omega_a + \omega_m$. The small magnetron frequency ω_m is then subtracted to obtain the true anomaly frequency [cf. Eq. (2.88) and the discussion leading to it]. The use of a field with this symmetry to make $g-2$ transitions was discussed by Gräff, Klempt, and Werth (1969) and by Walls (1970).

This simple situation is altered by the fluctuations which can be represented by an effective strong axial magnetic field with a small fluctuating component. Introducing the complex notation where, for example,

$$b(t) = b_x(t) + i b_y(t) \, , \tag{5.40}$$

and following the development that led to Eq. (5.17), we see that in the limit of a very weak driving field applied during the time interval (t_2, t_1), the spin transition probability is given by

$$P = \frac{1}{4} \left[\frac{eg}{2mc} \right]^2 \int_{t_1}^{t_2} dt \int_{t_1}^{t_2} d\bar{t} \left\langle b(t) \exp\left[-i \int_{\bar{t}}^{t} dt_1 \omega_1(t_1) \right] b(\bar{t})^* \right\rangle . \tag{5.41}$$

Here, we recall,

$$\omega_1(t) = \omega_s [1 + \xi(t)] \tag{5.42}$$

in which $\xi(t)$ is a random, fluctuating variable.

The (complex) magnetic field $b(t)$ is linearly related to (the complex) $\rho(t)$. This radial coordinate is maintained in excitation by driving the cyclotron motion with a microwave field $\mathscr{E}(t)$, as described by Eq. (5.28). We can neglect the very small variation in factors involving

$$\omega_2(t) = \omega'_c [1 + \xi(t)] \, , \tag{5.43}$$

since only accumulated phases are important in Eq. (5.41). Hence we may write

$$\rho(t) = \frac{-i}{\omega'_c} v(t) \tag{5.44}$$

with

$$v(t) = \frac{e}{m} \int_{-\infty}^{t} dt' \exp\left[i \int_{t'}^{t} dt_2 \omega_2(t_2) \right] e^{-\gamma_c(t-t')/2} \mathscr{E}(t') \, , \tag{5.45}$$

the solution of Eq. (5.28). Using Eq. (5.39) and Eqs. (5.44) and (5.45) in Eq. (5.41) and keeping only the significant resonant terms gives an explicit formula for the transition probability P. In the experiments, the time interval $t_2 - t_1$ during which the anomaly drive is on is much longer than any relaxation time. Hence we may change integration variables to $T = \frac{1}{2}(t + \bar{t})$ and $\tau = t - \bar{t}$, and integrate over $-\infty < \tau < +\infty$. The resonant contributions to P are time-translationally invariant; they are independent of T. Hence the T integration simply produces an overall factor of $t_2 - t_1$, and we find that the transition rate is given by

$$P/(t_2 - t_1) = \left[\frac{eg}{2mc} \right]^2 \left[\frac{eb_1}{4m\omega'_c} \right]^2$$

$$\times \int_{-\infty}^{\infty} d\tau \, e^{i\omega_{ad}\tau} \int_{-\infty}^{\tau} dt' \mathscr{E}(t') \int_{-\infty}^{0} dt' \mathscr{E}(\bar{t}')^* e^{-\gamma_c(\tau - t' - \bar{t}')/2}$$

$$\times \left\langle \exp\left[-i \int_{0}^{\tau} dt_1 \omega_3(t_1) \right] \exp\left[-i \int_{\bar{t}'}^{t'} dt_2 \omega_2(t_2) \right] \right\rangle . \tag{5.46}$$

Here

$$\omega_3(t) = \omega_a'[1 + \xi(t)] \tag{5.47}$$

describes the fluctuating anomaly frequency.

The statistical average appearing in Eq. (5.46) is a generalization of that encountered previously [Eq. (5.18)] in the derivation of the line profile function. There are, however, two situations in which this more complex statistical average reduces to the previous correlation function, and these are the cases of experimental importance.

The first case is that in which the cyclotron drive is white noise. In this case one makes the replacement

$$\mathscr{E}(t')\mathscr{E}(\bar{t}')^* \to \mathscr{E}_N^2 \delta(t' - \bar{t}') \tag{5.48}$$

in Eq. (5.46). Referring back to Eq. (5.45), we see that this white noise produces an average cyclotron excitation given by

$$\langle E_c \rangle = \tfrac{1}{2} m \langle |v|^2 \rangle = \frac{e^2 \mathscr{E}_N^2}{2m\gamma_c} . \tag{5.49}$$

Inserting Eq. (5.48) in Eq. (5.46), we find that

$$P/(t_2 - t_1) = \left[\frac{eg}{2mc} \right]^2 \frac{b_1^2}{8m\omega_c'^2} \langle E_c \rangle$$

$$\times \int_{-\infty}^{\infty} d\tau \, e^{i\omega_{ad}\tau} e^{-\gamma_c |\tau|/2} \widetilde{\chi}_A(\tau) , \tag{5.50}$$

where

$$\widetilde{\chi}_A(\tau) = \left\langle \exp\left[-i \int_0^\tau dt \, \omega_3(t) \right] \right\rangle \tag{5.51}$$

is identical to the previous correlation function except that the cyclotron frequency ω_c' is replaced by the anomaly frequency ω_a'. The factors out front in Eq. (5.50) for the transition rate can be placed in a perspicuous form.

The ratio

$$\frac{\langle E_c \rangle}{\tfrac{1}{2} m\omega_c'^2} = \langle \rho^2 \rangle \tag{5.52}$$

defines an average cyclotron radius. Remembering that the driving field (5.39) corresponds to linear, not circular, polarization, we see that

$$\left[\frac{eg}{2mc} \right]^2 \frac{b_1^2 \langle \rho^2 \rangle}{4} = \langle \Omega_a^2 \rangle \tag{5.53}$$

defines an effective squared Rabi frequency, with the additional factor of $\tfrac{1}{4}$ arising from the circular component of the linear polarization. Finally, we note that the Fourier transform of a product is the convolution of the separate Fourier transforms. Therefore

$$P/(t_2 - t_1) = \tfrac{1}{4} \langle \Omega_a^2 \rangle$$

$$\times \int_{-\infty}^{\infty} d\omega' \left[\frac{\gamma_c}{(\omega_{ad} - \omega')^2 + \gamma_c^2/4} \right] \chi_A(\omega') \tag{5.54}$$

If the cyclotron decay rate γ_c is much smaller than the linewidth parameter $\delta\omega_a$, $\chi_A(\omega')$ is slowly varying in the interval γ_c, and the limit $\gamma_c \to 0$ may be taken in the term in the large parentheses to produce $2\pi\delta(\omega_{ad} - \omega')$. In this case

$$P/(t_2 - t_1) = \frac{\pi}{2} \langle \Omega_a^2 \rangle \chi_A(\omega_{ad}) , \tag{5.55}$$

which is exactly the form of the simple spin resonance result, Eq. (5.19).

The second case is the situation when the cyclotron decay time $1/\gamma_c$ is much longer than the noise correlation time $1/\gamma$. In this case, the statistical average in Eq. (5.46) may be replaced by the factored form

$$\left\langle \exp\left[-i \int_0^\tau dt_1 \omega_3(t_1) \right] \exp\left[-i \int_{\bar{T}'}^{t'} dt_2 \omega_2(t_2) \right] \right\rangle \to \left\langle \exp\left[-i \int_0^\tau dt_1 \omega_3(t_1) \right] \right\rangle \left\langle \exp\left[-i \int_{\bar{T}'}^{t'} dt_2 \omega_2(t_2) \right] \right\rangle$$

$$= \widetilde{\chi}_A(\tau) \widetilde{\chi}_C(t' - \bar{t}') . \tag{5.56}$$

The correction to this approximate factorization is generally exponentially damped in a time $1/\gamma$. The difference of the times t' and $\bar{t}'$ in Eq. (5.46) is limited by $|t' - \bar{t}'| \leq 1/\delta\omega_c$. On the other hand, the extent of the average time $\tfrac{1}{2}(t' + \bar{t}')$ in Eq. (5.46) is limited by the large cyclotron decay time $1/\gamma_c$. Hence the bulk of the time integrations in Eq. (5.46) is in a region in which $|\tau - \tfrac{1}{2}(t' - \bar{t}')|$ is large on the scale set by $1/\gamma$, and the factorization shown by Eq. (5.56) may be employed. The correction to this approximation is of the order γ_c/γ. Using now a rotating, coherent field

$$\mathscr{E}(t) = \mathscr{E}_0 e^{i\omega_{cd}t} \tag{5.57}$$

to drive the cyclotron motion, we have, with $\gamma_c/\delta\omega_c \ll 1$,

$$P/(t_2 - t_1) = \left[\frac{eg}{2mc} \right]^2 \left[\frac{eb_1}{4m\omega_c'} \right]^2 2\pi\chi_A(\omega_{ad})$$

$$\times \frac{2\pi}{\gamma_c} \mathscr{E}_0^2 \chi_C(\omega_{cd}) . \tag{5.58}$$

The factors appearing in Eq. (5.58) may also be put in perspicuous form. Remembering Eq. (5.38), we see that

$$E_c = \frac{e^2 \mathscr{E}_0^2}{2m\gamma_c} 2\pi\chi_C(\omega_{cd}) \tag{5.59}$$

defines the excitation energy of the cyclotron motion. Moreover,

$$\rho_c^2 = \frac{E_c}{\frac{1}{2}m\omega_c'^2} \tag{5.60}$$

defines the radius of this excitation, and so again we encounter an effective Rabi frequency

$$\Omega_a^2 = \left[\frac{eg}{2mc}\right]^2 \frac{b_1^2\rho_c^2}{4} , \tag{5.61}$$

with Eq. (5.58) now reading

$$P/(t_2 - t_1) = \frac{\pi}{2}\Omega_a^2 \chi_A(\omega_{ab}) \tag{5.62}$$

just as before.

We have seen that the rate of anomaly transitions for very weak drives is proportional to the line profile function $\chi_A(\omega_{ad})$. When the drives are strong, one may use statistical arguments similar to those outlined in Sec. V.A to prove that the probability exponentiates, giving the anomaly line shape

$$P = \frac{1}{2}\{1 - \exp[-\pi\Omega_a^2(t_2 - t_1)\chi_A(\omega_{ad})]\} . \tag{5.63}$$

D. Motional fields flip spin?

In the previous section we described one method for inducing anomaly transitions. This entailed the technical complication of splitting electrodes so as to obtain effective current loops. The experiment would be simplified if the transition could be produced by simply driving the endcaps at the anomaly frequency. Motional magnetic fields might appear to provide such an alternative mechanism to flip the spin.

The idea (Dehmelt and Ekstrom, 1973) is as follows. Suppose that an additional alternating voltage is applied between the two endcaps of the Penning trap. This gives an additional electric field $\mathscr{E}(t) = \mathscr{E}_0 \cos\omega_d t$ near the center of the trap, which is directed along the magnetic field, $\mathscr{E}_0 || \hat{z}$. We may neglect the slow magnetron drift for our present purpose, with the charged particle simply moving about a circle at the cyclotron angular frequency ω_c. Thus there is a small alternating magnetic field $b(t) = c^{-1}v(t) \times \mathscr{E}(t)$ in the particle's rest frame, which is perpendicular to the large constant magnetic field. This alternating magnetic field has a frequency component at $\omega_c + \omega_d$, and so a spin-flipping resonance occurs at $\omega_c + \omega_d = \omega_s = \frac{1}{2}g\omega_c$ or when the drive frequency equals the anomaly frequency, $\omega_d = \frac{1}{2}(g-2)\omega_c = a\omega_c$. On resonance, the rate at which the spin flipping proceeds is given by the Rabi frequency $\Omega_a = \frac{1}{2}(eg/2mc)(v/c)\mathscr{E}_0$. Recalling from Sec. II that for the electron $v/c \approx 10^{-4}$ and using $2mc^2/e \approx 10^6$ V, we see that to obtain a usable rate, $\Omega_a/2\pi \approx 1$ sec^{-1}, a rather strong but still accessible electric field is required, $\mathscr{E}_0 \approx 2$ V/cm.

The scenario we have just presented is, unfortunately, not the whole story. Other effects conspire to reduce the spin-flip rate to an inaccessible value. Since our answer is a negative one, we shall not present the details (Brown, 1983) of its derivation here, but simply outline its physical

ingredients and state the final result.

(i) The constant electric quadrupole potential also acts on the particle. If this field were strong, the particle would be bound to a point where the total electric field vanished, and the motional magnetic field disappeared. In general, this effect produces an overall factor of $\omega_d^2/(\omega_d^2 - \omega_z^2)$ in the spin precession frequency Ω_a.

(ii) Relativistic corrections are more important. They arise both from the kinematic Thomas precession and from relativistic velocity-dependent torques. These effects are described by the spin-dependent part of the $1/c^2$ correction to the Hamiltonian given in Sec. VII.B. Including the nonrelativistic limit, the spin total precession frequency is given by

$$\omega = \frac{e}{2mc}[(g - v^2/c^2)\mathbf{B} + (1 + 2a)\mathbf{E}\times\mathbf{v}/c$$
$$- a(\mathbf{B}\cdot\mathbf{v})\mathbf{v}/c^2] . \tag{5.64}$$

It is convenient to analyze the spin precession in the frame that rotates at the unperturbed spin frequency $\omega_s = (eg/2mc)\mathbf{B}$. In this frame, the major motion is given by $\dot{\mathbf{v}} = -a(eB/mc)\hat{z}\times\mathbf{v}$. Thus adding a total time derivative

$$\frac{d}{dt}(\hat{z}\cdot\mathbf{v}\hat{z}\times\mathbf{v}/2c^2)$$

to the spin precession frequency given in Eq. (5.64) removes the last term from this equation and also adds

$$\hat{z}\cdot\dot{\mathbf{v}}\hat{z}\times\mathbf{v}/2c^2 = -(e/2mc^2)\hat{z}\cdot\mathbf{E}\hat{z}\times\mathbf{v} ,$$

which essentially cancels the unity in the $(1 + 2a)$ factor in the third term in Eq. (5.64). The total time derivative can be neglected, since it does not give rise to a persistent, secular perturbation. We see that the effective spin-flip frequency is reduced by an overall factor of the small anomaly a.

(iii) The axial alternating field $\mathscr{E}(t)$ produces, via the Maxwell displacement current, a perpendicular alternating magnetic field. This magnetic field also causes spin flips at a rate comparable to that given by the relativistically corrected motional field effect, with the rate involving an overall factor of the anomaly a.

The net result of the effects we have described is to produce a spin rotation (Rabi) frequency given by

$$\Omega_a = \frac{ea(g + 4)}{4mc^2} \frac{\omega_d^2}{\omega_d^2 - \omega_z^2}\mathscr{E}(t)\times\mathbf{v}(t) . \tag{5.65}$$

The overall factor of $a \approx 10^{-3}$ makes this spin-flipping rate too low to be useful.

VI. MAGNETIC BOTTLES

A magnetic bottle is a particular kind of distortion of the homogeneous magnetic field. While such a distortion is not part of a Penning trap as such, it is difficult to overstate the importance of magnetic bottles for measurements of the g value of the electron and positron. The

use of magnetic bottles for the detection of cyclotron transitions and spin flips was proposed early in the history of these experiments (Dehmelt and Ekstrom, 1973), and all measurements of these lepton g values completed so far with a Penning trap have depended in a crucial way upon a magnetic bottle (see, for example, Van Dyck, Schwinberg, and Dehmelt, 1978). How this detection scheme works and the way that the motion of a trapped particle in a Penning trap is modified by the addition of a magnetic bottle is discussed in Sec. VI.A. How the magnetic bottles have been produced in the laboratory is the subject of Sec. VI.B.

The distortion of the magnetic field by a magnetic bottle does, unfortunately, limit the accuracy of measurements by broadening the observed resonance linewidths of the cyclotron, spin, and anomaly transitions. Further increases in the experimental accuracy of the measured g values make it necessary to deal with this broadening. One approach now being taken (Gabrielse and Dehmelt, 1981a) is to eliminate the magnetic bottle entirely and instead make use of very small relativistic couplings (see Sec. VII.B). Although this is difficult, progress has been made (Gabrielse, Dehmelt, and Kells, 1985). A second approach being used is to calculate the line shapes that pertain when a magnetic bottle is present (Brown, 1984,1985) and use these calculated line shapes to split the measured lines (Van Dyck, Schwinberg, and Dehmelt, 1984). The line shape calculation is reviewed in Sec. VI.C. A third approach now being tested (Van Dyck, Moore, Farnham, and Schwinberg, 1986) is to utilize a superconducting current loop to form a superconducting flux transformer, which provides a magnetic bottle whose strength can be varied during the experiment. This is described in Sec. VI.D.

A. Modification of the motions

For our purposes, a "magnetic bottle" is a particular kind of inhomogeneous magnetic field given by

$$\Delta \mathbf{B} = B_2 [(z^2 - \rho^2/2)\hat{B} - (\hat{B}\cdot \mathbf{z})\rho] , \qquad (6.1)$$

where $\hat{B}$ is the direction of the homogeneous magnetic field to which the bottle is added.[18] In the successful measurements of the lepton g values, the constant B_2 is approximately equal to 150 G/cm^2 (Van Dyck, Schwinberg, and Dehmelt, 1978). To understand why this field distortion is called a "bottle," consider the effect of $\Delta \mathbf{B}$ upon a magnetic moment μ that is aligned along $\hat{B}$ and that for convenience is located on the z axis. The interaction Hamiltonian $-\mu \cdot \Delta \mathbf{B}$ for this special case is given by

$$\Delta H(\rho=0,z) = -\mu B_2 z^2 . \qquad (6.2)$$

----

[18]We assume that $\Delta \mathbf{B}$ changes sign when the direction of the main magnetic field $\mathbf{B}$ is reversed, as is the case for a bottle made with magnetic materials (Sec. VI.B).

With $B_2 < 0$, the magnetic moment is axially confined (as if it were in a "bottle"), and it will oscillate harmonically along the z axis.

The magnetic bottles used in the geonium experiments are very weak. The axial confinement provided by the superimposed, electrostatic quadrupole potential discussed earlier is very much stronger than that associated with the magnetic bottle. A magnetic bottle (or a suitable replacement) is required for detection. This requirement arises because of the large magnetic fields used and because of the small mass of the electron. An electron trapped in such a large magnetic field has a large cyclotron frequency, $\omega_c/2\pi \approx 160$ GHz for $B \approx 60$ kG. The difficulty is that such large cyclotron (and spin) frequencies are high microwave frequencies, which are not easy to observe directly. The large magnetic fields are desirable because the small fluctuating fields present in the laboratory (including fluctuations in the Earth's field) are relatively smaller. Moreover, the large field separates the cyclotron energy levels enough that the 4-K blackbody radiation (from the trap electrodes, which are in thermal equilibrium with a liquid helium bath) excites the cyclotron motion out of the lowest quantum state less than 13% of the time.

The axial frequency of a trapped particle is a radio frequency ($\omega_z/2\pi \approx 60$ MHz), which can be monitored much more easily. Extremely small shifts in this frequency ($\Delta \omega_z/\omega_z < 2 \times 10^{-8}$) can be routinely observed. For an ideal trap without a magnetic bottle, however, the only coupling of the cyclotron and spin motions to the axial oscillation is by way of the extremely small relativistic couplings discussed in Sec. VII. The magnetic bottles that were added to the electron and positron experiments increased the coupling of the spin and cyclotron motions to the axial oscillation frequency by approximately a factor of 30 over the relativistic couplings. How the coupling comes about is already evident in the interaction Hamiltonian in Eq. (6.2) for a magnetic moment on the z axis, since the spin, cyclotron, and magnetron motions are each associated with a magnetic moment, which is parallel or antiparallel to the z axis because of the strong magnetic field along this axis. By Eq. (6.2), a change in any of these magnetic moments changes the axial restoring force slightly and produces a measurable shift $\Delta \omega_z$ in the axial oscillation frequency. The shift, as we show below, is given for an electron and positron by (approximately)

$$\Delta \omega_z = \Delta \tilde{\omega}_z \left[\frac{gs}{4} + n + \frac{1}{2} + \frac{\omega_m}{\omega_c'}(l + \tfrac{1}{2}) \right] , \qquad (6.3)$$

where $\Delta \tilde{\omega}_z$ is a constant to be described presently. The spin and cyclotron quantum numbers, $s/2$ and n, enter this expression on an equal footing when $g = 2$ because in this case the spin and cyclotron moments are proportional to the energy in these motions with (essentially) the same constant. The magnetic moment associated with the magnetron motion, however, is proportional to the kinetic energy in this motion. The kinetic energy in the magnetron motion is smaller than the total energy in this

motion by the very small ratio ω_m/ω_c', which multiplies the magnetron quantum number l in Eq. (6.3).

The constant $\Delta\widetilde{\omega}_z$ is the axial frequency shift that results from either a spin flip or a unit change in the cyclotron quantum number. It is a convenient measure of the strength of a magnetic bottle. For the electron and positron measurements referred to earlier, $\Delta\widetilde{\omega}_z/2\pi \approx 1$ Hz. Changes in the axial frequency of this size could be observed, so that a single flip was observed (Van Dyck, Wineland, Ekstrom, and Dehmelt, 1976). In general,

$$\frac{\Delta\widetilde{\omega}_z}{\omega_z} = \frac{\hbar}{2m\omega_m}\frac{B_2}{|B|}\frac{\omega_c}{\omega_c'-\omega_m} \ . \tag{6.4}$$

Three aspects of this formula should be noted. First, $\Delta\widetilde{\omega}_z$ is independent of the charge of a trapped particle. An electron and a positron interact identically with the magnetic bottle. Second, $\Delta\widetilde{\omega}_z$ is independent of the magnetic field (since $\omega_m \sim B^{-1}$), except insofar as the magnetic field may affect the size of B_2. Finally, $\Delta\widetilde{\omega}_z$ is inversely

proportional to the mass of the trapped particle. This makes it very difficult to use magnetic bottles in the same way with particles more massive than the electron.

The preceding results and more details are obtained by evaluating the consequences of $\Delta\mathbf{B}$ using first-order perturbation theory. The vector potential for the homogeneous magnetic field is modified by the addition of

$$\Delta\mathbf{A} = \tfrac{1}{2}B_2(z^2-\rho^2/4)\hat{B}\times\boldsymbol{\rho} \ , \tag{6.5}$$

which must be included in the perturbation Hamiltonian

$$\Delta H = -\frac{ge\hbar}{4mc}\boldsymbol{\sigma}\cdot\Delta\mathbf{B} - e\mathbf{v}/c\cdot\Delta\mathbf{A} \ , \tag{6.6}$$

where $\mathbf{v}$ is the velocity operator. Matrix elements

$$\Delta E(nkls) = \langle nkls \mid \Delta H \mid nkls \rangle$$

are most easily evaluated using the raising and lowering operators introduced in Sec. II.B. The result is that

$$\Delta E(nkls) = \hbar\Delta\widetilde{\omega}_z\left[\left[\left[k+\frac{1}{2}-\frac{\omega_z(n+l+1)}{2(\omega_c'-\omega_m)}\right]\right]\left[n+\frac{1}{2}+\frac{\omega_m}{\omega_c'}(l+\tfrac{1}{2})\right]\right.$$
$$\left.-\frac{\omega_z\omega_c}{2\omega_c'(\omega_c'-\omega_m)}[(n+\tfrac{1}{2})(l+\tfrac{1}{2})+\tfrac{1}{4}]+\frac{gs}{4}\frac{\omega_c'-\omega_m}{\omega_c'}\left[k+\frac{1}{2}-\frac{\omega_z}{\omega_c'-\omega_m}(n+l+1)\right]\right] \ . \tag{6.7}$$

Shifts in the eigenfrequencies that occur because the magnetic bottle is present can be obtained from this expression by evaluating the appropriate differences of the energy-level shifts. The axial frequency shift, for example, can be obtained by taking the difference of $\Delta E(n,k+1,l,s)$ and $\Delta E(n,k,l,s)$. This gives the earlier expression for the axial frequency shift in Eq. (6.3), except that there we used the very good approximation that $\omega_c'-\omega_m \approx \omega_c'$ [cf. Eq. (2.12)]. We shall return to such shifts in the eigenfrequencies in Sec. X, where we contrast the shifts produced by magnetic bottles with those due to electrostatic anharmonicity shifts and those due to relativistic corrections.

B. Laboratory bottles

The magnetic bottles that were central to the measurements of the electron and positron g values were realized by placing a small loop of ferromagnetic material in the xy plane of the Penning trap, centered on the z axis. The ferromagnetic materials saturate when strong magnetic fields are used ($B > 20$ kG). Iron and nickel, for example, have the saturation magnetizations, in cgs units, of

$$M(\mathrm{Fe}) = 1714 \tag{6.8}$$

and

$$M(\mathrm{Ni}) = 485 \ . \tag{6.9}$$

At the same time, the paramagnetism and diamagnetism of the trap electrodes themselves produce a magnetic bottle. Owing to the strong magnetic fields used, this intrin-

sic bottle has been as large as 20% of the deliberately introduced ferromagnetic bottle. The magnetizations of paramagnetic (>0) and diamagnetic (<0) materials are much smaller than those for iron and nickel, and they also vary with temperature. At $B = 60$ kG and $T = 4.2$ K, the magnetizations for the commonly used trap materials, copper, molybdenum, and MACOR are given by[19] (in cgs units)

$$M(\mathrm{Cu}) = -0.05 \ , \tag{6.10}$$

$$M(\mathrm{Mo}) = +0.96 \ , \tag{6.11}$$

and

$$M(\mathrm{MACOR}) = +0.78 \ . \tag{6.12}$$

To establish the relationship between the quantity and location of magnetic material near the center of a Penning trap and the magnetic bottle that is produced, we first examine the magnetic field produced by a thin ring of magnetic material, which is axially symmetric about the z axis, following Gabrielse and Dehmelt (1981b). This ring of uniformly distributed dipoles is characterized by a magnetization dipole moment per unit volume M, a radius ρ', and a small cross-sectional area $d\rho'dz'$. As shown

---

[19]The values for copper and molybdenum are from the *Handbook of Physics and Chemistry* (1983), and the MACOR value was measured by Thompson (1982).

in Fig. 24, the ring is located at r' and θ' in spherical coordinates, or equivalently at ρ',z' in cylindrical coordinates.

Because $\nabla \times \Delta \mathbf{B}=0$, the magnetic field perturbation can be written as the gradient of a scalar potential Ψ,

$$\Delta \mathbf{B}(\mathbf{r})=-\nabla \Psi(\mathbf{r}) \ , \tag{6.13}$$

and Ψ satisfies the Laplace equation since $\nabla \cdot \Delta \mathbf{B}=0$. On the z axis, the scalar potential for a dipole can be written as the derivative of the familiar potential of a monopole, so that

$$\Psi(z)=-M\,2\pi\rho'd\rho'dz'\frac{\partial}{\partial z}[\rho'^{\,2}+(z'-z)^2]^{-1/2} \ . \tag{6.14}$$

To obtain the magnetostatic potential near the center of the trap (but not necessarily on the z axis), we expand Eq. (6.14) in powers of z and identify the coefficients B_l of the general multipole expansion

$$\Psi(\mathbf{r})=-\sum_{l=1}^{\infty} l^{-1}B_{l-1}r^l P_l(\cos\theta) \ . \tag{6.15}$$

This is an easy task, since the inverse square root in Eq. (6.14) is the generating function for $P_l(\cos\theta)$. We now include an integration over rings that represent the actual axially symmetric magnetic material in the trap, to obtain the general formula

$$B_l=(l+1)(l+2)2\pi \int \rho'd\rho'dz'M(\rho',z')(r')^{-l-3}$$
$$\times P_{l+2}(\cos\theta') \ . \tag{6.16}$$

The integrand decreases very rapidly with increasing distance from the center of the trap, r'. Only magnetic materials that are close to the center of the trap will contribute appreciably to $\Delta \mathbf{B}$.

A little calculation using familiar relations among Legendre polynomials shows that the gradient of the multipole expansion for $\Psi(\mathbf{r})$ given in Eq. (6.15) produces the magnetic field perturbation

$$\Delta \mathbf{B}(\mathbf{r})=\sum_{l=0}^{\infty} B_l r^l[P_l(\cos\theta)\hat{z}-(l+1)^{-1}P_l^1(\cos\theta)\hat{\rho}] \ , \tag{6.17}$$

where $P_l^1(\cos\theta)=\sin\theta\,dP_l(\cos\theta)/d\cos\theta$ is an associated Legendre polynomial. The leading term in the multipole expansion is a constant magnetic field, $\Delta \mathbf{B}=B_0\hat{z}$, which adds to the basic homogeneous magnetic field. The magnetic material in the trap is usually symmetric under the reflection $z\rightarrow -z$ in addition to being axially symmetric. In this case, the next term in the multipole expansion (the dipole term with $l=1$) vanishes, and the leading nonuniform field perturbation is the quadrupole field of a magnetic bottle, exactly as in Eq. (6.1) because of our normalization.

Experimental advantage can be taken of the symmetry of the integrand. In particular, magnetic material placed on the quadrupole asymptote where $P_2(\cos\theta')$ of Eq. (6.16) vanishes will not shift the homogeneous magnetic field. Similarly, magnetic material placed at the zeros of $P_4(\cos\theta')$, at $\theta' \approx 30°$ and $\theta' \approx 71°$, will produce no magnetic bottle. Moreover, since the signs of $P_2(\cos\theta')$ and $P_4(\cos\theta')$ change at their zeros, the effect of magnetic material in producing either B_0 or B_2 can be cancelled by placing additional magnetic material in the region where the sign of the appropriate Legendre polynomial is opposite. Figure 25 shows the zeros of $P_4(\cos\theta')$ superimposed upon a representation of the Penning trap of Fig. 1. Both the ring and endcap electrodes are located primarily in a region where $P_4(\cos\theta')>0$, and the possible

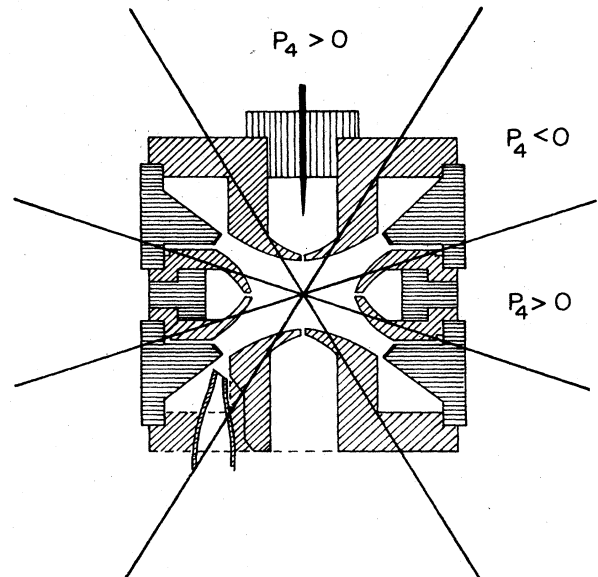FIG. 24. Coordinates for a little ring of magnetization.

FIG. 25. The zeros of $P_4(\cos\theta')$ superimposed over the Penning trap of Fig. 1.

paramagnetism of these electrodes therefore contributes to a magnetic bottle with $B_2 > 0$. This residual bottle could be cancelled by placing additional ferromagnetic material in the asymptotic region where $P_4(\cos\theta') < 0$.

Let us consider several numerical examples. First, a nickel ring of radius $\rho' = 0.55$ cm and cross-sectional area 2.0×10^{-3} cm^2 was included in the electron trap reported by Van Dyck, Schwinberg, and Dehmelt (1978), giving $B_0 = 20$ G and $B_2 = 150$ G/cm^2, which in turn makes $\Delta\tilde{\omega}_z/2\pi \approx 1$ Hz. Paramagnetic contributions are much smaller. Numerically integrating over the endcap and ring electrodes of the trap represented in Fig. 1, for example, yields $B_2/M \approx -30$/cm^2. For molybdenum quadrupole electrodes at 4.2 K in a magnetic field of 60 kG, this means that $B_2 \approx -29$ G/cm^2 and thus that $\Delta\tilde{\omega}_z/2\pi \approx 0.2$ Hz. While this is somewhat smaller than the $\Delta\tilde{\omega}_z/2\pi \approx 1$ Hz for the nickel rings, it is still much larger than the analogous relativistic coupling discussed in Sec. VII, for which $\Delta\tilde{\omega}_z/2\pi \approx 0.05$ Hz. Such a large intrinsic magnetic bottle would have masked the relativistic couplings that have been observed (Gabrielse, Kalinowsky, and Kells, 1985). While the intrinsic bottle could be canceled with additional magnetic material, as outlined above, it is cleaner and simpler to use copper quadrupole electrodes instead, since copper is diamagnetic with a small magnetization. The trap represented in Fig. 1 is made of copper.

C. Line profiles

In Sec. V we presented the general framework for the line shape brought about by small fluctuations in the large uniform magnetic field B. The random, Brownian motion of the axial oscillation of the charged particle in the magnetic bottle field described by Eq. (6.1) causes such fluctuations. Thus a spin, cyclotron, or anomaly frequency, which we denote generically by ω_0, is modified by the fluctuating variable $z(t)$ to become

$$\omega(z) = \omega_0(1 + \varepsilon z^2) . \tag{6.18}$$

With the typical values $B_2 = 150$ G/cm^2 and $B = 51$ kG for the recent experiments utilizing the bottle, we see that $\varepsilon = B_2/B \simeq 0.003$/cm^2. The fluctuating axial motion $z(t)$ has been explained in some detail in Sec. III.B. Here we recall that the harmonic axial motion of the electron of mass m and frequency ω_z is coupled to an external circuit, and thus put into thermal equilibrium at temperature T. Hence the axial motion fluctuates, with the equipartition of energy giving

$$\tfrac{1}{2}m\omega_z^2\langle z^2\rangle = \tfrac{1}{2}k_B T , \tag{6.19}$$

and a linewidth parameter

$$\Delta\omega = \omega_0\varepsilon\langle z^2\rangle . \tag{6.20}$$

Using the value $\langle z^2\rangle \approx 9 \times 10^{-6}$ cm^2 from Table III and $\varepsilon \simeq 0.003$/cm^2, one has $\Delta\omega/\omega_0 \simeq 10 \times 10^{-9}$. In view of the precision of 4×10^{-9} of the recent experiments (Van Dyck, Schwinberg, and Dehmelt, 1984), we see that the linewidth is a significant effect, which must be under-

stood if use is to be made of this precision.

According to the development of Sec. V, the line profiles in geonium are described by the Fourier transform

$$\chi(\omega) = \int \frac{dt}{2\pi} e^{i\omega t}\tilde{\chi}(t) \tag{6.21}$$

of the correlation function

$$\tilde{\chi}(t) = e^{-i\omega_0 t}\left\langle \exp\left[-i\omega_0\varepsilon\int_0^t dt' z(t')^2\right]\right\rangle . \tag{6.22}$$

As described in Sec. III.B, the axial motion $z(t)$ is basically harmonic, but it is also coupled to an external circuit at temperature T. Since the atomic processes in the external circuit are very fast in comparison with the basic harmonic motion, this thermal bath drives the oscillator with a force that is uniformly distributed in frequency ("white noise"). Thus there are only two parameters in our problem:[20] The axial damping constant[21] γ_z and the temperature T or, equivalently, in view of Eqs. (6.19) and (6.20), the linewidth parameter $\Delta\omega$.

Although the line profile $\chi(\omega)$ is not a simple function for general values of the parameters $\Delta\omega$ and γ_z, it is simple in the two limits.

(i) The axial motion $z(t)$ is loosely coupled to the thermal bath, $\gamma_z \ll \Delta\omega$. In this case, the amplitude of $z(t)$ remains constant during the time $\sim 1/\Delta\omega$ required to establish the frequency ω. On the other hand, $\omega_z \gg \Delta\omega$, and so $z(t)^2$ may be replaced by its average over an oscillator cycle,

$$z(t)^2 \to \bar{z}^2 = \frac{E}{m\omega_z^2} , \tag{6.23}$$

where E is the total energy of the axial oscillation. This amplitude remains constant over the time required to perform a single, idealized experimental "run." The line profile is obtained by averaging over a large number of such "runs," with the axial motion allowed to come into thermal equilibrium between the "runs." Thus the line profile is given by a sharp δ function averaged over the Boltzmann distribution of axial energies,[22]

$$\chi(\omega) = \int_0^\infty dE\, \delta\left[\omega - \omega_0\left[1 + \frac{\varepsilon E}{m\omega_z^2}\right]\right]k_B T e^{-E/k_b T}$$

$$= \frac{\theta(\omega - \omega_0)}{\Delta\omega}\exp\left[-\frac{\omega - \omega_0}{\Delta\omega}\right] . \tag{6.24}$$

Here we have used Eqs. (6.19) and (6.20) to identify $\Delta\omega$,

---

[20]The axial frequency ω_z is another parameter that could possibly enter into the line profile. However, as shown in Brown (1985), it gives modifications on the orders $(\gamma_z/\Delta\omega_z)^2$ and $(\Delta\omega/\omega_z)^2$, which are very small. There are also sidebands at $\omega_0 \pm 4\omega_z, \ldots$, but these are far away and small in amplitude.

[21]It follows from Eqs. (3.47) and (3.26) that $1/\gamma_z$ is also the noise correlation time used in Sec. V.

[22]This line shape was presented in Dehmelt (1981).

and $\theta(x)$ is the step function $\theta(x)=0$ for $x<0$, $\theta(x)=1$ for $x>0$. Thus there is no response below $\omega=\omega_0$. The response jumps discontinuously as ω passes ω_0 and then decreases exponentially with increasing ω.

(ii) The axial motion $z(t)$ is tightly coupled to the thermal bath, $\gamma_z \gg \Delta\omega$. In this case $z(t)^2$ relaxes quickly to its average value, and Eq. (6.22) becomes

$$\widetilde{\chi}(t)=\exp[-i\omega_0(1+\varepsilon\langle z^2\rangle)t] . \tag{6.25}$$

This gives a sharp but displaced line,

$$\chi(\omega)=\delta(\omega-\omega_0-\Delta\omega) . \tag{6.26}$$

As we shall show below, this limiting distribution is approached through a sequence of Lorentzian profiles of the form

$$\chi(\omega)=\frac{\Delta\omega^2/\pi\gamma_z}{(\omega-\omega_0-\Delta\omega)^2+(\Delta\omega^2/\gamma_z)^2} . \tag{6.27}$$

To obtain the form of the line shape that interpolates between the limits (6.24) and (6.27), use must be made of the general formulation of the Brownian motion of the axial oscillation given in Sec. III.B, particularly Eqs. (3.46), (3.47), and (3.26). Since this entails considerable mathematical calculation, which is presented in detail elsewhere (Brown, 1985), we shall simply state the method and the result. The statistical average displayed previously in Eqs. (3.46) and (3.47) may be expressed as a functional or path integral. The path-integral representation of the correlation function (6.22) produces a Fredholm determinant, which is related to the Green's function of a simple quantum-mechanics problem, the scattering on a square barrier. Thus the infinite determinant can be evaluated with the result

$$\widetilde{\chi}(t)= \begin{cases} e^{-i\omega_0 t}/F(t), & t>0 \\ e^{-i\omega_0 t}/F(-t)^*, & t<0 , \end{cases} \tag{6.28}$$

where

$$F(t)=\frac{1}{4\gamma'\gamma_z}[\,(\gamma'+\gamma_z)^2 e^{(\gamma'-\gamma_z)t/2} \\ -(\gamma'-\gamma_z)^2 e^{-(\gamma'+\gamma_z)t/2}] , \tag{6.29}$$

with

$$\gamma'=(\gamma_z^2+4i\gamma_z\Delta\omega)^{1/2} . \tag{6.30}$$

Let us first note that this result reproduces the previous limits.

(i) With $\gamma_z \ll \Delta\omega$, we may take the limit $\gamma_z \to 0$ to obtain

$$\widetilde{\chi}(t)=\frac{e^{-i\omega_0 t}}{1+i\Delta\omega t} . \tag{6.31}$$

The Fourier transform (6.21) of Eq. (6.31) produces the limit (6.24).

(ii) With $\gamma_z \gg \Delta\omega$ we have

$$\widetilde{\chi}(t)=e^{-(\Delta\omega^2/\gamma_z)|t|}e^{-i(\omega_0+\Delta\omega)t} , \tag{6.32}$$

whose Fourier transform produces the limiting form (6.27).

The line profile for arbitrary values of $\gamma_z/\Delta\omega$ is given by the Fourier transform (6.21) of the correlation function (6.28). Expanding out the denominator and then performing the time integration, one finds that
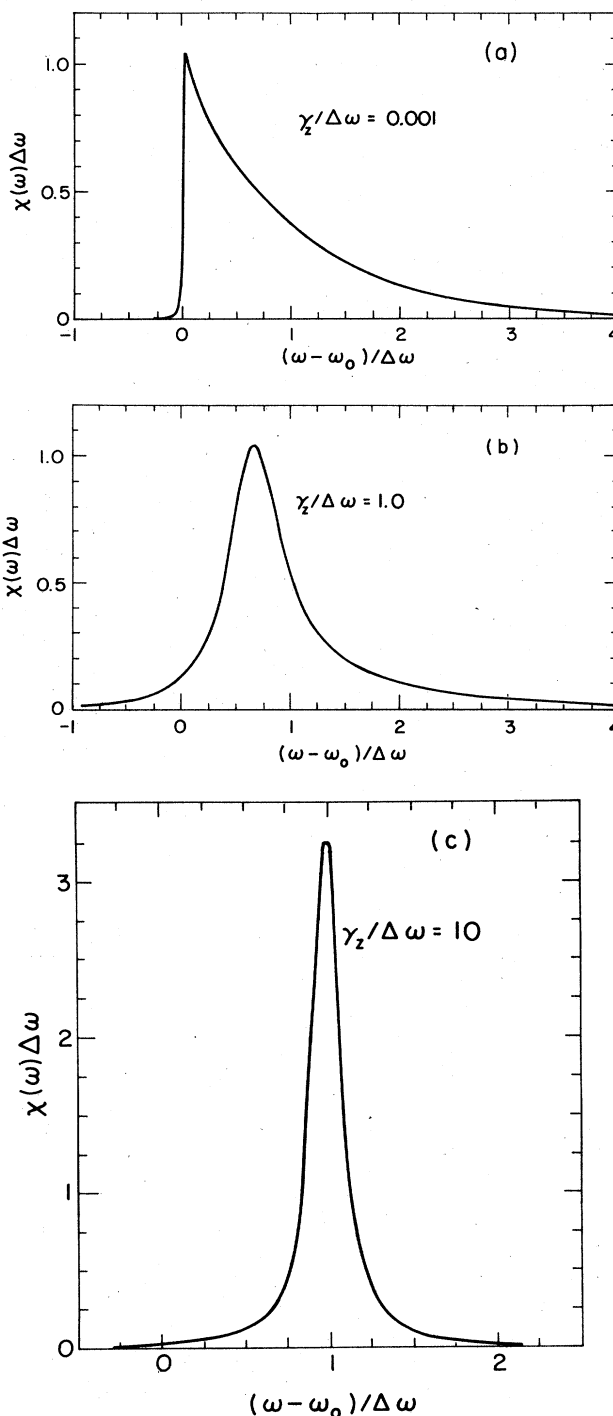

FIG. 26. Line profiles for various values of $\gamma_z/\Delta\omega$.

$$\chi(\omega) = \frac{4}{\pi} \, \mathrm{Re} \, \frac{\gamma' \gamma_z}{(\gamma' + \gamma_z)^2}$$

$$\times \sum_{n=0}^{\infty} \frac{(\gamma' - \gamma_z)^{2n}(\gamma' - \gamma_z)^{-2n}}{(n + \frac{1}{2})\gamma' - \frac{1}{2}\gamma_z - i(\omega - \omega_0)} \, , \qquad (6.33)$$

where Re denotes the real part. This general result is displayed in Fig. 26 for a wide range in the ratio $\gamma_z / \Delta\omega$. The curve for $\gamma_z / \Delta\omega = 0.001$ is very close to the limit (6.24), and the curve for $\gamma_z / \Delta\omega = 10$ is very close to the limit (6.27).

The cyclotron resonance is measured by driving it with various frequencies ω for a fixed time interval and then turning off the drive and measuring the cyclotron magnetic moment at a time T later. The moment is determined by the technique discussed in Sec. VI.A. The moment is proportional to the energy in the cyclotron motion. As discussed in Sec. V.B, this excitation energy is in turn proportional to the line profile function, with Eq. (5.38) giving

$$E_c(T) = \frac{\pi e^2 \mathscr{E}_0^2}{m \gamma_c'} e^{-\gamma_c T} \chi_C(\omega) \, . \qquad (6.34)$$

Here $\mathscr{E}_0$ is the amplitude of the drive field, γ_c the cyclotron decay constant, and $1/\gamma_c'$ a time interval over which the drive is effective. The line profile function $\chi_C(\omega)$ is obtained by replacing the generic ω_0 by the (trap modified) cyclotron frequency ω_c'. Since $\nu_c' \approx 150$ GHz and the linewidth is about a part in 10^8, we have $\Delta\omega_c \approx 1 \times 10^4$ sec^{-1}, which is much larger than (Table III) $\gamma_z \simeq 40$ sec^{-1}. Hence the limit (6.24) applies to this transition. Figure 27 shows a typical experimental measurement of the cyclotron line profile. Note that the cyclotron frequency is determined by the sharp left-hand edge of the profile, and no fitting to the line is yet required.

The nature of the anomaly resonance was discussed at some length in Sec. V.C. An anomaly drive at various frequencies ω is applied for a fixed time interval T_d, and then spin is measured by the bottle shift of the axial fre-
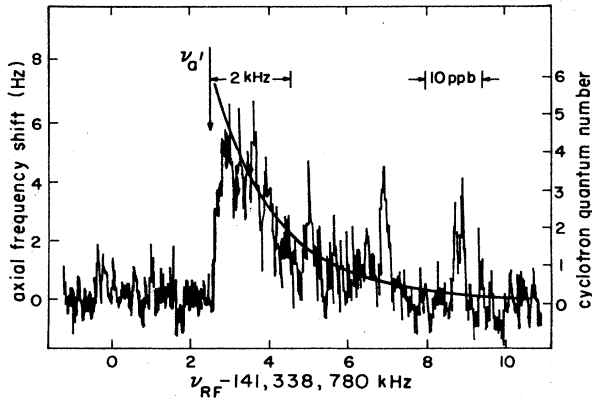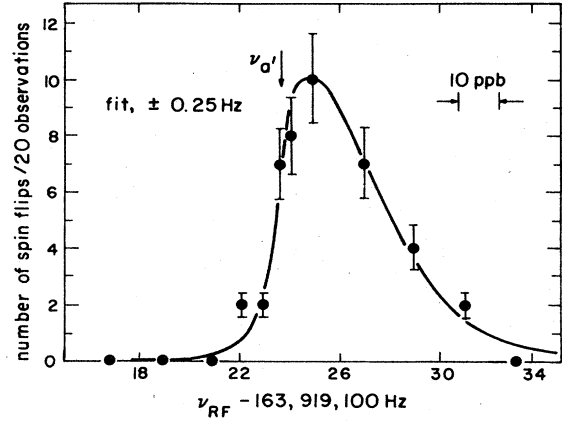

FIG. 28. Experimental anomaly resonance that is not saturated. The solid curve is a fit to the line profile function (6.33) (Van Dyck, Schwinberg, and Dehmelt, 1984).

quency. According to Eq. (5.63), the probability that the spin is flipped is given by

$$P = \frac{1}{2} \{ 1 - \exp[-\pi \Omega_a^2 T_d \chi_A(\omega)] \} \, . \qquad (6.35)$$

Here Ω_a is an effective Rabi frequency, which involves the product of the average cyclotron excitation energy and the square of the amplitude of the anomaly drive. The line profile function $\chi_A(\omega)$ is obtained by replacing the generic ω_0 with the (trap modified) anomaly frequency ω_a'. Since $\omega_a' \approx 10^{-3} \omega_c'$, we now have $\gamma_z / \Delta\omega \approx 4$. We see that a precise determination of the anomaly frequency already requires a fitting to a general line profile function, whose shape is approximately that in Fig. 26(b), which corresponds to $\gamma_z / \Delta\omega = 1$. A recent experimental fit to the anomaly line profile is shown in Fig. 28. For this run,

FIG. 27. Experimental cyclotron resonance. The solid curve is that given by Eq. (6.24) (Van Dyck, Schwinberg, and Dehmelt, 1984).
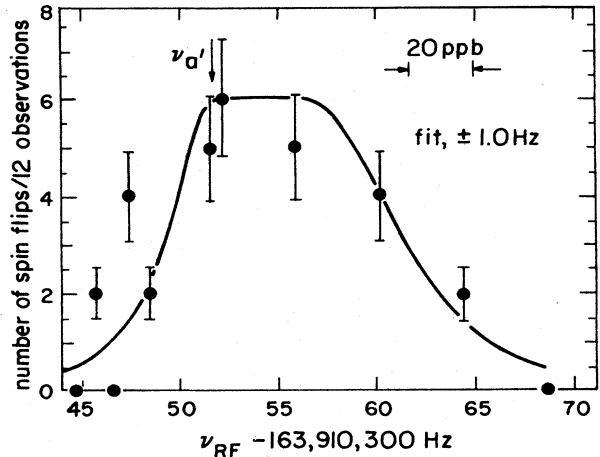

FIG. 29. Experimental anomaly resonance that is saturated. The solid curve is a fit to the line profile function (6.33), including the exponentiation given in Eq. (6.35). The g value determined from this fit and a simultaneous measurement of the cyclotron frequency is consistent with that deduced from the run shown in Fig. 28 (Van Dyck, Schwinberg, and Dehmelt, 1984).

the transition has not been saturated, the exponential in Eq. (6.35) can be expanded to first order, and the probability is proportional to $X_A(\omega)$. Figure 29 shows an experimental anomaly resonance at higher drive power, resulting in a strong saturation on the peak. In this case, the full exponential form of Eq. (6.35) must be employed to describe the resonance. Fitting such saturated anomaly resonances to the exponentiated form removes a previous systematic power shift in the anomaly frequency (Van Dyck, Schwinberg, and Dehmelt, 1984).

Finally, we should note that the axial drive should be removed during cyclotron or anomaly excitation. With the drive on, the lines are broadened and shifted, although the sharp leading edge of the cyclotron profile remains. Since in the experiments the axial drive is removed during these excitations, we shall not give the details of the shifts and broadening here. An account of these effects does appear in the literature (Brown, 1985).

D. Variable bottle

We have just seen that currently the magnetic bottle is crucial for detecting spin and cyclotron transitions, but that it does introduce an unwanted linewidth. Although the line shape has been calculated, the experiments would be improved if the line were narrowed, avoiding the line splitting. The purpose of this section is to examine the possibility of substituting a current-carrying loop for the ring of magnetic material, to produce a bottle that could be switched on and off. Transitions could be induced in the purely homogeneous field with the current off, and take place with no bottle-generated linewidth. The transitions could then be detected by turning the current on and measuring the axial frequency change in the resulting bottle field.[23] We shall first consider the bottle produced by a simple current loop, and then examine the desirability of using a superconducting loop with current induced in it by a flux transformer (Schwinberg, Van Dyck, and Dehmelt, 1979). Finally we discuss an improved two-loop variation suggested and demonstrated by Van Dyck, Moore, Farnham, and Schwinberg (1986).

A magnetic bottle can be made in principle by sending a current I_t through a loop, which is a circle of radius R_t about the center of the trap in the xy symmetry plane. The magnetic vector potential $\mathbf{A}$ produced by this loop can be expressed in terms of the complete elliptic integrals K and E [see, for example, Jackson (1975), Sec. 5.5]. By virtue of the cylindrical symmetry, the vector potential points in the azimuthal direction $\hat{\varphi}$, and using cylindrical coordinates one has

$$\mathbf{A} = A_\varphi(\rho, z)\hat{z} \times \hat{\rho},\tag{6.36}$$

where

$$A_\varphi(\rho, z) = \frac{4I_t R_t}{c(R_t^2 + z^2 + \rho^2 + 2R_t\rho)^{1/2}} \times \left[\frac{(2-k^2)K(k) - 2E(k)}{k^2} \right],\tag{6.37}$$

with

$$k^2 = \frac{4R_t\rho}{R_t^2 + z^2 + \rho^2 + 2R_t\rho}.\tag{6.38}$$

Near the center of the trap, the loop produces a magnetic field given by

$$\mathbf{\Delta B} = \mathbf{\nabla} \times \mathbf{A}$$
$$= \Delta B_0 \hat{z} + B_2[(z^2 - \rho^2)\hat{z} - z\rho].\tag{6.39}$$

The change in the uniform field is given by

$$\Delta B_0 = \frac{2\pi I_t}{cR_t},\tag{6.40}$$

in terms of which the bottle coefficient may be written as

$$B_2 = -\frac{3\Delta B_0}{2R_t^2}.\tag{6.41}$$

To obtain $B_2 \approx 150$ G/cm^2 with a typical trap dimension $R_t = 1.0$ cm, we see that $\Delta B_0 \approx 100$ G, which requires that $I_t \approx 20$ A turns. Even for a coil of many turns, there are large experimental difficulties involved in transporting such a current down into a helium Dewar and into the vacuum enclosure of a trap. In particular, a large current could entail unacceptably large resistive heat losses into the helium bath. But this difficulty is largely circumvented if the current loop is a closed superconducting loop, with the current induced by a flux transformer.

To see how this works, we first need to recall a general theorem about closed superconducting circuits in magnetic fields: The magnetic flux through any surface bounded by the circuit cannot be changed. To prove this theorem one integrates the Maxwell equation

$$\frac{\partial \mathbf{B}}{\partial t} = -c\mathbf{\nabla} \times \mathbf{E}\tag{6.42}$$

over such a surface and uses Stokes's formula to obtain

$$\frac{d\Phi}{dt} = \frac{d}{dt}\int d\mathbf{S}\cdot\mathbf{B}$$
$$= -c\oint d\mathbf{l}\cdot\mathbf{E},\tag{6.43}$$

where the line integral runs over the complete circuit with the contour running on and parallel to the surface of the superconducting wire. Since the electric field vanishes within the superconductor and the tangential electric field is continuous across the surface of any conductor, the line integral vanishes. Thus if an external magnetic field is applied to a closed superconducting circuit, a super-

---

[23]Alternatively, it may be possible to put an oscillating current in the coil, modulating the bottle and thereby also modulating the detected shift in the axial frequency (Schwinberg and Van Dyck, 1981). Narrow-band detection techniques could thus be used to minimize the effect of the noise and the effect of trapping potential variations that change the axial frequency.

current is induced that gives rise to an additional magnetic field, which precisely cancels the applied flux, giving no change in the total flux:[24]

$$\Delta\Phi = 0 . \tag{6.44}$$

Since the topology of the surface can be complex, it is often conceptually convenient to write the change in the magnetic field in terms of the change in a vector potential and once again use the Stokes formula to write the condition as

$$\oint dl \cdot \Delta \mathbf{A} = 0 , \tag{6.45}$$

where again the line integral runs over the closed circuit just outside the surface of the wire. This line-integral formulation is also of practical utility, since it involves a simple one-dimensional integral rather than a two-dimensional surface integral.

We can now see how the superconducting flux transformer operates. The system is warm and not superconducting when it is inserted into the large main magnetic field $\mathbf{B}$. Hence at this stage there is no induced supercurrent. The loop is then cooled and made superconducting. A current I_s is induced in the small superconducting loop of radius R by applying an additional magnetic field $\Delta B_0^{(ext)}$. This field could be produced, for example, by a solenoid outside the trap that is not superconducting. To compute the current I_s, we recall that Eq. (6.37) gives the vector potential for a circular loop of wire of infinitesimal thickness. Evaluating this expression at a distance a from the infinitesimal wire gives an approximation for the vector potential at the surface of a finite wire of radius a. If the wire were straight, this would, by symmetry and Ampere's law, be exact. Hence this approximation entails an error of order a/R. Since a/R is quite small, this is a good approximation. Using Eq. (6.37) one finds in this way that the vector potential on the surface of the superconducting wire due to the superconducting current itself is given by

$$A_\varphi^{(S)} = \frac{2I_s}{c} \left[\ln\left[\frac{8R}{a}\right] - 2 \right] . \tag{6.46}$$

The supercurrent I_s is determined by inserting this in the flux cancellation condition (6.45) along with the field produced by the solenoid. For simplicity, let us assume that the field produced by the solenoid is a uniform field $\Delta B_0^{(ext)}$, reducing the flux cancellation condition to

$$2\pi R A_\varphi^{(S)} + \pi R^2 \Delta B_0^{(ext)} = 0 . \tag{6.47}$$

Using Eq. (6.46), this determines the supercurrent I_s; then Eqs. (6.40) and (6.41) give the alteration in the uniform and bottle fields at the center of the trap caused by the supercurrent loop:

$$\Delta B_0^{(S)} = -\frac{\pi\Delta B_0^{(ext)}/2}{\ln(8R/a) - 2} , \tag{6.48}$$

and

$$B_2^{(S)} = -\frac{3\Delta B_0^{(S)}}{2R^2} . \tag{6.49}$$

Taking a typical value $a/R \sim \frac{1}{30}$, we have $\Delta B_0^{(S)} \approx -\Delta B_0^{(ext)}/2$ and $B_2^{(S)}/B_2^{(ext)} \approx -\frac{1}{2}(R_t/R)^2$. We see that with a radii ratio $R_t/R \approx 10$, the bottle field is increased by about a factor of 50 with a corresponding reduction in the current needed to drive the solenoid.

Although the presence of the superconducting loop does cancel about half of the uniform component of the applied field, there does remain a change in the field, about 2 G in comparison to the main magnetic field of about 50 kg—an effect of order 4×10^{-5}. This might not be too serious if both the spin and cyclotron transitions were made with the bottle turned off and then measured with the bottle turned on. But the cyclotron decay time is too short for this to be done with the cyclotron resonance, and it must be measured in the presence of the bottle. Thus one needs a coil arrangement that does not alter the uniform component B_0 when it is switched on. This can be done by having two concentric superconducting rings of radii $R_1 < R_2$ connected so as to have a common current in both rings, flowing in the same direction, as shown in Fig. 30 (Van Dyck, Moore, Farnham, and Schwinberg, 1986). Because of the $1/R^3$ dependence of
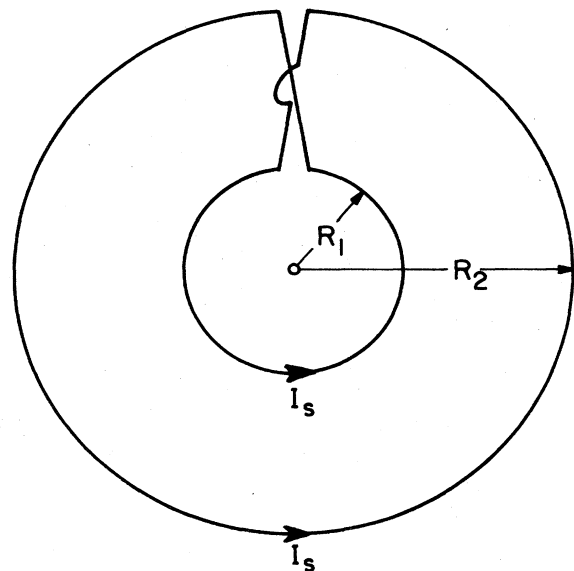

FIG. 30. Two-loop superconductor scheme of Van Dyck, Moore, Farnham, and Schwinberg (1986). With the "magic" ratio of R_2/R_1 (which depends on the wire radius a), switching on a perpendicular uniform magnetic field does not change the value of the magnetic field at the center, but it does induce a bottle field. (We assume that the wires connecting the two loops are close together in comparison with their radius, so that their effects can be neglected.)

the bottle strength, the additional outside loop of radius R_2 has little effect on the bottle. On the other hand, it can add a sufficient uniform field component so that both loops together now cancel the externally applied field at the center of the trap. Again for simplicity let us assume that an external uniform field change $\Delta B_0^{(ext)}$ is imposed upon this configuration, say by a pair of Helmholtz coils outside the trap. The supercurrent I_s is determined by the no-flux-change condition (6.45), but this supercurrent I_s can be varied by varying the radii ratio R_1/R_2. Thus a radii ratio can be found such that the uniform field pro-

duced by the superconducting loops precisely cancels the applied uniform field,

$$\frac{2\pi I_s}{c}\left[\frac{1}{R_1}+\frac{1}{R_2}\right]=-B_0^{(ext)} , \tag{6.50}$$

while maintaining the no-flux-change condition. Using Eqs. (6.50) and (6.37) for the vector potentials produced by the superconducting loops, one finds that the no-flux-change condition (6.45) may be expressed as

$$2\left[\frac{R_1^2+R_2^2}{R_1+R_2}K(k)-(R_1+R_2)E(k)\right]+R_1\left[\ln\left[\frac{8R_1}{a}\right]-2\right]-R_2\left[\ln\left[\frac{8R_2}{a}\right]-2\right]=\frac{\pi}{2}\left[\frac{1}{R_1}+\frac{1}{R_2}\right](R_1^2+R_2^2) , \tag{6.51}$$

where

$$k^2=\frac{4R_1R_2}{(R_1+R_2)^2} . \tag{6.52}$$

Equation (6.51) determines the radii ratio R_2/R_1 as a function of, say, the ratio of the wire radius to the radius of the inner loop, a/R_1. The result is plotted in Fig. 31. For example, with $a/R_1=\frac{1}{30}$, we have the "magic" ratio $R_2/R_1=2.58$.

Some final comments need to be made. First of all, even if there were no need for a variable magnetic bottle, the introduction of the two-loop superconducting configuration with the "magic ratio" into the trap is still useful, since it keeps the magnetic field at the center of the trap stable, even though the main magnetic field may be changing slightly. Second, we should emphasize that the present experimental precession requires that the cyclotron frequency be measured to an accuracy better than a few parts in 10^9. This requires a corresponding stability in the magnetic field. As discussed at the beginning of the previous paragraph, a single superconducting loop

gives rise to a field change (when the bottle is turned on and off) on the order of a few parts in 10^5. Allowing for the error in the theoretical calculation of order a/R and for errors in construction, even if the theory were improved, an actual double-loop system gives a residual field change on the order of 10^{-7}. This is much too large to be acceptable. However this residual field change can be tuned out by the addition of a circular trim coil in the symmetry plane of the trap (Van Dyck, Moore, Farnham, and Schwinberg, 1986). Such a coil, with a radius R_t not too much larger than R_2, does not produce a uniform magnetic field over the double-loop superconducting arrangement. Hence its contribution to the central field B_0 will not be cancelled by loops with the "magic" R_2/R_1 ratio. The proper current I_t in the trim coil can be determined by making it a constant fraction of the current I_d in the "Helmholtz" coils that drive the bottle, $I_t=\lambda I_d$, with the constant of proportionality λ set by the condition that the observed cyclotron frequency not change when the drive current I_d is varied. Finally, we note that the actual effect of such a trim coil can be computed by the use of Eq. (6.37) for the vector potential of a single loop. Moreover, this formula may also be used to calculate more accurately the effect of nonideal "Helmholtz" and trim coils by representing these coils as a sum of loops.
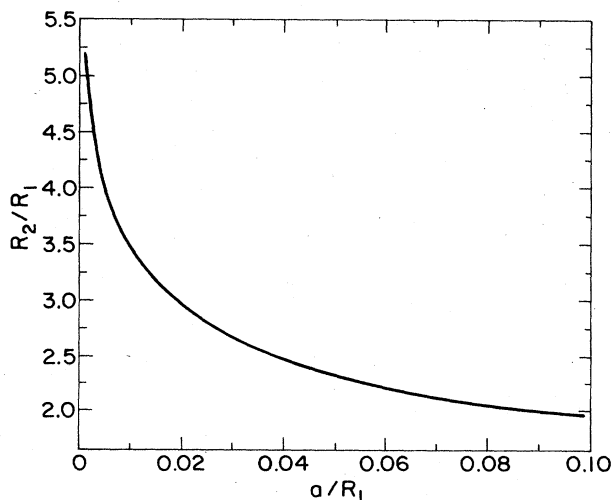
VII. RELATIVISTIC EFFECTS

Our discussion of the motion of a particle in a Penning trap has so far been nonrelativistic. We now examine the modifications to the motions that are due to special relativity. The relativistic effects are extremely small because $(v/c)^2$ is usually less than 10^{-6}. Nonetheless, the high precision being achieved with a single trapped electron has made it possible to observe relativistic couplings between the cyclotron and axial motions (Gabrielse and Dehmelt, 1981a) and to observe a resulting bistability and hysteresis in the cyclotron motion (Gabrielse, Dehmelt, and Kells, 1985). In fact, special relativity makes possible the best signal-to-noise ratio ever observed with a trapped particle. We review the theory of these experiments in Sec. VII.A. In Sec. VII.B we discuss the quantum-

FIG. 31. "Magic" ratio R_2/R_1 for the two-loop scheme as a function of the scaled wire radius a/R_1.

relativistic energy levels starting with the Dirac Hamiltonian. We obtain essentially the same results given by Gräff, Klempt, and Werth (1969). Relativistic shifts to the energy levels and eigenfrequencies must certainly be included in the analysis of present measurements of the magnetic moments of the electron and positron. (We contrast these shifts with the shifts due to other important perturbations in Sec. X.) We consider the related "Lamb shifts" in Sec. VII.C. These shifts are large, but all the energy levels shift together, giving no measurable shift in an eigenfrequency.

A. Nonlinear, relativistic cyclotron motion

The nature of an anharmonic axial resonance was discussed in Sec. III.D. As was explained there, even small nonlinear corrections can have substantial effects if the damping of the motion is very small—a periodic motion with very small "viscosity" can be significantly affected by small perturbations. This is dramatically evident in the cyclotron motion of an electron, which has a quality factor $Q_c = \omega_c / \gamma_c \approx 3 \times 10^{11}$ (Table I). In this case the nonlinearities in the motion arising from relativistic corrections even for $v^2/c^2 \approx 10^{-7}$ put the resonance curve well into the nonlinear regime. This possibility, which was under experimental investigation for several years, has now been very clearly demonstrated by Gabrielse, Dehmelt, and Kells (1985). While the experiments were in progress, the theory of such a nonlinear motion was discussed independently by Kaplan (1982). We review this effect here. A classical description is entirely adequate for the large excitation that has been observed.

Including relativistic corrections, the driven and damped cyclotron equation of motion is given by

$$\frac{d}{dt} \left[\frac{\mathbf{v}(t)}{(1 - v^2/c^2)^{1/2}} \right] = \omega_c' \hat{z} \times \mathbf{v}(t) - \frac{1}{2}\gamma_c \mathbf{v}(t) + \frac{e}{m} \mathscr{E}(t) .$$

(7.1)

Here the use of the modified cyclotron frequency ω_c' defined by Eq. (2.16) takes account, to sufficient accuracy, of the effect of the electrostatic quadrupole trapping potential. We also use the dipole approximation for the driving electric field $\mathscr{E}(t)$, which often has some rather complex form of polarization. However, as usual, we can write this field as a sum of co-rotating and counter-rotating components and neglect the counter-rotating component, since it is nonresonant. That is, there is no essential loss of generality in assuming that $\mathscr{E}(t)$ is co-rotating. We use complex coordinates where, for example, $v(t) = v_x(t) + iv_y(t)$, and assume that the drive is of high spectral purity, so that it may be represented by a single Fourier component,

$$\mathscr{E}(t) = \mathscr{E}_0 e^{i\omega t} .$$

(7.2)

The equation of motion (7.1) is now simplified by passing to a frame rotating at the drive angular frequency ω by

writing the four-velocity as

$$\frac{v(t)}{[1 - |v(t)|^2/c^2]^{1/2}} = u(t)e^{i\omega t} .$$

(7.3)

Since v^2/c^2 is very small, it suffices to solve for the $v(t)$ in terms of $u(t)$ only to second order in u^2/c^2, when the velocity appears multiplied by the large cyclotron frequency ω_c'. Thus, in the rotating frame, the equation of motion (7.1) can be written as

$$\dot{u}(t) + i\{\omega - \omega_c'[1 - \frac{1}{2}|u(t)|^2/c^2]\}u(t)$$

$$+ \frac{1}{2}\gamma_c u(t) = \frac{e}{m}\mathscr{E}_0 . \quad (7.4)$$

We are mainly interested in the steady-state solution where $\dot{u}(t) = 0$. In this case the cyclotron equation of motion (7.4) is identical in form to the nonlinear oscillator equation (3.73) of Sec. III.D. The only difference is that with a purely rotating drive, Eq. (7.4) entails no approximation (other than the neglect of higher orders in u^2/c^2), while Eq. (3.73) required the omission of higher overtones. Since the nonlinear cyclotron problem is essentially identical to the nonlinear oscillator problem that was discussed at some length in Sec. III.D, we shall give only a brief treatment here and refer the reader to Sec. III.D for further details. The maximum response is obtained at a drive frequency ω, which makes the curly brackets in Eq. (7.4) vanish, giving

$$|u_{\max}|^2 = \left[\frac{2e}{m\gamma_c}\right]^2 |\mathscr{E}_0|^2 .$$

(7.5)

It is convenient to scale the amplitude in the general case by this maximum amplitude, and to define

$$w = \frac{|u|^2}{|u_{\max}|^2} .$$

(7.6)

In terms of this variable, the absolute square of Eq. (7.4) [with, of course, $\dot{u}(t) = 0$] gives

$$w = \left[1 + 4\left[\frac{\omega - \omega_c'}{\gamma_c} - Nw\right]^2\right]^{-1} ,$$

(7.7)

where now

$$N = -\frac{1}{2}\left[\frac{\omega_c'}{\gamma_c}\right]\left[\frac{|u_{\max}|^2}{c^2}\right] .$$

(7.8)

Equation (7.7) is identical in form to Eq. (3.81), and thus the response curves for w are just as those given in Fig. 11, except that since N is negative they tilt to the left rather than to the right as $|N|$ increases. The onset of the triple-valued region appears at $N = -1$. As remarked in Sec. III.D, the portion of the resonance curve between the points labeled by A and B in[25] Fig. 32 is a region of unstable motion. This is simple to prove for the cyclotron

---

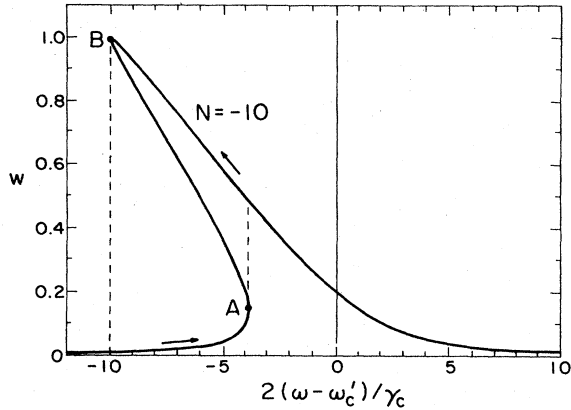[25]This figure is the mirror image of Fig. 12, since $N = -10$.

FIG. 32. Nonlinear, relativistic cyclotron resonance.

case. First we note that Eq. (7.7) is easily solved to give the frequency difference $\omega - \omega_c'$ as a function of normalized squared amplitude w:

$$\frac{\omega - \omega_c'}{\gamma_c} = Nw \pm \frac{1}{2} \left[\frac{1}{w} - 1 \right]^{1/2} . \tag{7.9}$$

(This is the easy way to plot the resonance curve; rotating the result by 90° and reflecting gives w vs $\omega - \omega_c'$.) The lower branch of the curve in the $w, \omega - \omega_c'$ plane corresponds to the minus root. Next we note that the slope of the curve as a function of w is given by

$$S = N \mp \frac{1}{4w^2} \left[\frac{1}{w} - 1 \right]^{-1/2} . \tag{7.10}$$

The points A and B are determined by setting $S = 0$ [corresponding to infinite slope in the w vs $(\omega - \omega_c')$ plot] and by solving this constraint simultaneously with Eq. (7.9). This is done with the plus sign in Eq. (7.10), which applies to the lower branch. The slope S is negative between the two roots given by A and B. We now study the small oscillations about the steady-state solution and show that they are unstable in this region of negative S between A and B.

To do this we write

$$u(t) = u + u_1(t) , \tag{7.11}$$

where u is the previous steady-state solution, and $u_1(t)$ is a small perturbation. Without any loss of generality, we may take u to be real with, in vector notation, $\mathbf{u}$ lying along the x axis. We insert the decomposition (7.11) into the equation of motion (7.4), keep only the first-order terms in $u_1(t)$, and identify real and imaginary parts corresponding to the x and y components. Writing the result in matrix form gives

$$\dot{U}_1(t) = (\Omega - \tfrac{1}{2}\gamma_c) U_1(t) , \tag{7.12}$$

where

$$U_1(t) = \begin{bmatrix} u_{1x} \\ u_{1y} \end{bmatrix} \tag{7.13}$$

and

$$\Omega = \begin{bmatrix} 0 & \omega - \omega_c'(1 - u^2/2c^2) \\ -[\omega - \omega_c'(1 - 3u^2/2c^2)] & 0 \end{bmatrix} . \tag{7.14}$$

The square of this matrix is proportional to the unit matrix, with

$$\Omega^2 = - [\omega - \omega_c'(1 - u^2/2c^2)]$$
$$\times [\omega - \omega_c'(1 - 3u^2/2c^2)] . \tag{7.15}$$

If Ω^2 is negative, the eigenvalues of Ω are imaginary, and Eq. (7.12) shows that the perturbations U_1 oscillate and damp in time. If Ω^2 is positive, there are two equal but oppositely signed real eigenvalues. With $\Omega^2 < \gamma_c^2/4$, the positive eigenvalue is less than γ_c, and each of the two solutions of Eq. (7.12) decay in time. However, for $\Omega^2 > \gamma_c^2/4$, the positive eigenvalue exceeds $\gamma_c/2$, and Eq. (7.12) has an unstable solution that increases exponentially with time. Using Eqs. (7.9) and (7.10) one finds that

$$\Omega^2 - \tfrac{1}{4}\gamma_c^2 = \pm \gamma_c^2 w \left[\frac{1}{w} - 1 \right]^{1/2} S . \tag{7.16}$$

Along the resonance curve between A and B, the negative root applies. Since S is negative in this region, the right-hand side of Eq. (7.16) is positive. We conclude that the cyclotron motion is unstable along the portion of the resonance curve between the points labeled by A and B.

Since the region between A and B is unstable, the cyclotron resonance exhibits hysteresis: Sweeping down in frequency, the amplitude follows the resonance curve until point B is reached, at which point the amplitude abruptly falls to the lower curve, as indicated by the dashed line in Fig. 32, and then continues along this curve as the drive frequency is further decreased. On the other hand, sweeping up in frequency, the amplitude follows the lower branch of the resonance curve until it reaches point A, at which point the amplitude jumps discontinuously to the upper branch, as indicated by the dashed line, and then continues along this branch as the drive frequency is further increased.

This hysteresis phenomenon has been very clearly demonstrated in an experiment (Gabrielse, Dehmelt, and Kells, 1985) from which the magnetic bottle was carefully eliminated. See Fig. 33. The method for measuring the level of the cyclotron excitation is itself novel, since it also relies on the effects of special relativity. The comparatively fast cyclotron motion gives an effective mass increase $m \rightarrow m(1 + v^2/2c^2)$, which alters the axial oscillation frequency ω_z. Since $\omega_z^2 \sim 1/m$, we have a change in this frequency given by

$$\Delta \omega_z = -\tfrac{1}{4}(v^2/c^2)\omega_z . \tag{7.17}$$

Changes of $\Delta \omega_z/2\pi = 1$ Hz out of $\omega_z/2\pi = 62$ MHz can be observed, so that cyclotron velocities with $v^2/c^2 \geq 7 \times 10^{-8}$ can be detected. This corresponds to a cyclotron energy of $E_c \geq 2 \times 10^{-2}$ eV. Since the
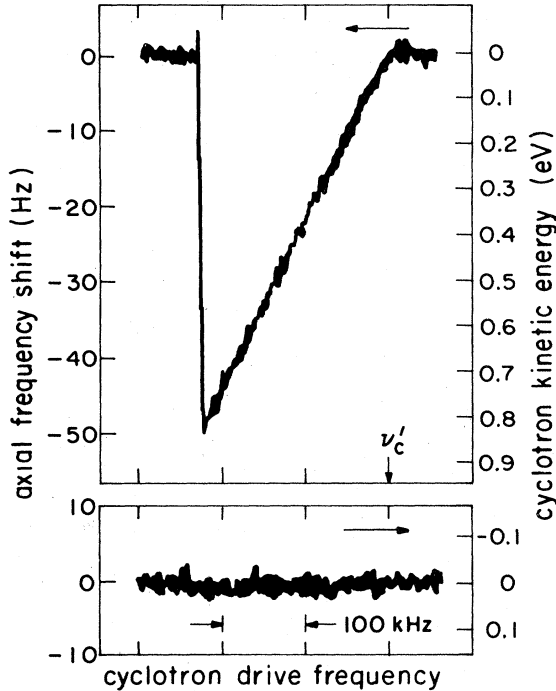
FIG. 33. Experimental observation of the relativistic cyclotron resonance (Gabrielse, Dehmelt, and Kells, 1985).

quantum-mechanical energy level spacing is given by $\hbar\omega_c \approx 7 \times 10^{-4}$ (Table I), we see that the cyclotron quantum number is large, $n \geq 30$, and that our classical treatment applies to this experiment. Moreover, the anharmonicity parameter is very large in magnitude $|N| \geq 1 \times 10^4$. Thus, in view of Eq. (7.7), the resonance curve for the most part is a narrow sheaf of thickness $\delta\omega \approx \gamma_c$ about the line[26] (cf. Fig. 14),

$$(\omega - \omega_c')/\gamma_c = Nw = -\omega_c'(v^2/c^2)/2\gamma_c . \qquad (7.18)$$

As shown in Fig. 33, only the upper branch of this narrow sheaf is observed, the branch that appears when the drive frequency is swept from high to low frequencies. The maximum observed axial frequency shift in Fig. 33, $\Delta\omega_z/2\pi \approx -50$ Hz, corresponds to $v_{max}^2/c^2 \approx 4 \times 10^{-6}$ and $E_c^{max} \approx 0.8$ eV, which gives $N \approx -5 \times 10^5$. Excitations as large as $E_c^{max} = 10$ eV have been observed.

---

[26]Comparing the slope of this line with that of the axial frequency shift given in Eq. (7.17) gives $[(\omega - \omega_c')/\omega_c']/[\Delta\omega_z/\omega_z] = 2$. A shim of the superconducting magnet is adjusted so that the observed ratio of slopes is within 0.5% of this factor of 2. Referring back to Eqs. (6.3) and (6.4), it is easy to find that the presence of a magnetic bottle would alter this ratio by the factor $[1 + (2c^2/\omega_z^2)(B_2/B)]$. Thus, for this experiment, $|B_2/B| \leq 5 \times 10^{-7}/\text{cm}^2$, which is about a factor of 5000 smaller than the bottle field discussed in Sec. VI.C.

The theory of the nonlinear, relativistic cyclotron resonance that we have presented is incomplete in two important aspects: We have neglected the effects both of quantum mechanics and of noise. We have treated the drive as a perfect, monochromatic force. In reality, the cyclotron drive does have a small, broad noise pedestal, which proves to be very important experimentally. Moreover, the cyclotron motion interacts with the 4-K blackbody radiation in the trap. Although these noise sources are quite small, they cannot be treated as first-order perturbations, since the basic motion is highly nonlinear. With regard to the quantum aspect, we noted in the previous paragraph that the cyclotron quantum number must be large, $n \geq 30$, for the resonance to be detected. Although a classical description is entirely adequate in this region, the excitation of the cyclotron motion starts in the quantum regime, since initially $n \approx 1$. Even for $n \approx 1$ the corresponding classical motion is highly nonlinear, since the anharmonicity parameter is large, $N \approx -300$. The relativistic, quantum-mechanical level structure is derived in the next section. Nonetheless, we do not have a detailed description of the initial stages of the anharmonic excitation. Such a detailed description is needed in order to understand fully the precise measurements of the cyclotron frequency that are necessary in experiments that do not employ a magnetic bottle. The two outstanding problems of noise and quantum effects are difficult problems that very much deserve further investigation.

B. Relativistic quantum mechanics

Although the effects of special relativity are exceedingly small for the slowly moving particle in a Penning trap, the geonium experiments are exceedingly precise, and as we have just seen, these effects are measurable. Moreover, it may be that the relativistic effects can be exploited so as to provide a measurement of the state of the particle, thereby dispensing with the magnetic bottle, which hinders the precision of the experiments. In this section we shall derive the quantum level structure of a particle in a Penning trap, starting with the full Dirac Hamiltonian and then performing a nonrelativistic reduction including also the $1/c^2$ corrections. We do this in some detail for two reasons. First, although the results we derive have been obtained previously by Gräff, Klempt, and Werth (1969), that paper contains a few misprints. Second, and more importantly, the relativistic motion of a spin is subtle and warrants a careful exposition. We shall show that the Foldy-Wouthuysen nonrelativistic reduction produces a Hamiltonian accurate to order $1/c^2$, which is identical to its classical counterpart if the spin operator is identified with the spin observed by performing a Lorentz transformation to the particle's rest frame.

The Dirac Hamiltonian for a charged particle with an anomaly $a = (g - 2)/2$ in a Penning trap has the form

$$H^D = \boldsymbol{\alpha} \cdot \boldsymbol{\Pi} c + \beta mc^2 + eA^0 - \frac{ea\hbar}{4mc}\beta\sigma^{\mu\nu}F_{\mu\nu} , \qquad (7.19)$$

in which

$$\mathbf{\Pi} = \frac{\hbar}{i}\nabla - \frac{e}{c}\mathbf{A} \qquad (7.20)$$

is the kinetic momentum operator and A^0 is the scalar potential. The Dirac matrices α_k and β are Hermitian and obey the rules

$$\{\alpha_k, \alpha_l\} = 2\delta_{kl} , \qquad (7.21\text{a})$$

$$\{\beta, \alpha_k\} = 0 , \qquad (7.21\text{b})$$

and

$$\beta^2 = 1 , \qquad (7.21\text{c})$$

where the curly brackets denote the anticommutator. Writing out the field strength tensor $F_{\mu\nu}$ in terms of the electric and magnetic fields gives

$$\tfrac{1}{2}\sigma^{\mu\nu}F_{\mu\nu} = \boldsymbol{\sigma}\cdot\mathbf{B} - i\boldsymbol{\alpha}\cdot\mathbf{E} , \qquad (7.22)$$

with

$$\sigma^k = -(i/2)\varepsilon^{klm}\alpha_l\alpha_m . \qquad (7.23)$$

We shall use the representation where

$$\sigma^k = \begin{bmatrix} \sigma^k & 0 \\ 0 & \sigma^k \end{bmatrix} , \qquad (7.24)$$

in which the matrix entries are the ordinary 2×2 Pauli matrices and where

$$\beta = \begin{bmatrix} 1 & 0 \\ 0 & -1 \end{bmatrix} , \qquad (7.25)$$

in which the unit entries are now 2×2 unit matrices. Using the decomposition (7.22) in the Dirac Hamiltonian (7.19), we may write

$$H^D = H_1^D + H_2^D \qquad (7.26)$$

with

$$H_1^D = \boldsymbol{\alpha}\cdot\mathbf{\Pi}'c + \beta mc^2 , \qquad (7.27)$$

where

$$\mathbf{\Pi}' = \mathbf{\Pi} - \frac{iea\hbar}{2mc^2}\beta\mathbf{E} \qquad (7.28)$$

and

$$H_2^D = eA^0 - \frac{ea\hbar}{2mc}\beta\boldsymbol{\sigma}\cdot\mathbf{B} . \qquad (7.29)$$

As it stands, the Dirac Hamiltonian couples "large" and "small" components of the wave function Ψ in the Dirac equation

$$E\Psi = H^D\Psi , \qquad (7.30)$$

and the nonrelativistic limit is not evident. We perform a unitary Foldy-Wouthuysen transformation,

$$\Psi = U\psi , \qquad (7.31)$$

to exhibit the nonrelativistic limit, as well as to obtain the

order $1/c^2$ corrections to this limit. The transformed wave function ψ obeys

$$E\psi = H\psi , \qquad (7.32)$$

where

$$H = U^{-1}H^D U . \qquad (7.33)$$

To our stated accuracy, it suffices to take U to be a unitary operator formed from the anti-Hermitian operator $\beta\boldsymbol{\alpha}\cdot\mathbf{\Pi}'/mc$,

$$U = U(\beta\boldsymbol{\alpha}\cdot\mathbf{\Pi}'/mc) . \qquad (7.34)$$

Thus

$$U^{-1} = U^\dagger = U(-\beta\boldsymbol{\alpha}\cdot\mathbf{\Pi}'/mc) . \qquad (7.35)$$

Since H_1^D anticommutes with $\beta\boldsymbol{\alpha}\cdot\mathbf{\Pi}'$, we have

$$U^{-1}H_1^D U = H_1^D U^2(\beta\boldsymbol{\alpha}\cdot\mathbf{\Pi}'/mc) . \qquad (7.36)$$

Accordingly, taking U^2 to be the unitary operator

$$U^2 = \frac{mc - \beta\boldsymbol{\alpha}\cdot\mathbf{\Pi}'}{[m^2c^2 + (\boldsymbol{\alpha}\cdot\mathbf{\Pi}')^2]^{1/2}} \qquad (7.37)$$

yields

$$U^{-1}H_1^D U = \beta c\,[m^2c^2 + (\boldsymbol{\alpha}\cdot\mathbf{\Pi}')^2]^{1/2} . \qquad (7.38)$$

This piece of the transformed Hamiltonian has the desired structure: it does not couple "large" and "small" components, and the nonrelativistic limit is evident.

The remaining part of the Dirac Hamiltonian H_2^D is already of order 1 in the $1/c$ expansion. Hence to our accuracy $1/c^2$ we may use

$$U \simeq \exp(-\beta\boldsymbol{\alpha}\cdot\mathbf{\Pi}/2mc) , \qquad (7.39)$$

which is an approximate square root of the expression in Eq. (7.37), including terms of order $1/c^2$. Note that since the Bohr magneton $e\hbar/mc$ multiplies the magnetic field B, it should be counted as a dipole moment, not as a term of order $1/c$. We now specialize to the case relevant to the Penning trap where the magnetic field is constant and the electric field is divergence free ($\nabla\cdot\mathbf{E}=0$). Expanding through second order in $1/c$, we find after a little calculation that the terms remaining in Eq. (7.33) are now given by

$$U^{-1}H_2^D U = eA^0 - \frac{ae\hbar}{2mc}\beta\boldsymbol{\sigma}\cdot\mathbf{B} - \frac{e\hbar}{4m^2c^2}\boldsymbol{\sigma}\cdot\mathbf{E}\times\mathbf{\Pi}$$
$$+ \frac{ea\hbar}{4m^3c^3}\boldsymbol{\sigma}\cdot\mathbf{\Pi}\mathbf{B}\cdot\mathbf{\Pi} + \frac{ie\hbar}{2mc}\beta\boldsymbol{\alpha}\cdot\mathbf{E}$$
$$+ \frac{iea\hbar}{2m^2c^2}\gamma_5\mathbf{B}\cdot\mathbf{\Pi} . \qquad (7.40)$$

Here the operator products are implicitly understood to be taken in a symmetrized, Hermitian form. The Dirac matrix γ_5 is defined by $\gamma_5 = -\alpha^1\alpha^2\alpha^3$. The last two terms on the right-hand side of Eq. (7.40) couple large and small components of the Dirac wave function. They are of higher order and may be deleted.

We may now expand out Eq. (7.38) to order $1/c^2$

[remembering the definition (7.28) of Π'] and combine the result with that given in Eq. (7.40) to arrive at the structure

$$H = H_{NR} + H_{RC} , \tag{7.41}$$

where H_{NR} is the usual nonrelativistic Hamiltonian and H_{RC} contains the $1/c^2$ corrections to this nonrelativistic limit. Using

$$(\boldsymbol{\alpha}\cdot\boldsymbol{\Pi}')^2 = \boldsymbol{\Pi}^2 + \frac{e^2\hbar^2 a^2}{4m^2c^4}\mathbf{E}^2 - e\hbar\boldsymbol{\sigma}\cdot\mathbf{B} + \frac{e\hbar a}{mc^2}\beta\boldsymbol{\sigma}\cdot\boldsymbol{\Pi}\times\mathbf{E} , \tag{7.42}$$

it is easy to see that the nonrelativistic Hamiltonian

$$H_{NR} = \frac{\boldsymbol{\Pi}^2}{2m} + eA^0 - g\frac{e\hbar}{4mc}\boldsymbol{\sigma}\cdot\mathbf{B} \tag{7.43}$$

is supplemented by the $1/c^2$ correction

$$H_{RC} = -\frac{(\boldsymbol{\Pi}^2 - e\hbar\boldsymbol{\sigma}\cdot\mathbf{B}/c)^2}{8m^3c^2}$$
$$-(1+2a)\frac{e\hbar}{4m^2c^2}\boldsymbol{\sigma}\cdot\mathbf{E}\times\boldsymbol{\Pi} + \frac{ea\hbar}{4m^3c^3}\boldsymbol{\sigma}\cdot\boldsymbol{\Pi}\mathbf{B}\cdot\boldsymbol{\Pi} . \tag{7.44}$$

Here we have deleted the rest energy mc^2 from H and replaced the matrix β by its appropriate eigenvalue $\beta' = +1$.

The presence of the first term in Eq. (7.44) is clear. It results from the expansion of the relativistic form for the energy $c(m^2c^2 + \boldsymbol{\Pi}^2)^{1/2}$, with $\boldsymbol{\Pi}^2/2m$ augmented by the magnetic energy $-e\hbar\boldsymbol{\sigma}\cdot\mathbf{B}/2mc$. Note that this is the magnetic energy for $g = 2$. The relativistic effects of the anomaly $a = (g-2)/2$ are rather subtle. Our method of

derivation of Eq. (7.44) directly from the Dirac equation is conceptually straightforward. The spin-dependent part of the Hamiltonian H_{RC} given in Eq. (7.44), however, must also follow from a purely classical argument for the precession of the spin vector $\frac{1}{2}\hbar\boldsymbol{\sigma}$, since this precession equation does not explicitly involve Planck's constant $\hbar$. Moreover, the spin precession equation for constant fields suffices to determine the spin-dependent terms in H_{RC}, and the classical equation for this is on firm footing. It is, in fact, not difficult to check that the spin-dependent terms in Eq. (7.44) do indeed agree with the $1/c^2$ terms in the classical expression for the spin precession in the particle's rest frame [see, for example, Jackson (1975), Eq. (11.170)].

As we discussed in Sec. II, the quantum state of a particle bound to a Penning trap is described by the quantum numbers: $k = 0,1,\ldots$, axial oscillation; $n = 0,1,\ldots$, cyclotron motion; $l = 0,1,\ldots$, magnetron motion; $s = \pm 1$, spin; the nonrelativistic energy eigenstate is denoted by $|\, klns \,\rangle$. The nonrelativistic energy eigenvalue is given by

$$E_{klns}^{NR} = \hbar\omega_z(k+\tfrac{1}{2}) - \hbar\omega_-(l+\tfrac{1}{2})$$
$$+ \hbar\omega_+(n+\tfrac{1}{2}) + \tfrac{1}{2}g\hbar\omega_c\tfrac{1}{2}s . \tag{7.45}$$

Including the $1/c^2$ relativistic corrections, we have

$$E_{klns} = E_{klns}^{NR} + E_{klns}^{RC} , \tag{7.46}$$

where, according to first-order perturbation theory,

$$E_{klns}^{RC} = \langle klns \,|\, H_{RC} \,|\, klns \rangle . \tag{7.47}$$

This expectation value is easily evaluated if we make use of the formalism developed in Sec. II.B. Using this formalism, we find, after some calculation, that

$$E_{klns}^{RC} = -\frac{\hbar^2}{2mc^2}\left[\frac{\omega_+^2(n+\tfrac{1}{2}) + \omega_-^2(l+\tfrac{1}{2})}{\omega_+ - \omega_-} + \tfrac{1}{2}\omega_z(k+\tfrac{1}{2}) + \omega_c\tfrac{1}{2}s\right]^2$$

$$-\frac{\hbar^2}{4mc^2}\frac{\omega_z^4}{(\omega_+ - \omega_-)^2}[(n+\tfrac{1}{2})(l+\tfrac{1}{2}) - \tfrac{1}{4}] - \frac{\hbar^2}{16mc^2}\omega_z^2[(k+\tfrac{1}{2})^2 + \tfrac{3}{4}]$$

$$+(1+2a)\frac{\hbar^2}{4mc^2}\omega_z^2 s\frac{\omega_+(n+\tfrac{1}{2}) + \omega_-(l+\tfrac{1}{2})}{\omega_+ - \omega_-} - a\frac{\hbar^2}{4mc^2}\omega_c\omega_z s(k+\tfrac{1}{2}) . \tag{7.48}$$

Here we use the notation $\omega_+(=\omega_c')$ and $\omega_-(=\omega_m)$ for the cyclotron and magnetron frequencies.

As a check on the calculation, we note that the relativistic correction (7.48) of the geonium energy levels yields the cyclotron and axial frequency shifts used above in Sec. VII.A. In the classical limit and neglecting a magnetron motion correction, we have $(n+\tfrac{1}{2})\hbar\omega_c'/mc^2 = v^2/2c^2$, and the derivative of Eq. (7.48) with respect to $n\hbar$ produces the cyclotron frequency shift given in Eq. (7.18), while the derivative of Eq. (7.48) with respect to $k\hbar$ produces the axial frequency shift given by Eq. (7.17). A detailed discussion of the relativistic eigenfrequency shifts in the classical limit is presented in Sec. X.

In contrast to the classical limit, the low-lying spin and cyclotron energy levels are sketched in Fig. 34. There are two spin ladders, the left corresponding to spin-down, the right to spin-up. Only the first line of Eq. (7.48) makes a significant contribution, and it suffices to set $\omega_- = 0$, $\omega_+ = \omega_c$. Thus we obtain a state-dependent cyclotron frequency shift given by

$$\delta\omega_c' = -\delta(n+1+\tfrac{1}{2}s) , \tag{7.49a}$$

where

$$\delta = \omega_c(\hbar\omega_c/mc^2) . \tag{7.49b}$$

For the electron experiment (Table I), we have $\delta/2\pi \approx 200$ Hz out of $v_c' \approx 160$ GHz. Experiments to observe this small shift are very close to success (Gabrielse, Dehmelt, and Kells, 1985). Once sufficient resolution is achieved, so that the individual cyclotron frequencies can be resolved, it will be possible to distinguish the spin state as well.

C. Radiative corrections

There are radiative corrections to the energy-level structure of the geonium "atom." These are analogs to the Lamb shift in the hydrogen atom. In leading order, the radiative level shifts are simply the dispersion associated with the absorption that gives the radiative decay. The radiative effects shift the energy by the complex amount $\Delta E - i(\hbar/2)\Gamma$, where Γ is the radiative decay constant. The real energy shift ΔE and the decay width $-(\hbar/2)\Gamma$ are the real and imaginary parts of the same analytic function. Using the lowest-order formula for the decay width, Eq. (2.98), we can therefore immediately write down the leading radiative correction:

FIG. 34. Relativistic shifts of the spin-cyclotron energy levels for an electron.

$$\Delta E - (i\hbar/2)\Gamma = -\frac{2}{3\pi}\alpha\left\langle klns \left| \frac{\mathbf{v}}{c}\cdot(H-E)\ln\left[\frac{H-E}{K}\right]\frac{\mathbf{v}}{c} \right| klns \right\rangle .$$

(7.50)

Here $\alpha = e^2/\hbar c \approx \frac{1}{137}$ is the fine-structure constant and K is an ultraviolet cutoff, which must be introduced to make the nonrelativistic calculation converge. Including relativistic kinematics gives convergence, and so $K \approx mc^2$. The Hamiltonian H is the nonrelativistic form given by Eq. (7.43). An additive constant has been arranged so that ΔE vanishes for a free particle—the energy shift has been properly renormalized. Finally, we note that since $\operatorname{Im}\ln(H-E) = -\pi$ for an excited level, we recover Eq. (2.98) for the decay width Γ.

The radiative level shift is of order $\alpha(v/c)^2$ relative to the basic level splittings. Since $(v/c)^2 \approx 10^{-8}$ for the electron in the geonium atom, the shift is very small, of relative order 10^{-10}. The observable shifts are, in fact, yet smaller because all the motions in geonium are basically harmonic. Thus the velocity operator $\mathbf{v}$ can be expressed in terms of various creation and annihilation operators $a^{\dagger}$ and a, and the operator in the matrix element in Eq. (7.50) is a sum of terms, each of the form

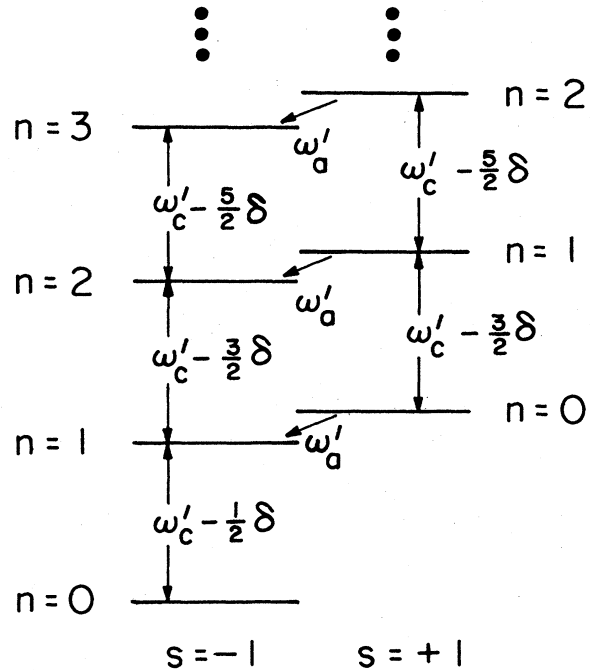$$a^{\dagger}(H-E)\ln\left[\frac{H-E}{K}\right]a + a(H-E)\ln\left[\frac{H-E}{K}\right]a^{\dagger} .$$

(7.51)

Using the properties of the creation and annihilation operators it is easy to show that (in the real part) such expressions are constants, independent of the quantum state. Hence the ΔE given by Eq. (7.50) is a common shift for all the levels, and it cancels in the transition frequencies.

There are, of course, state-dependent radiative corrections in higher order, corrections both to the orbital motion and in the anomalous magnetic moment. These have been worked out in detail for the motion in a constant magnetic field, which gives the major effect since this cyclotron motion is by far the fastest (Newton, 1954; Tsai and Yildiz, 1973). These corrections are of relative order $\alpha(\hbar\omega_c/mc^2)^2 \approx \alpha(v/c)^4$. We conclude that the radiative level shifts in geonium are certainly negligible.

VIII. CAVITY SHIFTS

We consider here the shifts in the cyclotron frequency and decay time of an electron or positron that are brought about by the presence of a microwave cavity formed by the trap electrodes themselves. As mentioned earlier, the first observation of the inhibition of the spontaneous decay of a radiating system because of a surrounding microwave cavity was for the cyclotron motion of a single

electron in a Penning trap[27] (Gabrielse and Dehmelt, 1985). This observation was subsequently confirmed in a second trap (Van Dyck, Schwinberg, and Dehmelt, 1984). The hyperbolic shape of the Penning trap electrodes, along with the holes and slits in the electrodes, make it difficult to calculate the mode structure for these traps. A cylindrical cavity, however, is a tractable problem. It is of direct experimental interest both as a model of the hyperbolic electrodes and also because this geometry may be sufficient to produce an adequate quadrupole electrostatic trapping potential. Such a trapping configuration (Gabrielse and MacKintosh, 1984) is reviewed in Sec. IX. Thus we describe the alteration of the cyclotron motion brought about by a cylindrical cavity. In this we follow the work of Brown, Gabrielse, Helmerson, and Tan (1985a,1985b). The frequency shift can easily be so large as to have important consequences for the $g - 2$ measurements, and this systematic effect warrants a thorough experimental investigation. As a byproduct, we shall also discuss the corresponding alterations in the cyclotron motion of a particle in the midplane between two infinite parallel conductors.

To assess the accuracy needed in the theoretical formula that relates the observed cyclotron frequency $\bar{\omega}_c$ to the cyclotron frequency ω_c in the absence of the cavity, we note that the anomaly involves the difference of the free-space values of the spin and cyclotron frequencies, as shown in Eq. (2.66). Thus if the cavity frequency shift

$$\Delta\omega_c = \bar{\omega}_c - \omega_c \tag{8.1}$$

is not accounted for, it leads to a systematic error in the anomaly given by

$$\frac{\Delta a}{a} = \frac{1}{a}\frac{\Delta\omega_c}{\omega_c} . \tag{8.2}$$

Since the present precision in the anomaly is $\Delta a/a \approx 4 \times 10^{-9}$ (Van Dyck, Schwinberg, and Dehmelt, 1984) and $a \approx 1.2 \times 10^{-3}$, we see that the current experimental precision is upset if the cavity shift is larger than $\Delta\omega_c/\omega_c \approx 5 \times 10^{-12}$. As we shall see, the shift in the cyclotron frequency can easily be much larger than this figure. Calculations have been published (Barton and

---

[27]That the radiation of an accelerated charge can be substantially modified by enclosing it in a microwave cavity was pointed out long ago by Purcell (1946). Cavitylike effects on the radiation of a molecule separated from a single conducting plate by a thin dielectric layer have been reviewed by Drexhage (1974). A variety of theoretical techniques have been used to study the radiation of an atom near a plate or between plates: Morawitz (1969), Kuhn (1970), Stehle (1970), Philpott (1973), Milonni and Knight (1973), Chance, Prock, and Silbey (1975). More recently, Kleppner (1981) discussed the radiative properties of an atom in a cavity, and the inhibition of the radiation of a Rydberg atom between closely spaced plates was observed by Hulet, Hilfer, and Kleppner (1985).

Grotch, 1977; Fischbach and Nakagawa, 1984,1984b; Svozil, 1985) which imply that there are also large cavity-induced corrections to the spin frequency, corrections that are large enough to modify the results of the present experiments. This work, however, led to a demonstration by Boulware, Brown, and Lee (1985) that, to within a high order of accuracy, the exact apparatus of quantum electrodynamics yields the classical result, with a negligible effect upon the spin frequency. (See also Boulware and Brown, 1985.) Thus the classical development of Brown, Gabrielse, Helmerson, and Tan suffices.

Neglecting insignificant image magnetic forces, the presence of a surrounding metallic cavity alters the charged-particle equation of motion to read

$$\dot{\mathbf{v}} - \omega_c \times \mathbf{v} + \frac{e}{m}\nabla V(\mathbf{r}) + \tfrac{1}{2}\gamma_c\mathbf{v} = \frac{e}{m}\mathbf{E}'(\mathbf{r}) . \tag{8.3}$$

Here $\mathbf{E}'(\mathbf{r})$ is the electric field at the position $\mathbf{r}(t)$ of the charged particle which is produced by the effective image charges that represent the cavity walls. It is the electric field acting on the particle, omitting the trap field $[-\nabla V(\mathbf{r})]$ and also excluding the proper field of the particle itself. This proper field is accounted for by using the observed (free-space) electron mass m and by employing the free-space damping constant $\gamma_c(\omega_c) = 4e^2\omega_c^2/3mc^3$ discussed in Sec. II.E. It is convenient to split the field $\mathbf{E}'$ into longitudinal and transverse parts,

$$\mathbf{E}' = {}^{(L)}\mathbf{E}' + {}^{(T)}\mathbf{E}' . \tag{8.4}$$

The longitudinal part ${}^{(L)}\mathbf{E}'$ is the gradient of the radiation-gauge scalar potential, while the transverse part ${}^{(T)}\mathbf{E}'$ is the time derivative of the radiation gauge vector potential. As we shall soon see, the major effect of ${}^{(L)}\mathbf{E}'$ is to alter the electrostatic binding field by an insignificant amount (in agreement with the previous estimate of Wineland and Dehmelt, 1975b), while it is the effect of ${}^{(T)}\mathbf{E}'$, which corresponds to the effects of the dynamical cavity modes, that can have significant consequences.

The longitudinal piece ${}^{(L)}\mathbf{E}'$ is obtained from the alteration brought about by the trap electrodes on the static scalar potential produced by the charged particle. Thus

$${}^{(L)}\mathbf{E}'(\mathbf{r}) = -\nabla e\mathscr{D}'(\mathbf{r},\mathbf{r}')\big|_{\mathbf{r}'=\mathbf{r}} . \tag{8.5}$$

Here $\mathscr{D}'(\mathbf{r},\mathbf{r}')$ is a solution to the homogeneous Laplace equation. Adding it to the free-space Green's function $1/|\mathbf{r}-\mathbf{r}'|$ produces the Coulomb Green's function appropriate to the cavity, a function that vanishes when either $\mathbf{r}$ or $\mathbf{r}'$ lies on the electrode surface. Since the charged particle moves about a small orbit near the center of the trap, the first nontrivial term in the power-series expansion of ${}^{(L)}\mathbf{E}'(\mathbf{r})$ suffices. The symmetry of the Penning trap electrodes gives ${}^{(L)}\mathbf{E}'(0) = 0$. Small trap imperfections make ${}^{(L)}\mathbf{E}'(0)$ nonvanishing, but this very small constant electric field is canceled by a very small shift in the equilibrium position of the harmonic trapping potential. Thus the first nontrivial term is given by

$$\frac{e}{m}{}^{(L)}E'_k(\mathbf{r}) = \sum_{l=1}^{3}\Omega_{kl}r_l , \tag{8.6}$$

where

$$\Omega_{kl} = -\frac{e^2}{m}[\nabla_k \nabla_l \mathscr{D}'(\mathbf{r},\mathbf{r}')\,|_{\mathbf{r}'=\mathbf{r}} + \nabla_k \nabla_l' \mathscr{D}'(\mathbf{r},\mathbf{r}')\,|_{\mathbf{r}'=\mathbf{r}}]\,.$$

(8.7)

The first term in the square brackets is symmetrical in the vector indices k,l and traceless, since $\mathscr{D}'(\mathbf{r},\mathbf{r}')$ obeys the Laplace equation. Moreover, this term shares the axial symmetry of the trap electrodes. Hence its effect is absorbed by a small redefinition of the trapping potential. Since the Green's function is symmetric,

$$\mathscr{D}'(\mathbf{r},\mathbf{r}') = \mathscr{D}'(\mathbf{r}',\mathbf{r})\,,$$

(8.8)

the second term in the square brackets is symmetrical in the vector indices k,l. This second term also has axial symmetry, but it is not traceless. The scalar part

$$\overline{\Omega}_{kl} = \delta_{kl}\Omega\,,$$

(8.9)

$$\Omega = \tfrac{1}{3}\sum_{m=1}^{3}\Omega_{mm}\,,$$

(8.10)

cannot be absorbed by a redefinition of the trapping potential. This part upsets the relation amongst the magnetron, axial, and cyclotron frequencies $\omega_m = \omega_z^2/2\omega_c'$ discussed in Sec. II. The correction is, however, very small: The double gradient of $\mathscr{D}'(\mathbf{r},\mathbf{r}')$ is of order $1/d^3$, where d is the characteristic trap size. Hence

$$\Omega \approx \frac{e^2}{md^3} = \left[\frac{a_0}{d}\right]\left[\frac{e^2}{a_0}\right]\frac{1}{md^2}\,.$$

(8.11)

Here we have introduced the Bohr radius $a_0 \approx 5\times 10^{-9}$ cm, since the binding energy of the hydrogen atom $e^2/2a_0 \simeq 14$ eV is about e times the voltage on the trap electrodes (a voltage produced by batteries). Therefore

$$\Omega \approx \left[\frac{a_0}{d}\right]\omega_z^2 \approx 10^{-8}\omega_z^2\,,$$

(8.12)

and we see that this correction is negligible.

The transverse electric field may be expressed as

$$^{(T)}E_k'(t,\mathbf{r}) = -\frac{\partial}{\partial t}\int dt'\sum_{l=1}^{3}D_{kl}'(t-t';\mathbf{r},\mathbf{r}(t'))ev_l(t')/c^2\,.$$

(8.13)

Here $D_{kl}'(t-t';\mathbf{r},\mathbf{r}')$ is the retarded, transverse, radiation gauge Green's-function alteration brought about by the trap electrodes. Adding it to the free-space Green's function produces the full Green's function, which obeys the relevant boundary conditions on the trap electrodes that behave as cavity walls. Since the charged particle is confined to a small region near the center of the trap, it suffices to set $\mathbf{r}=0=\mathbf{r}(t')$ in Eq. (8.13). Only the fast cyclotron motion has any significant correction from this field. Adopting complex coordinates and Fourier transforming according to

$$v(t) = v_x(t) - iv_y(t) \sim e^{-i\omega t}\,,$$

(8.14)

with

$$D_{kl}'(t-t';\mathbf{r},\mathbf{r}') = \int \frac{d\omega'}{2\pi}e^{-i\omega'(t-t')}\tilde{D}_{kl}'(\omega';\mathbf{r},\mathbf{r}')\,,$$

(8.15)

one finds that inserting the field (8.13) into the equation of motion (8.3) yields the condition

$$\omega - \omega_c' + i\gamma_c/2 = -\omega r_0 \tilde{D}_{xx}'(\omega;0,0)\,,$$

(8.16)

where $r_0 = e^2/mc^2$ is the classical electron radius. The effect of the trapping potential is to replace the cyclotron frequency ω_c by the modified frequency ω_c' defined in Eq. (2.16), which appears on the left-hand side of Eq. (8.16). The simplicity of the right-hand side of Eq. (8.16) results from the axial symmetry which implies that $\tilde{D}'(\omega;0,0)$ is proportional to the unit dyadic in the xy plane, with the proportionality constant $\tilde{D}_{xx}'(\omega;0,0) = \tilde{D}_{yy}'(\omega;0,0)$.

In general, the Green's-function modification $\tilde{D}_{xx}'(\omega;0,0)$ is a complex number, and thus the presence of the cavity modifies the cyclotron decay constant away from its free-space value γ_c. In the limit of a perfect cavity with perfectly conducting walls, the imaginary part of $\tilde{D}_{xx}'(\omega;0,0)$ cancels γ_c exactly. In this limit there is no decay of the cyclotron motion because there is no dissipative process to absorb the energy.

To assess the size of the correction to the cyclotron frequency given by the right-hand side of Eq. (8.16), we note that simple dimensional analysis informs us that

$$\tilde{D}_{xx}'(\omega;0,0) = F(\omega d/c)/d\,,$$

(8.17)

where d is the characteristic trap size and F is a dimensionless function of the dimensionless ratio $\omega d/c = d/\lambda$. This function describes the retarded propagation of the radiation field emitted by the motion of the image charges that represent the cavity walls, and thus one expects that $F(\omega d/c)$ will be roughly of order unity even for a large argument. For the typical trap parameters given in Table I, we have $r_0/d \approx 1\times 10^{-12}$ and $\omega d/c \approx 10$. Taking $F(\omega d/c) \approx 1$, we see that the correction to the cyclotron frequency is roughly on the order of 10^{-12}, which is almost as large as the current precision of the experiments. Clearly this effect warrants a more careful examination.

Such an examination has been made for a cylindrical cavity, as shown in Fig. 35, in the work of Brown, Gabrielse, Helmerson, and Tan, which we are summarizing. The results for this geometry should give a good indication of the size of the effects in the hyperbolic traps. Moreover, as we shall discuss in Sec. IX, a trap with a cylindrical shape can be used as a Penning trap. But before passing to the quantitative treatment, some more qualitative, clarifying remarks are in order. We first ignore the renormalization problem so that the Green's-function correction $\tilde{D}_{xx}'(\omega;0,0)$ on the right-hand side of Eq. (8.16) is replaced by the full Green's function, and the decay constant γ_c is omitted on the left-hand side. In this case we may express the Green's function by a mode sum to obtain

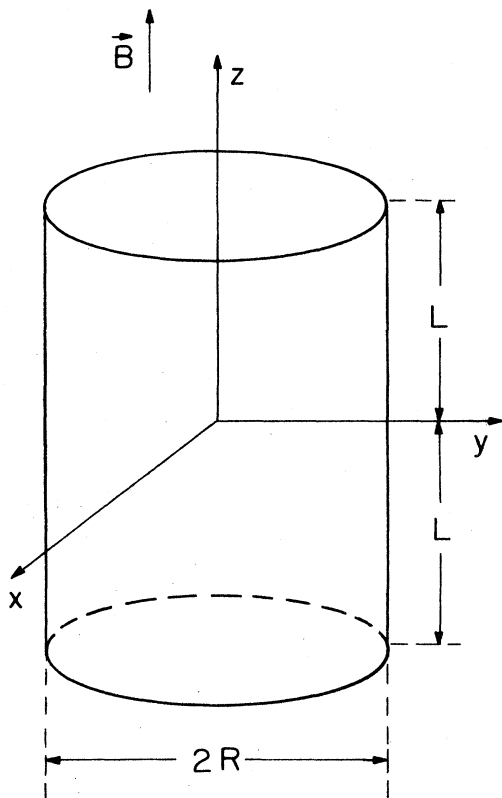$$\omega - \omega_c' = \omega \sum_N \frac{\lambda_N^2}{\omega^2 + i\omega\Gamma_N - \omega_N^2}\,.$$

(8.18)

FIG. 35. Cylindrical cavity of radius R and length $2L$. A uniform magnetic field **B** is aligned along the axial symmetry axis of the cavity, and the charged particle is in a small orbit in the center of the cavity.

Here ω_N is the eigenfrequency of the Nth mode and Γ_N is the decay constant of this mode with $Q_N = \omega_N/\Gamma_N$ the corresponding quality factor of the mode. The coupling constant λ_N^2 in the numerator is related to the square of a wave function, and so it is a positive number, while the sign of the damping term $+i\omega\Gamma_N$ in the denominator is dictated by the causal requirement of decay rather than growth in time. Equation (8.18) expresses the frequency shift of the cyclotron motion, which is essentially harmonic, in terms of its interaction with the infinite number of cavity modes of the radiation field, each of whose amplitudes is a harmonic oscillator. Thus Eq. (8.18) represents the cyclotron frequency shift in terms of the solution of an (infinite) set of coupled harmonic oscillators. A simple dimensional argument shows that λ_N^2 is of order $(r_0/d^3)c^2 \sim (r_0/d)\omega_N^2$. Therefore, away from any cavity resonance $\omega = \omega_N$, we have a small frequency shift of the order $(\omega - \omega_c')/\omega \sim r_0/d$, in agreement with our previous estimate. However, near a cavity resonance, we have a frequency shift (from this one mode) as large as $(\omega - \omega_c')/\omega \sim \pm(r_0/d)(\omega_N/\Gamma_N) = \pm(r_0/d)Q_N$, which is much larger. This frequency shift disappears exactly on resonance, but in this case there is a large change in the cyclotron decay constant of order $(r_0/d)Q_N\omega \sim \gamma_c Q_N$.

(In these last two estimates we have neglected purely numerical factors, which may be fairly large.)

The story we have just told suffers from a serious omission, the omission of the necessity of a renormalization. Replacing the cavity walls with an absorbing material and taking the limit of an infinitely large cavity must yield the free-space limit. In this limit, the imaginary part of the right-hand side of Eq. (8.18), the absorptive contribution, must reproduce the free-space decay constant $-i\gamma_c/2$. But in this limit, the real part of the right-hand side of Eq. (8.18) is infinite, since it contains the reactive effect of the proper field of the charged particle. Clearly, this divergence also appears in the original cavity configuration. As is well known, this infinity is correctly dealt with by removing the free-space reactive contribution of the charged particle's proper field and employing the observed free-space value of the charged particle's mass. Thus the formal mode sum in Eq. (8.18) diverges, and it must be renormalized by subtracting out the real part of the free-space limit. Since this is a delicate operation, we shall instead return to the previous equation (8.16), which expresses the (complex) frequency shift in terms of the alteration $\tilde{D}'_{xx}(\omega;0,0)$ of the Green's function brought about by the presence of the cavity.

To have a tractable problem, but one of direct experimental interest, we are considering a right-cylindrical cavity, as illustrated in Fig. 35. The magnetic field **B** is aligned along the cavity axis, and the charged particle moves about this field in a small orbit at the center of the cavity. We take account of dissipation by replacing the individual cavity widths Γ_N with an average value Γ. Referring to the (formal) mode sum (8.18), we see that since $\Gamma^2 \ll \omega_N^2$, this is tantamount to dropping the $i\omega\Gamma_N$ term and replacing the frequency ω by the complex number $\omega + i\Gamma/2$. To determine unambiguously the renormalized alteration $\tilde{D}'_{xx}(\omega;0,0)$, we note that the limit in which the cavity radius R is taken to infinity, with the cylindrical side replaced with an absorbing material, yields a geometry with two parallel, infinite perfectly conducting planes a distance $2L$ apart. Thus we express the Green's function as the sum of the Green's function for the parallel plate problem and the solution to the homogeneous wave equation, which corrects for the presence of the cylindrical wall. This gives

$$\omega - \omega_c' = -\frac{i}{2}I(\omega) + R(\omega)$$

$$= -\frac{i}{2}\gamma_c(\omega) + \omega\left[\Sigma_P\left[\omega + \frac{i}{2}\Gamma\right]\right.$$

$$\left. + \Sigma_S\left[\omega + \frac{i}{2}\Gamma\right]\right], \quad (8.19)$$

where Σ_P is the parallel plate contribution to Eq. (8.16), including the imaginary cyclotron decay contribution, and Σ_S is the correction due to the cylindrical side of the cavity. In the first line of Eq. (8.19) we have separated out

the real and imaginary parts, with $I(\omega)$ being the cavity-modified cyclotron decay rate at frequency ω and $R(\omega)$ the cavity frequency shift. Since these changes are very small, ω can be replaced by ω_c' on the right-hand sides of Eq. (8.19). Now since the Green's function for the two-parallel-plate geometry can be expressed as an infinite sum of image contributions, the removal of the proper

field term is now trivial: One simply omits the direct contribution from the sum.

The parallel plate problem has some interest in its own right (see footnote 27), and we pause to describe briefly the results for this case where the charged particle moves about a cyclotron circle in the midplane between the two conductors. Using the method of images one obtains

$$\Sigma_P(\omega) = \frac{r_0}{L} \ln(1 + e^{2i\omega L/c}) - \frac{r_0}{L} \sum_{n=1}^{\infty} (-1)^n \left[e^{2in\omega L/c} \left(\frac{ic}{2n^2 L\omega} - \frac{c^2}{4n^3 L^2 \omega^2} \right) + \frac{c^2}{4n^3 L^2 \omega^2} \right] . \tag{8.20}$$

The cavity dissipation can be modeled by writing the cavity width as

$$\Gamma = \omega \delta/L , \tag{8.21}$$

where δ is the skin depth of the conducting plates and $2L$ is the distance between the plates. Since there is only one scale in this problem, L, it is convenient to introduce the dimensionless variable

$$\xi = \frac{\omega L}{\pi c} = \frac{2L}{\lambda} , \tag{8.22}$$

which is the (fractional) number of wavelengths at frequency ω that fit between the plates. The decay constant $I_P(\omega)$ for perfectly conducting plates ($\Gamma = 0$) given by Eq. (8.20) is plotted in Fig. 36. With $\xi < \frac{1}{2}$, less than half a wavelength fits between the plates. In this case electromagnetic waves cannot propagate between the plates, the charged particle cannot radiate, and $I_P(\omega) = 0$. The decay constant $I_P(\omega)$ jumps discontinuously to $3\gamma_c$ and then decreases as ξ increases past $\xi = \frac{1}{2}$, which is the first threshold for propagating waves. Further discontinuous jumps take place as ξ passes through thresholds at odd half-integers. (There are no thresholds at the integers, since there is a node at the midplane position of the

charged particle when an even number of wavelengths fits between the two plates.) As ξ becomes large, there is no obstacle to the radiation of the charged particle, and $I_P(\omega)$ approaches the free-space value γ_c. The effect of nonvanishing dissipation of a common size (say $\delta/L = 10^{-3}$) is only to smooth the sharp discontinuities and to produce a very small contribution below the first threshold $\xi = \frac{1}{2}$. In Fig. 37 we plot $R_P(\omega)$, taking $\delta/L = 1 \times 10^{-3}$. Note that this frequency shift vanishes at two points between successive odd half-integer values of ξ, while $R_P(\omega_c')L/\omega r_0$ approaches $\frac{1}{2}\ln 2$ when $\omega \to 0$ and vanishes when $\omega \to \infty$. The large peaks appear when ξ is an odd half-integer because for these values of ξ the retardation phase exactly cancels the alternating signs of the image charges, and the resultant infinite image sum would be the divergent sum of $1/n$ if it were not for the damping of this sum resulting from cavity dissipation, which produces instead a large logarithm.

We turn now to the problem that is our major interest, the frequency shift and modification of the decay rate for a small cyclotron orbit bound to the center of a cylindrical cavity, as illustrated in Fig. 35. We denote the radius of the cavity by R, the length by $2L$. The alteration of the Green's function brought about by the presence of the

FIG. 36. The decay constant $I_P(\omega)/\gamma_c(\omega)$ for a charged particle moving in the midplane between two perfect conducting planes. The abscissa is in units of ξ, the number of wavelengths at frequency ω that fit between the planes.
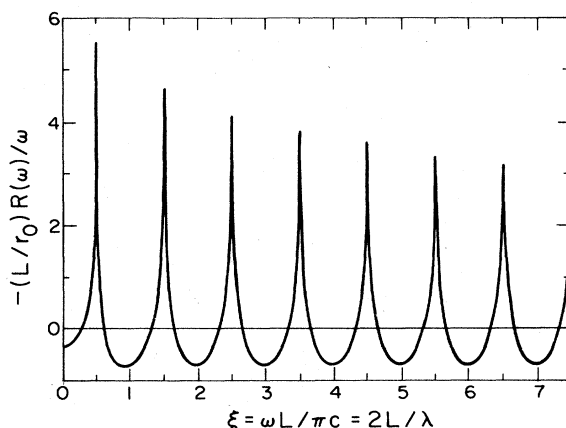

FIG. 37. Plot of the frequency shift $-(L/\omega r_0)R_P(\omega)$ vs ξ for the cyclotron motion of a charged particle in the midplane between two imperfect conducting plates with $\delta/L = 1 \times 10^{-3}$.

circular side can be expressed in terms of an infinite sum over the axial standing waves that fit between the two endcap planes. The wave numbers of the waves that do not vanish at the midplane location of the charged particle are given by

$$k_n = (n + \tfrac{1}{2})\pi/L , \qquad (8.23)$$

where $n = 0, 1, 2, \ldots$. With ω below the first axial threshold, $\xi < \tfrac{1}{2}$, the radial waves are exponentially damped with the damping constant

$$\mu_n = (k_n^2 - \omega^2/c^2)^{1/2} . \qquad (8.24)$$

In terms of this decomposition, the cavity side addition to the complex frequency shift (8.19) is given by

$$\Sigma_S(\omega) = -\frac{r_0}{L} \sum_{n=0}^{\infty} \left[\frac{K_1'(\mu_n R)}{I_1'(\mu_n R)} + \frac{k_n^2 c^2}{\omega^2} \left[\frac{K_1(\mu_n R)}{I_1(\mu_n R)} - \frac{K_1(k_n R)}{I_1(k_n R)} \right] \right] , \qquad (8.25)$$

where the prime denotes a derivative. The first ratio of Bessel functions is the TE contribution, the terms in the large parentheses are the TM contribution. When ω is near the nth threshold, μ_n becomes small, and the nth term in the sum (8.25) has a large logarithmic contribution that cancels the large logarithm in the parallel plate term. As ω passes the threshold, μ_n becomes a negative imaginary number. In the limit of vanishing dissipation ($\Gamma = 0$), the imaginary part of the Bessel function ratios cancels the imaginary part of the parallel plate term. Past a threshold, the Bessel functions in the denominator can vanish, producing poles corresponding to the normal modes of the cavity. The replacement $\omega \rightarrow \omega + i\Gamma/2$ changes these poles into Lorentzian forms of width Γ. The sum in Eq. (8.25) converges very rapidly: for large n, $\mu_n \sim k_n \sim n\pi/L$, and it is exponentially damped. Thus the sum is easily calculated on a digital computer. Adding the result to the previous parallel plate contribution gives the complete shift of Eq. (8.19).

We use the aspect ratio $R/L = 1.186$ for the cylindrical cavity, the aspect ratio for the cylindrical trap discussed in Sec. IX. So as to exhibit the general features of our result, we first choose a low quality factor $Q = 50$ and examine a large range $0 < \xi < 7.5$. The decay constant $I(\omega)$ is plotted in Fig. 38. At lower frequencies it has distinct

peaks corresponding to the cavity normal modes, but these merge as the frequency increases into the region where the mode spacing is less than the cavity width. At large frequencies, $I(\omega)$ approaches the free-space value $\gamma_c(\omega)$. The corresponding frequency shift $R(\omega)$ is shown in Fig. 39. There are dispersive structures in the low-frequency region that correspond to the absorptive peaks in Fig. 38, but as the frequency increases these structures become less distinct.

Experiments are generally performed in the region $3.5 < \xi < 4.5$, and we illustrate the results in this region. But before passing to this, we note that the various cavity modes have different quality factors. In the region that we are considering, the quality factors for perfect cylindrical geometry for the TE modes Q_E are, to within about 10%, twice the quality factors Q_M of the TM modes. We approximately account for this difference in cavity widths by using the complex frequency $\omega(1 + i/2Q_E)$ in the TE denominator function $I_1'(\mu_n R)$ in Eq. (8.25), while all the other complex frequencies are given by $\omega(1 + i/2Q_M)$, with $Q_M = Q_E/2$. (By keeping all the other complex frequencies the same, we preserve the threshold cancellation discussed above, as we must.) Actual cylindrical Penning traps contain holes and slits, and their quality factors are difficult to calculate accurately. Thus, although one could alter the individual modes in the interval $3.5 < \xi < 4.5$ by putting in the exact widths, this is not

FIG. 38. The decay constant $I(\omega)/\gamma_c(\omega)$ for a charged particle moving in a small orbit about the axis and centered in the midplane of a cylindrical cavity with $Q = 50$ and an aspect ratio $R/L = 1.186$. The ticks denote the positions of the TE and TM modes.
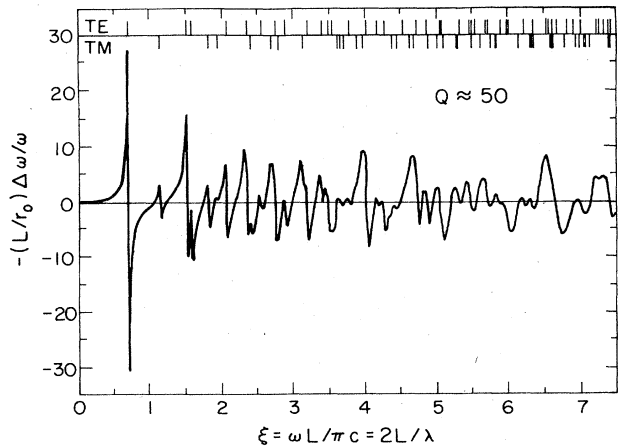
FIG. 39. Frequency shift corresponds to the decay constants of Fig. 38.

warranted by the uncertainty in our knowledge of the widths of the experimental traps. Thus we use the simple substitution described above to compute the decay constants and frequency shifts plotted in Figs. 40 and 42 for a typical quality factor $Q_E = 1000$. We see that $I(\omega)$ varies from $0.06\gamma_c(\omega)$ to $21\gamma_c(\omega)$. A Q of about 1000 is required to make possible the decrease in the damping constant by the factor of 10 which has been observed by Van Dyck, Schwinberg, and Dehmelt (1984). Figure 41 shows how the experimentally measured cyclotron damping constant in a hyperbolic Penning trap changes by a factor of 4 when the cyclotron frequency is changed by 0.5%.

To set the scale for the frequency shifts, we note that in the experimental traps $r_0/L \approx 8 \times 10^{-13}$, while the current experimental precision in the $g-2$ measurement is equivalent to a shift in the cyclotron frequency given by $\Delta\omega/\omega \approx 5 \times 10^{-12}$. We see from Fig. 42 that, on this scale, very large shifts occur in the vicinity of the normal mode frequencies: One can have shifts as large as $\Delta\omega/\omega \approx 70 \times 10^{-12}$, although for the most part the shifts are on the order of $\Delta\omega/\omega \approx 8 \times 10^{-12}$ when the cyclotron decay time is longer than that in free space. In view of the uncertainties in the theoretical value of the anomaly (Kinoshita and Sapirstein, 1984), a frequency shift as large as $\Delta\omega_c/\omega_c = 140 \times 10^{-10}$ would not be revealed by comparing the experimental and theoretical values for the anomaly. We conclude that an experimental search for
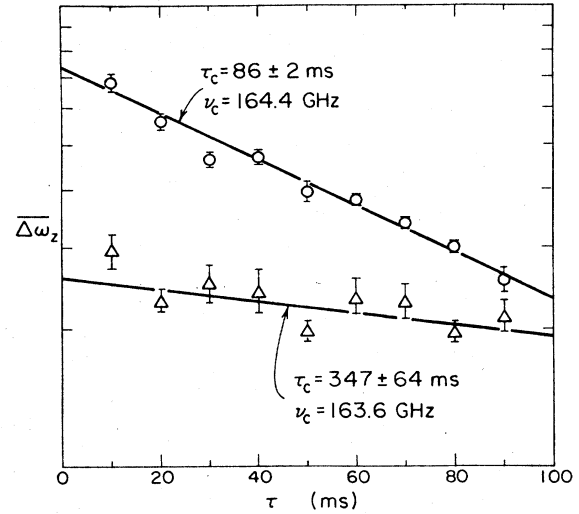
FIG. 41. The energy in the cyclotron motion is proportional to the relativistic mass shift of the axial frequency, as discussed in Sec. VII. In this figure the measured decay with time in such shifts after the cyclotron drive has been turned off are plotted for two values of the cyclotron frequency obtained by changing the magnetic field (Gabrielse and Dehmelt, 1985).

this systematic effect should be made to confirm the present value of the g factor of the electron.

IX. ELECTROSTATICS OF THE PENNING TRAP

A charged particle in a Penning trap is most conveniently treated as a bound system as in our previous discussion. To emphasize that a synthetic atom has been manufactured in the laboratory, the bound system has frequently been called "geonium"—a particle bound to the Earth. The binding potential is not the Coulomb potential produced by a nucleus, but the quadrupole potential

FIG. 40. Cavity effects for $R/L = 1.186$ and $Q_E = 1000$: (a) decay constant; (b) magnified section of the smaller values of the decay constant.
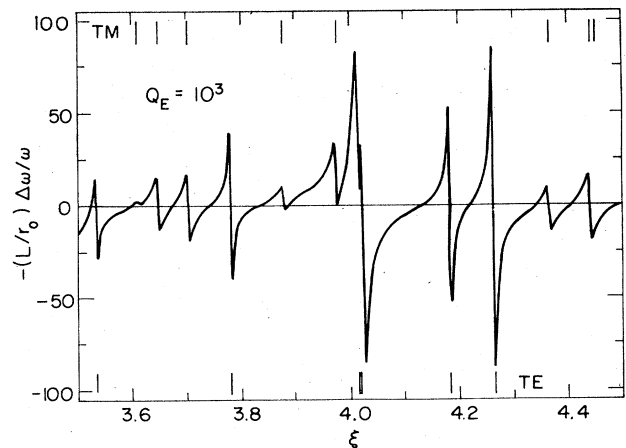
FIG. 42. Frequency shifts corresponding to the decay constants of Fig. 40.

of Eq. (2.2) produced by the electrodes of a Penning trap. Just as perturbations of the Coulomb potential determine the fine details of atomic energy levels, the deviations from a quadrupole potential make small modifications to the equally spaced energy levels shown in Fig. 8. Such deviations are always present in a laboratory Penning trap and are the subject of this section. They are extremely important because of the high precision achieved and sought in geonium experiments.

The geonium trapping potential also differs from that in an ordinary atom in that it can be directly modified. The potential on extra compensation electrodes is adjusted, while an experiment is in progress, to improve the trapping potential.[28] Without such adjustments, the electron, positron, and proton experiments mentioned earlier could not have taken place. A theoretical description of anharmonicity compensation is simplified by the fact that only four parameters are generally required to describe the potential in the center of the trap, where particles are located (Sec. IX.A). A complication is that these parameters must be calculated via a numerical solution of Laplace's equation. Electrostatic screening (by the endcap and ring electrodes) primarily determines the values of these parameters. We pay particular attention to the configuration of hyperbolic electrodes used in all of the existing traps for high-precision geonium measurements (Sec. IX.B) and to an improved configuration of electrodes that has been proposed (Sec. IX.C). Our discussion and examples are based on a more detailed discussion and calculation by Gabrielse (1983), whose numerical techniques are beyond the scope of this review.

Additional small potentials can be added to the electrodes to translate the center of the axial oscillator or to drive this oscillation (see Sec. IX.D). Although the latter additions are oscillatory potentials at radio frequencies, the interior of the trap is in the "near field" of the oscillatory radiation, since the wavelength of the electromagnetic radiation is much larger than the dimensions of a trap. The potential within the trap at any particular time is thus the electrostatic potential produced by the instantaneous boundary potentials. A numerical solution to Laplace's equation is again required, by a technique similar to that used for the trapping and compensation potentials (Gabrielse, 1984). The possible use of a simple, cylindrical geometry for the trap electrodes of precision traps is reviewed in Sec. IX.E (Gabrielse and MacKintosh, 1984). This electrode configuration is a promising alternative for studies of the interaction of an electron cyclotron oscillator with a surrounding microwave cavity discussed in Sec. VIII. Finally, holes and slits in the quadrupole electrodes contribute to trap anharmonicity. These are treated as perturbation multipoles in Sec. IX.F in order to provide estimates that are useful for trap design.

A. Potential in the center of a compensated trap

The idealized electrodes of Fig. 6 are located on hyperbolas given earlier for the endcap electrodes by

$$z^2 = z_0^2 + \rho^2/2 , \tag{2.3}$$

and for the ring by

$$z^2 = \tfrac{1}{2}(\rho^2 - \rho_0^2) . \tag{2.4}$$

These electrodes are flawless and infinitely extended. Potentials $V_0/2$ and $-V_0/2$ applied to these electrodes produce the quadrupole potential[29]

$$V_2 = V_0 \frac{z^2 - \tfrac{1}{2}\rho^2}{2d^2} + V_0 C . \tag{9.1}$$

Distances are scaled by the characteristic trap dimension d defined earlier by

$$d^2 = \tfrac{1}{2}(z_0^2 + \rho_0^2/2) . \tag{2.5}$$

The constants z_0 and ρ_0 are the distances to the endcap and ring electrodes along the z and ρ axes, respectively.

Although great care is taken in the construction of high-precision traps, the potential V that is realized differs from V_2 for several reasons. In the first place, it is generally necessary to put holes and slits in the quadrupole electrodes to admit particles and various radiofrequency and microwave drives, as illustrated by the cross section of an actual trap represented in Fig. 1. In the second place, the quadrupole electrodes are slightly imperfect, misaligned, and truncated. In the third place, the potential on extra electrodes introduced into the asymptotic region of a compensated Penning trap contributes to V and allows V to be changed.

Near the center of the trap, where particles are located [at position (r,θ,φ) in spherical coordinates with $r/d \ll 1$], the potential is given by

$$V = V_2 + \tfrac{1}{2} V_0 \sum_{k=0}^{\infty} C_k \left[\frac{r}{d} \right]^k P_k(\cos\theta) . \tag{9.2}$$

Terms which go as odd powers of the coordinates are smaller because of the symmetry under the reflection $z \to -z$ that is carefully maintained in the construction of precision traps, and hence these terms are not considered here. The actual potential V differs from V_2 principally by a modification of the strength of the quadrupole potential ($k = 2$) and by the addition of a term that is quartic in the coordinates ($k = 4$). We thus focus upon C_2 and C_4.

The coefficient C_4 quantifies the most significant

---

[28]The first compensated trap was reported by Van Dyck, Wineland, Ekstrom, and Dehmelt (1976).

[29]The constant C is unobservable. However, to produce the simple boundary conditions introduced later in Fig. 44(b) we must take $C = (\tfrac{1}{2}\rho_0^2 - z_0^2)/4d^2$.

anharmonicity.[30] A nonzero C_4 produces highly undesirable shifts in the oscillation frequencies of a trapped particle which depends upon the oscillation amplitudes. These shifts will be discussed in more detail in Sec. X. Of greatest importance, the axial oscillatory frequency is shifted by an amount $\Delta\omega_z$, which is proportional to the classical energy E_z in the axial oscillation,

$$\frac{\Delta\omega_z}{\omega_z} \approx \tfrac{3}{2}C_4\frac{\overline{z}^2}{d^2} \approx \tfrac{3}{2}C_4\frac{E_z}{eV_0} . \qquad (9.3)$$

This follows from the work in Sec. III (with λ in the equations of Sec. III.D given by $\lambda=3C_4/4$). A fluctuation in the axial excitation energy E_z, when the axial motion is kept in thermal contact with the effective detection resistor, produces a fluctuation in the axial frequency and hence an additional axial linewidth. The anharmonicity thus limits the detection of small shifts in the axial frequency that are crucial for precision geonium measurements. It is extremely important to tune the trapping potential to make C_4 as close to zero as possible. Without such anharmonicity compensation, in fact, the precision electron, positron, and proton experiments described earlier would not have been possible. The most common method for reducing C_4 is to adjust a compensation potential V_c, which is applied to extra compensation electrodes introduced into the trap to minimize the axial linewidth or the axial frequency shift that occurs in response to changes in the axial excitation energy E_z. Based upon the observed linewidths and shifts, Eq. (9.3) can be used to estimate the residual value of C_4. Without anharmonicity compensation, C_4 is typically between 10^{-1} and 10^{-2}, with the lowest $|C_4|$ realized being about 10^{-3} (Gabrielse and Dehmelt, 1981a). Compensated traps reduce this by about a factor of 20 (Van Dyck, Wineland, Ekstrom, and Dehmelt, 1976) to $|C_4| \lesssim 5\times10^{-5}$.

The effect of a nonvanishing coefficient C_2 is much less important in principle, but it has important consequences in practice. It represents an addition to the quadrupole potential for an idealized trap with the same ρ_0 and z_0, so that Eq. (2.7) for the axial frequency is modified to read

$$\omega_z^2 = \frac{eV_0}{md^2}(1+C_2) . \qquad (9.4)$$

This modification is not particularly serious as long as C_2 is stable, because changes in ω_z are the crucial observables for precision experiments, and the absolute values of V_0 and d are not known very precisely in any case. The complication in practice is that C_2 is generally a function of the compensation potential, as we shall discuss. The required adjustments in the compensation potential, to

make C_4 as small as possible, therefore produce corresponding shifts in the axial frequency which are highly undesirable [cf. the discussion following Eq. (9.13)].

To understand anharmonicity compensation in hyperbolic traps, consider the electrode model represented in Fig. 43. The hyperbolic endcap and ring electrodes are at potentials $V_0/2$ and $-V_0/2$, respectively, and the compensation electrode is at potential V_c. Gaps between electrodes are taken to be negligibly small. The model compensation electrode is symmetric about the asymptote and is characterized by the opening angle α, but this angle is not crucial. Axial symmetry about the z axis is assumed, as is symmetry under the reflection $z\to-z$. Holes and slits in the electrodes are not yet included (see Sec. IX.F). The boundary conditions just described are the superposition of the boundary conditions for V_2 and the boundary conditions in Figs. 44(a) and 44(b), so that

$$V = V_2 + V_c\varphi_c + V_0\Delta\varphi_0 . \qquad (9.5)$$

Here φ_c is the dimensionless potential produced by the compensation electrode boundary at value 1 and the endcap and ring boundaries at 0, as shown in Fig. 44(a). The potential $\Delta\varphi_0$ satisfies the boundary conditions shown in Fig. 44(b), which differ only on the compensation boundary. The sum of $\Delta\varphi_0$ and V_2/V_0 corresponds to a compensation boundary at value 0 and the endcap and ring boundaries at $\tfrac{1}{2}$ and $-\tfrac{1}{2}$, respectively. The potential at each point on the dashed compensation boundary in Fig. 44(b) is thus equal to $-V_2/V_0$, and this dashed boundary is not an equipotential. The potential V for traps with a certain relative geometry are fully characterized by only these two solutions to Laplace's equation (in addition to V_2) for all V_0, V_c, and d.

Near the center of the trap

$$\Delta\varphi_0 = \tfrac{1}{2} \sum_{\substack{k=0 \\ \text{even}}}^{\infty} C_k^{(0)} \left[\frac{r}{d}\right]^k P_k(\cos\theta) \qquad (9.6)$$
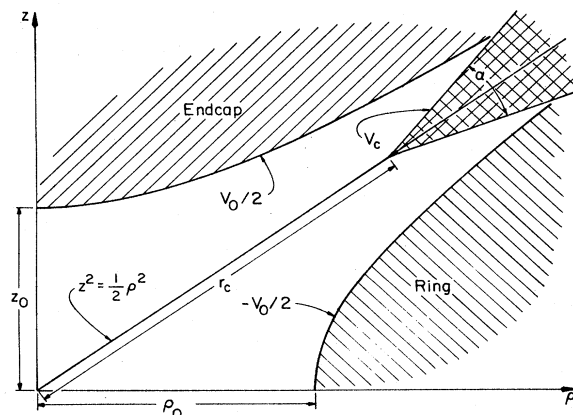

FIG. 43. Model of a hyperbolic Penning trap, which is invariant under rotations about the z axis and under the reflection $z\to-z$.

---

[30]The small effects arising from nonzero C_6 and departures from symmetry under the reflection $z\to-z$ are discussed by Gabrielse (1983) and in more detail by Gabrielse and MacKintosh (1984).

(a)

(b)
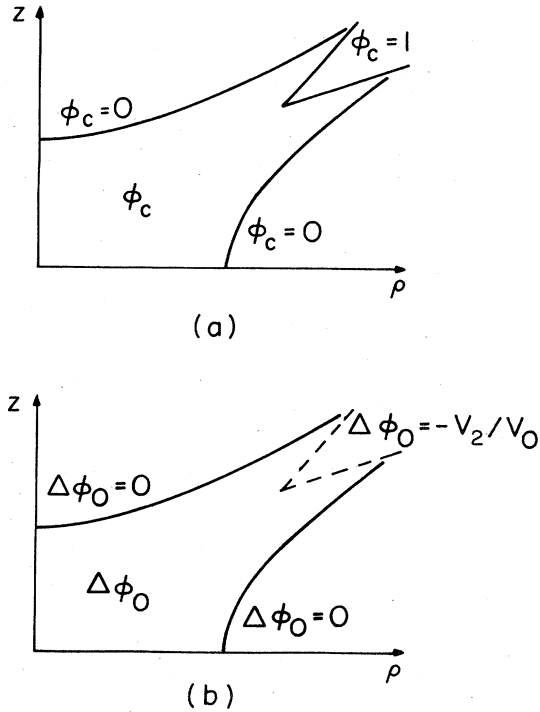
FIG. 44. Boundary conditions that uniquely determine the solutions to Laplace's equation, φ_c in (a) and $\Delta\varphi_0$ in (b). The boundaries are invariant under rotations about the z axis and under the reflection $z \to -z$. The dashed boundary in (b), located at the compensation electrode, is not an equipotential. The potential at each point on this boundary is given by the value of $-V_2/V_0$ at this point.

and

$$\varphi_c = \frac{1}{2} \sum_{\substack{k=0 \\ \text{even}}}^{\infty} D_k \left[\frac{r}{d} \right]^k P_k(\cos\theta) , \qquad (9.7)$$

with the expansion coefficients $C_k^{(0)}$ and D_k independent of particular values of V_0, V_c, and d. These expansion coefficients can be calculated by solving Laplace's equation for the appropriate boundary conditions and then fitting the potential near the center to the above series. Comparing the expansion for V in Eq. (9.2) with the above expansions shows that

$$C_k = C_k^{(0)} + D_k \frac{V_c}{V_0} . \qquad (9.8)$$

Anharmonicity compensation occurs when the compensation potential V_c is chosen so that the two terms on the right cancel each other for $k=4$. The major part of the trap anharmonicity is tuned out, since the net C_4 vanishes (see footnote 30).

Notice that the D_k are not only dimensionless expansion coefficients for φ_c, but also measure the amount that the net C_k is changed by a given change in the normalized compensation potential V_c/V_0. To emphasize this, the D_k may be written as a derivative of C_k,

$$D_k = V_0 \frac{\partial C_k}{\partial V_c} . \qquad (9.9)$$

Since C_2 is related to the net trapping potential by Eq. (9.4),

$$D_2 = \frac{\partial\omega_z/\partial V_c}{\partial\omega_z/\partial V_0} , \qquad (9.10)$$

so that D_2 is the relative sensitivity of the axial frequency ω_z to variations in the compensation and trapping potentials, V_c and V_0. Less stability is required in the compensation potential V_c than in the trapping potential V_0 by a factor of D_2. This relative sensitivity is easily measurable and has ranged from 10^{-2} to 10^{-3} for useful traps. In the precision experiments mentioned earlier, standard cells are used for V_0 to provide a sufficiently stable and noise-free axial frequency. A stability of $\Delta V_0/V_0$ better than 10^{-8} is required to permit the observations of 1-Hz shifts in an axial frequency of 62 MHz that are often made.

While a D_2 of small magnitude is clearly desirable to minimize the dependence of the axial frequency on the compensation potential, a large

$$D_4 = V_0 \frac{\partial C_4}{\partial V_c} \qquad (9.11)$$

is also desirable to ensure that C_4 can be made to vanish with a reasonable compensation potential. It is thus desirable to minimize the ratio

$$\gamma \equiv \frac{D_2}{D_4} , \qquad (9.12)$$

which may be defined as a quality factor for compensated Penning traps.

B. Anharmonicity compensation in asymptotically symmetric traps

All of the precision measurements that we have reviewed were carried out in Penning traps such as the electron trap in Fig. 1, with electrodes along hyperbola of revolution [Eqs. (2.3) and (2.4)], that are related by $\rho_0 = \sqrt{2}z_0$. Far from the center of the trap, such electrodes become symmetric about the quadrupole asymptote. While a better electrode configuration is discussed in the next section, we shall use this asymptotically symmetric configuration of electrodes to illustrate the simple physics principles involved. Details of the numerical calculation are given in Gabrielse (1983) and will not be reviewed here.

The most important phenomenon involved in compensated Penning traps with hyperbolic electrodes is the severe electrostatic screening of the compensation potential by the endcap and ring electrodes. The screening is dramatically demonstrated in Fig. 45, where D_2 is plotted versus the normalized distance to the compression electrodes from the center of the trap, r_c/d. Notice that the logarithmic vertical scale covers nearly 7 orders of magni-

tude, while r_c/d on the horizontal scale changes only by a factor of 4 as it covers the range over which compensated, asymptotically symmetric traps have been built. The rapid fall is due to the severe screening of the compensation potential by the endcap and ring electrodes. As is well known, the potential at a large distance r from a line of charge or from a flat electrode is reduced by a factor of $\exp(-\pi r/l)$ when grounded, perfectly conducting plates spaced a distance l apart are located as shown in Figs. 46(a) or 46(b), respectively. Locally, the slopes of the curves in Fig. 45 are approximately described by this exponential factor, with $r = r_c$ and l taken to be the separation of the endcap and ring electrodes at $r = r_c$.

The solid line in Fig. 45 represents the tunability D_2 for flat compensation electrodes perpendicular to the asymptote ($\alpha = 180°$ in Fig. 43). The dashed line represents $\alpha = 30°$. These two choices are plotted to allow comparison with three available values measured using Eq. (9.10). The comparison is encouraging considering that the traps are imperfectly modeled and especially considering the steep fall with increasing r_c/d. For the proton trap (the smallest of the three traps in Fig. 45), a change in the location of the compensation electrode by only 2.5×10^{-2} cm changes D_2 by a factor of 3.

The strong electrostatic screening not only causes the rapid fall of D_2 with increasing r_c/d but also completely shapes the potential that penetrates to the center of the trap. The result is that the ratios of the D_k are essentially independent of r_c/d. To illustrate this, the ratios of D_4, D_6, and D_8 to D_2 are plotted in Fig. 47 versus the location of the compensation electrode r_c/d, although we shall discuss only D_4 here. The ratios (and hence the

FIG. 46. Two-dimensional screening models. Parallel flat plate electrodes screen the potential produced (a) by a line of charge and (b) by a perpendicular electrode. In both cases, for $r \gg l$, a screening of the potentials by a factor of $\exp(-\pi r/l)$ results.

shape of the potential near the center of the trap) converge with increasing r_c/d to values that are strikingly independent of both the location of the compensation electrodes (represented by r_c/d) and the shape of the compensation electrode (as modeled by α). Even for compensation electrodes extending as far into the trap as $r_c/d = 1.5$
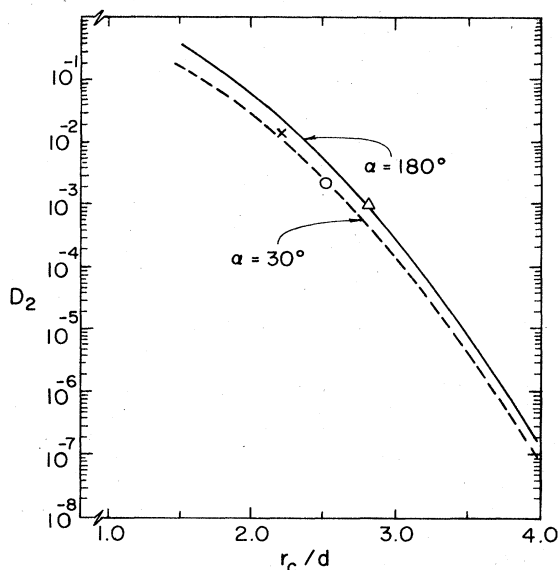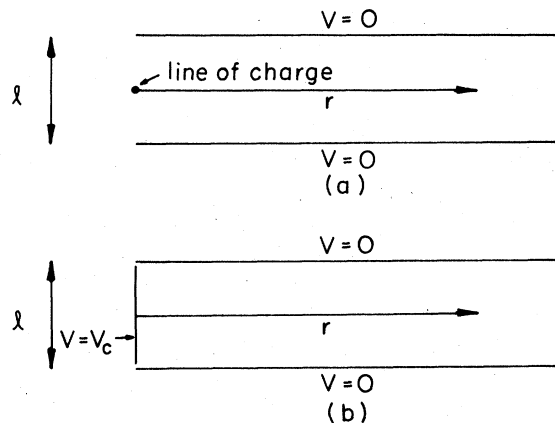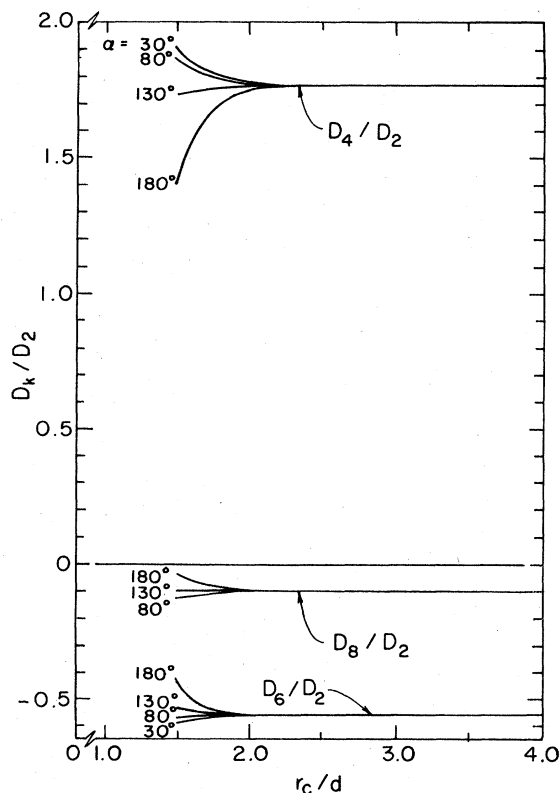

FIG. 45. The steep dependence of D_2 upon r_c/d, the normalized distance of the compensation electrode from the center of the trap. Dashed and solid lines are for $\alpha = 180°$ and $\alpha = 30°$, respectively, and several experimental values (from Gabrielse, 1983, and Van Dyck et al., 1985) are indicated.

FIG. 47. Ratios of the D_k for asymptotically symmetric Penning traps, with $\rho_0 = \sqrt{2} z_0$. The D_k individually change by nearly 7 orders of magnitude over the range of r_c/d plotted here.

the dependence on the opening angle of the compensation electrodes α is slight enough to allow plotting the ratios on a linear vertical scale (in Fig. 47), despite the fact that the D_k are individually changing by 7 orders of magnitude over the range of r_c/d covered in this figure. For a particular r_c/d, changing from $\alpha=180°$ to $0°$ reduces each D_k by roughly a factor of 2. The choice of α for the compensation electrode is therefore only important insofar as it establishes an effective r_c/d for an equivalent flat compensation electrode.

The quality factor γ in Eq. (9.12) is the inverse of the ratio plotted as the upper curve in Fig. 47. As we have discussed, it represents the undesirable change $\Delta\omega_z/\omega_z$ per unit change ΔC_4 brought about by adjusting the compensation potential. The successful compensated traps referred to earlier all have $r_c/d>2$ and thus share the same quality factor

$$\gamma=0.56 , \tag{9.13}$$

which is independent of the location and shape of the compensation electrode. Innovations in the shape and location of the compensation electrodes clearly have not improved and cannot improve the quality factor for asymptotically symmetric traps. This means that a rather common change of $\Delta C_4=10^{-4}$ made by adjusting the compensation potential is accompanied by a shift in the axial frequency of 2 kHz out of 60 MHz. This is very much larger than an axial resolution of 1 Hz. Each small adjustment of the compensation potential must thus be accompanied by a relatively large and troublesome adjustment of the trapping potential to keep the axial frequency constant.

Once D_4 is accurately known for a particular trap, the net C_4 can be changed in calibrated increments by appropriate changes in the compensation potential. The sensitivity of axial linewidths and frequency shifts to such incremental changes gives a good indication of the minimum residual C_4 that can be obtained. For traps that are well modeled by Fig. 43, the calculated values of the D_4 can be used directly. For example, a value of $D_2=-1\times10^{-3}$ and $D_4=-2\times10^{-3}$ is calculated for the electron trap represented in Fig. 1, so that a change in V_c/V_0 of approximately 5% is required to produce a change $\Delta C_4\approx10^{-4}$. A value of $D_2=-1\times10^{-3}$ is also measured in this trap. For hyperbolic traps with compensation electrodes that are not well modeled by Fig. 43, advantage may be taken of the insensitivity of γ to the location and shape of the compensation electrode. The measured value of D_2 and the calculated value of γ may be used to deduce D_4, with

$$D_4=D_2/\gamma . \tag{9.14}$$

For example, the first compensated trap[31] has ring and endcap electrodes truncated at $r/d\approx2.2$. Its compensa-

---

[31]Figure 9 of Van Dyck, Wineland, Ekstrom, and Dehmelt (1976).

tion electrodes are located much further back at $r_c/d\approx2.7$ and are not symmetric about the asymptote. Because γ is essentially independent of the shape and location of the compensation electrodes for $r_c/d>2.2$, the calculated value of $\gamma=0.56$ for asymptotically symmetric traps along with the measured value of $D_2\approx-3\times10^{-3}$ suggests that a change in V_c/V_0 of 2% produces a change $\Delta C_4\approx10^{-4}$, just as occurs for a trap with flat compensation electrodes at $r_c/d\approx2.6$.

So far we have concentrated upon anharmonicity compensation, rather than upon sources of anharmonicity, and we shall continue this emphasis until Sec. IX.F. We thus have studied φ_c and its expansion coefficients D_k, rather than $\Delta\varphi_0$ and its expansion coefficients $C_k^{(0)}$. The reason is that $\Delta\varphi_0$ as defined by the boundary conditions in Fig. 44(b) provides an unrealistic picture of a laboratory trap insofar as holes and slits in the quadrupole electrodes are neglected, along with electrode misalignments and imperfections. According to Eq. (9.8), the net C_4 can be made to vanish in a compensated trap by applying a compensation potential V_c/V_0 given by $-C_4^{(0)}/D_4$. This ratio must be very small when there are no holes, slits, or misalignments. To see this, recall that the boundary conditions for $\Delta\varphi_0$ and φ_c (in Fig. 44) differ only on the compensation electrode boundary. On this boundary, $\varphi_c=1$, but $\Delta\varphi_0$ varies from $\Delta\varphi_0=-\frac{1}{2}$ at the endcap to $\Delta\varphi_0=\frac{1}{2}$ at the ring. The strong electrostatic screening discussed earlier similarly shapes the equipotentials that penetrate from the compensation electrode to the center of the trap for both $\Delta\varphi_0$ and φ_c. The substantial dipole character of $\Delta\varphi_0$ on the compensation boundary (as viewed from the center of the trap), by contrast to the monopole character of φ_c on the same boundary, makes $\Delta\varphi_0$ much smaller than φ_c near the center of the trap. Thus, for the boundaries in Fig. 44, $C_4^{(0)}$ is much smaller than its counterpart D_4 and $|V_c/V_0|\ll1$. For asymptotically symmetric traps, this ratio is less than several percent.

For perfect electrodes like those shown in Fig. 43, which are hyperbolic except for truncation and the presence of compensation electrodes, the compensation potential required to tune the trap optimally would therefore always be very close to $V_c=0$, which is midway between the endcap and ring potentials. In actual traps, however, the situation is much different. Existing traps tune up at much larger values of V_c/V_0, ranging from -2 for the trap in Fig. 1 (Gabrielse, 1983) to -0.1 for a positron trap and 10 for a proton trap (Van Dyck, 1982). These compensation potentials correspond to values of $C_4^{(0)}$ of -4×10^{-3}, -2×10^{-3}, and 5×10^{-2}, which are considerably larger than the truncation effects. Possible sources of the additional anharmonicity include holes and slits in the electrodes (which we consider in Sec. IX.F) and misalignments of the electrodes, which we shall eventually conclude are more important.

C. Orthogonalized hyperbolic Penning trap

Once the dominant role of electrostatic screening is appreciated, it becomes clear that the quality factor $\gamma\approx0.56$

realized in all of the existing, compensated Penning traps is not at all optimal and could be improved. For an asymptotically symmetric trap, with $\rho_0 = \sqrt{2}z_0$, the endcap electrodes are closer to the center of the trap and to the asymptote than is the ring. The endcaps thus screen the compensation potential more strongly than does the ring. Equipotentials for φ_c which penetrate near the center of the trap thus are not symmetric about the asymptote $z^2 = \frac{1}{2}\rho^2$, but are shifted lower in the trap. On the other hand, for a trap with $\rho_0 = z_0$, the ring screens more strongly than the endcap, so that an equipotential penetrating near the center of the trap is shifted above the asymptote.

Intermediate between $\rho = \sqrt{2}z_0$ and $\rho_0 = z_0$ (at $\rho_0 \approx 1.16 z_0$, as we shall soon see), the screening of the compensation potential by the endcap and the ring electrodes are equal in the sense that an equipotential penetrating near the center of the trap is symmetric about the asymptote near the center of the trap. To appreciate the importance of this symmetry, recall that near the center of the trap

$$\varphi_c \approx \text{const} + \tfrac{1}{2}D_2 \left[\frac{r}{d} \right]^2 P_2(\cos\theta) + \cdots . \qquad (9.15)$$

The leading nonconstant term is proportional to the Legendre polynomial $P_2(\cos\theta)$, which vanishes on the

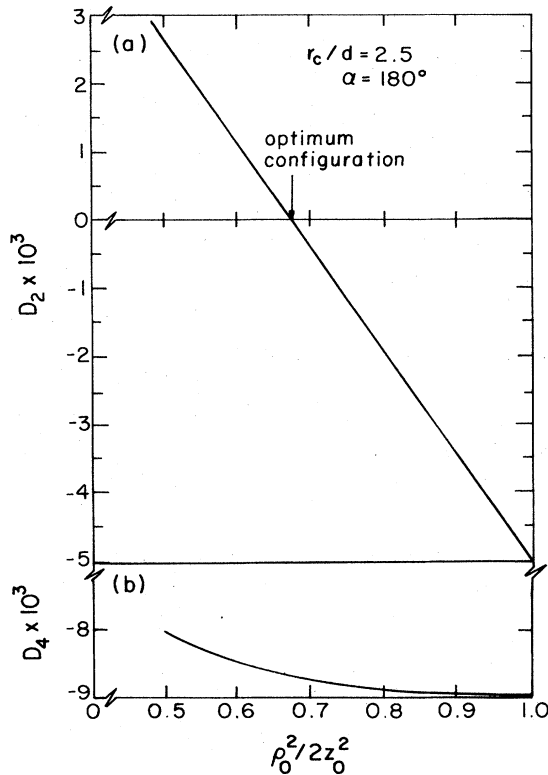

FIG. 48. Illustration of the different dependence of D_2 and D_4 upon the choice of hyperbolic surfaces represented by $\rho^2/2z_0^2$. The optimal electrode configuration with $\gamma = D_2 = 0$ is indicated.
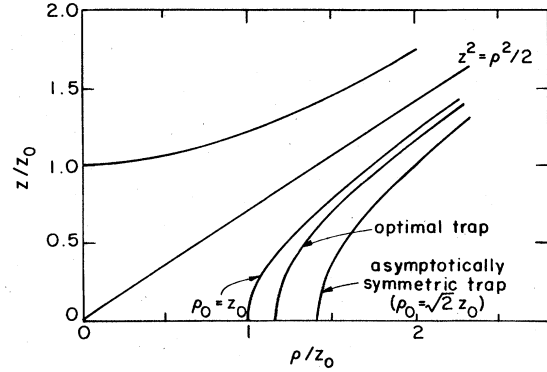

FIG. 49. Contours for the hyperbolic electrodes for a trap with $\rho_0 = z_0$, an optimal trap, and an asymptotically symmetric trap. The endcap contour is shared by all three configurations.

asymptote. Therefore φ_c is antisymmetric for small increases and decreases in θ about this asymptote. Thus symmetry about the quadrupole asymptote near the center of the trap corresponds to $D_2 \approx 0$. The Legendre polynomial $P_4(\cos\theta)$, on the other hand, changes very little across the quadrupole asymptote. Thus symmetry about the asymptote near the center of the trap corresponds roughly to the desired condition, $\gamma \approx 0$.

An illustration of the vanishing of D_2, and hence of γ as well, is shown in Fig. 48. Both D_2 and D_4 are plotted as functions of $\rho_0^2/2z_0^2$ ranging from $\frac{1}{2}$ (corresponding to $\rho_0 = z_0$) to 1 (corresponding to an asymptotically symmetric trap with $\rho_0 = \sqrt{2}z_0$). The choice of abscissa was made because D_2 varies linearly with $\rho_0^2/2z_0^2$ (for reasons not completely clear), going through zero at $\rho_0^2/2z_0^2 \approx 0.674$ [Fig. 48(a)]. By contrast, D_4 [Fig. 48(b)] varies only slightly, as might be expected since $P_4(\cos\theta)$ varies only slightly across the asymptote. The different electrode contours are plotted together in Fig. 49.

The location of the zero crossing point is represented in Fig. 50 as a function of the normalized location of the compensation electrode, r_c/d. Notice that for $r_c/d > 2$, the value of ρ_0/z_0 required to produce $\gamma = 0$ varies from

$$\rho_0/z_0 = 1.16 \qquad (9.16)$$

by less than 0.1% (Gabrielse, 1983). Higher-order D_k (with $k > 2$) for this electrode configuration are essential-
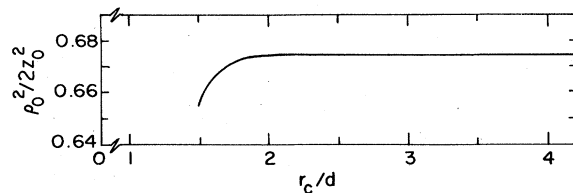

FIG. 50. Optimal value of $\rho_0^2/2z_0^2$ which makes $\gamma = 0$ as a function of r_c/d for $\alpha = 180°$.

ly the same for a particular r_c/d as those represented earlier for asymptotically symmetric traps in Figs. 45 and 47. In practice, it will be impossible to achieve $\gamma = 0$ because of imperfect mechanical tolerances. A factor of 20 or more improvement over the $\gamma = 0.56$ currently being achieved in asymptotically symmetric traps seems to be quite possible given the tolerances that are presently achieved.

D. Additional axial forces

If a potential $\frac{1}{2}V_A$ is added to the upper endcap electrode and a potential $-\frac{1}{2}V_A$ is added to the lower endcap, the trapped particle experiences the additional potential

$$\Delta V = V_A \varphi_A , \qquad (9.17)$$

where φ_A is a solution to Laplace's equation that is antisymmetric under the reflection $z \to -z$ and satisfies the boundary conditions shown in Fig. 51. The added potential V_A can be static or it can oscillate, provided that the wavelength associated with the oscillation is large compared to the trap dimensions. An additional static potential is sometimes used to translate the center of the axial motion. Oscillatory potential additions are used to drive the axial oscillation and to describe the resistive damping of the axial oscillation.

Near the center of the trap, φ_A can be expanded in the small ratio r/z_0 so that

$$\varphi_A = \frac{1}{2} \sum_{\substack{k=1 \\ \text{odd}}}^{\infty} c_k \left[\frac{r}{z_0} \right]^k P_k(\cos\theta) . \qquad (9.18)$$

This expansion differs from the earlier expansions for φ_c and $\Delta\varphi_0$ in that only terms with odd k are included, because φ_A is antisymmetric under the reflection $z \to -z$, and in that distances are scaled by z_0 rather than by d.
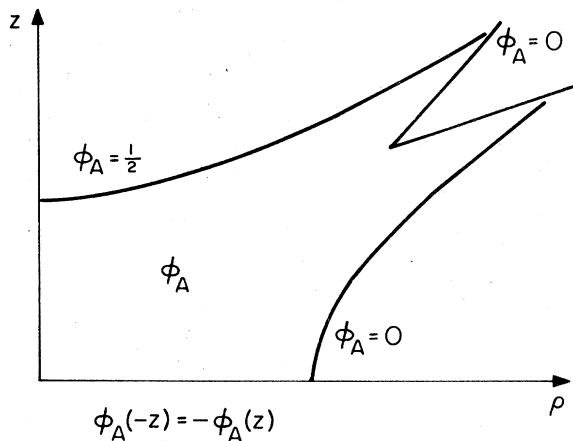

FIG. 51. Boundary conditions satisfied by φ_A. The boundary is invariant under rotations about the z axis and is antisymmetric under the reflection $z \to -z$.
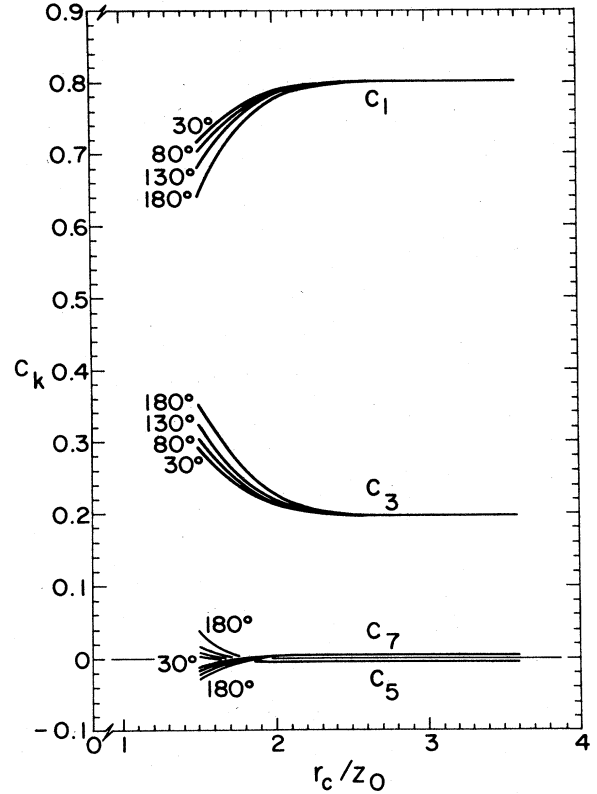

FIG. 52. The coefficients c_k for asymptotically symmetric Penning traps as a function of normalized distance to the compensation electrode for various α.

This latter choice makes it much easier to consider limiting cases, as we shall see. Figure 52 shows c_1 through c_7 for asymptotically symmetric traps. The coefficients are plotted as a function of the location of the compensation electrode (r_c/z_0 in Fig. 43) for variously shaped compensation electrodes (α in Fig. 43). The coefficients converge to limiting values,

$$c_1 \approx 0.80 \qquad (9.19)$$

and

$$c_3 \approx 0.20 , \qquad (9.20)$$

that are independent of both α and r_c/z_0 in the region $r_c/z_0 > 2.2$ where precision traps have been built. A surprise here is that $c_1 + c_3 \approx 1.00$ and that c_5 and c_7 are significantly smaller. This means that φ_A is described very well over much of the trapping volume by just the first two terms of expansion (9.18). The relaxation calculation of these coefficients is given in Gabrielse (1984).

Nearest the center of the trap, $\varphi_A \approx c_1 z/2z_0$. This is the potential of a spatially uniform electric field, and the constant κ used in Sec. III.A is equal to c_1. Parallel plate endcaps at $z = \pm z_0$ and a ring pulled back to $\rho_0 \gg z_0$ are thus described by $c_1 = 1$ with all other c_k vanishing. In Fig. 53, values of c_k are plotted as a function of $\rho_0^2/2z_0^2$. The dashed curves pertain to flat endcaps at $z = \pm z_0$ and
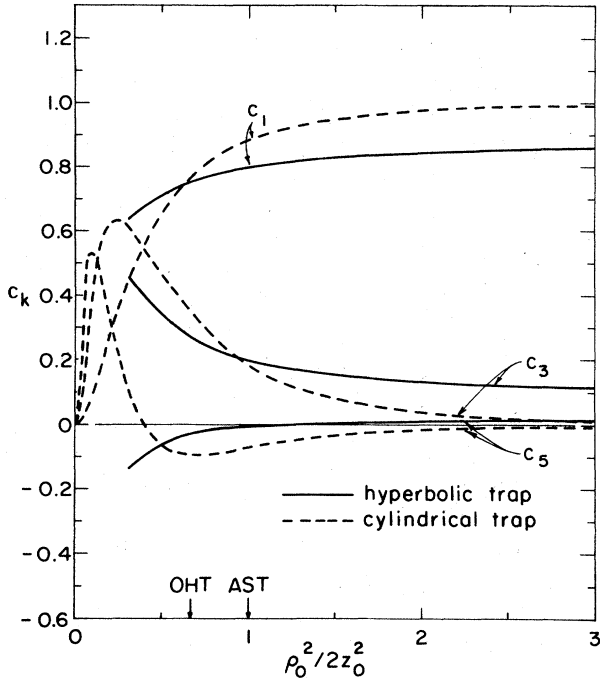
FIG. 53. The coefficients c_k for a hyperbolic Penning trap (with $r_c/d = 2.5$ and $\alpha = 180°$) and a cylindrical Penning trap. AST and OHT designate asymptotically symmetric and orthogonalized hyperbolic traps, respectively.

a cylindrical ring of radius ρ_0 (Fig. 54, discussed in Sec. IX.E below). The parallel plate limits are approached in the limit of large ring radius at the right of the figure. For decreasing ring radius, the ring screens the field through the center of the trap, so that c_1 is increasingly reduced from unity. In the limit of $\rho_0 \to 0$, the c_k for the
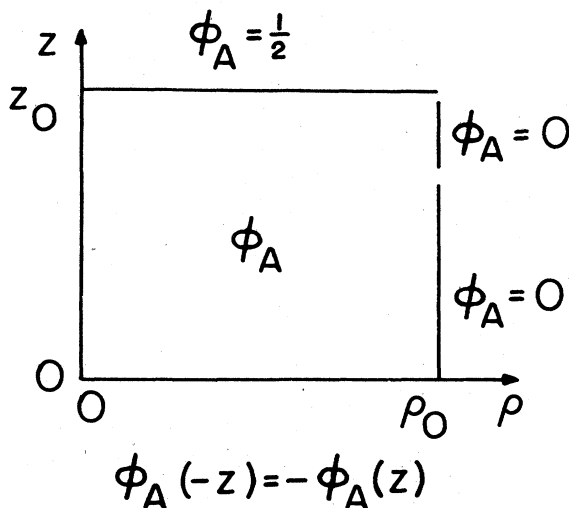

FIG. 54. Boundary condition satisfied by φ_A in the case of a cylindrical Penning trap. The boundaries are invariant under rotations about the z axis and are antisymmetric under the reflection $z \to -z$.

cylindrical trap vanish because of the onset of exponential screening.

The situation is qualitatively the same for hyperbolic electrodes, as illustrated by the solid curves in Fig. 53, but with slight quantitative differences. Hyperbolic endcaps are pulled back farther from the center of the trap than are flat endplates. The electric field through the center of the trap is therefore reduced (compared to the flat plates), so that the limiting value of c_1 is below unity. As the radius of the ring is decreased, more and more electric field lines from the endcap terminate on the ring instead of penetrating through the center of the trap and terminating on the other endcap. Thus c_1 decreases and both c_3 and c_5 increase in magnitude to compensate. These changes are much less severe for the hyperbolic trap because the hyperbolic ring screens less severely than does the cylindrical ring. The compensation electrodes pertaining to Fig. 53 are flat ($\alpha = 180°$) and are located at $r_c/d = 2.5$. These choices ensure that the calculated c_k are essentially independent of both α and r_c/z_0 for each ρ_0/z_0. The asymptotically symmetric configuration ($\rho_0 = \sqrt{2}z_0$) and the proposed, orthogonalized configuration reviewed in Sec. IX.C (with $\rho_0 \approx 1.16z_0$) are both indicated by arrows. A much wider range of $\rho_0/2z_0^2$ is plotted than is immediately useful for trap construction to display the limiting values of the c_k.

The shift of the center of the axial oscillation is an important diagnostic tool for measuring the size and location of a magnetic bottle (Sec. VI; Van Dyck, Schwinberg, and Bailey, 1980). A small static potential V_A shifts the center of the axial oscillation, but also shifts the frequency of this oscillation. Including this small antisymmetric potential, the total potential along the axis of the trap is given to a good approximation by

$$V = \tfrac{1}{2}V_0 \left[\frac{z}{d}\right]^2 + \tfrac{1}{2}V_A\left[c_1\left[\frac{z}{z_0}\right] + c_3\left[\frac{z}{z_0}\right]^3\right] + \text{const} .$$

$$(9.21)$$

This potential has a minimum at an equilibrium position $z = z_e$, which is the new center of the axial oscillation. To a good approximation,

$$\frac{z_e}{z_0} = -\frac{1}{2}\left[\frac{d}{z_0}\right]^2 \frac{V_A}{V_0}c_1 .$$

$$(9.22)$$

For the special case of an asymptotically symmetric trap, $z_e = -0.40z_0(V_A/V_0)$. For example, an antisymmetric potential of $V_A = 1$ V applied to the trap shown in Fig. 1 with $V_0 = 10$ V yields $z_e \approx 4 \times 10^{-2}z_0$, which is a displacement of 10^{-2} cm.

The product c_1c_3 can be measured easily. Expanding the potential (9.21) about the equilibrium position by writing $z = z_e + u$ yields

$$V \approx \tfrac{1}{2}V_0\frac{u^2}{d^2}\left[1 + 3c_3\frac{V_A}{V_0}\frac{z_ed^2}{z_0^3}\right] + \text{const} .$$

$$(9.23)$$

Hence the axial "spring constant" is also altered by the

addition of the antisymmetric potential V_A, and the axial frequency ω_z is changed to $\omega_z + \Delta\omega_z$, where

$$\frac{\Delta\omega_z}{\omega_z} \simeq -\frac{3}{4}\left[\frac{d}{z_0}\right]^4 c_1 c_3 \left[\frac{V_A}{V_0}\right]^2 . \qquad (9.24)$$

The product $c_1 c_3$ is measured by observing the quadratic dependence of the axial frequency shift upon V_A. The measured and calculated values agree in several traps where they have been measured.[32]

E. Cylindrical Penning traps

A simple cylindrical ring with flat endplates has often been used (with a magnetic field) to contain large clouds of particles. We examine here the possibility of including compensation electrodes in such a configuration to make the trapping potential sufficiently harmonic for precision single-particle spectroscopy. The compensated Penning trap of Fig. 55 is an analog of the hyperbolic electrodes modeled in Fig. 43. The ring and compensation electrodes are stacked cylinders of radius ρ_0, and the endcap electrodes are flat plates located a distance z_0 from the center of the trap. Cylindrical compensation electrodes of width Δz_c, adjacent to the two endcaps, are used to tune the trapping potential. This electrode configuration is much simpler to construct than are hyperbolic electrodes. The cylindrical electrodes also form a microwave cavity with well-known properties, a feature we made use of in Sec. VIII. Over a small trapping volume at the center of the cylindrical trap, the potential can be made to be a very good quadrupole potential. The key idea, which makes the cylindrical electrode configuration potentially useful for precision work, is that a judicious choice of the relative dimensions of the electrodes can make the axial oscillation frequency of a trapped particle completely independent of the necessary adjustments in the compensation potential. In the notation we used earlier, this corresponds to $\gamma = 0$. For large-amplitude oscillations within the trap, however, cylindrical electrodes will clearly be inferior to electrodes located on the equipotentials of the desired quadrupole potential. This may lead to difficulties in initial adjustments of the compensation potential, where larger-amplitude oscillations of the trapped particle can
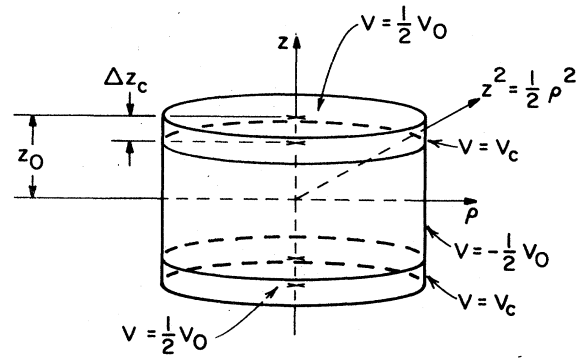

FIG. 55. Electrically compensated cylindrical trap.

be required. Our discussion is based upon the detailed treatment by Gabrielse and MacKintosh (1984).

The boundary conditions for the potential V within a cylindrical trap are shown in Fig. 56(a). These boundary conditions can be written as the sum of the boundary conditions for φ_0 in Fig. 56(b) and those for φ_c in Fig. 56(c). Invariance under rotations about the z axis and under the reflection $z \rightarrow -z$ is assumed. Thus

$$V = V_0\varphi_0 + V_c\varphi_c . \qquad (9.25)$$

Near the center of the trap,

$$\varphi_0 = \frac{1}{2}\sum_{\substack{k=0 \\ \text{even}}}^{\infty} (\delta_{k2} + C_k^{(0)})\left[\frac{r}{d}\right]^k P_k(\cos\theta) , \qquad (9.26)$$

and the potential φ_c is expanded exactly as for hyperbolic electrodes in Eq. (9.7). This choice, and the continued use of the trap dimension $d = [(z_0^2 + \rho_0^2/2)/2]^{1/2}$ from Eq. (2.5), make the expansion coefficients $C_k^{(0)}$ and D_k used here directly comparable to the coefficients used in previous sections for the hyperbolic traps.

One nice feature of a cylindrical Penning trap is that the potential within a trap can be obtained analytically using standard boundary-value techniques (e.g., Chap. III of Jackson, 1975). The nonvanishing expansion coefficients (k even) are given for $k \neq 0$ by

$$C_k^{(0)} = -\delta_{k2} + \frac{(-1)^{k/2}}{k!}\frac{\pi^{k-1}}{2^{k-3}}\left[\frac{d}{z_0}\right]^k \sum_{n=0}^{\infty}\frac{(-1)^{n+1}(2n+1)^{k-1}\cos^2[\frac{1}{2}(n+\frac{1}{2})\pi\Delta z_c/z_0]}{I_0[(n+\frac{1}{2})\pi\rho_0/z_0]} \qquad (9.27)$$

and

$$D_k = \frac{(-1)^{k/2}}{k!}\frac{\pi^{k-1}}{2^{k-3}}\left[\frac{d}{z_0}\right]^k \sum_{n=0}^{\infty}\frac{(-1)^n(2n+1)^{k-1}2\sin^2[\frac{1}{2}(n+\frac{1}{2})\pi\Delta z_c/z_0]}{I_0[(n+\frac{1}{2}\pi\rho_0/z_0]} . \qquad (9.28)$$

---

[32]The product $c_1 c_3$ has been measured by Van Dyck for a positron and a proton trap and by Gabrielse for the trap represented in Fig. 1.

FIG. 57. Lowest-order C_k for a cylindrical trap in the limit of a vanishing compensation electrode, $\Delta z_c \to 0$.
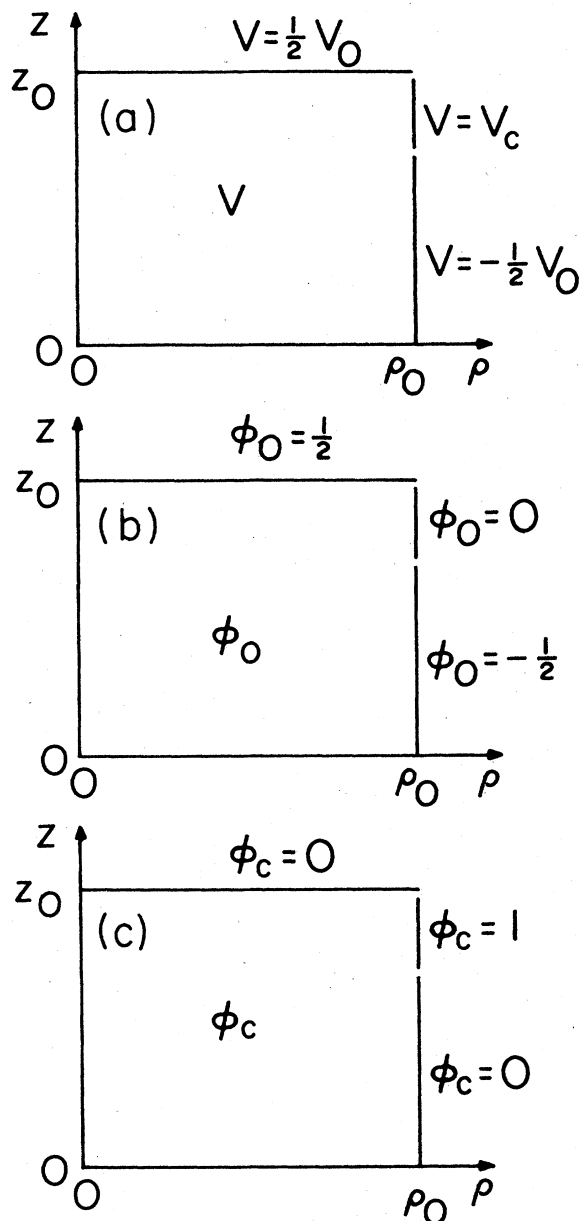

FIG. 56. Boundary conditions for the cylindrical trap in Fig. 55: (a) full potential V; (b) trapping potential φ_0; (c) compensation potential φ_c. Invariance under rotations about the z axis and under the reflection $z \to -z$ is assumed.

The coefficients are functions of only ρ_0/z_0 and $\Delta z_c/z_0$. The modified Bessel function I_0 ensures convergence with increasing n, since, for large arguments, $I_0(x)$ goes as $e^x/(2\pi x)^{1/2}$. The choice to scale distances with the trap dimension d (to allow direct comparison of the hyperbolic and cylindrical electrode geometries) slightly complicates these latter two expressions, since scaling by z_0 would be more natural here.

We first consider the simplest case with no compensation electrodes, $\Delta z_c \to 0$. This corresponds to a trap with only three electrodes, and the potential within this trap

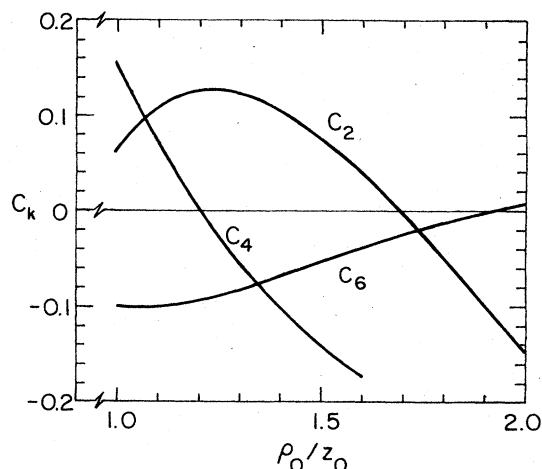cannot be electrically tuned. The coefficients D_k in Eq. (9.28) vanish term by term, so that the potential near the center of the trap is given by just the $C_k = C_k^{(0)}$ of Eq. (9.27). The lowest-order coefficients are plotted in Fig. 57 as a function of ρ_0/z_0. Not surprisingly, these coefficients are much larger than those typically obtained in hyperbolic traps, where $C_4 \approx 10^{-3}$ has been obtained without anharmonicity compensation. However, the leading anharmonicity coefficient, C_4, vanishes at $\rho_0/z_0 \approx 1.203$. For lower-precision applications, a cylindrical trap with such dimensions might well suffice.

The potential within such a trap can be improved during an experiment by mechanically adjusting ρ_0/z_0 about this value, by sliding an endcap in or out of the ring slightly. Such mechanical anharmonicity compensation has the very respectable quality factor $\gamma \approx -0.095$. Here we have generalized the definition of γ slightly to be

$$\gamma = \frac{\Delta C_2}{\Delta C_4}, \tag{9.29}$$

where ΔC_2 and ΔC_4 are small changes in the expansion coefficients C_2 and C_4 that result from the same adjustment of z_0/ρ_0. Achieving a reduction in anharmonicity comparable to that achieved in electrically compensated traps with hyperbolic electrodes requires very precise adjustment of z_0/ρ_0 to within 10^{-4}, since $\partial D_4/\partial(z_0/\rho_0) \approx 0.8$.

Electrical anharmonicity compensation requires a nonvanishing width of the compensation electrode, Δz_c. Although the electrodes correspond to those for an electrically compensated trap with hyperbolic electrodes, the situation differs significantly because the strong electrostatic screening is not present. However, for a given choice of Δz_c, a proper choice of ρ_0/z_0 will still make $D_2 = 0$, and hence the quality factor γ will vanish as well. In fact, the discussion associated with Eq. (9.15) can still be used to understand why this happens. The difference is that the relative proximity of the cylindrical ring and the flat endcaps shapes the equipotentials of φ_c near the center of the
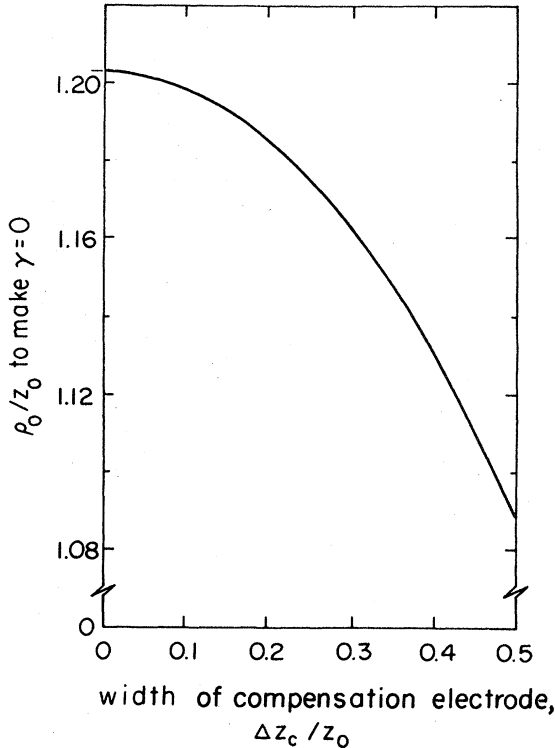
FIG. 58. The ratio ρ_0/z_0 required to make $\gamma = 0$, for a cylindrical Penning trap, as a function of the width of the compensation electrode.
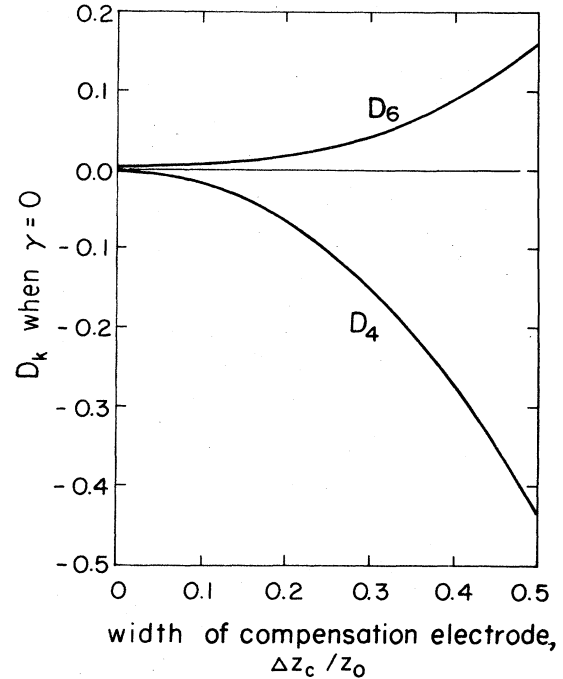

FIG. 59. The coefficients D_4 and D_6 as a function of the width of the compensation electrode, for a cylindrical trap with ρ_0/z_0 chosen to make $\gamma = 0$.

trap instead of the exponential screening. The ratio ρ_0/z_0 required to make $\gamma = 0$ is plotted in Fig. 58 as a function of the width of the compensation electrode. It varies only 10% for $\Delta z_c/z_0$ ranging from 0 to $\frac{1}{2}$ and varies about the value required to make γ vanish in a hyperbolic trap in Eq. (9.16). Mechanical imprecision in ρ_0/z_0 will, of course, prevent $\gamma = 0$ from being realized exactly. For traps with ρ_0/z_0 near the optimal value given in Fig. 58, the quality factor varies as $\partial \gamma / \partial (\rho_0/z_0) \approx 3$ over the range plotted. With achievable mechanical precisions in ρ_0/z_0 of order 10^{-3}, it should thus be possible to do much better than in the case of the existing hyperbolic traps with asymptotic symmetry.

The lack of the exponential electrostatic screening causes the coefficients D_k for $k > 2$ to be several orders of magnitude greater than for hyperbolic traps. This is illustrated in Fig. 59, where D_4 and D_6 are plotted as a function of the width of the compensation electrode, for cylindrical traps with ρ_0/z_0 chosen to make $\gamma = 0$. As a result, a much smaller change in the compensation potential is required to change D_4 by a given amount. The ratio of D_6 to D_4, however, is of the same order as for a hyperbolic trap.

Additional axial forces have already been discussed in Sec. IX.D. The coefficients c_k that pertain to a potential φ_A, which satisfies the boundary conditions in Fig. 54, were discussed and plotted in Fig. 53. These coefficients are obtained by solving for $\varphi_A - z/z_0$ using standard elec-

trostatics techniques. The result for $k > 0$ and odd is[33]

$$c_k = \delta_{k1} + \frac{2\pi^{k-1}(-1)^{(k-1)/2}}{k!} \sum_{n=1}^{\infty} \frac{(-1)^n n^{k-1}}{I_0(n\pi\rho_0/z_0)} .$$

(9.30)

This expression was evaluated to produce the dashed curves in Fig. 53. There is no qualitative difference from the hyperbolic case.

A compensated cylindrical electron trap is now being tested (Gabrielse and Helmerson, 1985). The relative width of the compensation electrode is given by $\Delta z_c/z_0 = 0.2$, and thus $\rho_0/z_0 = 1.186$ was chosen to make γ small. A trap size given by $z_0 = 0.385$ cm was selected to obtain the same relationship between the axial frequency and the applied trapping potential as pertains to the hyperbolic trap shown in Fig. 1. These dimensions are used in Sec. VIII because this trap is intended to be used in a study of the interaction of an electron cyclotron motion with the surrounding cylindrical microwave cavity. The cavity is formed by the electrodes of the cylindrical trap.

---

[33]A misprint in Gabrielse and MacKintosh (1984) omitted the $(-1)^n$ that appears in Eq. (9.30).

F. Holes and slits

In previous sections we focused upon the way that departures from a quadrupole potential within a trap could be tuned out by adjusting the potential on compensation electrodes. One source of the anharmonicity is holes and slits put into the electrodes to admit particles and various microwave and radio-frequency drives. In the notation of Sec. IX.A, these additions contribute to $C_4^{(0)}$. An estimate of the magnitude of these contributions is useful to determine whether D_4 is large enough so that $C_4^{(0)}$ can be canceled with a reasonable compensation potential [see Eq. (9.8)].

As a model, consider an infinite, parallel-plate capacitor. We designate the charge density on one plate by σ. If a hole of radius h is put into this plate, with h much smaller than the plate spacing, the charge distribution on the plate is modified only near the hole. The modification of the potential between the plates can thus be described by perturbation multipoles located at the small hole. There will be no monopole component to this charge distribution, since a monopole potential cannot satisfy the boundary condition that the potential be constant along the plate. The leading perturbation multipole that satisfies this boundary condition is a dipole, $\mathbf{p}$. At a distance $\mathbf{r}$ from the hole, the leading modification of the potential between the plates is thus given by

$$\delta\varphi = \frac{\mathbf{p}\cdot\mathbf{r}}{r^3} . \tag{9.31}$$

The dipole is perpendicular to the plate and has a magnitude scaled by the charge displaced by the small hole, $\sigma\pi h^2$, and by the radius h. Thus

$$p = \alpha(\sigma\pi h^2)h , \tag{9.32}$$

with α a constant of order unity.[34] Similarly, a slit of width $2s$ in one of the plates, with s small compared to the separation of the plates, makes a dipole moment per unit length that can also be scaled in terms of the displaced charge so that

$$p/l = \beta(\sigma 2s)s , \tag{9.33}$$

with β a constant of order unity.[35]

A simple qualitative argument establishes the direction of the dipole. Consider a conducting plate with a surface charge density σ, which we shall take to be positive for this illustration. Suppose now that a deep hole of radius

---

[34]For a very thin conducting plate with a hole of radius h, the problem can be solved exactly in prolate spheroidal coordinates (e.g., Chap. V of Smythe, 1950), with the result that $\alpha = 4/3\pi = 0.424$. For a very deep hole, $\alpha = 0.356$ was calculated by a numerical, relaxation technique (Gabrielse and MacKintosh, 1984).

[35]The potential for an infinitely deep slit in one of the conducting plates, of width $2s$, can be solved by a conformal mapping to give $\beta = 2/\pi = 0.637$.

h is put into this plate. As a first approximation, we can model the hole by superimposing a negative charge $-\sigma\pi h^2$ at the surface of the hole. This perturbation monopole distribution must be canceled, however, by the additional positive charge that is attracted to it and builds up around the outside rim of the hole and within the hole. A dipole remains, originating on the negative charge and pointing into the hole along its axis. A deep hole in a positively charged plate thus can be modeled by a dipole that points into the deep hole. A similar argument holds for a slit.

For a first quantitative estimate, we assume that the flat-plate model is appropriate. From Eqs. (9.31) and (9.32), we deduce that the hole of radius h makes a contribution to C_4 of order

$$\delta C_4^{(0)} \sim \left[\frac{h}{d}\right]^3 , \tag{9.34}$$

with the assumption that the hole is away from the center of the trap by a distance of order of the trap dimension d. This contribution is typically rather small. In the electron trap represented in Fig. 1, for example, there is a small hole in the endcap, on the z axis, and the contribution to C_4 from Eq. (9.34) is of order 10^{-5}. This trap also has a slit in the ring electrode that is centered on the xy plane. We observe that the length of this slit is of order d and use Eqs. (9.31) and (9.33) to conclude that the contribution to C_4 is of order

$$\delta C_4^{(0)} \sim \left[\frac{s}{d}\right]^2 . \tag{9.35}$$

For the example trap this contribution is of order 5×10^{-4}.

The electrodes of a hyperbolic Penning trap are not plane surfaces, of course. We might expect, therefore, that a perturbation monopole is present and important because of the curvature of the electrodes. On the other hand, the hole diameter h (or the slit width $2s$) is typically very small compared to the radius of curvature for the electrodes, which is of order of the trap dimension d. Since the effective monopole must vanish in the limit where the radius of curvature is very large, we expect that the naive monopole strength of a hole, $-\sigma\pi h^2$, must be reduced by at least a factor of h/d. This additional factor causes the possible monopole contribution to be of the same order as was estimated for the dipole in Eq. (9.34). Similarly, an additional factor s/d reduces possible slit monopole contributions to the order estimated in Eq. (9.35).

The contributions to $C_4^{(0)}$ estimated here are significantly smaller in magnitude than the measured values discussed at the end of Sec. IX.B. Holes and slits thus seem not to be the most important sources of anharmonicity in traps with dimensions comparable to those for the electron trap represented in Fig. 1. The source of the anharmonicity being tuned out seems to be located instead in electrode misalignments, rather than in the very small holes and slits being used. For larger holes and slits, how-

ever, and for smaller trap dimensions, the contribution to $C_4^{(0)}$ could be very significant.

X. PERTURBATION SUMMARY

As we discussed at length in Sec. II, the energy levels of an ideal Penning trap are given by the sum of the energies of the independent, noninteracting submotions

$$E^{(0)}(nkls) = E_n + E_k + E_l + E_s . \tag{10.1}$$

Here

$$E_n = (n + \tfrac{1}{2})\hbar\omega_c' , \tag{10.2a}$$

$$E_k = (k + \tfrac{1}{2})\hbar\omega_z , \tag{10.2b}$$

$$E_l = -(l + \tfrac{1}{2})\hbar\omega_m , \tag{10.2c}$$

$$E_s = \frac{s}{2}\hbar\omega_s , \tag{10.2d}$$

are the energies in the cyclotron, axial, magnetron, and spin motions, respectively. The quantum numbers (n,k,l) take on non-negative integer values, while $s = \pm 1$ is twice the spin projection eigenvalue. In sections subsequent to II, we considered small additions and corrections to this ideal trap model due to departures from an electrostatic quadrupole potential (Secs. III.D and IX), the addition of a weak magnetic bottle (Sec. VI.A), and to relativistic corrections (Sec. VII.B). Thus the energy level $E^{(0)}(nkls)$ in Eq. (10.1) is corrected to

$$E(nkls) = E^{(0)}(nkls) + \Delta E(nkls) , \tag{10.3}$$

where $\Delta E(nkls)$ is the sum of the small perturbations.

Shifts in the energy levels produce corresponding shifts in the measurable eigenfrequencies $\omega \to \omega + \Delta\omega$, which we display in this section in a simple form. This simple form permits a ready comparison of the perturbations, which can be very useful when planning an experiment and when evaluating possible systematic effects. We shall evaluate the frequency shifts in the classical limit. This gives manageable expressions and is justified, since the shifts are nearly always too small to observe unless the quantum numbers are enough to warrant a classical description. Thus with ω_a denoting generically the frequency corresponding to the motion with the quantum number a ($a = n,k,l$), we have[36]

$$\Delta\omega_a = \frac{1}{\hbar} \frac{\partial \Delta E}{\partial a} . \tag{10.4}$$

In the classical limit, the unperturbed frequencies can also

be expressed as a derivative with respect to the quantum number,

$$\omega_a = \frac{1}{\hbar} \frac{dE_a}{da} , \tag{10.5}$$

where E_n, E_k, E_l are the energies of the independent, unperturbed motions. Hence

$$\frac{\Delta\omega_a}{\omega_a} = \frac{\partial \Delta E}{\partial E_a} . \tag{10.6}$$

This is purely a classical result but, as we have just seen, its derivation is easy using quantum mechanics. Indeed, the frequency shifts could, of course, be computed in an entirely classical fashion, but they are most easily derived from the classical limit of the more familiar quantum energy shift formula, which is the path that we are following. In general, Eq. (10.6) implies that

$$\frac{\partial}{\partial E_a}\left[\frac{\Delta\omega_b}{\omega_b}\right] = \frac{\partial}{\partial E_b}\left[\frac{\Delta\omega_a}{\omega_a}\right] . \tag{10.7}$$

The particular perturbations that we are considering give energy shifts ΔE in the classical limit that are quadratic forms in $E_a E_b$. Hence Eq. (10.6) yields

$$\frac{\Delta\omega_a}{\omega_a} = \sum_{b=n,k,l} M_{ab} E_b , \tag{10.8}$$

with Eq. (10.7) requiring that the response matrix M_{ab} be symmetrical,

$$M_{ab} = M_{ba} . \tag{10.9}$$

The spin motion has not yet been included, since it is intrinsically quantum mechanical, with the spin frequency perturbation given by

$$\Delta\omega_s = \frac{1}{\hbar}[\Delta E(nkl, +1) - \Delta E(nkl, -1)] . \tag{10.10}$$

In the classical limit for the other motions, the leading contributions to $\Delta\omega_s$ are linear in the E_a. Including these in the matrix formulation, we have

$$\begin{bmatrix} \Delta\omega_c'/\omega_c' \\ \Delta\omega_z/\omega_z \\ \Delta\omega_m/\omega_m \\ \Delta\omega_s/\omega_s \end{bmatrix} = M \begin{bmatrix} E_n \\ E_k \\ E_l \end{bmatrix} . \tag{10.11}$$

The matrix M is now extended to a 4×3 matrix, with the upper 3×3 part the previous symmetrical 3×3 matrix. The matrix element M_{ab} gives the fractional frequency shift in the motion labeled by a in terms of the energy of excitation of the motion labeled by b. The matrix is not square because the spin energy is neglected in the classical approximation. This matrix formulation displays a considerable amount of information in a compact fashion: Each of the three perturbations (electrostatic, magnetic bottle, and relativistic) produces shifts in each of the four eigenfrequencies. Each of these shifts, in turn, is linear in

---

[36]There is actually an additional negative sign on the right-hand side of Eqs. (10.4) and (10.5) for the magnetron frequencies, $a = m$. This negative sign in the definition for $\Delta\omega_m$ and ω_m derives from the inverted energy levels for the magnetron motion. The sign difference, however, cancels in the ratio in Eq. (10.6).

the three classical excitation energies.

As the first application of this formalism, we consider the leading deviation from a pure quadrupole potential given by

$$\Delta V = V_0 C_4 \frac{z^4 - 3z^2\rho^2 + 3(\rho^2)^2/8}{2d^4} . \tag{10.12}$$

Although some consequences of this perturbation were discussed in Secs. III.D and IX, the resulting energy shift

$$\Delta E(nkls) = \langle nkls \mid e\Delta V \mid nkls \rangle \tag{10.13}$$

has yet to be calculated. Using the operator methods introduced in Sec. II.B, one finds that

$$\Delta E(nkls) = e \left[\frac{V_0 C_4}{2d^4} \right] \left[\frac{\hbar}{m} \right]^2 \left[\frac{3}{2\omega_z^2}(k^2 + k + \tfrac{1}{2}) - 3\frac{1}{\omega_z}\frac{1}{\omega_c' - \omega_m}(2k + 1)(n + l + 1) \right.$$

$$\left. + \frac{3}{2}\frac{1}{(\omega_c' - \omega_m)^2}[(n + \tfrac{1}{2})^2 + (l + \tfrac{1}{2})^2 + 4(n + \tfrac{1}{2})(l + \tfrac{1}{2}) + \tfrac{1}{2}] \right] . \tag{10.14}$$

In the classical limit, this perturbation is described by the response matrix

$$M_V = \frac{6C_4}{eV_0} \begin{bmatrix} \tfrac{1}{4}(\omega_z/\omega_c')^4 & -\tfrac{1}{2}(\omega_z/\omega_c')^2 & -(\omega_z/\omega_c')^2 \\ -\tfrac{1}{2}(\omega_z/\omega_c')^2 & \tfrac{1}{4} & 1 \\ -(\omega_z/\omega_c')^2 & 1 & 1 \\ 0 & 0 & 0 \end{bmatrix} . \tag{10.15}$$

Because it is generally true that $\omega_m \ll \omega_c'$, factors of $\omega_c' - \omega_m$ have been approximated by ω_c' to simplify this matrix. The spin frequency ω_s is not shifted by an electrostatic potential, and hence the row of zeros. The matrix elements are, of course, proportional to the strength of the perturbation C_4, and they are scaled by the quadrupole well depth eV_0.

All matrix elements which involve the cyclotron frequency are smaller by an additional factor $(\omega_z/\omega_c')^2$. For the typical electron and proton conditions in Tables I and II, this factor is 1×10^{-7} and 2×10^{-2}, respectively. The electrostatic perturbation in Eq. (10.12) is of much less importance for the cyclotron motion than for the axial and magnetron motions. The cyclotron motion is much more tightly bound, and it is much more difficult to excite it enough to make a cyclotron radius that is appreciable compared to the trap dimension.

As an illustration of how the matrix (10.15) can be used, we notice that the electrostatic anharmonicity produces a shift in the axial frequency

$$\frac{\Delta\omega_z}{\omega_z} = \frac{6C_4}{eV_0}(\tfrac{1}{4}E_k + E_l) , \tag{10.16}$$

neglecting the small cyclotron contribution. The term proportional to the axial excitation energy E_k is used to monitor and minimize C_4 as part of the anharmonicity compensation procedure (Sec. IX). The term proportional to the magnetron energy E_l has been used to monitor the magnetron energy as sideband cooling and heating drives were applied (see Fig. 21 and the related discussion in Sec. III.B). These uses require that the corresponding matrix elements for the other perturbations be much smaller, as they are. The cooling and heating experiment was done in a trap without a magnetic bottle.

The addition of a weak magnetic bottle adds

$$\Delta \mathbf{B} = B_2[(z^2 - \rho^2/2)\hat{B} - (\hat{B}\cdot\mathbf{z})\rho] \tag{10.17}$$

to the spatially homogeneous trapping field $\mathbf{B}$ of an ideal Penning trap, as discussed in Sec. VI.A. The corresponding energy shift ΔE is given in Eq. (6.7), whose classical limit yields the matrix

$$M_B = \frac{\Delta\tilde{\omega}_z}{\omega_z}\frac{1}{\hbar\omega_c'} \begin{bmatrix} -(\omega_z/\omega_c')^2 & 1 & 2 \\ 1 & 0 & -1 \\ 2 & -1 & -2 \\ -(\omega_z/\omega_c')^2 & 1 & 2 \end{bmatrix} , \tag{10.18}$$

where

$$\frac{\Delta\tilde{\omega}_z}{\omega_z}\frac{1}{\hbar\omega_c'} = \frac{1}{2m\omega_m\omega_c'}\frac{B_2}{|B|} = \frac{1}{eV_0}\left[\frac{B_2 d^2}{|B|}\right] \tag{10.19}$$

is purely a classical coefficient. Again the very good approximation that $\omega_m \ll \omega_c'$ is used to simplify this matrix. The perturbation matrix is scaled by the small ratio $\Delta\tilde{\omega}_z/\omega_z$, and the energy scale is set by $\hbar\omega_c'$. The constant $\Delta\tilde{\omega}_z$ is a measure of the strength of the magnetic bottle, which is defined more precisely in Eq. (6.4). To recall the significance of this parameter, we observe that

$$\Delta\omega_z = \Delta\tilde{\omega}_z \left[\frac{E_n - E_l}{\hbar\omega_c'} \right] . \tag{10.20}$$

A change in the cyclotron excitation by an energy $\hbar\omega_c'$ or one quantum number yields a shift in the axial frequency equal to $\Delta\tilde{\omega}_z$. This shift is the primary detection mechanism used in the measurements of the lepton g values that

make use of a magnetic bottle (Sec. VI.A). Again, the calibrated use of this effect presupposes that corresponding matrix elements of the other perturbations are much smaller. Comparing Eqs. (10.16) and (10.20) shows that the anharmonicity constant C_4 must be tuned out to be much smaller than 4×10^{-5} for an electron if the shift due to the magnetron energy E_l is to be unaffected by electrostatic anharmonicity.

The axial frequency is not shifted by an axial excitation because there is no coupling to any magnetic field in this case; hence the zero in the matrix in Eq. (10.18). In the very good approximation that $\omega_m \ll \omega_z \ll \omega_c'$, the magnetic bottle produces identical shifts in the spin and cyclotron frequencies. The shifts from cyclotron excitations are weaker by the very small factor $(\omega_z/\omega_c')^2$.

Finally, we turn to relativistic corrections. These are different from the electrostatic and magnetic bottle perturbations insofar as they are not under experimental control. The relativistic corrections thus provide a fixed limit upon the sizes of elements in the response matrix. The relativistic corrections to the energy levels were derived in Sec. VII.B. The classical limit of Eq. (7.48) yields

$$M_R = \frac{-1}{mc^2} \begin{bmatrix} 1 & \frac{1}{2} & -(\omega_z/\omega_c')^2 \\ \frac{1}{2} & \frac{3}{8} & -\frac{1}{4}(\omega_z/\omega_c')^2 \\ -(\omega_z/\omega_c')^2 & -\frac{1}{4}(\omega_z/\omega_c')^2 & \frac{1}{4}(\omega_z/\omega_c')^4 \\ \frac{2}{9} & \frac{1}{2} & -(\omega_z/\omega_c')^2 \end{bmatrix} . \tag{10.21}$$

To simplify this matrix we have made use of the hierarchy $\omega_m \ll \omega_z \ll \omega_c'$. The energy scale is set by the rest energy of the trapped particle.

Many of the elements in this matrix can be understood very simply when the leading relativistic correction acts as a mass shift. For example, increasing the energy in the cyclotron motion from 0 to E_n effectively increases the mass of the trapped particles from the rest mass m to $m + \Delta m$, where

$$\frac{\Delta m}{m} = \frac{E_n}{mc^2} . \tag{10.22}$$

The axial frequency is inversely proportional to the square root of the mass of the particle [Eq. (2.7)] and thus shifts down by

$$\frac{\Delta \omega_z}{\omega_z} = -\frac{E_n}{2mc^2} , \tag{10.23}$$

which corresponds to the M_{21} element in the relativistic response matrix (10.21). This relativistic mass increase is being used to detect cyclotron excitations in the recent experiments discussed in Sec. VII.A. The cyclotron frequency, on the other hand, is inversely proportional to the mass [Eq. (2.1)]. Thus a cyclotron excitation energy E_n and the resulting relativistic mass increase cause the cyclotron frequency to shift as well, giving

$$\frac{\Delta \omega_c'}{\omega_c'} = -\frac{E_n}{mc^2} , \tag{10.24}$$

which corresponds to M_{11}. This shift makes the observed cyclotron motion for a single trapped electron anharmonic, as discussed at length in Sec. VII.A.

We close this discussion with two observations. First, the kinetic energy in the magnetron motion is very low. Thus the relativistic mass increase and resulting frequency shifts are also very low, as evidenced by the very small ratios $(\omega_z/\omega_c')^2$ that appear in the response matrix whenever a ω_z/ω_c' in the magnetron frequency or a magnetron excitation energy is involved. Second, the rest energy mc^2 sets the scale and it will be difficult to observe relativistic shifts for trapped protons or heavier particles. The other perturbations will typically dominate.

ACKNOWLEDGMENTS

REFERENCES

Barton, G., and H. Grotch, 1977, J. Phys. A 10, 1201.
Bloch, F., and A. Siegert, 1940, Phys. Rev. 57, 522.
Boulware, D. G., and L. S. Brown, 1985, Phys. Rev. Lett. 55, 133.
Boulware, D. G., L. S. Brown, and T. Lee, 1985, Phys. Rev. D 32, 729.
Brown, L. S., 1983, Phys. Rev. A 27, 857.
Brown, L. S., 1984, Phys. Rev. Lett. 52, 2013.
Brown, L. S., 1985, Ann. Phys. (N.Y.) 159, 62.
Brown, L. S., and G. Gabrielse, 1982, Phys. Rev. A 25, 2423.
Brown, L. S., G. Gabrielse, K. Helmerson, and J. Tan, 1985a, Phys. Rev. Lett. 55, 44.
Brown, L. S., G. Gabrielse, K. Helmerson, and J. Tan, 1985b, Phys. Rev. A 32, 3204.
Chance, R. R., A. Prock, and R. Silbey, 1975, J. Chem. Phys. 63, 771.
Conti, R., D. Newman, A. Rich, and E. Sweetman, 1984, in Precision Measurements and Fundamental Constants II, edited by B. N. Taylor and W. D. Phillips (Natl. Bur. Stand. U.S. Spec. Publ. 617), p. 207.
Dehmelt, H. G., 1981, in Atomic Physics 7, edited by D. K. Kleppner and F. T. Pipkin (Plenum, New York).
Dehmelt, H. G., 1983, Yearbook of Science and Technology (McGraw-Hill, New York), p. 204.

Dehmelt, H. G., and P. Ekstrom, 1973, Bull. Am. Phys. Soc. **18**, 727.

Drexhage, K. H., 1974, in *Progress in Optics XII,* edited by E. Wolf (North-Holland, Amsterdam), p. 165.

Ekstrom, P., and D. J. Wineland, 1980, Sci. Am. **243**, 105.

Field, J. H., E. Picasso, and F. Combley, 1979, Usp. Fiz. Nauk. **127**, 553 [Sov. Phys.—Usp. **22**, 199 (1979)].

Fischbach, E., and N. Nakagawa, 1984a, Phys. Rev. D **30**, 2356.

Fischbach, E., and N. Nakagawa, 1984b, Phys. Lett. B **149**, 504.

Gabrielse, G., 1983, Phys. Rev. A **27**, 2277.

Gabrielse, G., 1984, Phys. Rev. A **29**, 462.

Gabrielse, G., and H. G. Dehmelt, 1981a, in *Precision Measurements and Fundamental Constants II,* edited by B. N. Taylor and W. D. Phillips (Natl. Bur. Stand. U.S. Spec. Publ. 617), p. 219.

Gabrielse, G., and H. G. Dehmelt, 1981b, Bull. Am. Phys. Soc. **26**, 598.

Gabrielse, G., and H. G. Dehmelt, 1982 (unpublished).

Gabrielse, G., and H. G. Dehmelt, 1985, Phys. Rev. Lett. **55**, 67.

Gabrielse, G., H. G. Dehmelt, and W. Kells, 1985, Phys. Rev. Lett. **54**, 537.

Gabrielse, G., and X. Helmerson, 1985 (unpublished).

Gabrielse, G, H. Kalinowsky, and W. Kells, 1985, in *Physics with Antiprotons at LEAR in the ACOL Era,* edited by U. Gastaldi, R. Klapisch, J. M. Richard, and J. Trán Thanh Ván (Editions Frontieres, Gif sur Yvette, France), p. 665.

Gabrielse, G., and F. C. MacKintosh, 1984, Int. J. Mass Spectrom. Ion Processes **57**, 1.

Gärtner, G., and E. Klempt, 1978, Z. Phys. **287**, 1.

Gräff, G., H. Kalinowsky, and J. Traut, 1980, Z. Phys. **297**, 35.

Gräff, G., and E. Klempt, 1967, Z. Naturforsch. **229**, 1960.

Gräff, G., E. Klempt, and G. Werth, 1969, Z. Phys. **222**, 201.

Handbook of Physics and Chemistry, 1983 (Chemical Rubber, Cleveland).

Hulet, R., E. S. Hilfer, and D. Kleppner, 1985, Phys. Rev. Lett. **55**, 2137.

Itano, W. M., and D. J. Wineland, 1982, Phys. Rev. A **25**, 35.

Jackson, J. D., 1975, *Classical Electrodynamics,* 2nd ed. (Wiley, New York).

Kaplan, A. E., 1982, Phys. Rev. Lett. **48**, 138.

Kinoshita, T., and J. Sapirstein, 1984, in *Atomic Physics 9,* edited by R. S. Van Dyck, Jr., and E. N. Forston (World Scientific, Singapore).

Kleppner, D., 1981, Phys. Rev. Lett. **47**, 233.

Kuhn, H., 1970, J. Chem. Phys. **53**, 101.

Landau, L. D., and E. M. Lifshitz, 1976, *Mechanics* (Pergamon, New York).

Milonni, P. W., and P. L. Knight, 1973, Opt. Commun. **9**, 119.

Morawitz, H., 1969, Phys. Rev. **187**, 1792.

Newton, R. G., 1954, Phys. Rev. **96**, 523.

Particle Data Group, 1984, Rev. Mod. Phys. **56**, S1.

Penning, F. M., 1936, Physica (Utrecht) **3**, 873.

Philpott, M. R., 1973, Chem. Phys. Lett. **19**, 435.

Purcell, E. M., 1946, Phys. Rev. **69**, 681.

Rich, A., and J. C. Wesley, 1972, Rev. Mod. Phys. **44**, 250.

Schupp, A. A., R. W. Pidd, and H. R. Crane, 1961, Phys. Rev. **121**, 1.

Schwinberg, P. B., and R. S. Van Dyck, Jr., 1981, Bull. Am. Phys. Soc. **26**, 598.

Schwinberg, P. B., R. S. Van Dyck, Jr., and H. G. Dehmelt, 1979, Bull. Am. Phys. Soc. **24**, 1202.

Schwinberg, P. B., R. S. Van Dyck, Jr., and H. G. Dehmelt, 1981a, Phys. Lett. A **81**, 119.

Schwinberg, P. B., R. S. Van Dyck, Jr., and H. G. Dehmelt, 1981b, Phys. Rev. Lett. **47**, 1679.

Shockley, W., 1938, J. Appl. Phys. **9**, 635.

Sirkis, M., and N. Holonyak, 1966, Am. J. Phys. **34**, 943.

Smythe, W. R., 1950, *Static and Dynamic Electricity* (McGraw-Hill, New York).

Sokolov, A. A., and Yu. G. Pavlenko, 1965, Opt. Spectrosc. **22**, 1.

Stehle, P., 1970, Phys. Rev. A **2**, 102.

Svozil, K., 1985, Phys. Rev. Lett. **54**, 742.

Thompson, J., 1982, private communication.

Tsai, W.-Y., and A. Yildiz, 1973, Phys. Rev. D **8**, 3446.

Van Dyck, R. S. Jr., 1982 (unpublished).

Van Dyck, R. S., Jr., P. A. Ekstrom, and H. G. Dehmelt, 1976, Nature **262**, 776.

Van Dyck, R. S., Jr., and G. Gabrielse, 1982 (unpublished).

Van Dyck, R. S., Jr., F. L. Moore, D. L. Farnham, and P. B. Schwinberg, 1985, Intl. J. Mass Spectrom. Ion Phys. **66**, 327.

Van Dyck, R. S., Jr., F. L. Moore, D. L. Farnham, and P. B. Schwinberg, 1986, Rev. Sci. Inst. (to be published).

Van Dyck, R. S., Jr., and P. B. Schwinberg, 1981, Phys. Rev. Lett. **47**, 395.

Van Dyck, R. S., Jr., P. B. Schwinberg, and S. H. Bailey, 1980, in *Atomic Masses and Fundamental Constants 6,* edited by J. A. Nolen and W. Benenson (Plenum, New York).

Van Dyck, R. S., Jr., P. B. Schwinberg, and H. G. Dehmelt, 1977, Phys. Rev. Lett. **38**, 1679.

Van Dyck, R. S., Jr., P. B. Schwinberg, and H. G. Dehmelt, 1978, in *New Frontiers in High Energy Physics,* edited by B. Kursunoglu, A. Perlmutter, and L. Scott (Plenum, New York).

Van Dyck, R. S., Jr., P. B. Schwinberg, and H. G. Dehmelt, 1984, in *Atomic Physics 9,* edited by R. S. Van Dyck, Jr. and E. N. Fortson (World Scientific, Singapore).

Van Dyck, R. S., Jr., P. B. Schwinberg, and H. G. Dehmelt, 1985 (unpublished).

Van Dyck, R. S., Jr., D. J. Wineland, P. A. Ekstrom, and H. G. Dehmelt, 1976, Appl. Phys. Lett. **28**, 446.

Vyatchanin, S. P., 1977, Dok. Akad. Nauk. SSSR **234**, 1295 [Sov. Phys.—Dokl. **22**, 321 (1977)].

Walls, F. L., 1970, Ph.D. thesis (University of Washington).

Walls, F. L., and H. G. Dehmelt, 1968, Phys. Rev. Lett. **21**, 127.

Wilkinson, D. T., and H. R. Crane, 1963, Phys. Rev. **130**, 852.

Wineland, D. J., 1979, J. Appl. Phys. **50**, 2528, Appendix.

Wineland, D. J., J. J. Bollinger, and W. M. Itano, 1983, Phys. Rev. Lett. **50**, 628; **50**, 1333(E).

Wineland, D. J., and H. G. Dehmelt, 1975a, Intl. J. Mass Spectrom. Ion Phys. **16**, 338; **19** 251(E).

Wineland, D. J., and H. G. Dehmelt, 1975b, J. Appl. Phys. **46**, 919.

Wineland, D. J., P. Ekstrom, and H. G. Dehmelt, 1973, Phys. Rev. Lett. **31**, 1279.

Wineland, D. J., and W. M. Itano, 1979, Phys. Rev. A **20**, 1521.

Wineland, D. J., W. M. Itano, J. C. Bergquist, J. J. Bollinger, and J. D. Prestage, 1984, in *Atomic Physics 9,* edited by R. S. Van Dyck and E. N. Fortson (World Scientific, Singapore).

Wineland, D. J., W. M. Itano, and R. S. Van Dyck, Jr., 1984, Adv. At. Mol. Phys. **19**, 135.